Spring 2018

Engineering surfaces using photopolymerization to improve cochlear implant materials

Braden Lynn Leigh
University of Iowa

ENGINEERING SURFACES USING PHOTOPOLYMERIZATION TO IMPROVE COCHLEAR IMPLANT MATERIALS

by

Braden Lynn Leigh

A thesis submitted in partial fulfillment
of the requirements for the Doctor of Philosophy
degree in Chemical and Biochemical Engineering in the
Graduate College of
The University of Iowa

May 2018

Thesis Supervisor: Professor C. Allan Guymon

Graduate College
The University of Iowa
Iowa City, Iowa

CERTIFICATE OF APPROVAL

_____

PH.D. THESIS

_____

This is to certify that the Ph.D. thesis of

Braden Lynn Leigh

has been approved by the Examining Committee for
the thesis requirement for the Doctor of Philosophy degree
in Chemical and Biochemical Engineering at the May 2018 graduation.

Thesis Committee: _____
C. Allan Guymon, Thesis Supervisor

_____
Marlan Hansen

_____
Jennifer Fiegel

_____
Julie Jessop

_____
David Rethwisch

To my parents, children, and dear wife who have filled my life with joy

After climbing a great hill, one only finds that there are many more hills to climb

-Nelson Mandela, *Long Walk to Freedom*

ACKNOWLEDGEMENTS

I would like to first thank my research adviser Dr. Allan Guymon for his contributions to my success as a graduate student. His dedication to my success in research and development as a professional have been constant and indispensable to my career. Dr. Guymon has helped me to substantially improve my technical communication skills, both writing and presenting, by providing invaluable feedback on manuscripts and presentations. He also provided me with a great undergraduate research experience for a summer as an REU student. Dr. Guymon's ambitious attitude is infectious and encouraged me to present my research and network with professionals from science and engineering.

Dr. Marlan Hansen has also been an excellent mentor and collaborator during my graduate school experience. His contribution to the research project and this work have been significant and indispensable. I have enjoyed his optimism and creativity in meeting the challenges associated with graduate school. I am so grateful for his attitude and humor through stressful times and his willingness to mentor me individually, both professionally and personally. More could be said about his influence and guidance on my graduate school experience but suffice it to say that I am profoundly grateful for his mentorship. There have also been many outstanding members from Dr. Hansen's research lab who were invaluable to the project. Linjing Xu, Elise Cheng, Na Shen, Mark Ramirez, Reid Bartholomew and Kristy Truong have all contributed significantly.

The many graduate students from the Guymon lab have also played a role to my success including Clint Cook, Kristan Worthington, Jon Scholte, Jacob McLaughlin, Brian Green, Erion Hasa, Dan Lippert, Huayang Fang, and importantly Brad Tuft, who provided much of the prior work and training for the project. These individuals have helped edit manuscripts, abstracts, and

posters, while providing valuable feedback for presentations and research. Not only have they contributed to my professional success but have also made the time here much more enjoyable. I have also had the opportunity to work with two undergraduates Corinne Andresen and Alexis Derk. These two were both instrumental in the data collection for the manuscripts we have published.

I have also had the opportunity to be associated with many exceptional professors prior to my graduate studies. I would like to thank Dr. Ty Redd for his eccentric style and exciting personality that pushed me to work hard and pursue my dreams and Dr. Amber McConnel, who was an exemplary mentor and helped me realize my potential.

I would not be where I am today had I not been born to such outstanding and exceptional parents. William and Julie Leigh have provided me with everything I needed to succeed and have believed in and supported me through my educational pursuits. I thank them for their example and dedication to my success. I also thank my father and mother-in-law, Robert and Christine Foisy, for their crucial help along the way.

Finally, I thank my dear wife, Camille, for her unwavering support and love as I have pursued this degree. I could not ask for a better friend and mother to our children. I thank her for the confidence in me as I completed my Ph.D.

ABSTRACT

Cochlear implants (CIs) help to restore basic auditory function in patients who are deaf or have profound hearing loss. However, CI patients suffer from limited voice and tonal perception due to spatial separation between the stimulating CI electrode and the receptor spiral ganglion neurons (SGNs). Directed regeneration of proximate SGN axons may improve tonal performance and implant fidelity by decreasing the spatial separation between the CI electrode and the neural receptor. Additionally, fibrous scar tissue formation on the surface of implanted electrodes further decreases tonal perception through current attenuation and spreading resulting in late-term hearing loss. Thus, designing surfaces that induce favorable responses from neural tissues will be necessary in overcoming signal resolution barriers. In this work, the inherent spatial and temporal control of photopolymerization was used to functionalize surfaces with topographical and biochemical micropatterns that control the outgrowth of neural and other cell types. First, laminin, a cell adhesion protein was patterned using a photodeactivation process onto methacrylate polymer surfaces and was shown to direct the growth of spiral ganglion neurons (SGN), the primary auditory neural receptors. These protein patterns could even overcome low amplitude/high periodicity competing topographical cues. Additionally, glass substrates were patterned with linear zwitterionic polymers and fibroblasts, astrocytes, and Schwann cells all showed dramatically decreased cell adhesion on 100 μm precocity patterns. Further, SGN neurites showed excellent alignment to these same patterns. Next, poly(dimethyl siloxane) (PDMS) was coated with a crosslinked zwitterionic thin film using a single step photografting/photopolymerization process to covalently bind the hydrogel to PDMS. These coated surfaces showed dramatically lower levels of protein, cell, and bacterial adhesion. Finally, zwitterionic hydrogels were strengthened by changing the concentration of poly(ethylene glycol)

diacrylate (PEGDA) and 2-hydroxyethyl methacrylate (HEMA) in the formulation. The direct relationship between changing zwitterionic hydrogel formulation to strengthen the hydrogel and the anti-fouling properties were established. The fundamental understanding and design of cochlear implant materials described herein serves as a foundation for the development of next generation neural prosthetics.

PUBLIC ABSTRACT

Cochlear implants (CIs) help to restore basic auditory function in patients who are deaf or have profound hearing loss. However, CI patients suffer from limited voice and tonal perception due to spatial separation between the stimulating CI electrode and the receptor spiral ganglion neurons (SGNs). Directed regeneration of proximate SGN axons may improve tonal performance and implant fidelity by decreasing the spatial separation between the CI electrode and the neural receptor. Additionally, fibrous scar tissue formation on the surface of implanted electrodes further decreases tonal perception through current attenuation and spreading resulting in late-term hearing loss. Thus, designing surfaces that induce favorable responses from neural tissues will be necessary in overcoming signal resolution barriers. In this work, the inherent spatial and temporal control of photopolymerization was used to functionalize surfaces with topographical and biochemical micropatterns that control the outgrowth of neural and other cell types. First, laminin, a cell adhesion protein was patterned using a photodeactivation process onto methacrylate polymer surfaces and was shown to direct the growth of spiral ganglion neurons (SGN), the primary auditory neural receptors. These protein patterns could even overcome low amplitude/high periodicity competing topographical cues. Additionally, glass substrates were patterned with linear zwitterionic polymers and fibroblasts, astrocytes, and Schwann cells all showed dramatically decreased cell adhesion on 100 μm precocity patterns. Further, SGN neurites showed excellent alignment to these same patterns. Next, poly(dimethyl siloxane) (PDMS) was coated with a crosslinked zwitterionic thin film using a single step photografting/photopolymerization process to covalently bind the hydrogel to PDMS. These coated surfaces showed dramatically lower levels of protein, cell, and bacterial adhesion. Finally, zwitterionic hydrogels were strengthened by changing the concentration of poly(ethylene glycol) diacrylate (PEGDA) and 2-hydroxyethyl methacrylate (HEMA) in the formulation. The direct

relationship between changing zwitterionic hydrogel formulation to strengthen the hydrogel and the anti-fouling properties were established. The fundamental understanding and design of cochlear implant materials described herein serves as a foundation for the development of next generation neural prosthetics.

TABLE OF CONTENTS

TABLE OF FIGURES xiv

TABLE OF TABLES xxi

CHAPTER 1: INTRODUCTION 1

1.1 BIOMATERIALS 1
1.1.1 History 2
1.1.2 Silicones 5
1.1.3 Polyurethanes 6
1.1.4 Teflon® 7
1.1.5 Methacrylates 8
1.2 THE FOREIGN BODY RESPONSE 9
1.2.1 Mitigating the Foreign Body Response 13
1.2.2 Zwitterionic Polymer Fabrication 18
1.3 COCHLEAR IMPLANTS 21
1.3.1 History 22
1.4 GOALS FOR IMPROVING COCHLEAR IMPLANTS 24
1.4.1 Topographical/Physical Cues 26
1.4.2 Biochemical Cues 29
1.4.3 Mitigating Fibrosis on Cochlear Implant Surfaces 31
1.5 PHOTOPOLYMERIZATION AND BIOMATERIALS 32

CHAPTER 2: OBJECTIVES 37

CHAPTER 3: METHODS AND MATERIALS 42

3.1 MATERIALS FABRICATION 42
3.1.1 Activated Glass Slide Preparation 42
3.1.2 Physical Micro-pattern Substrate Fabrication and Characterization 43
3.1.3 Biochemical Functionalization and Patterning 44
3.1.4 Carboxybetaine Methacrylate Synthesis 46
3.1.5 Zwitterion-functionalized PDMS 48
3.1.6 Zwitterionic Hydrogel Fabrication 49
3.2 MATERIALS CHARACTERIZATION 50
3.2.1 Nonspecific Protein Adsorption 50
3.2.2 Surface Characterization 51
3.2.3 Physical Properties 53
3.2.4 Scanning Electron Microscopy (SEM) 55
3.3 CELL CULTURE AND QUANTIFICATION 55

3.3.1 Preparing Polymers for Culture 55
3.3.2 Dissection 56
3.3.3 Preparation of Explants 57
3.3.4 Preparation of Dissociated Cultures 58
3.3.5 Enriching for Spiral Ganglion Schwann Cells 59
3.3.6 Fixation and Immunocytochemistry 59
3.3.7 Quantifying Neurite Alignment 60
3.3.8 Quantifying Schwann Cell Alignment 60
3.3.9 Notes 61

CHAPTER 4: TUNING SURFACE AND TOPOGRAPHICAL FEATURES TO INVESTIGATE COMPETITIVE GUIDANCE OF SPIRAL GANGLION NEURONS[203] 66

4.1 ABSTRACT 66
4.2 INTRODUCTION 67
4.3 MATERIALS/METHODS 70
4.3.1 Functionalization of Glass Slides 70
4.3.2 Physical Micro-pattern Substrate Fabrication and Characterization 70
4.3.3 Biochemical Patterning and Characterization 71
4.3.4 Spiral Ganglia Cell Culture and Neurite Guidance Determination . 72
4.3.5 Determination of Neurite Progression 73
4.4 RESULTS AND DISCUSSION 73
4.4.1 Photopolymerization and Micro-groove Fabrication 73
4.4.2 Alignment of SGN Neurites 78
4.4.3 SGN Neurite Alignment to Competing Patterns of Varying Periodicity 79
4.4.4 SGN Neurite Alignment to Competing Patterns of Varying Amplitude 84
4.5 CONCLUSIONS 86

CHAPTER 5: PHOTOPOLYMERIABLE ZWITTERIONIC POLYMER PATTERNS CONTROL CELL ADHESION AND GUIDE NEURAL GROWTH[204] 87

5.1 ABSTRACT 87
5.2 INTRODUCTION 87
5.3 EXPERIMENTAL 92
5.3.1 Materials and Synthesis 92
5.3.2 Zwitterion-functionalized Glass Substrate Fabrication and Characterization 93
5.3.3 Protein Adsorption 94
5.3.4 Cell Culture and Immunofluorescence 95
5.3.5 Quantification of Cell Density and Alignment to Micropatterns 96
5.3.6 Statistics 97
5.4 RESULTS AND DISCUSSION 97

5.4.1 Zwitterion-functionalized Substrate Fabrication and Characterization 97
5.4.2 Fibroblast and Astrocyte Adhesion 105
5.4.3 Schwann Cell Adhesion and Alignment 109
5.4.4 SGN Neurite Alignment to Zwitterionic Micropatterns 112
5.5 CONCLUSIONS 115

CHAPTER 6: ANTI-FOULING PHOTOGRAFTABLE ZWITTERIONIC COATINGS ON PDMS SUBSTRATES 117

6.1 ABSTRACT 117
6.2 INTRODUCTION 117
6.3 EXPERIMENTAL 120
6.3.1 Materials and Synthesis 120
6.3.2 Zwitterion-functionalized PDMS Substrate Fabrication and Characterization 122
6.3.3 Protein Adsorption 124
6.3.4 Cell Culture and Density Quantification 124
6.3.5 Bacterial Ahesion 125
6.3.6 Statistics 126
6.4 RESULTS AND DISCUSSION 126
6.4.1 Surface-initiated Zwitterionic Graft Polymerization 126
6.4.2 Characterization of the Photografted Zwitterionic Polymer 128
6.4.3 Cell and Protein Adsorption to Zwitterion-coated PDMS 135
6.4.4 Bacterial Adhesion to Zwitterion-coated PDMS 140
6.5 CONCLUSIONS 142

CHAPTER 7: STRENGTHENING ZWITTERIONIC HYDROGELS FOR COATING PDMS MATERIALS 144

7.1 ABSTRACT 144
7.2 INTRODUCTION 144
7.3 MATERIALS/METHODS 147
7.3.1 Materials 147
7.3.2 Hydrogel Fabrication 147
7.3.3 Mechanical Properties 149
7.3.4 Protein Adsorption and Cell Adhesion 150
7.4 RESULTS AND DISCUSSION 150
7.4.1 Characterization of SBMA:PEGDA Hydrogels 150
7.4.2 Characterization of SBMA:HEMA Hydrogels 153
7.4.3 Anti-fouling Properties of SBMA:PEGDA Hydrogels 156
7.4.4 Anti-fouling Properties of SBMA:HEMA Hydrogels 158
7.5 CONCLUSIONS 160

CHAPTER 8: CONCLUSIONS AND RECOMMENDATIONS 161

8.1 CONCLUSIONS 161
8.2 RECOMMENDATIONS 165

REFERENCES 176

TABLE OF FIGURES

Figure 1.1. A modern intraocular lens. Photo courtesy of the Macular Degeneration Association. (macularhope.org)..... 3

Figure 1.2. Silicone wound dressing. Photo courtesy of Elkem Silicones. 6

Figure 1.3. The temporal variation in the acute inflammatory response, chronic inflammatory response, granulation tissue development, and foreign body reaction to implanted biomaterials. Adapted from reference 55. 12

Figure 1.4. Zwitterionic functional groups and one zwitterated siloxane. Adapted from reference 65. 16

Figure 1.5. Cartoon representing the resistance to nonspecific protein adsorption. Upper: An anionic surface attracts positively-charged regions on a protein facilitating protein adsorption. Lower: A zwitterionic surface has minimal ionic interactions with a protein and high hydration prevents the nonspecific adsorption of protein to the surface. Adapted from reference 65 17

Figure 1.6. Diagram of cochlear implant speech processing. (1) A microphone located on the behind-the-ear sound processor unit processes, codes, and sends the tonal information via transcutaneous radiofrequency link to the (2) implanted receiver-stimulator package. The data are then sent to (3) the electrode array. The spiral ganglion cell populations are then stimulated by an applied current at various positions along (4) the cochlea (auditory nerve) to simulate hearing. (Photo provided courtesy of Cochlear Americas, © 2011 Cochlear Americas.)..... 21

Figure 1.7. Diagram of the cochlea. The cochlea is made up of three canals wrapped around a bony axis. These canals are: the scala tympani (3), the scala vestibuli (2) and the scala media (or cochlear duct) (1). The spiral ganglion neurons (4) are the primary neural receptors. The auditory nerve (5) transmits signals from the spiral ganglion neurons back to the central nervous system. Image courtesy of www.cochlea.edu. 23

Figure 1.8. Schematic representing stimulation of auditory nerve cells for normal hearing (left) and cochlear implant patients (right). Spatial separation and fibrosis lead to significant current spread and decreased resolution. 25

Figure 1.9. Goal for improved cochlear implant performance. Using surface chemistry and topography, SGN neurites can be regrown to close the gap between the neural receptors and the stimulating electrode. Zwitterionic polymer coatings can also prevent the accumulation of fibrosis on the implant surface. 26

Figure 1.10. Topographies presented to neurons in vitro. Adapted from reference 8. 28

Figure 1.11. Neurite growth from dissociated SGNs on (A) unpatterned and (B) 50 μm periodicity, 3 μm amplitude photopolymerized polymer substrates. Adapted from reference 147 29

Figure 1.12. Schematic representing the events leading up to fibrosis and biofilm formation (left side). The right side depicts the use of zwitterionic polymers on cochlear implant electrode arrays to resist biofouling. 32

Figure 1.13. Schematic of the basic reactions involved in the surface grafting with benzophenone as an initiator of a vinyl monomer. Adapted from reference 199. 34

Figure 3.1. Monomers, photoinitiator, and grafting agent used to generate micropatterned topographical samples. 44

Figure 3.2. Schematic of photopatterning process. Monomer is selectively exposed to UV light through transparent bands of the photomask resulting in raised microfeatures across the polymer surface. 45

Figure 3.3. Chemical structures of the monomers and photoinitiator used to generate zwitterionic thin film hydrogels and coatings. 46

Figure 3.4. Schematic of CBMA synthesis. 47

Figure 3.5. Drawing of the mold used to polymerize free-standing zwitterionic hydrogels. Prepolymer is represented by orange, glass mole is shown in blue, and small binder clips are seen in black. Adapted from reference 205. 50

Figure 3.6. Calibration curve for BP adsorbed onto PDMS substrates as measured by UV/Vis spectroscopy. 53

Figure 3.8. Method for quantifying neurite alignment to linear patterns. Alignment ratio is defined as the ratio of neurite length to end-to-end distance. As the length of the neurite increases over the end-to-end distance, the alignment ratio increases. A perfectly aligned neurite would have an alignment ratio of 1 60

Figure 4.1. Schematic depicting the photodeacivation and patterning process. A protein solution is applied to an acrylate polymer and illuminated with UV-light through a photomask. Exposed protein is deactivated resulting in an active protein pattern in shadowed regions. 75

Figure 4.2. Epifluorescent images of the laminin patterned substrates. A) A 50 µm vertical laminin pattern on a smooth acrylate polymer substrate. Active laminin stripes are represented by green bands where dark bands represent photodeactivated areas. B) Laminin patterned onto a physically patterned acrylate polymer (50 µm periodicity and 1.5 amplitude). The protein pattern is shown vertically and the physical pattern runs horizontally. Both images were visualized using immunofluorescent imaging. The physical pattern observed in B can be seen due to autofluorescence of the polymer. 76

Figure 4.3. Relative fluorescence of the laminin as a function of illumination time with and without photoinitiator. The fluorescence decreases over time with photoinitiator increasing the photobleaching process. 77

Figure 4.4. Schematic demonstrating the angle quantification method used to evaluate neurite alignment. 78

Figure 4.5. SGN alignment on laminin patterned and uniformly-coated substrates. A) Epifluorescent image of neurites grown on uniformly-coated smooth polymer substrates. B) Epifluorescent image depicting neurites grown on a vertical laminin patterned smooth surface. Many neurites are observed following the vertical pattern in response to the laminin stripes. C) Angle quantification of neurites grown on uniformly-coated smooth polymer substrates (n=417). D) Angle quantification of neurites seeded onto smooth substrates containing a vertical laminin pattern (n=261). The box in the top left corner of the histograms represents the pattern present for the quantification (green stripes for the vertical laminin pattern). 81

Figure 4.6. Neurites from dissociated SGN grown on: (A) a uniformly laminin coated 20 μm periodicity, 1.5 μm amplitude physical pattern, (B) a 20 μm physical pattern with an amplitude of 1.5 μm (strong physical cue) and a perpendicular 50 μm laminin pattern and (C) a 50 μm physical pattern with an amplitude of 1.5 μm (weak physical cue) and a perpendicular 50 μm laminin pattern. The physical pattern is oriented horizontally and the laminin pattern vertically. Cultures were stained with anti-NF200 antibodies. 81

Figure 4.7. Quantification of SGN neurites grown on patterned substrates with variable periodicity. The top row of histograms are the quantification of SGN neurites cultured on physically patterned substrates with a uniform coating of laminin with the periodicities of 20 μm (A, n=21), 33 μm (B, n=133) and 50 μm (C, n=405). The bottom row of graphs represents the quantification of SGN neurites cultured on physically patterned substrates containing a perpendicular 50 μm laminin pattern with the periodicities of 20 μm (D, n=391), 33 μm (E, n=229) and 50 μm (F, n=319). Periodicity increases from left to right as the strength of the physical cue decreases. The box in the top left corner of each histograms represents the pattern present for the quantification (green stripes for the vertical laminin pattern and black stripes for the horizontal physical pattern). 83

Figure 4.8. Quantification of SGN neurites grown on patterned substrates with variable amplitude. Epifluorescent images of neurites grown on (A) uniformly laminin coated 50 μm periodicity and 8 μm amplitude physically patterned and (B) perpendicularly patterned laminin on a 50 μm periodicity and 8 μm amplitude physical pattern. The top row of histograms represents the quantification of SGN neurites seeded on substrates with a uniform coating of laminin and amplitudes of 3 μm (C, n=135) and 8 μm (E, n=158). The bottom row of histograms represents the quantification of SGN neurites seeded on substrates with a 50 μm perpendicular laminin pattern and amplitudes of 3 μm (D, n=175) and 8 μm (F, n=217). The box in the top left corner of each histograms represents the pattern present for the quantification (green stripes for the vertical laminin pattern and black stripes for the horizontal physical pattern). Cultures were stained with anti-NF200 antibodies. 85

Figure 5.1. Molecular structures of zwitterionic monomers, methacrylate coupling agent, and photoinitiator. 90

Figure 5.2. Schematic of the photografting/patterning process. UV-light is used to initiate polymerization and grafting of zwitterionic monomers forming polymer thin films in

exposed regions. Functionalization is limited to illuminated regions, which in turn repel protein and cell adhesion. 94

Figure 5.3. Characterization of zwitterion-coated glass surfaces using XPS. A) Representative XPS spectra for glass, activated glass, SBMA-coated glass (20 wt% monomer solution), and CBMA-coated glass (20 wt% monomer solution). The zwitterion-coated glass curves both show a characteristic N1s peak at 402 eV and the SBMA-coated sample exhibit S2s and S2p peaks at 231 and 168 eV respectively. B) Percent nitrogen as a function of wt% monomer for both SBMA- and CBMA-coated glass. Nitrogen percent increases for both zwitterions with monomer wt% and is shown to approach the theoretical maximum (pure polymer composition) at 20 wt%. 99

Figure 5.4. Tuning of physicochemical properties of (A) SBMA- and (B) CBMA-functionalized glass surfaces through varying the wt% monomer in solution. Relative protein adsorption (bars) refers to the left axis and is measured compared to an activated glass slide control. Contact angles (•) refer to the right axis. A strong correlation is observed between contact angle and relative protein adsorption. 103

Figure 5.5. Epifluorescent images of protein (human fibrinogen) adsorption to zwitterionic stripes on glass substrates: A) SBMA stripes with a100 µm periodicity. B) CBMA stripes with 100 µm periodicity. Protein adsorbs to uncoated regions as observed by the green bands, while protein does not adsorb to zwitterion-coated bands as seen in black. 106

Figure 5.6. Representative epifluorescent images of fibroblasts grown on (A) glass, (B) uniformly SBMA-coated, (C) uniformly CBMA-coated, and (D) CBMA-striped surfaces and immnolabeled with anti-vimentin antibody (green). Nuclei are labeled with DAPI (blue). E) Fibroblast cell density on uniformly coated surfaces. A significant difference was observed between all groups (SBMA, CBMA, and uncoated glass) with CBMA exhibiting the lowest cell density (*p < 0.001 one way ANOVA). F) Fibroblast cell density on striped substrates, both on and off the zwitterionic pattern. A significant difference was determined between coated and uncoated regions for both SBMA- and CBMA-coated substrates (**p < 0.001 t-test). Cell density was shown to be statistically different between SBMA- (image not shown) and CBMA-coated stripes (*p < 0.001 one way ANOVA). Zwitterionic micropatterns used for cell culture have a periodicity of 100 µm. Error bars represent standard error of the mean. 106

Figure 5.7. Representative epifluorescent images of astrocytes grown on (A) glass, (B) uniformly SBMA-coated, (C) uniformly CBMA-coated, and (D) CBMA-striped surfaces and immunostained with anti-GFAP antibody (green). Nuclei are labeled with DAPI (blue). E) Astrocyte cell density on uniformly coated surfaces. A significant difference was observed between the glass control and SBMA- and CBMA-coated surfaces (*p < 0.001 one way ANOVA). F) Astrocyte cell density on striped substrates, both on and off the zwitterionic pattern. A significant difference was determined between coated and uncoated regions for both SBMA- and CBMA-coated substrates (**p < 0.001 t-test). Cell density was shown to be statistically different between SBMA- (image not shown) and CBMA-coated stripes (*p < 0.001 one way ANOVA). Zwitterionic micropatterns used for striped substrates have a periodicity of 100 µm. Error bars represent standard error of the mean. 108

Figure 5.8. Representative epifluorescent images of Schwann cells cultured on (A) unmodified glass, (B) uniformly SBMA-coated, (C) uniformly CBMA-coated, and (D) CBMA-striped substrates and immunostained with anti-S100 antibody (green). Nuclei are labeled with DAPI (blue). E) Schwann cell density on uniformly coated substrates. A statistical difference was found between Schwann cells cultured on coated (both SBMA and CBMA) and uncoated (plain glass) surfaces (*p < 0.001 one way ANOVA). F) Schwann cell density on SBMA- and CBMA-striped substrates. Analysis of cell density showed significantly fewer cells adhered to both SBMA- and CBMA-coated stripes than the uncoated regions (**p < 0.001 t-test). Zwitterionic micropatterns used for striped substrates have a periodicity of 100 μm. Error bars represent standard error of the mean. 110

Figure 5.9. Representative image of Schwann cells cultured on 100 μm SBMA-striped substrates (A). Schwann cells elongate and extend between SBMA stripes occasionally forming bridges between SBMA bands. Cell alignment was determined by measuring the angle (θ) of an ellipse fitted to the major axis of the cell relative to the pattern. B) Average angle of Schwann cell alignment on uncoated and zwitterion-striped surfaces. A significant difference was found across all groups (* p < 0.001 one way ANOVA) with CBMA exhibiting the lowest average angle from the micropattern. The number inside or above each column represent the total number of cells evaluated. Cultures were immunostained with anti-S100 antibody (green). Nuclei are labeled with DAPI (blue). Error bars represent standard error of the mean. 112

Figure 5.10. Alignment of SGN neurites on glass (A), SBMA-striped (B), and CBMA-striped (C) surfaces. Cultures were immunostained with anti-NF200 antibody (green) to label neurons. Nuclei are labeled with DAPI (blue). SGN neurites extend randomly on unpatterned glass substrates (A), but elongate and extend between SBMA (B) and CBMA (C) bands. D) Alignment ratios of SGN neurites grown on uncoated and zwitterion-striped surfaces. Quantification of alignment ratios confirms statistical difference between all groups (* p < 0.001 one way ANOVA). CBMA-coated surfaces exhibited the strongest alignment. The number inside or above each column represent the total number of neurites measured. A periodicity of 100 μm was used for patterned samples. Error bars represent standard error of the mean. 114

Figure 6.1. Schematic of the photografting process. UV-light is used to initiate polymerization and grafting of zwitterionic monomers from the PDMS surface forming a polymer thin film hydrogel covalently attached to the material substrate. 123

Figure 6.2. Schematic representing the basic chemistry of the photografting process. Benzophenone (BP) adsorbed on the substrates initiates covalent grafting and polymerization of the polymer to the PDMS. 128

Figure 6.3. Quantification of BP surface concentration with respect to BP feed concentration. The surface concentration increases with increasing feed concentration. 129

Figure 6.4. SEM images of photografted zwitterionic polymers. Shown are SBMA-coated PDMS using A) 2.5 and C) 50 mg/mL BP feed concentration and CBMA-coated PDMS using B) 2.5 and D) 50 mg/mL BP feed concentration. 130

Figure 6.5. Schematic representing shear adhesion experiments. A benzophenone activated sample was covalently bound to methacrylate-functionalized glass by photografting/photopolymerizing the zwitterionic polymer between substrates. The samples were strained until fracture by applying a force to both ends of the substrates. The samples showed either adhesive failure (left image), where the polymer remains adhered to the glass, or cohesive failure (right image), where the film itself fractures yet remains adhered to both substrates. 133

Figure 6.6. Maximum force per area results as measured using shear adhesion experiments as a function of BP feed concentration for zwitterion-grafted thin films to PDMS substrates. A) Shear adhesion test data for SBMA-grafted thin films. B) Shear adhesion results for CBMA-coated PDMS. Max force per area increases with increasing BP feed concentration. Shaded area represents samples that failed cohesively. 134

Figure 6.7. Characterization of protein adsorption. Representative epifluorescent images of immunostained fibrinogen (green) on A) uncoated, B) SBMA-coated, and C) CBMA-coated PDMS. D) Fibrinogen adsorption on uncoated, SBMA-coated and CBMA-coated PDMS as measured by epifluorescent microscopy. SBMA- and CBMA-coated substrates significantly reduce fibrinogen adsorption (*$p < 0.001$ one way ANOVA). Error bars represent standard deviation of the mean. 136

Figure 6.8. Representative epifluorescent images of fibroblasts grown on A) uncoated, B) SBMA-coated, and C) CBMA-coated PDMS without FBS in the culture medium. Fibroblast cytoskeletal actin is labeled with Alexa 488-phalloidin to demonstrate morphology (green). D) Fibroblast cell density on uncoated SBMA-coated, and CBMA-coated PDMS substrates. SBMA- and CBMA-coated PDMS significantly reduce fibroblast cell adhesion (*$p < 0.001$ one way ANOVA). Error bars represent standard error of the mean. 137

Figure 6.9. Representative epifluorescent images of fibroblasts grown on A) uncoated, B) SBMA-coated, and C) CBMA-coated PDMS with FBS in culture medium. Fibroblast cytoskeletal actin is labeled with Alexa 488-phalloidin to demonstrate morphology (green). D) Fibroblast cell density on uncoated SBMA-coated, and CBMA-coated PDMS substrates. SBMA- and CBMA-coated PDMS significantly reduce fibroblast cell adhesion (*$p < 0.001$ one way ANOVA). Error bars represent standard error of the mean. 139

Figure 6.10. Representative epifluorescent images of fibrobasts grown on A) uncoated, B) SBMA-coated, and C) CBMA-coated PDMS after substrate immersion in culture medium for 14 days. Fibroblasts are labeled with Alexa 488-phalloidin (green). D) Fibroblast cell density at 0 and 14 days in culture medium for uncoated, SBMA-coated, and CBMA-coated PDMS. A significant difference was observed between uncoated and the zwitterion-coated PDMS at 0 and 14 days. No significant increase in cell density was observed after the 14 day incubation for all substrates. Error bars represent standard error of the mean. 140

Figure 6.11. Bacterial adhesion onto coated and uncoated PDMS substrates in vitro. S. aureus (A) and S. epidermidis (B) growth at 48 h on implants treated with and without FBS. * indicates a statistical difference between groups (*p<0.001 one way ANOVA). ** indicates a statistical difference between groups (p=0.0119 one way ANOVA) 141

Figure 7.1. Characterization of the material properties of SX hydrogels. A) Swelling ratios of variable PEGDA hydrogels. The water uptake increases with lower crosslink density. B) Compressive modulus of variable PEGDA hydrogels. Lower crosslink density decreases the modulus. Error bars represent the standard deviation of the mean. .. 152

Figure 7.2. Characterization of the material properties of SH hydrogels. A) Swelling ratios of variable HEMA hydrogels. B) Compressive modulus of variable HEMA hydrogels. Lower HEMA concentrations decrease the modulus. Error bars represent the standard deviation of the mean..... 154

Figure 7.3. Tensile mechanical properties of SH hydrogels. A) Stress/strain curves of variable HEMA hydrogels. B) Toughness calculations of variable HEMA hydrogels. Higher HEMA concentrations increase the toughness. Error bars represent the standard error of the mean. 156

Figure 7.4. Fouling properties of SX hydrogels. A) Protein adsorption and B) cell adhesion onto variable PEGDA hydrogels. Error bars represent standard error of the mean. 158

Figure 7.5. Fouling properties of SH hydrogels. A) Protein adsorption and B) cell adhesion onto variable HEMA hydrogels. Error bars represent standard error of the mean. 159

LIST OF TABLES

Table 3.1. Formulations of the variable HEMA/PEGDA hydrogels. 50

CHAPTER 1: INTRODUCTION

As healthcare markets and the number of medical procedures expand, the demand for materials that interface well with host tissue has increased. The worldwide medical device industry was valued at over $300 billion in 2016 and is expected to continue to grow to over $400 billion by 2019.[1] This industry includes a broad range of materials with various intended interactions with host tissue ranging from dental resins, which require high stiffness and excellent adhesion to bone, to neural prosthetics, which require intimate communication between stimulating electrodes and target neurons. The added complexity and variety of applications have prompted an increasing demand on materials scientists to push the boundaries for micro- and nano-materials innovation.[2–4] For example, nanoparticles have been engineered to increase loading and delivery of a drug for targeted applications.[5] Further, the surface of nanoparticles can be functionalized to increase blood circulation times.[6,7] An additional example is the addition of micro- and nano-topography to a surface that can control cell-material interactions and growth.[8–10] The function of current medical devices relies heavily on decades of innovation in biomaterials research. Implantable medical devices are an essential part of a modern medical practice, and they have saved many lives and improved the lives of many others. Herein, a brief history of biomaterials and their applications and common biomaterials used today will be explored. Second, an introduction to the foreign body response to implantable materials will be discussed. Cochlear implants will then be discussed. Finally, the goal for improving cochlear implants using photopolymerized biomaterials will be addressed.

1.1 BIOMATERIALS

The majority of growth in the biomaterial and medical device industry has taken place within the last 70 years. Before this time, biomaterials and implantable devices as we now know

them were nonexistent. During this relatively short time, the industry has expanded to include medical devices such as joint replacements, intraocular lenses, feeding tubes, dental implants, pacemakers, renal dialyzers, stents and urinary catheters to name a few.[11] The advent of such a diverse group of materials with a variety of mechanical, chemical, biological, optical and adhesive properties has ushered in a new era of materials science engineering. The distinct set of challenges faced by engineers and scientists in developing materials that interact with biological systems requires a multidisciplinary approach. Achieving a desired function from a biomaterial often demands expertise in the fields of chemistry, chemical engineering, materials science, mechanics, surface science, bioengineering, biology, and medicine.[11] Furthermore, devices often require input from ethics groups, government-regulated standards, and entrepreneurs.

1.1.1 History

The history of biomaterials can be traced back to almost 2,000 years ago (with some historians dating sutures back at least 32,000 years).[12–14] Most of these early implanted materials had little chance at success largely due to the lack of knowledge regarding infection and bodily response to a foreign material. One of the first reports of the modern era for an implantable material was observed by British ophthalmologist Harold Ridley in the late 1940s.[15] He observed shards of canopy plastic unintentionally imbedded in the eyes of pilots of Spitfire and Hurricane fighter planes incurred during World War II. He noted that the implanted plastic, made from poly(methyl methacrylate) (PMMA), seemed to heal without any adverse reaction from the body. For many of the pilots, the fragments remained in place for years following the war. The conventional wisdom of the time was that the body would not tolerate foreign implanted objects. His observation that the implanted fragments had healed in place without any long-term inflammatory response led him to conclude that the plastic was “tolerable” to the body. Today

we would now call the healing of an implanted object without any damage to the surrounding tissue "biocompatible" or "bioinert."[11,13,16] These findings were perhaps the first observations of "biocompatibility" in the modern era and were crucial to the development of future implantable materials. His work and innovation later led to the invention of the modern-day intraocular lens (Figure 1.1), which has revolutionized the treatment for individuals suffering from cataracts.[15]

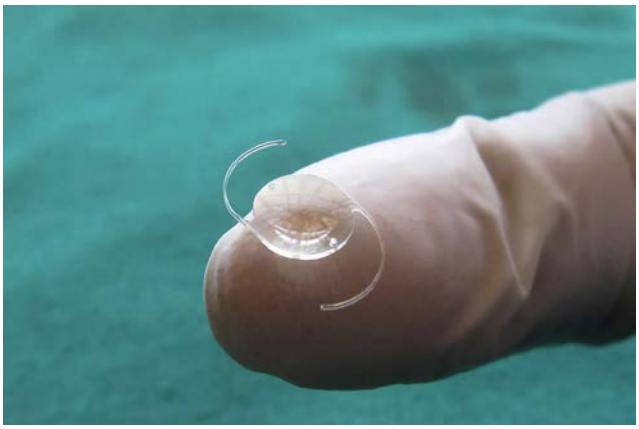

Figure 1.1. A modern intraocular lens. Photo courtesy of the Macular Degeneration Association. (macularhope.org)

The advancement of biomaterials from the work of Ridley was only the beginning of innovation and biomedical device implantation. For example, in 1952, a fortuitous discovery was made by Per Ingvar Brånemark, a Swedish physician and researcher. He implanted a metal cage into a rabbit to observe healing reactions.[17] The cage was made from titanium and was screwed into the bone for several months. After the experiment was complete, he observed that the titanium was tightly integrated to the bone. Dr. Brånemark's work was groundbreaking for the fusion of metals to bone and he termed the process "osseointegration." Today most dental and orthopedic implants are made from titanium and its alloys. A further advance in biomaterials built upon prior knowledge of osseointegration in 1961 when Dr. John Charnley developed the first successful hip joint replacement.[18] His device used an ultrahigh molecular weight polyethylene ball cup, which proved much more effective than previous attempts using metal or acrylic materials.[19] Charnley's innovation with hip replacement materials led to the development of a total knee replacement in 1971, pioneered by two surgeons, Frank Gunston and John Insall.[20]

Throughout most of history, renal failure meant certain death, with no viable treatment. In 1943, Willem Kolff, a young Dutch physician, built a drum dialyzer using cellulose sausage casing as the membrane.[21] His device was only partially successful until he later took the idea to the United States in 1960.[22] Kolff's innovation in dialysis, along with many others, led to the first dialysis center being opened in Seattle WA in 1962.[23] The development of coronary stents was also a major breakthrough in vascular health. The first arterial stent was implanted by Dr. Andreas Gruntzig in 1977 which allowed coronary atherosclerotic blockages to be opened without the need for open chest surgery.[24,25] Coronary arterial stents are now implanted in well over 1.5 million people annually.[13] Another example of a life-saving biomaterial is the pacemaker. While other researchers had designed portable pacemakers, it was Wilson Greatbatch, an engineer, and cardiologist W.M. Chardack who developed the first fully functional implantable pacemaker in 1972.[26,27] The device was encased in epoxy to prevent inactivation by leakage of bodily fluids into the electronics.

Up until the early 1960s, biomaterials were largely fabricated from off-the-shelf materials that happened to be compatible with bodily fluid/tissue. The new generation of materials has entered an era of engineered materials tailored for specific applications and has ventured away from using commodity materials as the basis for device fabrication. The onset of such a diverse group of devices interacting with various tissues, fluids, and cellular environments has ushered in the use of materials with a variety of mechanical properties and chemistries. Many applications require a high modulus material, such as a dental implant or joint replacement, while others must be flexible and soft such as a contact lens or urinary catheter. The following section will give a brief overview and history of the various polymeric biomaterials used in current medical devices.

1.1.2 Silicones

Poly(dimethyl) siloxanes (PDMS) are often referred to as silicones. Due to their unique and diverse material properties, they have found widespread use in health care. Silicones maintain excellent *biocompatibility* (non toxic) and *biodurability* (resistance to degradation).[28] Their unique physical properties include low surface tension, hydrophobicity, and chemical and thermal stability. These characteristics make silicones one of the most highly used polymers in the medical device industry. Chapter 6 will discuss in depth the coating of PDMS to tune the biological response.

While silicone-based materials have been studied for many years, it wasn't until the early 1940s when Eugene Rochow of General Electric (GE) pioneered the direct scale-up process of silicones using silicon and methyl chloride.[29] Rochow commented on the low toxicity of the silicones, but never proposed their use for biomedical applications. In 1946, researchers from the University of Toronto and Manitoba coated syringes, needles, and vials with methylchlorosilane.[30] Upon rinsing the substrates, the surface hydrolyzed to form a hydrophobic silicone coating. This surface treatment gave a coating that resisted blood clotting for many hours. Soon after the coating of needles, syringes, and blood collection vials became common-place, and silicone coatings are still used today for the same applications.[28] Silicone elastomers have also found a prominent place in the biomedical device industry. In 1946, Dr. Frank Lahey gave the first report of silicone elastomers being implanted in humans when he discussed his implantation of these materials for bile duct repair.[31] Further work in the field was conducted by Dr. DeNicola who implanted an artificial urethra using the same silicone tubing used by Lahey. After fourteen months of implantation, there was no evidence of any rejection of the material from the body.[32] These early innovations in silicone-based materials led to substantial interest in

Figure 1.2. Silicone wound dressing. Photo courtesy of Elkem Silicones.

designing materials for health-care applications. By 1959, the Dow Corning Corporation was so flooded with research requests from physicians and scientists that they founded the Dow Corning Center for Aid to Medical Research to supply silicone-based materials for research purposes. Currently, silicone-based biomaterials are used in a variety of applications including orthopedics, catheters, drains, shunts, cochlear implants, extracorporeal equipment, wound dressings (Figure 1.2), and aesthetic implants to name a few.[28]

1.1.3 Polyurethanes

Polyurethanes (PU) represent a diverse group of materials due to their structure/property relationship and their compatibility with biological systems. Utilizing the structure property relationship of PUs, one can design polymers ranging in materials properties from engineering polymers to those mimicking soft tissue.[33] They can be stiff (high modulus) and elastic (low modulus) and everything in between. Further, PUs demonstrate very good long term mechanical properties when exposed to dynamic or static loads, and as a result have use in many long-term

applications. It is therefore unsurprising that PUs have found a strong place in biomedical applications.

The development of other biomaterials (PVC, fluoropolymers, polyethylene, natural rubber, and silicones) occurred prior to the widespread use of PUs. Thus, many initial findings and applications of PUs for biomedical applications went unnoticed. A paper published in Science in 1967 by Boretos and Pierce describing the use of "Biomer™," a PU elastomer for biomedical applications, garnered interest from the scientific and medical communities.[34] This segmented polymer had been available for several years already from Ethicon Inc. A second paper published four years later by Boretos and Pierce confirmed the blood compatibility of Biomer™, reporting positive results after two years in blood-contacting applications.[35] In the years that followed, Biomer™ gained wide acceptance due to its high modulus and tensile strength,[36] physiological acceptability,[37] high blood tolerability,[38] hydrolytic stability,[39] and implantation stability.[40] While Biomer™ was withdrawn from the market in 1991, it was instrumental in the advancement and general acceptance of PU materials and their compatibility with blood and tissue. Today PU materials are still used extensively in the biomedical industry including catheter and general purpose tubing, hospital bedding, surgical drapes, wound dressings, as well as in a variety of injection molded devices.[33] The most common use is in short-term implants.

1.1.4 Teflon®

Poly(tetrafluoro ethylene) (PTFE or Teflon®) is a fluorocarbon, which is chemically inert to most substances. The hydrophobic and non-stick properties are the most well-known characteristics of this unique polymer, but it also maintains low coefficients of friction, biological inertness, corrosion resistance, heat resistance, electrical and thermal insulation, and

non-biodegradibility. It is these advantageous properties that have led to the use of Teflon® in biomedical applications. Gore-Tex®, a porous form of Teflon®, and similar expanded forms of PTFE are used in vascular grafts, surgical meshes, ligament and tendon repair.[41–45]

The discovery of PTFE happened serendipitously in 1938 when Roy Plunkett was working with the gas tetrafluoroethylene (TFE) for refrigerant applications.[46] When examining a TFE gas cylinder, Plunkett stumbled upon the polymerized form of the gas (PTFE). The Teflon® trademark was coined by Chemours, and the first products were sold commercially starting in 1946. In 1969, Bob Gore discovered that, when heated and stretched, PTFE forms a porous membrane (Gore-Tex®). This porous membrane was particularly useful because it allows the body's own tissues to grow through the material. These advantages are the reason PTFE has become the leading synthetic vascular graft materials and is also used in numerous other applications.[41,47]

1.1.5 Methacrylates

Methacrylates represent a group of polymers used for biomaterial applications requiring a rigid structure. Their stiffness can be attributed to the high degree of crosslinking and high glass transition temperatures. Methacrylate polymers have a characteristic α-unsaturated ester that allows them to be radically polymerized across the double bond. As mentioned previously in the introduction, poly(methyl methacrylate) (PMMA) was the material discovered in the eyes of World War II fighter pilots years after implantation.[15] As Ridley noted, polymerized methacrylates are biologically inert and can be implanted without significant adverse reaction.[48] Methacrylate polymers are often used in applications that require *in situ* polymerization. In particular, bone cements, composed of PMMA, are used for fixation of implants in various orthopedic applications.[49] These types of applications require that the resin be applied while in

liquid form and polymerized in place to conform to a specific geometry. Additionally, due to their radical polymerization, methacrylate monomers can be photopolymerized, an aspect that is particularly pertinent to this work. This process allows methacrylates to be polymerized with the temporal and spatial control of a photoinitiated reaction. These advantages have allowed methacrylates to be used almost exclusively in the resins for tooth fillings.[50] A more descriptive introduction to photopolymerization will be discussed later in this chapter. Methacrylates can also be used in soft tissue applications. For example poly(ethylene glycol) (PEG) (meth)acrylate and hydroxy ethyl methacrylate (HEMA) derivatives have been studied as hydrogels for tissue engineering.[51,52]

While this is not an all-inclusive list of polymeric biomaterials, it provides an overview for many of those most commonly used in medical devices and implants. It is important to note that, as the understanding of biological systems evolves, the cell-material understanding and engineering will continue to develop. As our understanding of cell-surface receptors, growth factors, nuclear control of protein expression, stem cells, and gene delivery continues to progress, so will the necessity to develop new materials that interact appropriately with the body. While the advances to the current materials are significant and instrumental in current biomedical device function, considerable room for growth remains in understanding and engineering the response to an implantable material. This bodily response will be discussed in detail in the following section.

1.2 THE FOREIGN BODY RESPONSE

Implantation of a biomaterial, prosthesis, or medical device into a host results in injury to tissue or organs.[53] This initial perturbation from homeostasis leads to a cascade of events that elicit wound healing. This process is designed to digest and/or remove any foreign material,

followed by repair and regeneration of the damaged tissue.[54] When the implanted material is non-digestible, such as a medical device or prosthesis, it cannot be phagocytosed and removed. The disruption in the bodily response to digest the foreign object leads to encapsulation of the material with a dense layer of fibrotic connective tissue.[55,56] This bodily reaction to an implanted material has been called the foreign body response or foreign body reaction (FBR). For the purpose of this work, the FBR to non-biodegradable materials, or materials that will not degrade over time and are intended to be implanted long-term, will be addressed. This bodily response is of particular importance to implantable materials that require transport of biomolecules such as proteins to and from the implanted material. For example, an implantable blood glucose monitor will foul shortly after exposure to host blood and proteins which will terminate function of the device.[57–59] The deleterious effects that the FBR has on the function of neural prosthetic devices such as a cochlear implant are of particular importance.[60] Neural prosthetics rely on intimate communication between a stimulating electrode or electrode array and receptor neurons. This communication is achieved by way of electrical current transmitted through the host fluid. When a dense avascular capsule is formed on the surface of a neural prosthetic, the transport of electrical current is also disrupted and communication between the electrode and the receptor neurons can be detrimentally impacted.[61] The effect of the FBR on cochlear implant devices will be discussed in more detail later in this chapter. In this section, a description of the FBR will be discussed including the biological cascade of events and the important time scales leading up to encapsulation of an implanted device.

The blood-material interactions of an implanted material are intimately linked with the inflammatory response. In fact the early response to injury involves mainly blood and vasculature.[53,62] An early inflammatory response is activated by damage or injury to vascularized

connective tissue. Immediately following implantation of a material, proteins, blood cells, and other biomolecules found in the blood stream come into contact with the surface of the implant. From a wound healing perspective, the early deposition of these biomolecules on a biomaterial surface is considered provisional matrix formation. The provisional matrix consists of fibrin, inflammatory products, inflammatory cells, and endothelial cells.[63] The formation of this provisional matrix occurs within minutes to hrs following implantation of a medical device. In particular, the adsorption of proteins, such as fibronectin, laminin, proteoglycans collagens is considered the first step in the FBR.[64–66] These initial events initiate the repair process which involves the recruitment of inflammatory cells and fibroblasts.[55]

The sequence of events occurring after the initial adsorption of proteins and other small molecules in the host fluid is illustrated in Figure 1.3. Neutrophils are inflammatory cells that are the first to travel to the site of an infection. They help fight the infection by digesting bacteria and releasing enzymes that kill them. Neutrophils are a type of white blood cell, and their initial intensity is high. The presence of neutrophils is diminished within hrs to days after the initial response. A second initial responding cell type is mononuclear leukocytes, which have a similar function to neutrophils in that they have a digestive role in inflammation. Their initial intensity is also high after which they quickly differentiate into macrophages, the cells principally responsible for normal wound healing in the FBR. These macrophages have much longer lifespans, remaining at the implant site for days to months and are recruited to digest the foreign material. Because implants are typically not biodegradable, the macrophages are unable to digest the implant. When phagocytosis is not possible the macrophages become frustrated and fuse together and form foreign body giant cells, which release inflammatory cytokines and induce

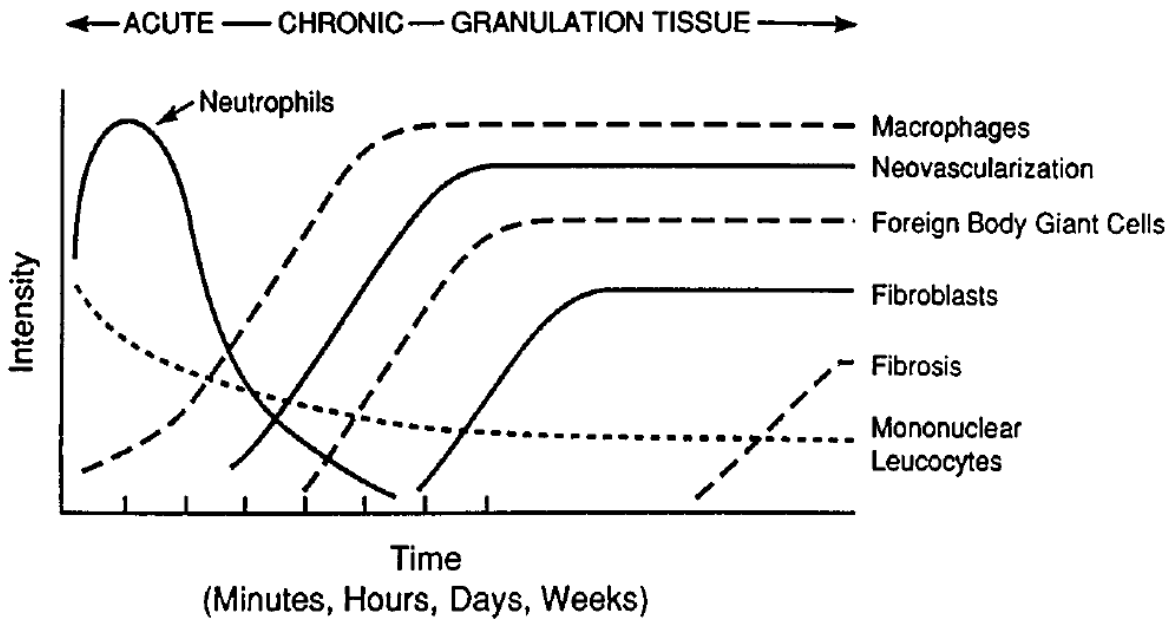

Figure 1.3. The temporal variation in the acute inflammatory response, chronic inflammatory response, granulation tissue development, and foreign body reaction to implanted biomaterials. Adapted from reference 55.

fibroblast adhesion.[16,67–70] These foreign body giant cells may remain adhered to the implant surface for the lifetime of the implant.

Once the foreign body giant cells have formed, fibroblasts quickly adhere to the surface and begin forming the framework of connective tissue.[55] Fibroblasts are a type of cell that synthesizes collagen and the extracellular matrix. They are instrumental in the wound healing process and are also the most common cells of connective tissue. Once the fibroblasts are adsorbed onto the biomaterial surface, they quickly begin to form a network of cells and fuse together to form a fibrous capsule around the implant.[16] The process of encapsulating a biomaterial after implantation lasts about three weeks. This encapsulation permanently isolates the device and often renders the implant less effective or even nonfunctional due to lack of transport to and from the surface. Thus, developing strategies to address the FBR from a

materials standpoint has the potential to significantly impact the biomedical device industry and healthcare in general.

Engineering materials that resist the FBR has the potential to dramatically improve the effectiveness and the long-term stability of a wide variety of neural prostheses. For example, cochlear implant users have the potential to achieve greater perception of complex auditory stimuli such as speech understanding in background noise and music appreciation. Retinal prostheses may provide significantly greater resolution of visual images while central nervous system prostheses, e.g. deep brain stimulators, could provide more precise activation of targeted neural populations. The materials innovations described herein stand to dramatically improve the function and stability of numerous other medical implants (e.g. intraocular lenses, arterial stents, heart valves, orthopedic implants, among others) by enhancing integration and preventing fibrosis.

1.2.1 Mitigating the Foreign Body Response

Compatibility of a biomaterial with host tissue has significant implications and can vary widely based on the chemistry and geometry of an implanted device.[16] Many materials, while non-toxic, elicit a significant FBR and as such can cause challenges integrating with host tissue. For example, PDMS materials are known to induce a significant FBR and ultimate encapsulation with fibrous tissue.[71] However, the addition of a hydrophilic group such as a PEG or zwitterionic material to the PDMS surface can dramatically reduce the adsorbed biomolecules associated with the FBR.[72–74] The two materials engineering approaches which have been demonstrated to be the most effective in reducing fibrosis on implant surfaces are 1) fabricating porous materials with defined pore size[16,75] and 2) the use of hydrophilic polymers that resist protein and other biomolecule adsorption that lead up to the FBR.[64,76,77] Significant advances in these innovations

in biomaterials science have occurred in the last two decades. One interesting approach was largely pioneered by Buddy Ratner at the University of Washington with his development and characterization of porous materials with a monodistributed mesh size.[16,75,78] Another approach of altering material chemistry to reduce the FBR has been investigated by many individuals[64,79] with the most notable advances from Dr. Shaoyi Jiang and his work with zwitterionic materials.[76,80]

The advances in engineering the pore size of a material to alter the FBR occurred as early as 1973. During this time, it was demonstrated that materials in the solid form and materials in the porous state will heal differently when implanted. The porous materials were shown to increase the number of blood vessels around the implant.[81] While many papers were published on the subject in the following years, the relationship between the pore size and the healing response was never clearly characterized. In the early 1990s, the University of Washington set out to better establish this relationship. Researchers there developed a new set of materials with uniform pore size, spherical shape, and an interconnected network. This advancement led to the characterization that pores in the 30-40 μm range healed with excellent blood vessel growth and little fibrosis.[78,82,83] Further, it was found that the FBR was mitigated independent of the material used to fabricate the porous implant.

The second approach, engineering polymers that prevent the adsorption of biomolecules that lead to the FBR, is a focus of this work and will thus be discussed in greater detail. The overall goal of these studies, and perhaps the most widely used method to characterize the ability of a material to resist the FBR, is to mitigate the initial steps leading up to an immune response (i.e. nonspecific protein adsorption).[84] Strategies to engineer these types of materials have focused largely on hydrophilic polymers that are either neutral in charge or weakly negative.

Numerous polymers have been investigated including acrylamides, polysaccharides and most commonly derivatives of PEG.[85,86] PEGylation, as it has been called, refers in general to the functionalization of a surface or particle with PEG in order to decrease interactions with a biological environment.[87] While these approaches have been successful in mitigating nonspecific protein adsorption *in vivo*, the implants will ultimately still become encapsulated in fibrotic tissue after implantation.[88]

More recently, zwitterionic materials have emerged as an excellent alternative to PEGylation.[89,90] The term zwitterion comes from the German word zwitter meaning hybrid and the word ion.[91] A zwitterion describes a molecule composed of two or more functional groups of which at least one has a positive and one has a negative electrical charge, but the net charge of the entire molecule is zero (Figure 1.4). Because they contain a positive and a negative charge, they are also referred to as inner salts. Zwitterionic materials are unique in that they maintain excellent hydrophilicity while retaining a net neutral overall charge. Due to the charged groups, they are more hydrophilic than their PEG-based counterparts.

Using zwitterions to mitigate fouling was inspired by the external surface of mammalian cell membranes, which contain phospholipids bearing a zwitterionic headgroup.[92] These phospholipids contain the zwitterionic group phosphoryl choline, which contains a negatively charged phosphate group and a positively charged ammonium group. Examples of other common zwitterionic materials are shown in Figure 1.4. The three most well studied zwitterions are phosphoryl choline, sulfobetaine, and carboxybetaine derivatives. While all three zwitterions have shown decreases in protein and other biomolecule adsorption, the sulfobetaine and carboxybetaine derivatives have shown more promising performance and are the focus of this work.[64,65,93]

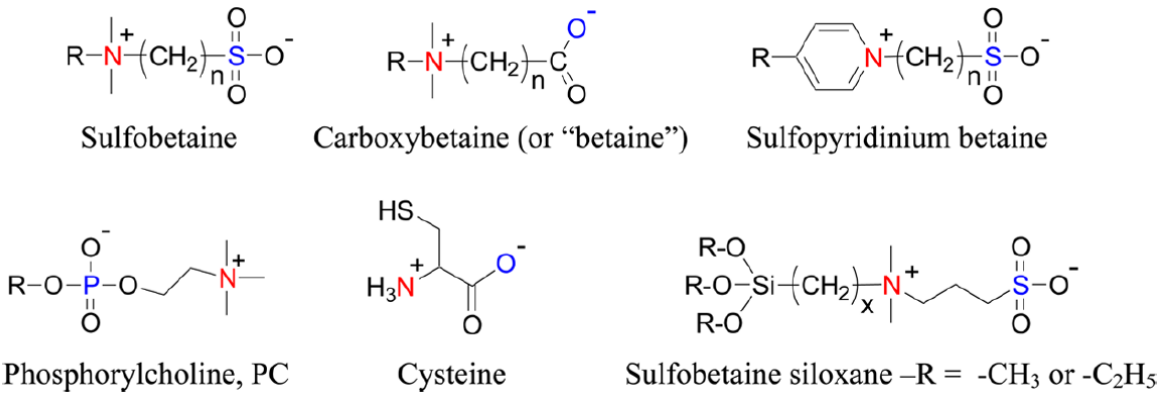

Figure 1.4. Zwitterionic functional groups and one zwitterated siloxane. Adapted from reference 65.

The research into zwitterionic materials has focused on two main areas: resisting the FBR and on more general nonfouling and resisting protein/biomolecule adsorption at interfaces. While these two general approaches are linked and have many similar features, there are some fundamental differences. For example a zwitterion that resists the FBR will also prevent nonspecific protein and other biomolecule adsorption.[94] However, resisting the FBR has more stringent requirements than simple nonadhesive properties.[95] Ideally, the material must not activate platelets.[96] The complex and transient milieu of biomolecules encountered by materials *in vivo* requires a higher standard for nonfouling. Thus, resisting the FBR and a nonfouling surface have different requirements.

The ability for zwitterionic materials to resist nonspecific adsorption of proteins and other biomolecules stems from their ability to strongly bind water. This hydrophilicity is due to the presence of charged groups. Four generally accepted explanations for the ability of zwitterionic materials to resist nonspecific protein adsorption are:[65] (1) surface energy mechanisms, (2) water structure, (3) excluded volume (steric) effects, and (4) ion-coupled driving forces. The surface energy mechanism (1) can be described by the surface of a material maintaining sufficient

hydration that it is in a similar state to bulk water. Thus, no free energy can be gained by replacing a protein/water interface with a protein/surface interface by adsorption.[94,97] Simply stated, a surface with low interfacial energy with water should discourage adsorption driven by interfacial energy change. The water structure argument (2) can be described by zwitterionic materials tightly binding water molecules in a hydrogen-bonded network. Disrupting this hydrogen-bonded network of water comes with a high energy cost and is reflected in a large water cohesive energy density.[98,99] This theory has been supported by molecular-level analysis of zwitterionic and other nonfouling materials.[100]

The excluded volume (steric) effect (3) describes a surface with a superhydrophilic diffuse surface.[97] The steric forces of compressing a hydrophilic, uncharged polymer brush of a given thickness grafted to a surface contribute to the resistance of a particle from invasion.[101,102] Finally, the ion-coupled driving (4) force describes the electrostatic effects that contribute to a nonfouling surface. A surface must not only be hydrophilic, but it also must maintain a net neutral overall charge. For example, silica is strongly hydrophilic with a contact angle around 0°, yet

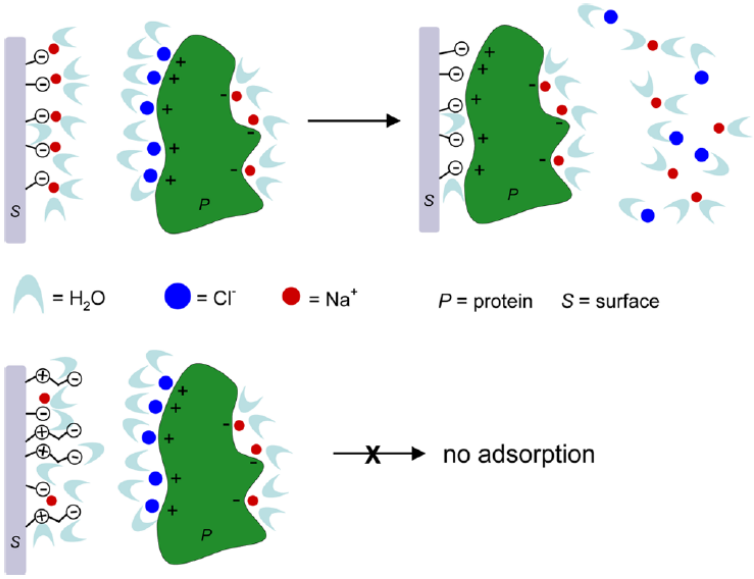

Figure 1.5. Cartoon representing the resistance to nonspecific protein adsorption. Upper: An anionic surface attracts positively-charged regions on a protein facilitating protein adsorption. Lower: A zwitterionic surface has minimal ionic interactions with a protein and high hydration prevents the nonspecific adsorption of protein to the surface. Adapted from reference 65

charged, and protein is strongly adsorbed onto this surface.[103] Proteins maintain charges on their surface where local patches of positive and negative charges can be found. Figure 1.5 depicts the electrostatic attraction of a negatively charged surface to a protein with localized positive charges. Therefore an electrostatic attraction between a charged surface and local charges found on protein surfaces contribute to protein adsorption. In contrast, a zwitterion maintains no electrostatic attraction, and thus no energetic driving force for water/ion displacement on the zwitterionic surface is present.[65,66] Whatever the reasons that allow the repulsion of protein, zwitterionic materials are effective at mitigating biomolecule adsorption.

1.2.2 Zwitterionic Polymer Fabrication

As previously mentioned, two zwitterionic polymers, sulfobetaine and carboxybetaine, are a primary focus of this work. The most widely studied form of these zwitterions is the methacrylate (carboxybetaine methacrylate (CBMA) and sulfobetaine methacrylate (SBMA)) and methacrylamide analogs. These reactive methacrylates allow convenient polymerization of the zwitterionic monomers to yield a polymer with a carbon backbone and zwitterionic side groups.[76] Due to the methacrylate/methacrylamide group, radical polymerization can be used to generate polymers. Functionalizing surfaces with linear polymers containing no crosslinks, also called polymer brushes, have been investigated for creating antifouling surfaces.[104,105]

Two general types of grafting processes are used for functionalizing surfaces with polymer brushes: grafting to and grafting from. The grafting to process involves generating a polymer in solution with subsequent binding to the substrate surface. The reactive polymers can be synthesized via conventional polymerization techniques such as radical, ionic, and other copolymerization methods. One major advantage of this approach is that the polymer can be thoroughly characterized prior to the grafting process. For example, Jiang et al. synthesized a

CBMA and SBMA polymer with pendant dopamine groups which could be subsequently grafted to a variety of polymeric and metal surfaces.[106,107] They further demonstrated the ability of these coatings to reduce nonspecific protein adsorption and characterized the dependence of fouling on polymer particle size. While the grafting to process is effective for functionalizing substrates with a zwitterionic polymer, the grafting from method has also been investigated.

The grafting from process involves covalently attaching an initiator for polymerization on the surface of a substrate which is then reacted with monomer in the solution and a polymer is then generated *from* the surface. The polymerization using the grafting from method often involves incorporating agents that control the polymerization. Surface initiated atom transfer radical polymerization (SIATRP) is a common approach which utilizes a bromine initiator immobilized on a substrate surface. A copper bromide catalyst in the solution controls the rate of polymerization from the surface to generate covalently grafted polymer brushes of uniform molecular weight and densely grafted surface.[108,109] Further, the thickness of the polymer brushes can be easily tailored by altering polymerization times.[73] Zwitterionic polymers generated using this technique have shown excellent resistance to nonspecific protein adsorption. For example, Jiang et al. reported both SBMA and CBMA polymer brushes grown on gold surfaces using SIATRP having ultralow nonspecific protein adsorption (9.1 and 0.4 ng/cm^2 respectively) from 100% blood plasma. [64,110] Further, various other surfaces have been functionalized using this method including glass,[111] metal,[64,109] and polymer[73] substrates.

Zwitterionic polymers can also be polymerized to form a hydrogel network.[112,113] To achieve network formation, a crosslinking agent must be incorporated. Early work fabricating zwitterionic hydrogels used non-zwitterionic crosslinkers such as poly(ethylene glycol) diacrylate (PEGDA) or N,N′-methylenebis(acrylamide) (MBA).[58,113,114] While the crosslinking

agent was used at relatively low concentrations, it could potentially disrupt the antifouling properties of the hydrogel material. Further, higher modulus (more densely crosslinked) materials cannot be achieved without significantly changing the zwitterionic chemistry of the hydrogel. Recently, Jiang et al. reported on a zwitterionic dimethacrylate crosslinker based on the carboxybetaine analog.[112] Using this crosslinker, they were able to synthesize hydrogels with an order of magnitude increase in modulus without changing the zwitterionic nature and fouling properties of the material. Perhaps most important to this work, Jiang et al. reported the implantation of carboxybetaine hydrogels, formed using this same crosslinker, into a mouse model for three months. Upon extraction and histological analysis of the tissue surrounding the implant, excellent compatibility with the surrounding tissue was observed and no signs of fibrosis were present.[80] Further, the zwitterionic hydrogels promoted angiogenesis in the surrounding tissue.

The ability of zwitterionic materials to prevent the adsorption of biomolecules even in complex media gives them promise for use in biomedical and engineering applications. This inherent antifouling characteristic has led to various studies including glucose sensing in 100% blood serum,[58,113] antigen detection in complex media,[115] and prolonging the blood circulation time of coated drugs[6] among others.[89,116] Zwitterionic polymers are not only able to achieve an ultra-low fouling surface, but they are capable of resisting the FBR *in vivo*.[80] This advantage makes zwitterion-based materials uniquely suited for applications that involve implantation and prolonged use in the body. Fibrotic tissue formation on implant surfaces, including CIs and other neural prosthetics, may decrease the effectiveness of these devices.[61] Due to the emphasis of this work on improving CI materials, the following section will discuss CIs, their history, function and the areas for improvement.

1.3 COCHLEAR IMPLANTS

Cochlear implants have revolutionized the treatment of deafness and severe hearing loss. Just over 50 years ago, no viable treatment for these conditions was available. The development of the CI has allowed individuals suffering from sensorineural hearing loss to perceive speech and even communicate with ease using a cell phone. To date, the CI remains the only viable treatment for auditory communication rehabilitation for individuals suffering from sensorineural hearing loss. Cochlear implants function by perceiving sound through a behind-the-ear microphone which processes the sound into a digital signal and encodes the signal into a radio frequency (Figure 1.6).[117] The digital information is then transmitted to an internal portion of the implant lying just under the skin behind the ear which decodes the signal into electrical current and sends the information to an electrode array positioned inside the cochlea.[118,119] The cochlea is a spiral shaped organ primarily responsible for the perception of sound and has channels that allow resonance of different frequency sound in specific regions of the organ. Higher frequency sound resonates near the base of the cochlea (20 kHz or greater) and lower frequency sound is perceived at the apex

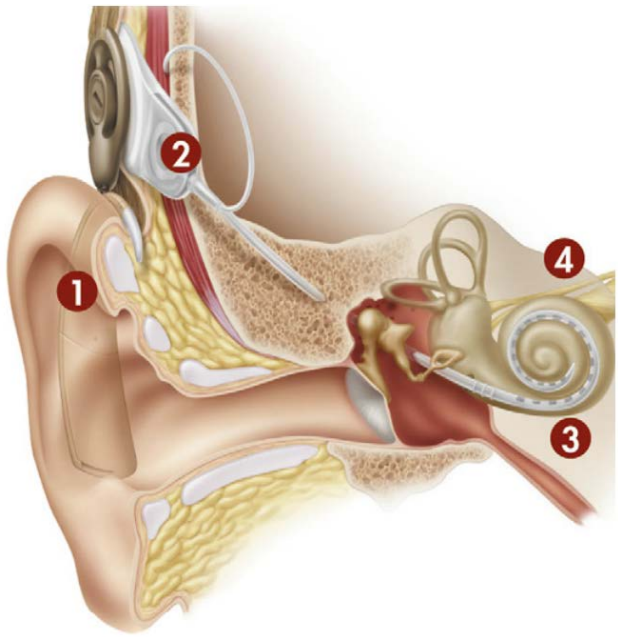

Figure 1.6. Diagram of cochlear implant speech processing. (1) A microphone located on the behind-the-ear sound processor unit processes, codes, and sends the tonal information via transcutaneous radiofrequency link to the (2) implanted receiver-stimulator package. The data are then sent to (3) the electrode array. The spiral ganglion cell populations are then stimulated by an applied current at various positions along (4) the cochlea (auditory nerve) to simulate hearing. (Photo provided courtesy of Cochlear Americas, © 2011 Cochlear Americas.)

(up to 20 Hz). The electrode array lies in a channel called the scala tympani located on the outer wall of the cochlea, which directly stimulates the auditory nerve with an applied current (Figure 1.7). The information is then relayed to the central nervous system where the brain perceives the applied current as sound. The tonotopic organization of the cochlea enables an electrode array to simulate different perceptual "tones" by stimulating electrodes positioned in different areas of the scala tympani (Figure 1.7). Through this stimulation process, CI patients perceive multiple tones and experience hearing.

1.3.1 History

The first report of auditory perception by electrical stimulation was recorded by Alexander Volta in the early 1800s.[120] His account describes connecting each pole of a battery to a metal probe and inserting the probes into opposing ears. Upon application of current, he described the sensation as a "jolt to the head" followed by a "crackling" or "bubbling" sound.[120] Years later in 1855, Duchenne de Boulogne stimulated the cochlea using an alternating current and described the sound as buzzing, hissing, and ringing.[121] Further, the experiment also stimulated multiple other non-auditory pathways including a metallic taste sensation.[122] In 1930, Wever and Bray recorded electrical signals that closely resembled the sound wave function in a feline cochlea, which led many to believe that auditory perception could be restored through electrical stimulation.[123] The first to directly stimulate the human auditory system were Djourno and Eyries. They implanted an electrode into the stump of the auditory nerve coupled to a receiver coil.[124] Post-operative testing revealed successful detection of electrical stimuli generated from a microphone. While transmission of sound was successful, the patients were unable to efficiently distinguish between different frequencies, but could rather differentiate intensities. Speech perception was very poor and limited to a few words, most likely due to

rhythmic patterns. While this was a remarkable step forward in the development of CIs, the device failed within a few weeks and the project was eventually abandoned.

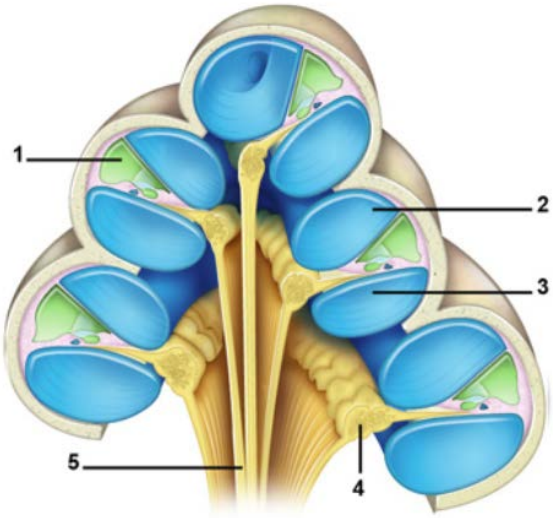

Figure 1.7. Diagram of the cochlea. The cochlea is made up of three canals wrapped around a bony axis. These canals are: the scala tympani (3), the scala vestibuli (2) and the scala media (or cochlear duct) (1). The spiral ganglion neurons (4) are the primary neural receptors. The auditory nerve (5) transmits signals from the spiral ganglion neurons back to the central nervous system. Image courtesy of www.cochlea.edu.

The work of Djourno and Eyries prompted Dr. William House and Dr. John Doyle in 1961 to develop a CI device that could be implanted long-term.[125] These devices consisted of an array of 5 electrodes that were inserted into the scala tympani through an incision in the round window membrane. The outcomes of these results were promising with limited frequency discretion and the ability to understand rudimentary phrases.[126] The insufficient biocompatibility led to compromised function of the implant and ultimately removal of the device. Later, in 1967, House teamed up with an electrical engineer by the name of Jack Urban. This partnership led to the development of CIs that could maintain long-term viability. Through this groundbreaking work, House is regarded as the pioneer or "father" of the modern-day CI. This early work resulted in the first commercially available device in 1972 with clinical trials beginning the following year.[127]

These successes were met with considerable resistance from the scientific community including leading otologists and neurophysiologists.[128] This skepticism was partially dissolved

when the National Institutes of Health (NIH) commissioned a study at the University of Pittsburgh to evaluate the performance of single channel CI devices.[121,129] A major advancement occurred when Graeme Clark developed a multi-channel electrode array where patients were capable of open-set word recognition.[130] The achievement was followed by FDA approval of single-channel devices and led to the development of multi-channel CIs capable of a broader frequency spectrum percepts and open-set word recognition. Through these advancements, multi-channel CI devices have significantly improved incorporating electrode arrays with varying number of electrodes, widths, lengths, and positioning technologies. These improvements to CI technology have substantially increased the number of perceptually distinct tones CI patients experience and overall standard of living. However, the stimulated hearing induced by CIs still has significant room for improvement.

1.4 GOALS FOR IMPROVING COCHLEAR IMPLANTS

While hearing restoration for profoundly deaf individuals is quite a remarkable feat, CI patients have difficulty distinguishing complex tonal information such as voice inflection, speech recognition with competing sounds, and appreciating music. This limited resolution is due, in large part, to the distance between the CI electrode array and target neurons. Electrical signals must be strong enough to reach the auditory neurons positioned hundreds to thousands of micrometers from electrode arrays, which causes significant current spread and overlap (Figure 1.8). The spread of the applied signal results in stimulation of a broad range of spiral ganglion neurons (SGNs) which are the target neurons of a CI. Signal broadening limits the resolution and tonal perception of CI patients. Advances in electrode fabrication technology have not been able to sufficiently address this major drawback due to the lack of perceivable differences between electrodes positioned in close proximity to one another. Thus, even devices with advanced

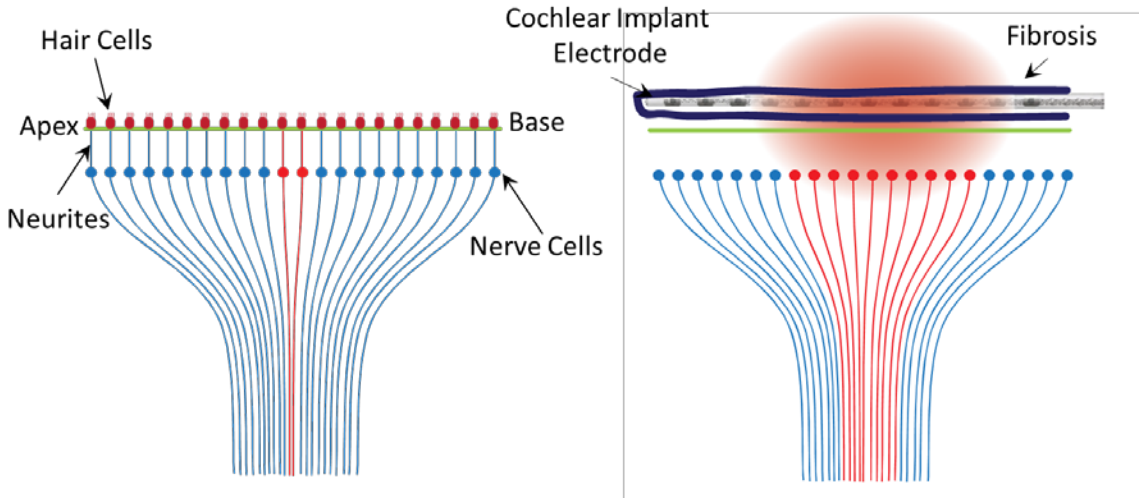

Figure 1.8. Schematic representing stimulation of auditory nerve cells for normal hearing (left) and cochlear implant patients (right). Spatial separation and fibrosis lead to significant current spread and decreased resolution.

electrical design and high number of distinct electrodes suffer from low resolution information.[131] Additionally, cochlear implants are made largely from poly(dimethyl siloxane) (PDMS) which accumulates a significant foreign body response as discussed previously. This dense tissue attenuates applied currents and increases stimulation thresholds, which further decreases the functional outcomes of CIs.[61,132] Late term hearing loss in CI patients has largely been attributed to the FBR.[60]

In order to overcome signal resolution barriers caused by spatial separation between SGNs and electrode arrays, it will be necessary to regenerate SGN neurites. Directing the regeneration of these neurites to approach or even contact the stimulating prosthetic have the potential to drastically reduce the current applied to stimulate hearing (Figure 1.9). By reducing the applied current and consequent current spread, a higher number of independent hearing channels will be achieved, significantly improving tonal perception for cochlear implant patients. This innovation will lead to greater specificity and targeted stimulation of the neural receptors.

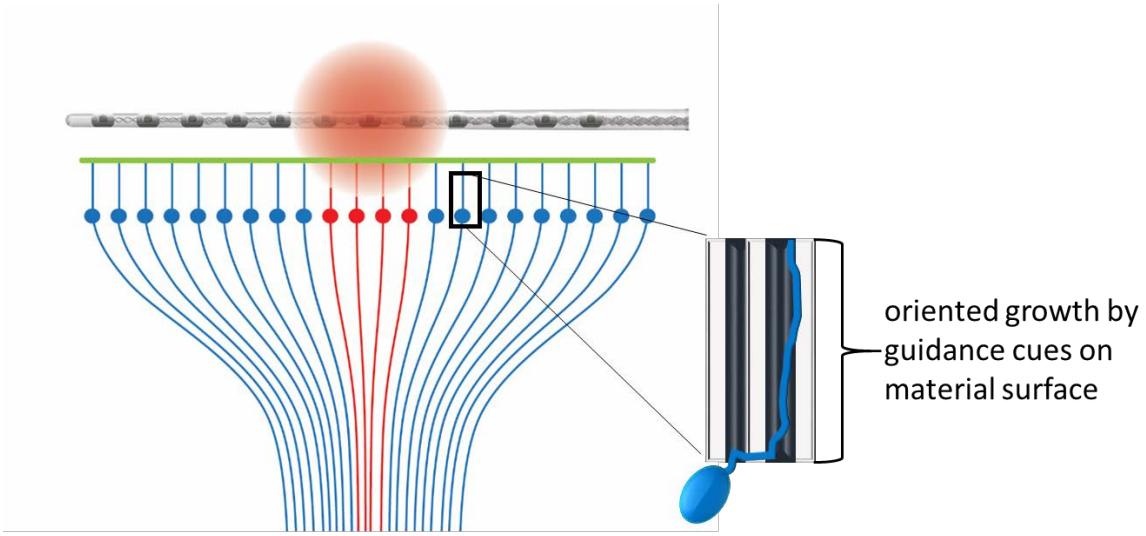

Figure 1.9. Goal for improved cochlear implant performance. Using surface chemistry and topography, SGN neurites can be regrown to close the gap between the neural receptors and the stimulating electrode. Zwitterionic polymer coatings can also prevent the accumulation of fibrosis on the implant surface.

While strategies to promote the regeneration of SGN neurites *in vivo* have proven effective,[133,134] neurite outgrowth extends randomly from the neural cell rather than following the path of the degenerate neurite.[135] Thus, guidance cues will be essential in directing the path of regeneration and maintaining the spatial order of neural elements. Two types of guidance cues will be discussed for directing the growth of cells: topographical or physical cues and biochemical cues.

1.4.1 Topographical/Physical Cues

Cells respond to multiple cues in their native microenvironment. These cues can determine spreading morphology, cell type, gene expression, and alignment.[8] When cells interact with a biomaterial, it is advantageous to regulate the response in a predictable manner. One approach to achieving a desired response is to modulate the extracellular milieu by controlling biomaterial surface characteristics. As early as 1912, Harrison observed that the solid material that supports cells has significant influence on their morphogenesis and migration, when describing how cells responded to being cultured on a spider web.[136] Other early observations

included Paul Weiss, who in 1945 described how contact guidance can be used as a method for cells to migrate from their source to their destination,[137] and Curtis and Varde in 1964 who used topography to control cell behavior.[138] It wasn't until the onset of micro- and nano-fabrication, almost 30 years ago, that researchers could probe the behavior of cells with well-defined shapes and geometries.[3] This innovation in materials construction has led to numerous studies investigating micro- and nano-scale surface features and the cellular response.[8,139]

Various types of imposed topography and their neural response has been studied *in vitro.* Two general categories of surface features can be defined: anisotropic and isotropic (Figure 1.10). Anisotropic features include those with directionality. Examples of these types are grooved surfaces, aligned fibers, guidance conduits, and cell-inspired (mimicking) topographies. Isotropic features are those that maintain no directionality. Two examples of these are pillars/posts and nanorough surfaces. These different features can vary widely in size scale and cellular response. For the purpose of this work, the focus will be on anisotropic topography, specifically grooved surfaces.

A number of studies involving microgrooved substrates have observed that neurite alignment increases with increasing groove depth between 0.2 and 4 μm.[140–142] No observable changes in alignment were recorded on features less than 200 nm. In studies involving dorsal root ganglia grown on submicron to micron-scale features, increasing groove height resulted in both increased alignment and increased restriction of cell soma and neurites on the groove or the ridges.[140] The feature depth, as well as the angle at which a neurite contacts a guidance feature have been shown to influence whether a neurite turns to follow the feature or crosses the cue.[143] For example, the distance between anisotropic topographical features has been shown to play a role in directing neurite growth.[144,145] In an additional study, Teixeira et al. observed that human

corneal epithelial cells aligned to ridge features as small as 70 nm wide with a depth of 600 nm and a width of 400 nm.[146] In this study, groove depth (150-600 nm) was shown to have a stronger effect on cell alignment than groove width (400-4000 nm).

Previous work in our lab by Tuft et al. showed that SGN neurites align strongly to photopolymerized parallel microgrooves (Figure 1.11) with increasing channel amplitude and increasing pattern frequency improving alignment.[147] Our lab further correlated the maximum slope of the microchannels with the alignment of SGN neurites. An additional study, using similar photopolymerized fabrication methods, examined SGN neurite alignment on 90° angled features.[148] SGN neurites grown on these substrates demonstrated a greater number of branching and crossing events occurring due to the changes in microchannel direction. The modulus of these photopolymerized micropatterns was also shown to influence SGN neurite pathfinding to parallel micropatterns.[149] Higher modulus substrates resulted in significantly improved alignment. An additional study from our lab demonstrated the ability of high frequency photopolymerized micropatterns to induce SGN neurites to overcome chemorepulsive borders.[150] While guiding neurite growth using topographical features has proven effective, biochemical signals can also induce alignment.

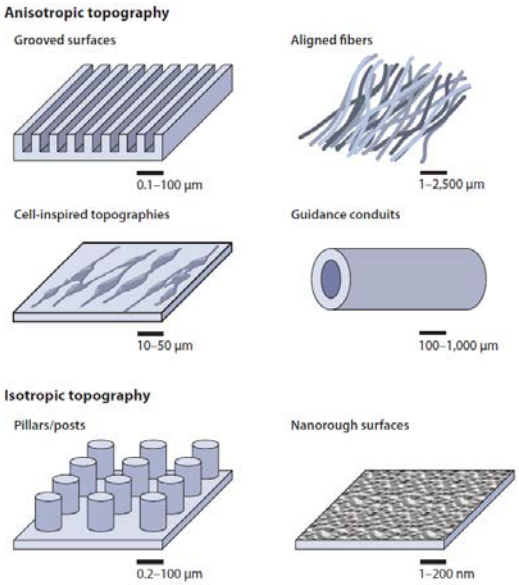

Figure 1.10. Topographies presented to neurons in vitro. Adapted from reference 8.

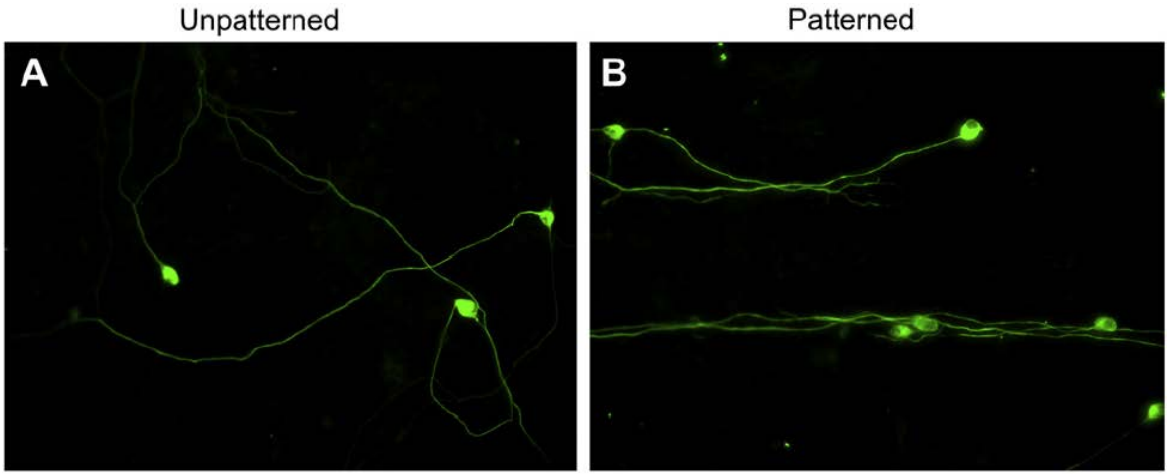

Figure 1.11. Neurite growth from dissociated SGNs on (A) unpatterned and (B) 50 µm periodicity, 3 µm amplitude photopolymerized polymer substrates. Adapted from reference 147

1.4.2 Biochemical Cues

Biochemical patterning can be achieved by spatially controlling the immobilization of a biologically relevant molecule. These molecules are designed to modulate the interactions a cell has with a surface. Examples of strong candidates for biochemical patterning are extracellular matrix (ECM) proteins such as fibronectin, vitronectin, collagen, and laminin.[151] Alternatively, their constitutional polypeptide motifs can be used such as arginine-glycine-aspartate (RGD).[152,153] These biomolecules are selected due to their ability to modulate the cell response to a surface. Specifically, these proteins/motifs have been shown to enhance adhesion of cells. This adhesion is due in large part to cell-ECM interactions which occur between transmembrane integrins and the ECM ligands, which are largely responsible for cell adhesion. Alternatively, biochemical patterns can be generated that repel cells, and thus prevent cells from adhering in coated areas. Selectively adsorbing adhesive/repellant biomolecules onto a surface can create biochemical patterns that control the adhesion of cells. Cells adhere onto and reside exclusively on areas that are cytophilic (coated with adhesion biomolecules or not coated by repellant

biomolecules) after random seeding. Thus, biochemical patterns guide the outgrowth of neurites by an adhesive/repulsive mechanism.

The most common approach for generating biochemical patterns on flat substrates is through microcontact printing (μCP). This technique involves adsorbing the biomolecule onto a micropatterned "stamp" (PDMS is often used as the substrate), which is then pressed against a flat substrate to transfer the biomolecules only in areas that come into contact with the surface.[154,155] These patterned surfaces can then direct the adhesion and growth of various cell types. For example, Juncker et al. showed that fibroblasts seeded onto PEG surfaces containing 10 μm wide fibronectin parallel stripes extended down the length of the protein pattern, avoiding interaction with the PEG substrate.[156] Further, Offenhäuser et al. demonstrated that neurites followed grid-like patterns of laminin and ECM proteins using polystyrene substrate.[157] Extending axons even made 90 degree turns at branch points in similar grid-like patterns showing the effectiveness of biochemical markers in directing neural processes.[158,159]

In addition to using μCP to pattern proteins onto substrate surfaces, photoinitiated reactions can be used to spatially control covalent attachment of molecules containing "ene" (double bond) and "thiol" functionalities[160,161]. Photoinitiated thiol-ene "click" chemistry selectively reacts thiol moieties with "ene" functionalities in a step growth mechanism. This fabrication method is effective for chemical patterning due to the precise spatial and temporal control over the reaction, while maintaining mild reaction conditions (photopolymerization will be discussed in more detail later). For example, Anseth et al. used a photomask to covalently pattern norbornene-functionalized proteins throughout a hydrogel matrix containing pendant thiols.[162] Alongside protein patterning, cell adhesion peptides such as arg-gly-asp (RGD) can also be photopatterned. Photopatterning the RGD peptide is more common than using native

ECM proteins due to increased robustness and decreased cost. Further, RGD peptides can be tethered to various functional groups, which allow for covalent attachment to surfaces and hydrogels through photopolymerization.[163,164] For example, Chen et al. showed that a thiol-terminated RGD-containing molecule could be patterned onto a “ene” and “yne” containing surface, which showed fibroblast cell attachment only in RGD-containing regions[165]. Therefore, biochemical cues, both protein and polypeptide-containing, can be photopatterned to effectively guide neural cells.

1.4.3 Mitigating Fibrosis on Cochlear Implant Surfaces

As previously mentioned, implantable devices accumulate fibrosis about 3 weeks after implantation. This fibrosis causes disruption of the communication between the electrode array inserted into the cochlea and the neural receptors, SGN, positioned on the inner side of the shell-shaped organ (Figure 1.7).[61,166] The current transmitted by the electrode array to the SGNs is attenuated by the dense fibrotic tissue formed on the implant surface further increasing current thresholds and current spread.[167,168] Thus, fibrosis on cochlear implant surfaces can contribute to late-term hearing loss. To circumvent the detrimental effects of fibrosis on CI surfaces, zwitterionic coatings are investigated in this work to prevent the cascade of processes from occurring that contribute to the FBR (Figure 1.12). By coating cochlear implant materials with zwitterionic polymers, fibrosis on the surface of CIs may be mitigated and current attenuation may be greatly decreased and subsequent late-term hearing loss in CI patients. Further, cochlear implants, like all implantable medical devices, are susceptible to bacterial infection and biofilm formation on the implanted material.[169] These infections often lead to removal of the in-dwelling device and additional pain and cost for patients. An additional advantage of zwitterionic coatings is that they have been shown to decrease bacterial adhesion dramatically.[170–172] Cochlear

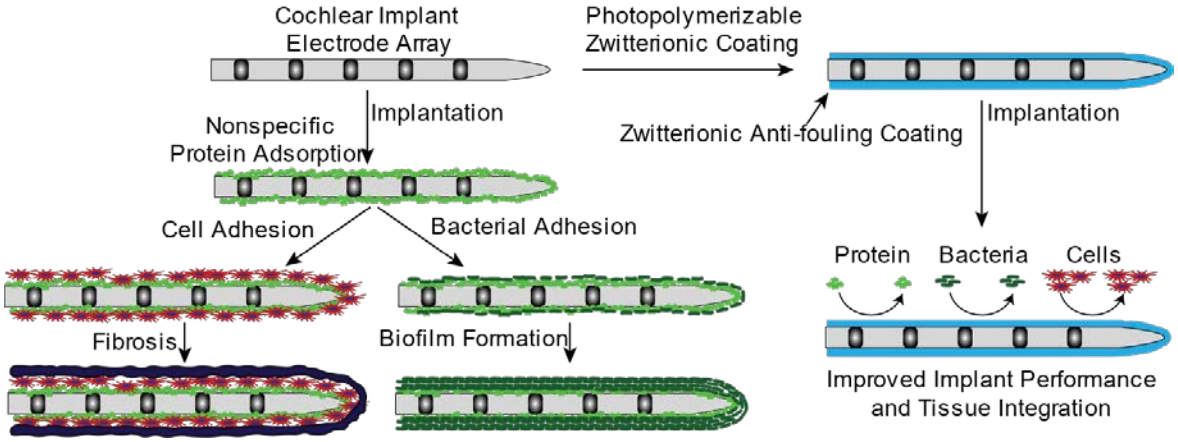

Figure 1.12. Schematic representing the events leading up to fibrosis and biofilm formation (left side). The right side depicts the use of zwitterionic polymers on cochlear implant electrode arrays to resist biofouling.

implants coated with these zwitterionic polymers will thus be able to prevent the onset of bacterial infections and biofilm formations associated with medical device implantation. Accordingly, this work describes the use of zwitterionic coatings on materials relevant to CIs to prevent protein, cellular, and bacterial adhesion. By so doing the long-term performance of CIs stands to be preserved.

1.5 PHOTOPOLYMERIZATION AND BIOMATERIALS

Photopolymerization involves the absorption of photons of light to initiate a polymerization reaction of monomers, oligomers, and functionalized prepolymers. To initiate a free-radical photopolymerization reaction, a photon is absorbed by a photoinitiating molecule (photoinitiator) which excites an electron and leads to cleavage of bonds to form radical species.[173–175] These radical species can then react with electron-rich double bonds, e.g. (meth)acrylates, to propagate a polymerization reaction and form a polymer network. Because the polymerization is initiated by photons, reaction rates are high which leads to ultra-fast curing in min or seconds. This provides a distinct advantage over thermal or redox cured systems which

have curing times on the order of hrs. These fast kinetics have allowed photopolymerization reactions to be widely implemented in industrial applications including coatings[176,177], adhesives[178], lithography[179–181], and 3D printing.[182,183] Additionally, curing of the polymer reaction can be achieved with relatively low initiator loadings at ≈1 wt% of the resin.

Another major advantage of a photoinitiated polymerization reaction is direct spatial and temporal control of reaction kinetics, which has led to the use of photopolymerization for a variety of patterning applications.[147,184,185] Through using a photomask, initiation events can be limited to areas that are exposed to light underneath the transparent regions. Thus, chemical[186–188] and physical patterns[147,185,189] can be selectively attached to be used in directing the adhesion and growth of cells. Temporal control is afforded through light shuttering to quickly attenuate polymerization once the light source is removed. For example, topographical features of a surface can be generated through a simple one-step process to form a ridge-groove pattern with variable channel depths achieved by variable light shuttering, as previously described by our lab.[147,185] Another critical advantage is the ability of a photopolymerization process to be carried out in conditions that are nontoxic to cells.[174,190–192] UV light is used most often in photoinitiation, which is toxic in high intensity to cells and can disrupt protein function.[193–196] However, the wavelength and intensity of light can be modulated to prevent cell death by radiation exposure. For example, Bahney et al. photoencapsulated human mesenchymal stem cells using visible light in a PEGDA scaffold using a photoinitiator system composed of eosin Y, triethanolamine and 1-vinyl-2-pyrrolidinone.[197] Plasmid DNA and cells were also coencapsulated in a degradable, methacrylate hydrogel without compromising the function of the plasmid DNA or viability of the encapsulated cells upon release.[198]

Photochemical processes can also be used to efficiently and quickly graft polymers to substrates. For example, a type II photoinitiator, such as benzophenone (BP), can be adsorbed onto a polymer surface followed by irradiation with UV light (Figure 1.13). The type II photoinitiator is excited by the light to a highly reactive diradical state when a photon is absorbed which then abstracts a hydrogen from the grafting surface, producing a radical that allows polymerization to occur from the surface.[199] Using this method, polymers can be covalently grafted from a variety of polymeric surfaces including PDMS, polyethylene, and polyurethanes. For example, Ishihara et al. grafted zwitterionic phosphoryl choline methacrylate polymerized from PDMS surfaces demonstrating decreased contact angles and reduced protein adsorption.[200] Polymers generated using this approach undergo a grafting from mechanism, due to the radicals being generated on the surface and the polymer propagating from the substrate.

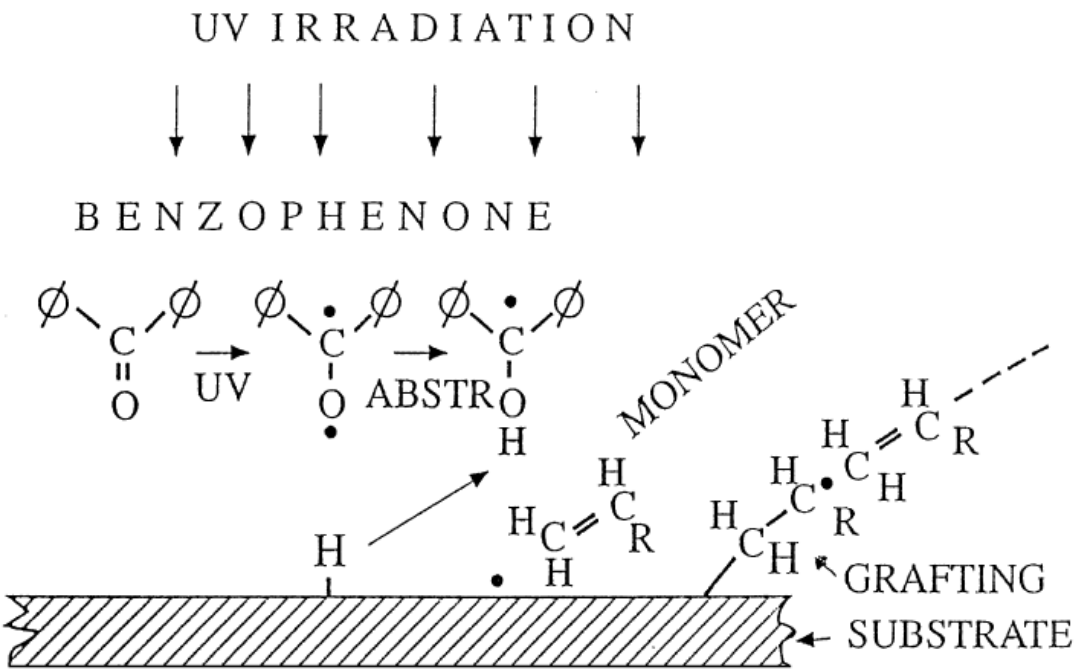

Figure 1.13. Schematic of the basic reactions involved in the surface grafting with benzophenone as an initiator of a vinyl monomer. Adapted from reference 199.

Many photopolymerizable biomaterials are composed of (meth)acrylate-based resins, which undergo a radical chain reaction to form a network.[190] The process of photopolymerization can be described in three steps: initiation, propagation, and termination. Initiation is the process by which a photoinitating molecule absorbs a photon which subsequently generates a radical molecule that can initiate polymerization. The most common initiators are Norrish type I, which undergo homolytic cleavage to directly transfer a radical to the monomer and initiate polymerization. The propagation step involves the growth of the polymer as more monomer units are added to the polymer backbone and the molecular weight increases. The final step involves the termination of the radical to end the growing polymer chain.

The photopolymerization reactions described in this work are based on (meth)acrylate chemistry and will involve the photopolymerization of monomers to engineer polymer surfaces that improve CI materials. The approach described herein involves the fabrication of micropatterned substrates to be used in directing the regeneration of SGN neurites, engineering anti-fouling surfaces to prevent fibrosis and subsequent current attenuation for CIs, and strengthening of zwitterionic hydrogel materials to improve the durability and longevity of these coatings. Chapter 4 will discuss the directed growth of neurites using topographical and chemical cues generated using a photo-induced processes. Chapters 5-6 will examine photografting zwitterionic polymers to glass and PDMS surfaces to mitigate the FBR. Furthermore, patterns were generated to locally control the adhesion and outgrowth of cells. Finally, Chapter 7 will focus on the strengthening of photopolymerizable zwitterionic hydrogels to improve modulus and durability for long-term *in vivo* use. Altogether these chapters aim to describe advances made in the field of surface engineering and with a particular emphasis on cochlear implant materials. The overall goal of this work is to improve the neural/tissue interface. The

understanding gained through this research aims to improve the quality of life for CI and other neural prosthetic patients with a broader application to all implantable medical devices.

CHAPTER 2: OBJECTIVES

Cochlear implants (CIs) help to restore basic auditory function in patients who are deaf or have profound hearing loss. However, implant patients suffer from limited voice and tonal perception due to spatial separation between the stimulating CI electrode and the receptor spiral ganglion neurons (SGNs). Regeneration of the proximate SGNs responsible for sensory function in the cochlea can be achieved but outgrowth of the neurites is random and may not decrease the separation or preserve the spatial order to improve implant fidelity. Directed regeneration of these SGN axons may improve tonal performance and implant fidelity by directing the neurites to approach or even contact CI electrodes while also maintaining the tonotopic organization of the neurons. Through generating patterned surface features (topographical and biochemical cues), the outgrowth of SGN neurites can be controlled to improve hearing outcomes for implant patients. Additionally, CI users also often suffer from late-term hearing loss which can cause significant decreases in hearing several months after cochlear implantation. This decrease in hearing has been attributed to fibrous scar tissue formation on the surface of the implanted electrodes. Engineering surfaces that resist the propensity for the body to form a fibrous capsule around cochlear implants has the potential to eliminate late-term hearing loss due to the foreign body reaction.

The approach described herein to improve implant performance involves overcoming these two major obstacles by 1) understanding the cues, both chemical and physical, that govern neurite pathfinding and 2) minimizing fibrous tissue formation through engineered durable polymer surfaces. Specific objectives for this work include:

1. Generate physical and biochemical micropatterns and verify their efficacy in directing the regeneration of SGN neurites independently and in competition.
2. Characterize photopatterned zwitterionic polymers onto glass substrates and evaluate the ability of these patterns to prevent fouling and direct the growth of neural cells.
3. Photograft zwitterionic polymers onto poly(dimethyl siloxane) (PDMS) surfaces using a type II photoinitiator and characterize the adhesion/anti-fouling properties of these films.
4. Engineer zwitterionic hydrogels by changing formulations to improve the durability while evaluating changes in fouling based on chemistry.

For the first objective (Chapter 4) SGN neural response to a combination of topographical (physical) and biochemical patterns is examined. In native tissue, neurite outgrowth is controlled by a complex array of physical and chemical cues that precisely guide and position neural elements. It is therefore important to understand the neural response to a combination of directing mechanisms. Additionally, neurites regenerated *in vivo* will experience many competing signals and overcoming a conflicting biological cue may be required to guide neural regeneration. To this end, acrylate substrates were topographically patterned using photopolymerization, after which laminin, a cell adhesion protein, was patterned perpendicular and parallel to the physical features. This system was used to study the relative effect of biochemical and physical cues on neurite guidance. These results demonstrate the ability of photopolymerized micro-features to modulate alignment of SGN neurites even in the presence of conflicting physical and biochemical cues.

In pursuit of the second research objective (Chapter 5) the efficacy of two zwitterionic polymers, sulfobetaine methacrylate (SBMA) and carboxybetaine methacrylate (CBMA), in reducing fouling was demonstrated. Using photopolymerization, zwitterionic polymers were grafted onto glass substrates. The surface properties, including composition, water contact angle, and relative fouling, were characterized to understand the changes to the surface upon functionalization. It was demonstrated that only a very thin layer (<10 nm) is required to significantly reduce the nonspecific protein adsorption and water contact angle. Further, utilizing the inherent spatial and temporal control afforded by photopolymerization, zwitterionic patterns were generated to control cell adhesion and growth of various cell types. Fibroblasts, oligodendrocytes, astrocytes, Schwann cell, and spiral ganglion neurons (SGNs) all exhibited a strong repulsion to zwitterion-coated regions on both patterned and unpatterned surfaces. Further, SGN neurite growth was also evaluated on the patterned zwitterionic substrates. Neurite extensions grew directly between zwitterion-coated bands avoiding interaction with the functionalized regions. While SGN neurites extend along SBMA stripes, CBMA patterns significantly improved alignment compared to SBMA patterns. These results demonstrate the efficacy of SBMA and CBMA polymers in preventing fouling and controlling cell adhesion and neurite outgrowth.

To achieve the third research objective (Chapter 6) zwitterionic polymers were coated using a novel technique onto PDMS, the housing material for CI electrode arrays. While PDMS is a durable, nontoxic biomaterial, it is known to elicit a significant FBR. Engineering zwitterionic coatings for PDMS materials has the potential to dramatically reduce the FBR and subsequent current attenuation. SBMA and CBMA films were covalently grafted to PDMS substrates using benzophenone (BP), a type II photoinitiator. The adhesion of the crosslinked

zwitterionic thin films to PDMS surfaces was characterized through the shear adhesion test. Increasing the surface concentration of BP improved the adhesion of the zwitterionic thin films to PDMS surfaces. To demonstrate the effectiveness of the zwitterionic thin films to resist the FBR, nonspecific protein adsorption was measured with significantly lower levels on zwitterion-coated samples compared to uncoated controls. Additionally, adhesion of fibroblasts and bacteria was significantly reduced on coated substrates. These results demonstrate the potential of this photografting process to quickly and easily coat the surface of existing implant materials with zwitterionic polymers.

Lastly, the fourth objective (Chapter 7) was achieved through strengthening zwitterionic hydrogels by changing formulations. While SBMA and CBMA hydrogels exhibit excellent anti-fouling properties, their long-term use is limited by their weak mechanical properties. Two approaches were employed to improve these properties: 1) altering the crosslink density and 2) adding a hydrogen bonding monomer, 2-hydroxyethyl methacrylate (HEMA), to enhance mechanical stability. These two approaches improved the toughness and modulus of the hydrogels. The direct relationship between changes in zwitterionic hydrogel formulation and fouling properties was established. These results demonstrate that improving the mechanical strength of zwitterionic materials through changing monomer formulations has compromises in fouling.

Improving the tissue-material interaction for cochlear implants could have significant impact on strategies to improve hearing quality and restoration. With a better understanding of how to control the neural response to a surface features of a biomaterial, the gap between cochlear implant electrode arrays and primary auditory receptors can be decreased. Further, engineering surfaces that prevent biofouling and the FBR could have significant impacts on late-

term hearing loss associated with fibrosis in the cochlea. These materials are also applicable to a diverse group of implantable devices and have the potential to significantly improve the function and longevity of biomedical devices. The work presented here will also contribute to improving the surface properties of implantable materials with an emphasis on neural prosthetics.

CHAPTER 3: METHODS AND MATERIALS

This chapter includes the synthesis, fabrication, and characterization of biomaterials as well as the cell culture using these substrates to improve cochlear implants. The first section describes the methods implemented to synthesize and fabricate the materials. The second section describes the characterization techniques associated with analyzing surface topography, composition, water contact angle, protein adsorption, water uptake, and mechanical properties. The final section describes the cell culture and quantification of SGN neurite and Schwann cell behavior on micropatterned polymer substrates and has been adapted from a book chapter.[201] The cell culture methods as outlined in the final section were conducted by Dr. Marlan Hansen's research lab and his lab has contributed significantly to this results described in this thesis.

3.1 MATERIALS FABRICATION

3.1.1 Activated Glass Slide Preparation

Functionalized glass slides were used as a substrate for micropatterned polymer attachment. A methacrylated silane coupling agent (3-(Trimethoxysilyl)propyl methacrylate, (TMSPMA, Sigma)) was used (Figure 3.1). Silane coupling agents have well-established chemistry that is used to graft various functional groups onto glass surfaces.[202] The methacrylates at the surface readily react with the monomers in the solution and form covalent bonds that prevent delamination of the photopolymerized thin films.[147,203,204] Samples grafted using this method remain adhered for months after fabrication. Further, these methacrylate-functionalized glass slides were also used to graft the zwitterionic thin films to glass as described in Chapter 5. A covalent bond between the films and the glass was formed that was stable for several months. These same methacrylated glass slides were also used in the shear adhesion testing of the crosslinked zwitterionic films described in Chapter 6.

Standard 2.54 cm x 7.62 cm glass microscope slides (VWR) were exposed to oxygen plasma for 3 min at 30 W RF power (PDC-001 Harrick Plasma Expanded Cleaner, Ithaca, NY). Immediately following removal from the chamber, the slides were immersed in a 1 v/v % solution of the grafting agent TMSPMA in hexanes overnight. Forceps were used to transfer the glass slides using caution not to contact the glass slides in areas of use. It is important to not shear the TMSPMA from the surface on portions that will be investigated. The samples were then washed with fresh hexanes after being removed from the solution and dried in a fume hood. The functionalized glass slides were then stored in a sealed container until use.

3.1.2 Physical Micro-pattern Substrate Fabrication and Characterization

For generating micropatterned topographies used in directing the growth of SGN neurites, a copolymer system was used consisting of hexyl acrylate (HA, Sigma, Figure 3.1) and 1,6-hexanediol diacrylate (HDDA, Sigma, Figure 3.1). All samples prepared using this system used 40 wt% HA and 59 wt% HDDA with the remaining one percent the photoinitiator 2,2-dimethoxy-1,2-diphenylethan-1-one (DMPA, BASF) (Figure 3.1). Previous work in our lab has shown excellent cell compatibility with the methacrylate analog of this system.[147] Further, the photopolymerization kinetics allow the HA/HDDA system to be polymerized through a photomask to yield microchannels. By changing illumination times, microchannels ranging from 1 μm to 8 μm can be generated. These amplitudes are on the same size scale as the neurons in study and allowed dynamic control of neurite alignment based on variations in amplitude and periodicity.[147]

A 20 μL volume of monomer solution was pipetted onto a functionalized glass slide and covered with a 2.54 cm x 2.54 cm glass-chrome Ronchi rule photomask (Applied Image Inc., Rochester, NY) or piece of glass cut to the same dimensions. The samples were then illuminated

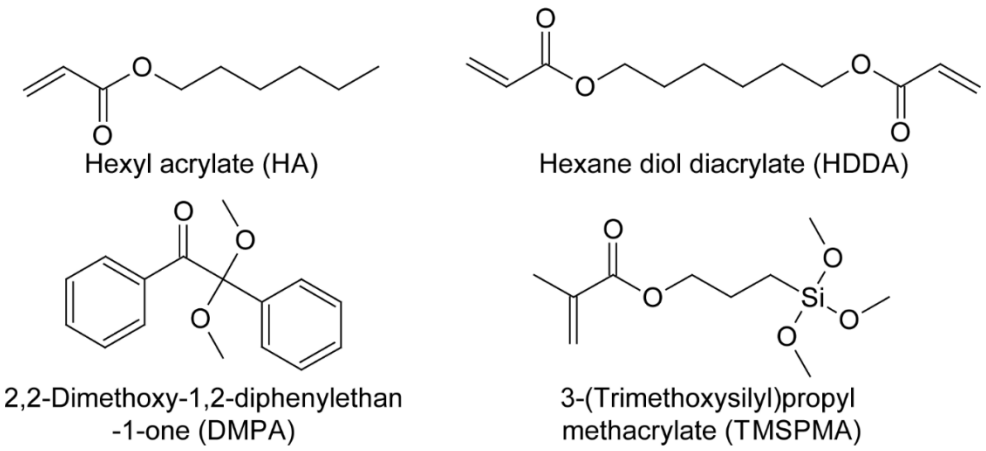

Figure 3.1. Monomers, photoinitiator, and grafting agent used to generate micropatterned topographical samples.

with UV-light (Figure 3.2) using a mercury vapor arc lamp (Omnicure S1500) at an intensity of 8 mW/cm2 measured at 365 nm using a Cole-Parmer Instrument Co. Series 9811 radiometer. The light was shuttered at variable times in order to attenuate polymerization and generate channels of different depth as previously described.[147] After polymerization, the photomask (or glass) was removed and the cured polymer was copiously rinsed with ethanol to remove residual monomer. The resulting micro-patterned polymers were dried and stored in a sealed container until use.

3.1.3 Biochemical Functionalization and Patterning

Acrylate polymers were biochemically patterned with the cell adhesion protein laminin and photodeactivated after exposure to UV light (as described in Chapter 4). Laminin was chosen because it is known to increase cell adhesion and has been patterned using microcontact printing methods. A 40 µL volume of laminin (50 µg/mL, Sigma) in PBS (Sigma) with 0.05 wt% HEPK was pipetted onto acrylate patterned and smooth polymers. A 2.54 cm x 2.54 cm photomask or glass slide (cut to these dimensions from standard glass slides) was then placed on the solution allowing even distribution across the surface by capillary forces. For substrates with

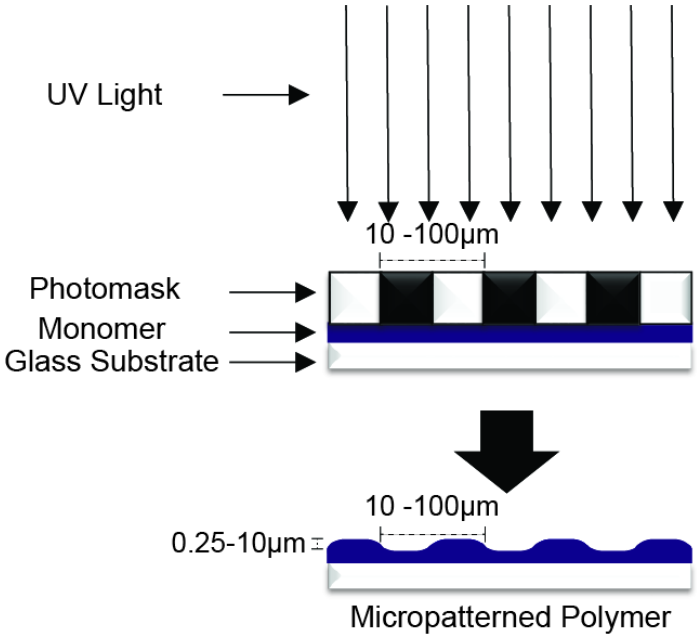

Figure 3.2. Schematic of photopatterning process. Monomer is selectively exposed to UV light through transparent bands of the photomask resulting in raised microfeatures across the polymer surface.

topography, the bands from the photomask were aligned perpendicular to the physical micropattern. The sample was illuminated for 50 seconds with UV-light using a mercury vapor arc lamp (Omnicure S1500) at an intensity of 16 mW/cm^2 as measured at 365 nm using a Cole-Parmer Instrument Co. Series 9811 radiometer. The photomask or glass slide was then removed and the surface was washed with PBS and submersed in PBS at room temperature until use.

Zwitterionic polymers were grafted from methacrylate-functionalized glass surfaces. Aqueous monomer mixtures of zwitterion (CBMA or SBMA at 0.1, to 20 wt%) in phosphate buffered saline PBS containing 0.05 wt% 1-[4-(2-hydroxyethoxy)-phenyl]-2-hydroxy-2-methyl-1-propane-1-one (HEPK, photoinitiator, Irgacure 2959 (I-2959), Figure 3.3) were pipetted onto activated glass surfaces. The liquid was then dispersed evenly across the sample using a 2.54 x 2.54 cm glass-chrome Ronchi rule photomask (Applied Image Inc., Rochester, NY) for patterned samples or a cut glass slide of the same dimensions for uniform samples. Substrates were subsequently illuminated for 10 min using a mercury vapor arc lamp (Omnicure S1500) at an

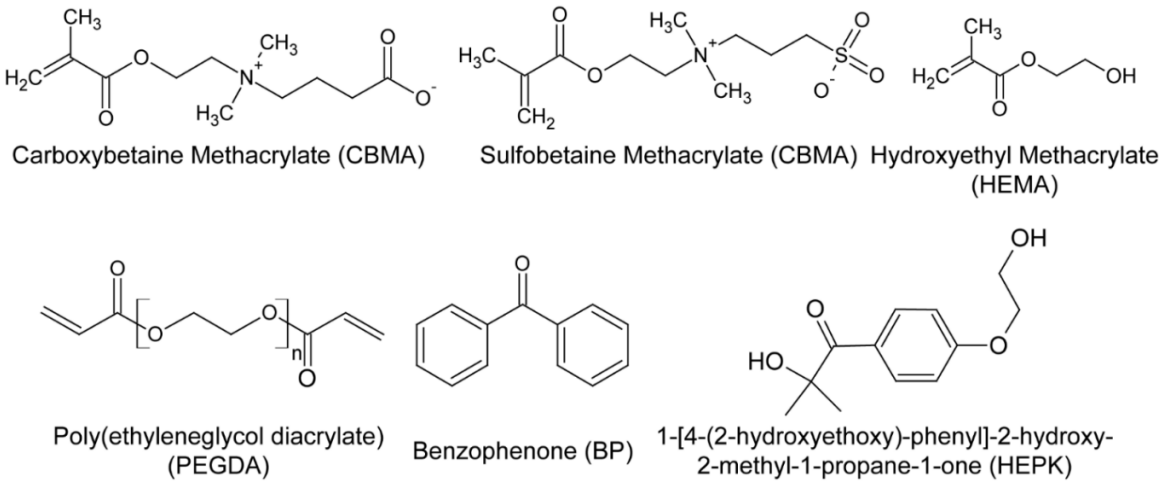

Figure 3.3. Chemical structures of the monomers and photoinitiator used to generate zwitterionic thin film hydrogels and coatings.

intensity of 16 mW/cm^2 measured at 365 nm using a Cole-Parmer Instrument Co. Series 9811 radiometer. Samples were then copiously washed with distilled H_2O and dried using a nitrogen stream. After functionalization, the samples exhibited noticeable qualitative changes in contact angle and the micropatterns were observable by streaks appearing when running water over the surface. The samples were kept under vacuum before XPS measurements or PBS for all other experiments.

3.1.4 Carboxybetaine Methacrylate Synthesis

Sulfobetaine methacrylate (SBMA, Figure 3.3) is a commercially available monomer that was obtained from Sigma Aldrich. Carboxybetaine methacrylate (CBMA, Figure 3.3) has limited commercial availability and required synthesis in our lab. The synthesis for CBMA described here was used for Chapters 5-6. The synthesis of CBMA has been outlined previously,[111] but will be described in detail (Figure 3.4). Because the reaction is water-sensitive, all glassware and needles were dried at 110^{o}C in an oven for at least 1 hr prior to use. The glassware was then cooled in a desiccator before use. All flasks were capped with a septum and purged with nitrogen. Acetone was used as the solvent for this reaction and was dried using sieves in a flask

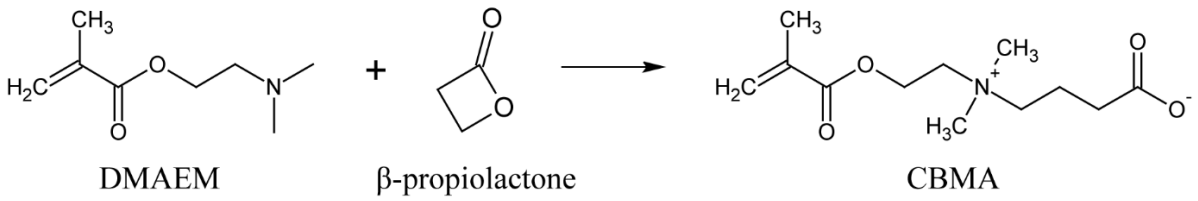

Figure 3.4. Schematic of CBMA synthesis.

under inert atmosphere for at least 24 hrs. 2-(N,N'-dimethylamino)ethyl methacrylate (DMAEM, 17.4 mmol, Sigma) was dissolved in ~80 mL of the dry acetone and cooled to 0°C in an ice bath. β-propiolactone (34.7 mmol, Sigma) was dissolved in ~15 mL of the dry acetone and added to the DMAEM solution dropwise under inert atmosphere over ~10 min It is important that this step is conducted slowly in order to avoid any side reaction products. The reaction was stirred overnight. After ~2 hrs of reaction, a white precipitate formed. When left overnight, the precipitate will dissolved. After overnight stirring, 10 mg of hydroquinone (Sigma) inhibitor was added. The solvent was removed using a rotary evaporator at room temperature. It is important that the water bath remains at room temperature when removing solvent to avoid any premature polymerization. The resulting residual oil was dissolved in 15 mL methanol and trimethylamine (2.4 mL, 17.35 mmol, Sigma) was added to quench any side reactions. The solution was then precipitated into chilled diethyl ether and filtered to yield a white solid. When conducting the filtering step it is important to work quickly when removing the solid from the filter paper. If left, the CBMA will dissolve in residual water from the air and product will be lost in the filter paper. The product was dried under vacuum and used without further purification. The NMR spectrum was recorded on a Bruker spectrometer (Avance 300). The following 1H NMR are present in the reaction product. (D2O, 300 MHz), δ 6.06 (s, 1H, =CH), δ 5.68 (s, 1H, =CH), δ 4.55 (t, 2H, OCH3), δ 3.70 (t, 2H, NCH2), δ 3.59 (t, 2H, NCH2), δ 3.10 (s, 6H, NCH3), δ 2.64 (t, 2H CH2COO), δ 1.84 (s, 3H =CCH3).

3.1.5 Zwitterion-functionalized PDMS

PDMS substrates were fabricated from the commercially available Sylgard 184 (Dow Corning). This two component system is formed by thoroughly mixing 10 parts base to 1 part curing agent. Crosslinking occurs through vinyl end groups on the PDMS chains reacting with Si-H bonds present in a crosslinking molecule. The reaction is catalyzed by platinum and will react spontaneously at room temperature but is accelerated by heating the samples to 80^{o}C for 2 hrs. Samples to be used for shear adhesion tests were transferred to custom-made aluminum molds with channels having a depth of 4 mm and a width of 8 mm. All other samples were transferred to standard size Petri dishes (100 mm). The samples were cured and cooled to room temperature. The slabs were then cut using a razor blade to approximately 25 mm long strips from the aluminum molds or 2.5 cm x 2.5 cm squares for the samples cured in petri dishes. The cut pieces were then submersed in a solution of benzophenone (BP, Figure 3.3) dissolved in acetone (0.01 to 50 mg/mL) for 1 hr. Immersing the PDMS in the solution was conducted to ensure even coating of the BP. After submersion, the BP-coated samples were removed and dried in a nitrogen stream to remove solvent droplets then dried in a vacuum for 1 hr to remove any absorbed solvent. The BP-coated PDMS slabs were kept in a sealed container until directly before use. For the samples to remain “active,” they should be used within 24 hrs of the coating process. Due to hydrophobic recovery of the PDMS substrates, storage of the BP-coated for longer than 2 days resulted in loss of adhesion upon photografting.

To test the adhesion of the zwitterionic thin films to the PDMS substrate, 2.5 µL of monomer solution was pipetted onto a functionalized glass substrate. A piece of PDMS formed using the aluminum molds was placed on top and capillary action dispersed the solution evenly between the glass and PDMS. The glass slides were marked 8 mm from the edge to generate an 8

mm square contact area. The solution was then polymerized for 10 min using a mercury vapor arc lamp (Omnicure S1500) at 30 mW/cm^2 measured at 365 nm using a Cole-Parmer Instrument Co. Series 9811 radiometer. As prepared samples were tested for adhesion directly after polymerization. Swollen samples were immersed in deionized water for 48 hrs prior to testing.

3.1.6 Zwitterionic Hydrogel Fabrication

Free-standing zwitterionic hydrogels were fabricated with varying composition. HEPK was dissolved in water at 1.5 wt% and used for all hydrogel formulations. All hydrogels were mixed with 2.5 wt% poly(ethylene glycol) diacrylate (PEGDA, MW 575, Sigma), 47.5 wt% photoinitiator/water solution, with the remaining 50 wt% varying between SBMA and 2-hydroxyethyl methacrylate (HEMA) or SBMA and PEGDA depending on the formulation. Hydrogels prepared with the following SBMA:HEMA ratios were investigated: 1:0, 4:1, 1:1, 2:3, 1:4 and 0:1. These hydrogels will be referred to throughout the text as SH Y:Z where SH represents SBMA:HEMA and Y:Z represents the ratio of the two components. Variable crosslinker hydrogels were similarly formulated using 50 wt% photoinitiator/water solution and the remaining percent being filled with PEGDA and SBMA in the following SBMA:PEGDMA ratios: 0:1, 1:3, 1:1, 3:1, and 19:1. These hydrogels will be referred to throughout the text as SX Y:Z where SX represents SBMA:PEGDA and Y:Z represents the ratio of the two components.

Hydrogel samples for dynamic mechanical analysis were fabricated using molds created by placing two standard 2.54 x 7.62 cm glass microscope slides together with a 1 mm thick piece of glass as a spacer as shown in Figure 3.5.[205] The liquid monomer was pipetted in the 1 mm space between the slides and illuminated for 10 min using a mercury vapor arc lamp at ~25 mW/cm^2 measured at 365 nm using a Cole-Parmer Instrument Co. Series 9811 radiometer. After polymerization, the glass slides were removed and the samples were punched into either disks

Table 3.1. Formulations of the variable HEMA/PEGDA hydrogels.

	wt% Component				
	Water	**HEPK**	**PEGDA**	**HEMA**	**SBMA**
SX 0:1	49.25	0.75	50	N/A	0
SX 1:3	49.25	0.75	37.5	N/A	12.5
SX 1:1	49.25	0.75	25	N/A	25
SX 3:1	49.25	0.75	12.5	N/A	37.5
SX 19:1	49.25	0.75	47.5	N/A	47.5
SH 0:1	46.8	0.7	2.5	50	0
SH 1:4	46.8	0.7	2.5	40	10
SH 2:3	46.8	0.7	2.5	30	20
SH 1:1	46.8	0.7	2.5	25	25
SH 4:1	46.8	0.7	2.5	10	40
SH 1:0	46.8	0.7	2.5	0	50

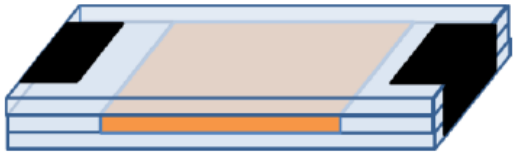

Figure 3.5. Drawing of the mold used to polymerize free-standing zwitterionic hydrogels. Prepolymer is represented by orange, glass mole is shown in blue, and small binder clips are seen in black. Adapted from reference 205.

using die punches or cut into rectangular films. The samples soaked in water for at least 24 hrs before characterization to remove residual monomer and swell the hydrogels to equilibrium.

3.2 MATERIALS CHARACTERIZATION

3.2.1 Nonspecific Protein Adsorption

For Chapters 4-5, relative levels of laminin/fibrinogen adsorption and protein micro-patterns were determined using immunofluorescence.[203] After protein application or patterning, the samples were rinsed three times with PBS followed by a blocking buffer (5% w/v bovine serum albumin, BSA, Sigma) solution being applied to block the areas not occupied by laminin/fibrinogen (Sigma) for 30 min at room temperature. Anti-laminin or anti-fibrinogen

rabbit polyclonal antibody (Sigma) was applied to the samples overnight at 4°C. The substrates were then rinsed 3 times with PBS, and an Alexa488 conjugated secondary antibody (1:1000, ThermoFischer) was applied for 1 hr at room temperature. The samples were washed 3 times with PBS, and coverslips were applied before epifluorescent imaging. Digital epifluorescent images were captured on a Leica DMIRE2 microscope (Leica Microsystems, Bannockburn, IL) with a Leica DFC350FX digital camera and Metamorph software (Molecular Devices, Silicon Valley, CA). Images were taken at each sample irradiation time, and gray-scale measurements were used to evaluate fluorescence intensity relative to an uncoated substrate in Image J software (NIH, Bethesda, MD). All samples were in triplicate and five representative images were taken for each condition.

For protein adsorption described in Chapters 6-7, a fluorescein-tagged bovine serum albumin (BSA, Sigma) was used to determine nonspecific protein adsorption. The tagged BSA (1 mg/mL) was pipetted onto substrates and dispersed by placing a glass coverslip on the solution followed by a 1 hr incubation at room temperature. The samples were then soaked in PBS for 1 hr with the PBS being changed every 15 min. After rinsing, coverslips were placed on the samples using Aqua-mount mounting media (Thermo Scientific) and quantification of the fluorescence was measured as described in the previous paragraph. The fluorescently-labeled BSA provided a direct measure of the nonspecific protein adsorption. Conversely, when using an antibody, the primary or secondary antibody may also bind nonspecifically to the substrate and interfere with fluorescent measurements.

3.2.2 Surface Characterization

To characterize the surface of zwitterion-coated glass substrates, X-ray Photoelectron Spectroscopy (XPS) was performed using a Kratos Axis Ultra x-ray photoelectron spectrometer

with concentric hemispherical electron energy analyzers combined with the established delay-line detector. The incident radiation monochromatic Al Ka X-ray (1486.6eV) at 150W (accelerating voltage 15 kV, emission current 15 mA) was projected 45° to the sample surface and the photoelectron data was collected at a takeoff angle of q = 90°. Survey scans were taken at a pass energy of 160 eV and carried out over a 1200 eV ~-5eV binding energy range with 1.0 eV steps and a dwell time of 200 ms. All spectral analyses were conducted using CasaXPS software. Shirley type calculations were used to account for the background spectrum when quantifying percent atom composition.[206] Relative sensitivity factors were used to normalize peak intensity for elemental quantification. The C 1s peak at 285.0 eV was used to calibrate all spectra before data analysis.

Water contact angles were measured using the sessile drop method on a Ramé-Hart Model 190 Goniometer. Five areas of each substrate were tested in triplicate at and the average contact angle was taken as the mean value of all fifteen measurements.

The concentration of BP adsorbed onto PDMS surfaces was measured using UV/Vis spectroscopy (Varian Cary 50, Mulgrave, Australia). The coated samples were sonicated in a 100% ethanol solution for 30 min to remove the adsorbed BP. Ethanol is not absorbed by the PDMS and will only remove the surface benzophenone. BP absorbs light in the UV region and can be quantified using a calibration curve with known concentrations. The concentrations must be kept within the limitations of the Beer-Lambert law. The concentration of BP in the ethanol solution was then measured by formulating a calibration curve and comparing UV/Vis absorbance at 253 nm to the absorbance of known concentrations at the same wavelength. The calibration curve showed excellent linearity ($R^2 = 0.9989$, Figure 3.6) and all BP concentration measurements were evaluated within the calibrated concentrations.

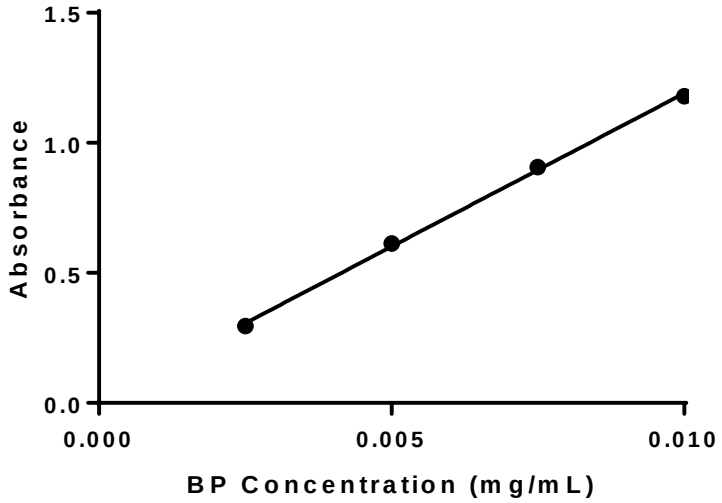

Figure 3.6. Calibration curve for BP adsorbed onto PDMS substrates as measured by UV/Vis spectroscopy.

3.2.3 Physical Properties

Mechanical testing of the hydrogels was completed using a dynamic mechanical analyzer (DMA; Q800 DMA TA Instruments). For compression testing, 6 mm diameter circular disks were used and compressed using a submersion compression clamp and a controlled force ramp rate of 0.5 N/min at room temperature. Before testing, the top portion of the compression clamp was put into contact with the hydrogel sample. A preload force applied by the instrument was set at 0.01 N in order to ensure contact between the sample and the clamp. All samples tested in compression mode were assumed to be cylindrical for stess/strain curves. For tensile measurements, hydrogels were cut into rectangular films and tested in tensile mode at a ramp rate of 0.1 N/min at room temperature. The slower ramp rate was used because many of the samples fractured quickly with a higher ramp rate making toughness calculations difficult. Careful consideration must be taken when loading the hydrogel thin film samples because they are easily broken.

From the displacement recorded on the DMA, the stress/strain curves can be generated to determine Young's modulus and toughness. Stress (σ) and strain (ε) were calculated using the following equations:

$$\sigma = \frac{C * F}{A} \tag{3.1}$$

$$\varepsilon = \frac{D - D_o}{z} \tag{3.2}$$

Where C is a corrective factor provided by the instrument manufacturer based on sample geometry, F is the instantaneous static force, A is the cross-sectional area of the disk, D is the instantaneous displacement, D_o is the initial displacement, and z is the original thickness of the samples before compression. The stress is plotted as a function of strain and the Young's modulus is taken as the linear portion of this curve. To determine toughness, data from tensile measurements was used, and the area under the stress/strain curve was calculated using the area function in Graphpad Prism 7.01 software.

To measure shear adhesion, DMA was used in tensile mode. The stress on adhered glass and PDMS samples was increased until fracture using a controlled force ramp rate of 0.5 N/min at room temperature. The force at break was recorded and normalized to the area of adhesion to the glass substrate to account for small variations in contact area.

To examine water uptake of zwitterionic hydrogels, 6-mm disks were cut from the free standing hydrogel films. The samples were immersed in water for at least 24 hrs and swollen mass was measured. The samples were then dried at ambient temperature overnight and then

placed in a vacuum for 12 hrs prior to recording the dry mass. The swelling ratio of the various formulations was calculated using the following equation:

$$Swelling\ Ratio = \frac{w - d}{d} \tag{3.3}$$

Where *w* is the swollen mass of the sample and *d* is the dry mass of the sample.

3.2.4 Scanning Electron Microscopy (SEM)

Thickness measurements of the zwitterion-coated thin films were measured using scanning electron microscropy (SEM, S-4800, Hitachi). Zwitterion-coated PDMS substrates were dried in a vacuum overnight to remove any residual water and prepare them for imaging. To view the sample cross-section, they were cut and mounted vertically on specimen stages. Prior to imaging, samples were sputter coated with gold for 1.5 min using an Emitech Sputter Coater K550. After sample loading, the microscope specimen stage was adjusted to ensure an aligned cross-sectional view of the samples. Electron accelerating voltage was set at 2.0 kV.

3.3 CELL CULTURE AND QUANTIFICATION

The methods for cell culture and quantification of neural cell behavior are described in the following section which has been adapted from a book chapter.[201] It should be noted that all cell culture experiments described herein and throughout this thesis were conducted by Dr. Marlan Hansen's research group.

3.3.1 Preparing Polymers for Culture

- Sterilize micropatterned polymers in a tissue culture hood by irradiating with a UV germicidal lamp in the hood for at least 5 min. Be sure that no laminin or poly L-ornithine

solutions are in the hood during this process, as the UV germicidal lamp may inactivate proteins.

- Pour poly L-ornithine to coat the micropatterned polymers for tissue culture and allow to coat at room temperature for 30 min, then remove.
- Pour 20 µg/mL laminin solution on the poly L-ornithine coated micropatterned polymer and allow to coat at room temperature for 30 min or overnight at 4°C, then remove.

3.3.2 Dissection

We recommend perinatal (p3-p6) rats or mice for cell cultures. All protocols should be approved by the Institutional Animal Care and Use Committee under the guidelines set forth by the National Institutes of Health.

- Decapitate the animal using heavy scissors and bisect the head in the midline with tissue scissors (*see* **Note 1**). Using a blunt instrument (such as the side of the scissors), gently remove the brain tissue from the cranial cavity, clipping attached cranial nerve roots with scissors as needed.
- Once the brain is removed, the tentorium cerebelli should be visible as a thin shelf of tissue just posterior to the temporal bone/otic capsule. Cut the area containing the otic capsule away from the rest of the skull and place in a Petri dish of PBS on ice under a dissecting microscope (*see* **Note 2**).
- Remove excess tissue and bone around the otic capsule (*see* **Note 3-4**). Stabilize the bone by grasping the lateral semicircular canal with forceps held in the non-dominant hand.
- Remove the bony capsule of the cochlea by flicking the bone off the exterior of the cochlea using forceps held in the dominant hand.

- Scrape off the spiral ligament and Organ of Corti, transecting the radial fibers extending outwards from the modiolus. The modiolus, containing the spiral ganglion neurons, should now look approximately like a pine tree, tapering towards the apex and widening towards the base.
- Using fine foreceps, remove as much of the modiolar connective tissue as possible without damaging the ganglion. Incomplete removal of connective tissue is acceptable in the interest of achieving a higher neuron yield, though it may increase fibroblast count.
- Once cleaning is complete, place the ganglion in a 1.5-2 cc tube of $HBSS^{+/+}$ on ice and continue to harvest as many spiral ganglia as indicated by experimental needs.
- When you have harvested as many spiral ganglia as needed, process the tissue for explants or dissociated culture.

3.3.3 Preparation of Explants

- Place a single ganglion in a Petri dish of PBS on ice under the dissecting microscope. Grasp the base of the ganglion or the stump of the cochlear nerve with fine forceps to stabilize.
- Using the blunt side of a scalpel blade or a second set of forceps, gently uncurl the ganglion so that it lies as flat as possible.
- Using a fresh scalpel blade, cut the ganglion into 4 pieces (or as many as desired). Keep track of which pieces are closest to the apex vs the base if these data are important.
- Using fine forceps, carefully place these explants in the desired position on your prepared substrate. It is best to have a very thin film of N2 medium on the surface of the substrate before putting the explants down, as surface tension and gravity will help keep the explant from floating away.

- Allow the explants to settle down for 1-2 h and attach to the substrate, then add more N2 medium. Be sure to supplement the N2 medium with NT-3 and BDNF if neuronal survival is desired.

3.3.4 Preparation of Dissociated Cultures

- Gently spin the tissue to the bottom of the tube of $HBSS^{+/+}$ or simply allow the tissue to settle to the bottom of the Eppendorf vial. Remove the $HBSS^{+/+}$ and in its place add 500mL of warmed 0.25% trypsin and 0.2% warmed collagenase. Close the vial and incubate at 37 ºC for 20 min with intermittent agitation.
- Add 100 µL of FBS to the Eppendorf vial to inactivate the trypsin. Allow the tissue to settle or spin briefly in a microfuge. Remove the supernatant and add a small amount of N2 medium. Shake lightly to rinse, allow to settle again, then repeat N2 rinse a second time.
- After the final rinse, add 0.5 mL of N2 medium to the tissue.
- Using the cut-off 1000 µL pipette tip, triturate by pipetting the digested tissue up and down 5-8 times. The solution should now be turbid.
- Using an uncut 1000 µL pipette tip, triturate again 5-8 X.
- Using an uncut 200 µL pipette tip, triturate again 5-8 X. It is acceptable that some small undissociated pieces of tissue remain at this point.
- Add the cell suspension onto your prepared substrate (*see* **Note 4**). Add N2 medium, which is now supplemented with NT-3 at 50 ng/mL and BDNF at 50 ng/mL, to the desired final volume and incubate at 37 °C in 6% CO_2.

3.3.5 Enriching for Spiral Ganglion Schwann Cells

- To treat with D-valine, make serum-free N2 medium using MEM with D-valine modification (*see* **Note 3**). Change the cell culture medium using this formulation (*see* **Note 5**). This type of medium may be used constantly and indefinitely.
- To treat with cytosine arabinoside (AraC) (*see* **Note 6**), supplement N2 medium with serum with AraC (20 μM, we keep our stock AraC at 200 mM so that it can be diluted 1:1000). Change the cell culture medium using the AraC supplemented medium, and incubate for 24 hrs. After 24 hrs, change to serum-free N2 medium for 48 hrs.

3.3.6 Fixation and Immunocytochemistry

- Remove your culture from the incubator. Remove medium, then add 4% PFA solution. Incubate at room temperature on shaker for 10-15 min.
- Rinse 3x in PBS.
- Permeabilize in 0.8% Triton in PBS for 30 min at room temperature on shaker.
- Incubate in blocking buffer for 1 hr at room temperature on shaker.
- Dilute primary antibodies in blocking buffer as desired (*see* **Notes 7-9**). Replace blocking buffer with primary antibody and incubate overnight at 4°C or at room temperature for 2 hrs.
- Rinse 3x in PBS.
- Dilute secondary antibodies in blocking buffer as desired (*see* **Note 10**). Incubate overnight at 4°C on shaker or at room temperature for 1 hr.
- Rinse 3x in PBS.
- Coverslip and proceed to imaging; microscopy instructions vary by manufacturer; we use the scan slide tool in Metamorph to generate an image the entire substrate surface using a 20X objective. This provides sufficient resolution to score neurite and Schwann cell alignment.

3.3.7 Quantifying Neurite Alignment

- Open a scan-slide image in Image J (*see* **Note 11**).
- In the toolbar, right-click the Line tool and select “Freehand line” option.
- Click Measure under the Analyze menu to open a window with measurements. Ensure that angle and distance are being measured (*see* **Notes 12 and 13**).
- Select the neurite(s) to be measured in the scan slide image and trace the neurite using the Freehand line tool (*see* **Note 14**). Record the length and angle for each segment by pressing Control-M, on a PC, or Command-M, on a Macintosh. Next, trace and measure the end-to-end distance of the pattern from the neuronal soma to the end of the neurite and corresponding distance along the pattern to calculate alignment ratio (Figure 3.6). Repeat these measurements as many times as needed within the image. Data can be imported and saved for analysis in Microsoft Excel, Sigmaplot or other data analysis software.

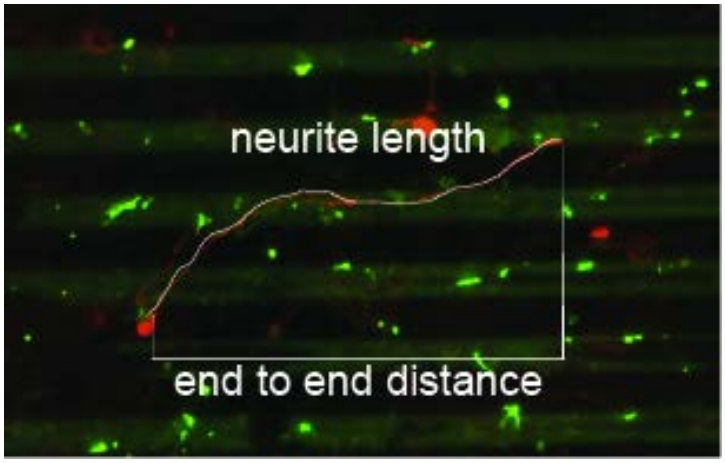

Figure 3.7. Method for quantifying neurite alignment to linear patterns. Alignment ratio is defined as the ratio of neurite length to end-to-end distance. As the length of the neurite increases over the end-to-end distance, the alignment ratio increases. A perfectly aligned neurite would have an alignment ratio of 1

3.3.8 Quantifying Schwann Cell Alignment

- Within Image J, open the images of the Schwann cell cultures (*see* **Note 11**).

- Select the “Freehand selections” tool and outline the periphery of the cell. Ensure that Major axis, Minor axis, and Angle are being measured (*see* **Notes 12 and 13**).
- Once the cell has been outlined, click Edit > Selection > Fit Ellipse in order to fit an ellipse to the outline of the cell (*see* **Notes 15-17**).
- Press control-M on a PC or command-M on a Macintosh to measure the angle of the major axis to the horizontal plane. A window with measurements (Major axis, Minor axis, Angle) should appear.
- Once you have measured the desired number of cells in each image, you can copy the measurement data into the data analysis software.
- After importing the data into a spreadsheet, correct all angles that are greater than 90^{o} by subtracting from 180^{o} (*see* **Note 18-20**).

3.3.9 Notes

1. Spray the rat or mouse pups with 70% EtOH and wipe prior to decapitation. This reduces the bacterial load on the skin and the chance for culture contamination.
2. Dissecting the otic capsule against a black background makes the tissue more visible. In order to perform dissections on ice, we will typically place a black rubber mat over a frozen cold pack. We mount a microscope in the laminar flow hood in order to maintain sterility of the tissue during dissection.
3. Rat middle ear anatomy features a tympanic bulla, a thin capsule of bone located on the inferior-lateral side of the skull, posterior to mandibular head. The tympanic bulla contains all the middle ear structures and the cochlea is located in the medial wall of the tympanic cavity. When inserting forceps into the external auditory canal, to remove the lateral wall of the tympanic bulla, avoid damaging the medial wall of the tympanic cavity with the forceps.

A clean dissection of the spiral ganglion is difficult, after damaging the bony capsule of the cochlea.

4. Because the otic capsule is harder than the surrounding bone, the surrounding bone can usually be flicked away from the otic capsule with relative ease. To separate the otic capsule from the remainder of the temporal bone, a quick and easy method is to grip one of the semicircular canals seen from the inside of the skull, then apply ventrally-directed pressure. The otic capsule, including the cochlea, should separate cleanly from the rest of the temporal bone.
5. To plate on only a small area of your surface, add a thin layer of N2 to the area of interest, then carefully add the cell suspension. After adding the cells, wait at least 30 min, but preferably 1 h, to allow cells to adhere. Then add the remainder of the medium.
6. Fibroblast count can be reduced by using medium containing only D-valine, an enantiomer of L-valine that Schwann cells metabolize, due to the expression of an enzyme that fibroblasts lack, D-amino acid oxidase.[207]
7. AraC is used to preferentially inhibit fibroblast growth. However, keep in mind that treating cells with this antimitotic agent also limits Schwann cell growth. Treatment with AraC is a three-day process. Make N2 media with 10% FBS and 20 µM AraC and incubate cells for 24 h with this solution. After 24 h of incubation, change media to serum-free N2 media and incubate for 48 h.
8. S100β is an excellent marker for Schwann cells, for which multiple antibodies are available from vendors. Our lab has the best results with Abcam's rabbit anti-S100β antibody. We typically store this reagent at a dilution of 1:2 in glycerol for better preservation, whereas we use the antibody at a dilution of 1:400 or 1:800 final..

9. Neurofilament 200 (NF200) is an excellent marker for neurons. for which multiple antibodies are also available. We have the best results with Invitrogen's mouse anti-NF200, which we typically use at a 1:800 dilution.
10. Vimentin is a marker for mesenchymal cells including fibroblasts, but it should be noted that not all fibroblasts stain for vimentin.
11. We typically use secondary antibodies conjugated to Alexa Fluor® dyes (Life Technologies, Grand Island, NY). Alexa Fluor® dyes are available in a variety of excitation and emission spectra. Be sure to co-stain with secondary antibodies conjugated to dyes with sufficiently different excitation and emission spectra to avoid bleed-through across stains. It is recommended to use dyes with emission spectra that are at least 100 nm wavelength apart.
12. A scan-slide of the sample is taken and stitched together using MetaMorph software, when quantifying neurite alignment. This approach is taken to avoid a bias towards neurites shorter than the size of the capture window, when only capturing single-frame images. For Schwann cell alignment, randomly taken pictures are sufficient, as they are almost always smaller than a capture window. However, only quantify alignment on Schwann cells that are entirely captured within your image.
13. Go to the "Select Measurements" tab under Measure and ensure that the Angle and Distance boxes are checked, if after selecting Measure or pressing control/command-M, you find that angle and distance are not recorded. Re-open the Measure tool to record measurements.
14. It is important to have the degree of magnification saved into the image so pixel-to-micron conversions are calculated automatically, when opening in another program (such as Image J). This save is crucial for the MATLAB program. If this is not the case, then be sure that a

pixels-to-actual measurement conversion factor is known for the magnification of the images taken, so you can convert your measurements to microns.

15. At high cell densities, neurites may overlap and make tracing difficult. Furthermore, cells at high densities may tend to direct each other's neurite growth, clouding the substrate's influence on neurite alignment. Therefore it is generally easier to use a low-density cell culture.
16. Zoom in to the image in order to improve the outline of your Schwann cells. This approach allows you to more closely follow the outline of the cell, though a perfect outline is usually not critical to fitting the best ellipse.
17. Because overlapping or adjacent cells can make this method difficult, and also because at higher cell densities Schwann cell alignment is increasingly affected by adjacent cells, it is best to use a lower-density culture.
18. When Schwann cells grow to confluence, it can be helpful to split them into containers with larger surface areas. When performing this procedure, you should expect a moderate amount of cell loss, and increased fibroblast growth given the additional room for cell proliferation. To split the cells, first prepare as many containers as desired by plating with poly L-ornithine then laminin as described above. Then, replace the cell culture medium with 0.25% trypsin-EDTA solution and incubate at 37ºC for 5 min or until the cells appear to be free-floating and round in shape when viewed with a light microscope. Using a pipette tip, suck up the trypsin-cell solution and transfer to a 15 mL conical centrifuge tube. Rinse the cell culture container with several mL of N2 medium and transfer this solution to the previous 15 mL conical tube containing the solution of cells. Spin down at 1250 xg for 5 min at 23°C. Remove the

supernatant, resuspend the cells in culture medium, and plate onto prepared surfaces as described previously.

19. Because we investigate linear patterns where 0 and 180^{o} alignment is equivalent, we correct all Schwann cell alignment measurements to a range of 0-90^{o}. For example, a measurement of 150^{o} is actually equivalent to a measurement of 30^{o}, except that it is left-leaning rather than right-leaning.
20. If the pattern is not horizontally aligned in the image you have taken, you may correct for the difference by measuring the angle of the pattern relative to horizontal in this image, then subtract this measurement from the major-axis angle measurements. Be sure to do this prior to correcting your measurements to the 90° range.

CHAPTER 4: TUNING SURFACE AND TOPOGRAPHICAL FEATURES TO INVESTIGATE COMPETITIVE GUIDANCE OF SPIRAL GANGLION NEURONS[203]

4.1 ABSTRACT

Cochlear Implants (CIs) suffer from limited tonal resolution due, in large part, to spatial separation between stimulating electrode arrays and primary neural receptors. In this work, a combination of physical and chemical micro-patterns, formed on acrylate polymers, are used to direct the growth of primary spiral ganglion neurons (SGNs), the inner ear neurons. Utilizing the inherent temporal and spatial control of photopolymerization, physical micro-grooves are fabricated using a photomask in a single step process. Biochemical patterns are generated by adsorbing laminin, a cell adhesion protein, to acrylate polymer surfaces followed by irradiation through a photomask with UV light to deactivate protein in exposed areas and generate parallel biochemical patterns. Laminin deactivation was shown increase as a function of UV light exposure while remaining adsorbed to the polymer surface. SGN neurites show alignment to both biochemical and physical patterns when evaluated individually. Competing biochemical and physical features patterns were also examined. The relative guiding strength of physical cues was varied by independently changing both the amplitude and the band spacing of the micro-grooves, with higher amplitudes and shorter band spacing providing cues that more effectively guide neurite growth. SGN neurites aligned to laminin patterns with lower physical pattern amplitude and thus weaker physical cues. Alignment of SGNs shifted towards the physical pattern with higher amplitude and lower periodicity patterns which represent stronger cues. These results demonstrate the ability of photopolymerized micro-features to modulate alignment of inner ear

neurites even in the presence of conflicting physical and biochemical cues laying the groundwork for next generation cochlear implants and neural prosthetic devices.

4.2 INTRODUCTION

The effectiveness of neural prosthetic devices, such as the cochlear or developing retinal implants, relies on successful integration with host tissue.[119,208] While rudimentary sensorineural function can be restored using these devices, complex information cannot be effectively relayed largely due to separation between stimulating electrodes and neural receptor cells.[117,209] For example, cochlear implant electrodes in the scala tympani are positioned hundreds to thousands of micrometers from the spiral ganglion neurons (SGNs), the target receptor neurons, which contributes significantly to signal broadening and overlap. This spatial separation dramatically limits the number of distinct independent channels a patient can discern and thereby reduces the frequency resolution provided by the implant. Thus, cochlear implants do not effectively recapitulate the precise tonotopic organization of the native cochlea. By decreasing the distance applied currents must traverse to stimulate SGNs, the number of independent perceivable tones can be significantly increased thereby improving cochlear implant resolution.

Strategies to close this gap in neural prosthetic devices have focused largely on engineering cellular cues that direct the outgrowth of neurites. In native environments, neural cells respond to a multitude of cues which help determine spreading, morphology, gene expression, and alignment.[8] In particular, micro- and nano-scale surface features and their effect on cell proliferation and orientation has been the topic of numerous studies.[8,9,142,204] For example, epithelial cells were found to elongate and align along patterns of grooves and ridges as small as 70 nm on silicon oxide substrates, whereas smooth substrates resulted in rounded cells, showing the impact of topography on cell morphology.[146] Adult mouse dorsal root and sympathetic

ganglia neurite growth showed alignment to nano-grooves with amplitudes as low as 100 nm when cultured on polymethylmethacrylate.[145] Groove depth and spacing were also found to significantly influence neurite alignment of dorsal root ganglia seeded on poly-D,L-lactic acid and poly(lactide-co-glycolide) substrates.[140] Our lab has also shown that neurite alignment correlates strongly to the maximum slope of gradually transitioning micro-grooves fabricated using photopolymerization.[147,185] Therefore, substrate topography plays a critical role in directing the regeneration of neural processes and surface cues will likely be useful in guiding neurites towards stimulatory elements.

Biochemical signals also play an integral role in directing cell growth. Extracellular matrix (ECM) proteins, such as laminin or fibronectin, have been used to influence axon outgrowth.[150,210,211] These ECM proteins can be patterned by micro-contact printing where a protein (or biomolecule) is adsorbed or "inked" onto a micro-patterned PDMS stamp. The stamp is then pressed against a surface, which only transfers the protein onto regions contacting the substrate.[154] When cells interact with the chemical patterns on the substrate, cell-substrate interactions are favorable/unfavorable in regions containing protein, resulting in extension and alignment of neural processes parallel to or on biomolecule patterns. For example, Juncker et al. showed that fibroblasts seeded onto poly(ethylene glycol) (PEG) surfaces containing 10 μm wide fibronectin parallel stipes extended down the length of the protein pattern and avoided interactions with the bare PEG substrate.[156] Micro-contact printed surfaces have also been effective in understanding the pathfinding of neurites. Offenhäuser et al. showed that neurites closely followed a grid-like pattern of laminin and ECM proteins on a polystyrene background.[157] Extending axons were observed making 90 degree turns at branch points in

similar grid-like patterns showing the effectiveness of biochemical markers in directing neural processes.[158,159]

In native neural environments, both physical cues (topographical) and biochemical cues (proteins, growth factors, etc.) promote and direct axon outgrowth. Neural response to physical[8] or chemical[152,153,155,212] cues have been extensively studied independently, but their synergy or antagonism is rarely examined in a single system. Recent research showed that embryonic hippocampal neuronal axons navigated a topographically complex environment, providing pronounced directional selectivity.[213] While this study provides insight into the neural response to a combination of physical and chemical cues, it did not explore the hierarchal relationships when chemical or physical cues present conflicting cues.

Understanding the interaction of chemical and physical cues that govern neurite pathfinding will provide vital information for regenerative therapies. The ability to engineer materials that can direct neurites, even in the presence of competing cues, will be necessary for future advances in neural prosthetic tissue engineering. In this work, we investigate the effects of competitive photogenerated topographical (surface micro-grooves) and biochemical (laminin) cues in directing the regrowth of SGN neurites. We demonstrate the precise control over chemical and physical patterns that allows us to finely dissect the contribution of these divergent stimuli. These aspects of neurite pathfinding have not yet been independently examined using SGN neurites. Biochemical patterns are generated using a novel technique where laminin is adsorbed onto acrylate polymer surfaces followed by illumination through a photomask to deactivate protein functionality in exposed regions. Additionally, gradually sloping micro-grooves were fabricated through photopolymerization and used as physical cues to guide neural processes. We have previously reported that SGN neurites and other cell types align to these

photopolymerized patterns, but have yet to examine SGN neural response to a combination of physical and biochemical cues.[147,189] Accordingly, perpendicular biochemical and physical cues were generated to test the ability of each cue to guide SGN neurites. The strength of physical cues is increased by decreasing the periodicity or increasing the channel depth.[147] Evaluation of SGN neurite response to competing cues demonstrates the ability of both chemical and physical stimuli to disrupt or direct the alignment of neurites to specific patterns.

4.3 MATERIALS/METHODS

4.3.1 Functionalization of Glass Slides

Functionalized glass slides were prepared in order to prevent delamination of acrylate polymers using methods reported previously.[147] Briefly, standard 2.54 cm x 7.62 cm glass microscope slides were exposed to oxygen plasma for 3 min at 30 W RF power (PDC-001 Harrick Plasma Expanded Cleaner, Ithaca, NY). Immediately following removal from the chamber, the slides were immersed in a 1 v/v % solution of 3-(methoxysilyl)propyl methacrylate (Sigma) in hexanes (Sigma) overnight. The samples were washed with fresh hexanes after being removed from the solution and dried in a fume hood. The functionalized glass slides were then stored in a sealed container until use.

4.3.2 Physical Micro-pattern Substrate Fabrication and Characterization

Monomer solutions of 40 wt% hexyl acrylate (HA, Sigma), 59 wt% hexanediol diacrylate (HDDA, Sartomer), and 1 wt% 2,2-dimethoxy-2-phenylacetophenone (DMPA, BASF) as the photoinitiator were used for all samples. A 20 µL volume of monomer solution was pipetted onto a functionalized glass slide and covered with a 2.54 cm x 2.54 cm glass-chrome Ronchi rule photomask (Applied Image Inc., Rochester, NY) or piece of glass cut to the same dimensions. The samples were then illuminated with UV-light using a mercury vapor arc lamp (Omnicure

S1500) at an intensity of 8 mW/cm^2 measured at 365 nm. The light was shuttered at variable times in order to attenuate polymerization and generate channels of different depth as previously described.[147] After polymerization, the photomask (or glass) was removed and the cured polymer was copiously rinsed with ethanol to remove residual monomer. The resulting micro-patterned polymers were dried and stored in a sealed container until use.

The absolute amplitude and periodicity of the micro-patterned polymers was characterized through white light interferometry (Dektak Wyko 1100 Optical Profiling System, Veeco). Periodicity was measured as the distance between minimum points in the pattern and was found to replicate the periodicity of the photomask used. The amplitude was the distance between minimum groove value and the adjacent maximum ridge value. Nine regions were measured from each sample and the average amplitude was reported.

4.3.3 Biochemical Patterning and Characterization

Acrylate polymers were biochemically patterned with the cell adhesion protein laminin and photodeactivation. A 40 µL volume of laminin (Sigma) in PBS (50 µg/mL) with 0.05 wt% 2-hydroxy-1-[4-(2-hydroxyethoxy)phenyl]-2-methyl-1-propanone (HEPK, Ciba), a photoradical generator, was pipetted onto acrylate polymers. A 2.54 cm x 2.54 cm photomask or glass slide was then placed on the solution allowing even distribution across the surface. The sample was illuminated for 50 seconds with UV-light using a mercury vapor arc lamp (Omnicure S1500) at intensity of 16 mW/cm^2 as measured at 365 nm. The photomask was then removed and the surface was washed with PBS and stored in PBS until use.

Relative levels of protein adsorption and protein micro-patterns were determined using immunofluorescence. After protein application or patterning, the samples were rinsed three times with PBS followed by a blocking buffer solution being applied to block the areas unoccupied by

laminin for 30 min at room temperature. Anti-laminin rabbit polyclonal antibody (ab30320, 1:400, Sigma, Full length native protein isolated from mouse EHS tumor) was applied to the samples overnight at 4° C. The substrates were then rinsed 3 times with PBS and an Alexa488 conjugated secondary antibody (1:1000, ThermoFischer) was applied for 1 hr at room temperature. The samples were washed 3 times with PBS and coverslips were applied before epifluorescent imaging. Digital epifluorescent images were captured on a Leica DMIRE2 microscope (Leica Microsystems, Bannockburn, IL) with Leica DFC350FX digital camera and Metamorph software (Molecular Devices, Silicon Valley, CA). Images were taken at each sample irradiation time and gray-scale measurements were used to evaluate relative fluorescence intensity in Image J software (NIH, Bethesda, MD). All samples were made in triplicate and five representative images were taken for each condition.

4.3.4 Spiral Ganglia Cell Culture and Neurite Guidance Determination

All cell culture and quantification was conducted by Dr. Marlan R. Hansen's research group. Dissociated spiral ganglion (SG) cultures from P3-5 rat pups were prepared as previously described.[214,215] All polymer substrates without laminin patterns were coated uniformly with poly-L-ornithine (100 µg/mL) and laminin (20 µg/mL). SGN cultures were maintained in Dulbecco's Modified Eagle Medium (DMEM) supplemented with N2 additives, 5% fetal bovine serum, neurotrophin-3 (NT-3, 50 ng/ml) and brain derived neurotrophic factor (BDNF, 50 ng/ml). Cultures were maintained in a humidified incubator with 6.5% CO2 and fixed with 4% paraformaldehyde after 48 hrs.

SG cultures were immunostained with anti-neurofilament 200 (NF200) antibodies (1:400, Sigma) to label neurons, respectively.[214] Alexa 488 conjugated secondary antibodies (Invitrogen)

were used to detect primary antibody immunolabeling. Slides were cover slipped with ProLong Gold anti-fading reagent with DAPI (Life Technology).

4.3.5 Determination of Neurite Progression

Alignment of neurites to the physical and biochemical micro-patterns was evaluated as previously described.[148] Briefly, a distribution of angles relative to the horizontal plane of 10 μm length neurite segments were counted. Neurites from immunolabeled images were traced in Image J for each condition and X−Y distance data were analyzed using Matlab software. The angle of each segment was calculated relative to horizontal (physical pattern) and all neurite angles were then binned in 10° segments from 10−90°. Random outgrowth would be evidenced by a relatively equal distribution among all angle bins. Neurites aligned to horizontal plane would be demonstrated by high population percentages in bins of 20° or less.

4.4 RESULTS AND DISCUSSION

4.4.1 Photopolymerization and Micro-groove Fabrication

Our lab has shown photoolymerization to be an effective method in creating micro-grooves for directing cell growth on (meth)acrylate-based polymers.[147–150,185,189] To form these patterns, a monomer solution is sandwiched between a glass substrate and photomask with alternating transparent and opaque bands. Collimated UV-light is then used to rapidly polymerize the sample. The light-induced reaction occurs most rapidly in regions directly below transparent bands, causing gelation of the monomer solution along the full path length. Polymerization also occurs in shadowed regions, but to a lesser extent, primarily due to growing polymer chain diffusion, diffracted and reflected light. Consequently, ridges are formed under transparent bands and grooves emerge under opaque regions. Furthermore, effective irradiation intensity, sample cure time, photoinitiator concentration, and photomask band spacing can be

altered to achieve user-defined channel amplitudes and repeating feature frequency.[147] In the current study, a hexyl acrylate (HA) and 1,6-hexanediol diacrylate (HDDA) mixture with 2,2-dimethoxy-2-phenylacetophenone (DMPA) as photoinitiator was used as an analog of previously studied polymers. This formulation was chosen because of ready control of the substrate topography and inherent substrate stiffness. The topography including channel depth and periodicity can be easily modulated. By changing cure time, light intensity, and photoinitiator concentration the depth of the channels are easily tuned as described previously.[147] Channel periodicity was determined by the photomask pattern used to generate the microchannels. In addition, these substrates are relatively stiff. Previous results also show that higher modulus materials guide SGN neurite growth more effectively.[149] Polymer topography, specifically channel amplitude and periodicity, was confirmed by white light interferometry using an optical profiling system.

To increase the biocompatibility of synthetic materials, proteins can be applied to hydrophobic and hydrophilic biomaterial surfaces.[216] Laminin, a cell adhesion protein, is often adsorbed onto biomaterial surfaces to increase cell attachment and control the neural response to a given material.[217–219] Exposure of laminin to UV light results in inactivation of the functional protein.[220] In this study, laminin is patterned using UV-light to deactivate the protein functionality including cell adhesive properties to spatially control neural response and adhesion. Accordingly, laminin is adsorbed onto the polymer surface by allowing a laminin-containing solution to contact the substrate, followed by illumination of the substrate through a photomask with 50 µm periodicity parallel bands (Figure 4.1). As UV light is absorbed by the protein or photoradical generator (HEPK), highly reactive radicals react with adjacent chemical bonds of the protein and other molecules in solution. The change in chemical bonds is believed to alter

protein structure, folding, and binding affinities of integrins, antibodies, and enzymes.[193–196] Furthermore, these rearrangements may alter the ability of SGN neurites and spiral ganglion Schwann cells to bind to cell adhesion motifs, ultimately affecting the affinity of the cells to the substrate.[221]

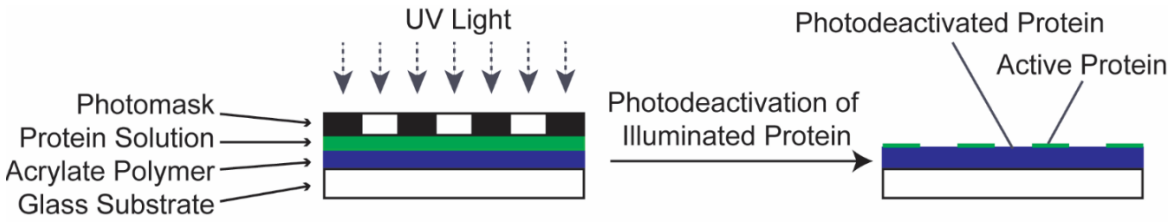

Figure 4.1. Schematic depicting the photodeacivation and patterning process. A protein solution is applied to an acrylate polymer and illuminated with UV-light through a photomask. Exposed protein is deactivated resulting in an active protein pattern in shadowed regions.

To quantify the changes in protein with illumination time, immunofluorescence of the protein was measured at variable illumination times. We used a polyclonal antibody that would bind multiple epitopes of the protein. Changes in binding of primary antibody to the adsorbed laminin indicates that alterations are occurring throughout the protein structure which, in turn, causes a change in affinity for the antibody. In Figure 4.2A, intact laminin stripes are detected by immuofluorescent labeling (green) and appear as the vertically stretching bands. Areas exposed to UV-light, and thus deactivated, are represented by the dark bands found between the green stripes. The ability to selectively deactivate laminin in specific patterns not only on smooth substrates, but also onto surfaces containing topographical features, such as sloped features or grooves, offers a distinct advantage over other patterning methods such as micro-contact printing techniques. Using micro-contact printing, for example, proteins can only be printed in areas that come into direct contact with the inked stamp.[154,222] Consequently, proteins cannot be effectively

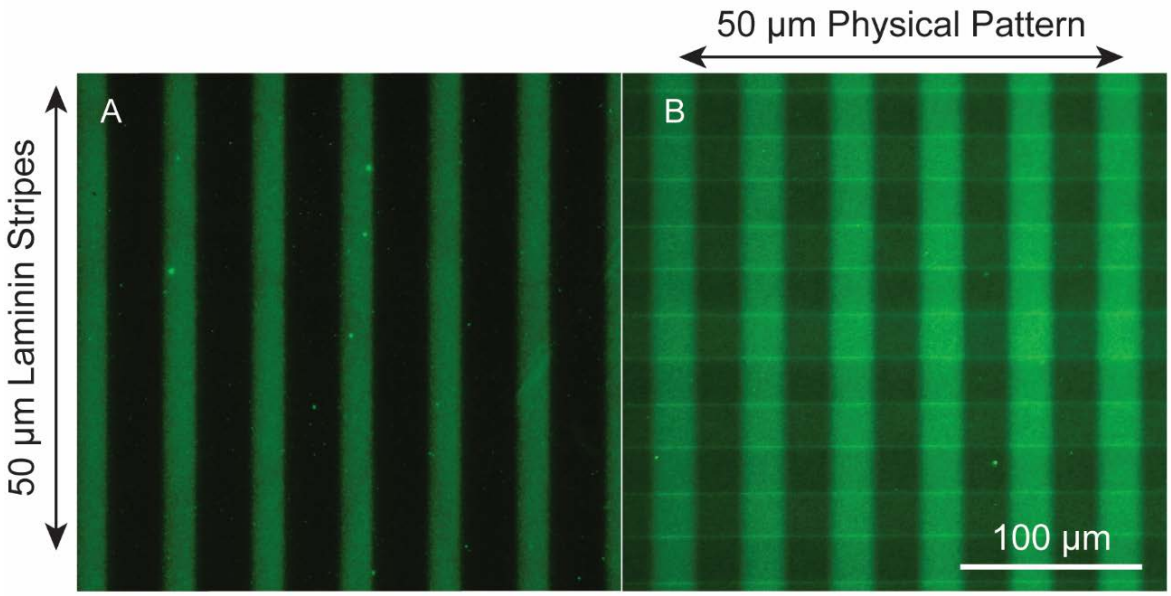

Figure 4.2. Epifluorescent images of the laminin patterned substrates. A) A 50 µm vertical laminin pattern on a smooth acrylate polymer substrate. Active laminin stripes are represented by green bands where dark bands represent photodeactivated areas. B) Laminin patterned onto a physically patterned acrylate polymer (50 µm periodicity and 1.5 amplitude). The protein pattern is shown vertically and the physical pattern runs horizontally. Both images were visualized using immunofluorescent imaging. The physical pattern observed in B can be seen due to autofluorescence of the polymer.

transferred in depressions on a surface, such as micro-grooves, where the stamp would not be able to contact the substrate. Using this photodeactivation process, laminin can be selectively deactivated on grooves, ridges, and sloped features to form a continuous laminin pattern along complex topographies as shown in Figure 4.2B. The stripes of active laminin, indicated by immunoreactivity, can be seen extending vertically while the physical pattern is visible stretching horizontally. The active laminin stripes are clearly visible on both ridges and grooves of the perpendicular physical pattern, confirming continuity of the biochemical cue.

To understand protein response to UV exposure and determine the potential added effect of a photoradical generator, laminin solutions with and without HEPK were applied to polymer surfaces and illuminated with UV light at varying time intervals (Figure 4.3). Immunostaining

was used to quantitatively assess laminin photodeactivation after irradiation followed by visualization using epifluorescence microscopy. Five representative images from the sample surface were taken and the relative fluorescence of these images was quantified using gray-scale measurements in Image J software. Exposure to UV light significantly decreases the relative fluorescence of adsorbed laminin stained with antibody (Figure 4.3). This trend is observed for HEPK-containing and HEPK-free samples, however HEPK-containing substrates were observed to bleach more quickly. After illumination for 50 seconds, the fluorescence of samples with HEPK decreased almost three times greater than those without HEPK (a decrease of 78% relative fluorescence compared to 36% relatively fluorescence). Photoradical generating molecules produce radicals upon the absorption of a photon. Thus, the number of radical species in the solution increases with HEPK. The number of events that could alter protein structure likely cause accelerated photodeactivation with systems containing HEPK. After 50 seconds, the HEPK samples reached a minimum in fluorescence and thus maximum deactivation. In contrast, samples without HEPK present continue to decrease after 50 seconds until reaching a minimum of around 40 percent relative fluorescence. The HEPK effectively accelerates the rate of photodeactivation without altering the maximum deactivation of the protein likely due to the free radicals generated by the photocleavage of HEPK. These radicals likely change protein structure by reacting with amino acids on the protein

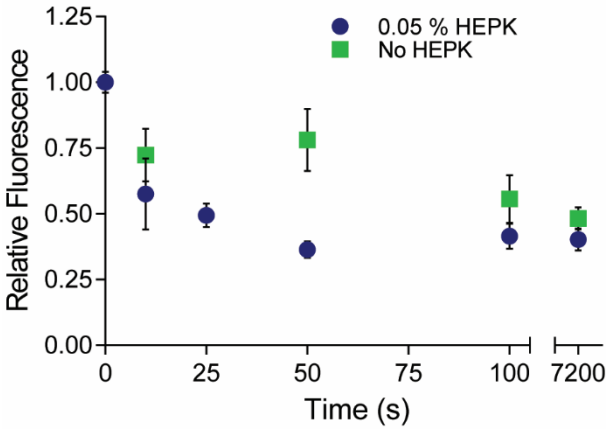

Figure 4.3. Relative fluorescence of the laminin as a function of illumination time with and without photoinitiator. The fluorescence decreases over time with photoinitiator increasing the photobleaching process.

surface, which can potentially alter molecular connectivity, protein structure, and folding. Further, the protein release from the surface was evaluated and showed no statistically significant decrease with illumination time.

4.4.2 Alignment of SGN Neurites

While decreases in intensity using immunofluorescence were observed, these decreases are not a direct measure of the binding affinity for cells. To determine the effect of UV-induced changes on neural cellular response, the alignment of SGN neurites to laminin patterned onto acrylate polymer surfaces was evaluated. SGN neurite alignment was quantified along active laminin stripes by sectioning each neurite into 10 µm long segments. The angle of the line connecting the endpoints of each segment from the horizontal was then measured (Figure 4.4).

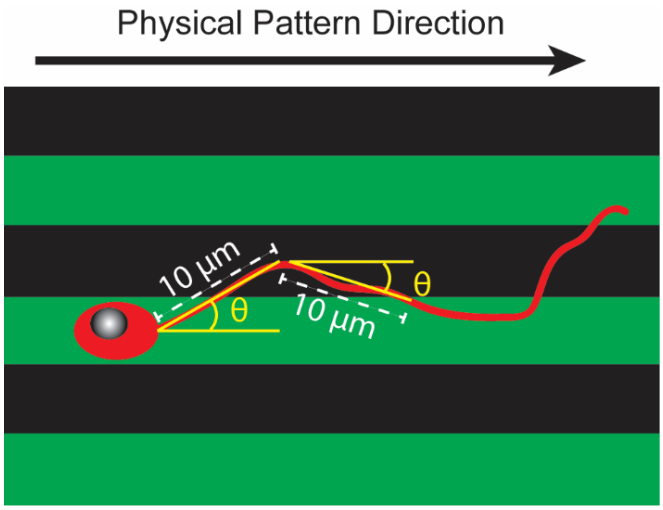

Figure 4.4. Schematic demonstrating the angle quantification method used to evaluate neurite alignment.

Sectioning the entire length of the neurite into segments enables evaluation on how the neurite extends along the full path length and determines the degree to which the physical or chemical cues guide neurite pathfinding. Alignment angles were categorized into 10 degree increments between zero and ninety degrees, with 0 degrees set as the horizontal direction and 90 degrees set as the vertical direction (laminin pattern direction). SGN neurites were cultured onto acrylate polymers containing a 50 µm periodicity laminin pattern and compared to a uniformly-coated control. As shown in Figure 4.5A, neurites grow randomly on unpatterned polymer surfaces, as

neurites are observed extending in multiple directions. In contrast, SGN neurites seeded onto the laminin patterned substrates show a distinct preference for the vertical active laminin stripes (Figure 4.5B). Interestingly, the neurites grew almost exclusively on active laminin regions, confirming that the decrease in immunoreactivity also reflects decreased protein activity for cell adhesion.

Quantification of neurites grown on uniformly laminin coated substrates showed no directional preference with the percentage of segments being evenly distributed between all angle groups (Figure 4.5C). In contrast, SGN neurites grown on laminin patterned surfaces showed strong alignment to the 90 degree active laminin stripes with over 70 percent of the segments aligned (within 20 degrees of the laminin pattern) and over 55 percent strongly aligned (within 10 degrees of the laminin pattern) (Figure 4.5D). For uniformly-coated polymers, less than 20 percent of the neurite segments were within 20 degrees of the vertical pattern, demonstrating the stark contrast between the patterned and uniformly-coated samples. These results indicate that laminin, patterned using this photodeactivation method, can be used to effectively guide inner ear neurite extensions.

4.4.3 SGN Neurite Alignment to Competing Patterns of Varying Periodicity

Natural neural outgrowth responds to multiple cues. It is therefore important to understand how SGN neurites respond to a combination of biochemical and physical cues as would be encountered *in vivo*. Therefore, understanding the relative contribution from physical and chemical patterns to guiding neural processes will help develop novel tissue engineering techniques to improve the resolution of neural prosthetics. Competing physical and biochemical guidance patterns will serve as a means to understand the ability of each guidance cue in directing neurite pathfinding and overcoming a conflicting cue. Using gradually sloping

photopolymerized micro-features, the relative guidance or strength of a physical patterned can be modulated by varying either the channel amplitude or the pattern periodicity (frequency).[147] Previous experiments in our lab have shown increases in alignment of SGN neurites with higher amplitude and decreasing periodicity of strictly physically patterned substrates.[147] Thus, the physical surface features can be tuned to induce changes in neurite response to a given topography.

To evaluate how SGN axons respond to these stimuli in competition, polymer microgrooves were fabricated with different periodicity and constant amplitude, followed by perpendicularly patterning 50 µm periodicity laminin stripes on the surface. To demonstrate the change in alignment behavior when applying the laminin stripes, uniformly laminin coated samples were tested with identical periodicity and amplitude. The periodicity of the physical micro-patterns was varied between 20 (strong cue), 33 (moderate cue), and 50 µm (weak cue) all with 1.5 µm amplitude. Alignment of neurites to the 20 µm periodicity uniformly-coated laminin sample is seen in Figure 4.6A, with many neurite segments following the horizontal physical pattern. In contrast, the 20 µm periodicity substrate with a perpendicular laminin pattern, showed a disruption of neurite alignment to the physical pattern. Many neurite segments are observed originally following the vertical laminin pattern then switching to follow the horizontal physical pattern and vice versa (Figure 4.6B). As the periodicity of the physical pattern increased and the strength of physical cue concomitantly decreased, neurites showed a lower degree of alignment to the physical pattern in both the uniformly laminin coated substrates as well as the perpendicularly laminin patterned competing cues. For the perpendicularly patterned substrates, neurites tended to follow the laminin stripes to a greater extent as the periodicity was increased to 33 and 50 µm (Figure 4.6C, 50 µm periodicity depicted).

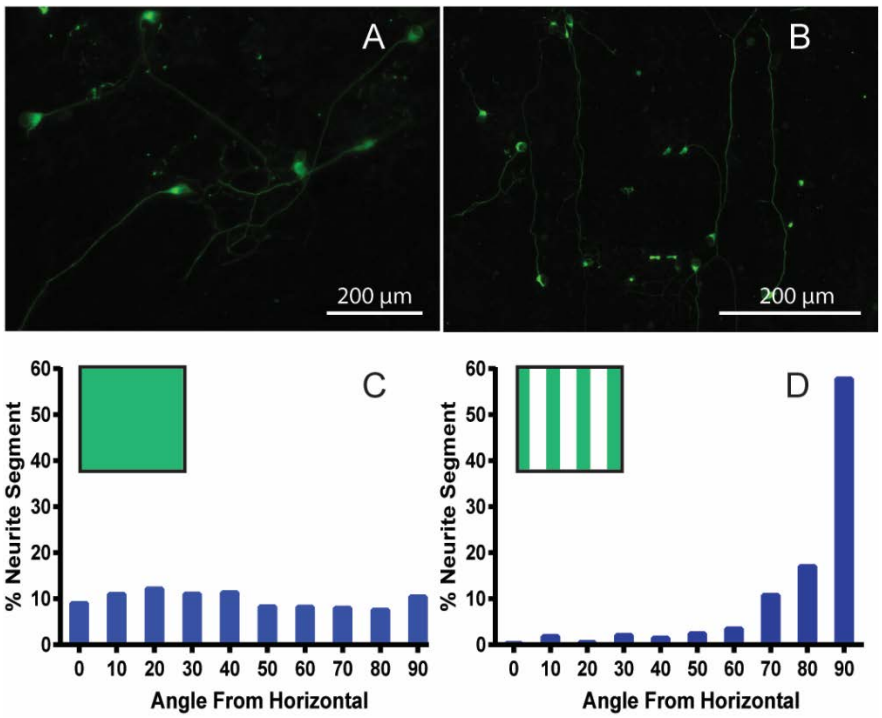

Figure 4.5. SGN alignment on laminin patterned and uniformly-coated substrates. A) Epifluorescent image of neurites grown on uniformly-coated smooth polymer substrates. B) Epifluorescent image depicting neurites grown on a vertical laminin patterned smooth surface. Many neurites are observed following the vertical pattern in response to the laminin stripes. C) Angle quantification of neurites grown on uniformly-coated smooth polymer substrates (n=417). D) Angle quantification of neurites seeded onto smooth substrates containing a vertical laminin pattern (n=261). The box in the top left corner of the histograms represents the pattern present for the quantification (green stripes for the vertical laminin pattern).

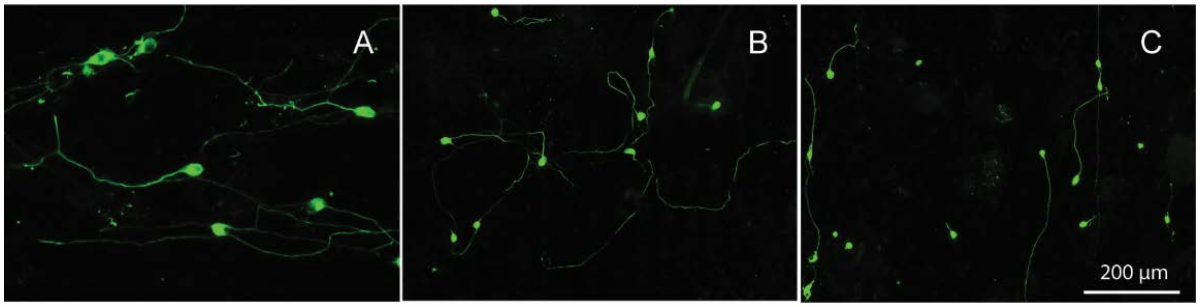

Figure 4.6. Neurites from dissociated SGN grown on: (A) a uniformly laminin coated 20 µm periodicity, 1.5 µm amplitude physical pattern, (B) a 20 µm physical pattern with an amplitude of 1.5 µm (strong physical cue) and a perpendicular 50 µm laminin pattern and (C) a 50 µm physical pattern with an amplitude of 1.5 µm (weak physical cue) and a perpendicular 50 µm laminin pattern. The physical pattern is oriented horizontally and the laminin pattern vertically. Cultures were stained with anti-NF200 antibodies.

Quantification of neurite alignment is shown in Figure 4.7. Similar to our previous observations with SGN neurites grown on uniformly coated micro-patterns,[147] alignment decreased with increasing periodicity of the physical pattern (Figure 4.7A-C). For the 20 µm periodicity substrate with uniform laminin, almost 60 percent of the neurite segments were aligned to the physical pattern, quantitatively demonstrating the ability of this low periodicity cue to guide neurites (Figure 4.7A). As this periodicity increased to 33 µm, fewer neurite segments aligned to the micro-pattern with less than 30 percent of the neurite segments aligned within 20 degrees of the pattern (Figure 4.7B). The 50 µm periodicity proved to be a very weak cue with a nearly random distribution of segment alignment (Figure 4.7C). For these samples, less than 30 percent of the neurite segments were within 20 degrees of the physical pattern, showing comparable alignment to physically unpatterned and uniformly laminin coated substrates. By increasing the periodicity of the physical pattern the neurite segments considered to be aligned decreased by approximately one third from a 20 µm to a 50 µm periodicity pattern.

By introducing a conflicting laminin pattern, the distribution of neurite segments shifted for each physical pattern. For the 20 µm physical pattern with perpendicular active laminin regions, neurites did not align to any specific angle (Figure 4.7D) with a nearly random distribution of roughly 10 percent of the neurite segments for each angle. However, there were slightly fewer neurite segments found between 40 and 50 degrees than the lower or higher angles, suggesting a greater number of neurite segments were found following either the physical or biochemical pattern. As the strength of the physical cue was weakened by increasing the periodicity to 33 µm, the neurite segments shifted to align to the laminin pattern, as observed in Figure 4.7E. Using these conditions, the distribution favored higher angles, indicating a moderate degree of alignment along the biochemical pattern.

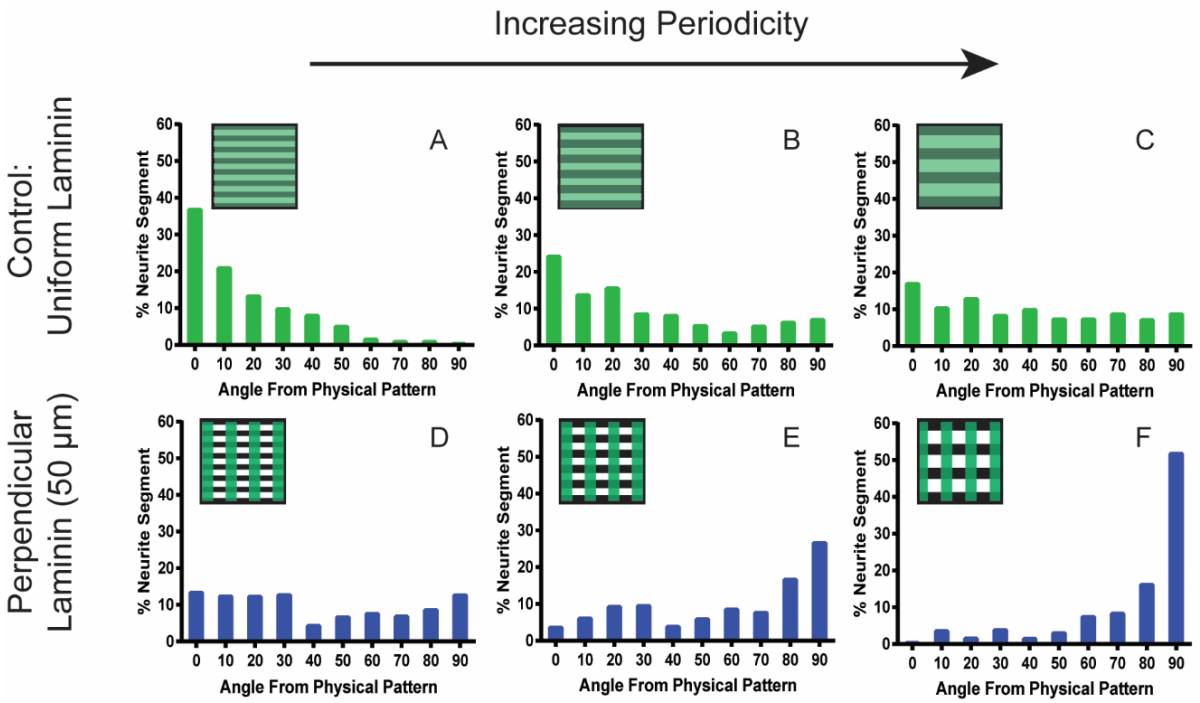

Figure 4.7. Quantification of SGN neurites grown on patterned substrates with variable periodicity. The top row of histograms are the quantification of SGN neurites cultured on physically patterned substrates with a uniform coating of laminin with the periodicities of 20 µm (A, n=21), 33 µm (B, n=133) and 50 µm (C, n=405). The bottom row of graphs represents the quantification of SGN neurites cultured on physically patterned substrates containing a perpendicular 50 µm laminin pattern with the periodicities of 20 µm (D, n=391), 33 µm (E, n=229) and 50 µm (F, n=319). Periodicity increases from left to right as the strength of the physical cue decreases. The box in the top left corner of each histograms represents the pattern present for the quantification (green stripes for the vertical laminin pattern and black stripes for the horizontal physical pattern).

At the weakest physical cue, neurite segments shifted to follow the laminin stripes strongly with roughly two thirds found within 20 degrees of the laminin pattern (Figure 4.7F). For these conditions, the neurites appear to be unaffected by the physical pattern and strictly follow the biochemical cue. Because the 50 µm periodicity uniformly laminin coated sample induced very weak alignment to the physical pattern (Figure 4.7C), it is not surprising that the neurites cultured on the 50 µm perpendicularly patterned samples strongly follow the biochemical cue. These observations demonstrate that the laminin micro-pattern generated from the photodeactivation process can be used to disrupt the alignment of SGNs to weak and

intermediate physical patterns as observed for the 33 µm and 50 µm periodicity physical patterns. However, the laminin pattern could not induce SGN neurites to strictly follow the biochemical cue, as evidenced by the 20 µm periodicity pattern, where many neurite segments followed either or both physical and biochemical patterns.

4.4.4 SGN Neurite Alignment to Competing Patterns of Varying Amplitude

Channel amplitude can be used as an additional means to alter the strength of a topographical cue, with increasing depth leading to significantly enhanced alignment.[140,141,147] Accordingly, micro-pattern amplitudes were varied as an additional method to evaluate neurite pathfinding with competitive cues. Polymer micro-grooves with a 50 µm pattern periodicity were fabricated with amplitudes of 3 µm (intermediate cue) and 8 µm (strong cue) in addition to a perpendicular 50 µm periodicity laminin pattern. A weak physical cue of 1.5 µm amplitude was discussed previously. To demonstrate the ability of the biochemical cue to disrupt neurite pathfinding to the micro-grooves, physically patterned samples with uniformly coated laminin were also used. As previously shown, neurite alignment to the physical pattern on the uniformly laminin coated controls increased with increasing amplitude and many observable neurites turned to follow the horizontal physical pattern (Figure 4.8A, 8 µm amplitude depicted).[147] Conversely, neurites grown on substrates with weaker physical cues showed disruption of the alignment to the physical pattern as observed in Figure 4.8B. Quantification of the neurite orientation on the uniformly coated controls showed an increase in alignment to the physical pattern with increasing amplitude (Figure 4.8C, E). At 3 µm amplitude, over 40 percent of the segments are aligned within 20 degrees of the physical pattern (Figure 4.8C). This percentage increased to almost 70 percent with the 8 µm amplitude substrates (Figure 4.8E) suggesting a significant increase in strength of the physical pattern. When the perpendicular biochemical cue

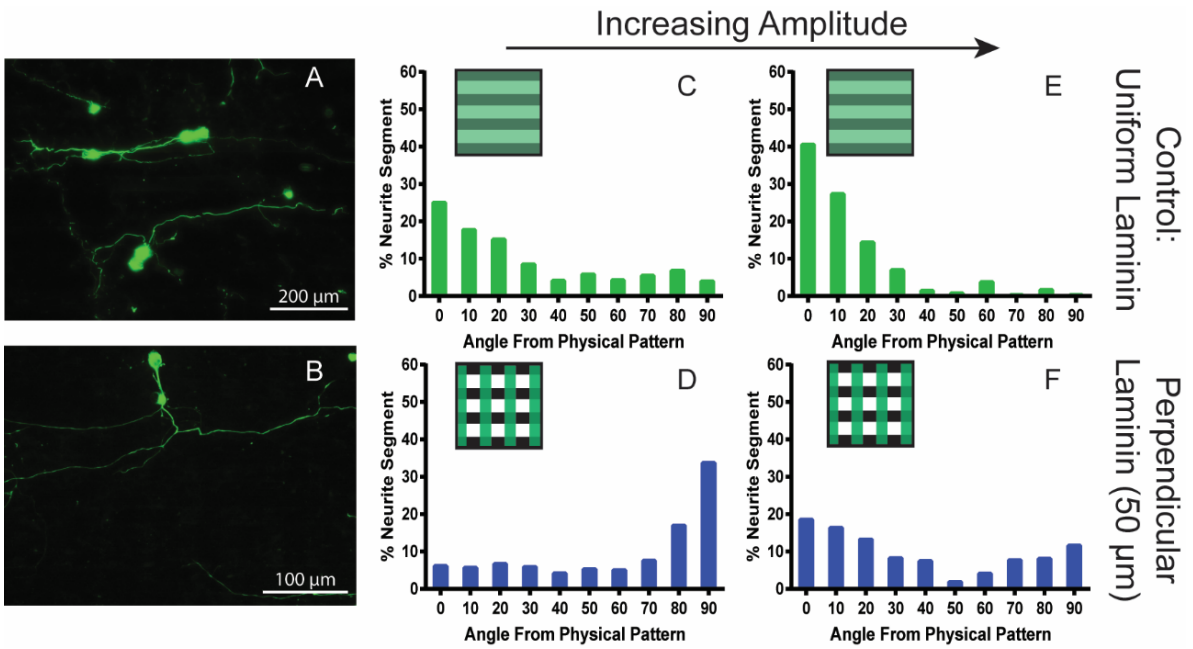

Figure 4.8. Quantification of SGN neurites grown on patterned substrates with variable amplitude. Epifluorescent images of neurites grown on (A) uniformly laminin coated 50 µm periodicity and 8 µm amplitude physically patterned and (B) perpendicularly patterned laminin on a 50 µm periodicity and 8 µm amplitude physical pattern. The top row of histograms represents the quantification of SGN neurites seeded on substrates with a uniform coating of laminin and amplitudes of 3 µm (C, n=135) and 8 µm (E, n=158). The bottom row of histograms represents the quantification of SGN neurites seeded on substrates with a 50 µm perpendicular laminin pattern and amplitudes of 3 µm (D, n=175) and 8 µm (F, n=217). The box in the top left corner of each histograms represents the pattern present for the quantification (green stripes for the vertical laminin pattern and black stripes for the horizontal physical pattern). Cultures were stained with anti-NF200 antibodies.

is added, the alignment along the physical pattern is disrupted. For the 3 µm amplitude substrate with perpendicular laminin, neurite alignment favors higher angles, or following the biochemical stripes with over half of the neurite segments aligning to the laminin pattern (Figure 4.8D). As the amplitude is increased to 8 µm, many neurite segments were weakly aligned to either the physical or the biochemical pattern. The fewest number of neurites were found between 50 and 60 degrees with just over 2 percent of the total segments (Figure 4.8C). The neurites also followed the physical pattern (lower angles) slightly more with a higher percentage of neurites segments found between 0-20 degrees than between 70-90 degrees. In this system, neurites

encounter both a strong physical cue and a strong chemical cue, which is indicated by a higher percentage of the neurite segments found following either the physical pattern (low angles) or chemical pattern (high angles). Even with strong physical cues (either more frequent and/or deeper micro-grooves) neurites growth and alignment is significantly influence by the chemical cue patterns.

4.5 CONCLUSIONS

Spatial control of neurite regeneration from sensory neurons stimulated by neural prosthetics may serve as a viable method to improve resolution for many devices, such as the cochlear implant. In this work, we report on a facile method to pattern laminin onto photopolymerizable acrylate polymers. Illuminating adsorbed laminin through a photomask deactivates protein to form active protein patterns in unexposed areas. The photodeactivation process described herein was shown to decrease binding of laminin to antibodies, while leaving the protein adsorbed to the surface. SGN neurites cultured on 50 μm periodicity active laminin stripes strongly aligned to the pattern. Perpendicular competing biochemical and physical cues were used to examine the neural response and pathfinding of neurites cultured on substrates with a combination of cues. At weak and intermediate physical cues, SGN neurites aligned more closely to the laminin pattern. When cultured on micro-patterns with stronger guidance cues, SGN neurite alignment to the laminin pattern was disrupted showing no distinct preference tp e either cue. These findings demonstrate that physical and/or biochemical cues can be used to align neurites and even overcome competing cues, which may be necessary for directing neurite *in vivo* when neurons encounter conflicting cues

CHAPTER 5: PHOTOPOLYMERIABLE ZWITTERIONIC POLYMER PATTERNS CONTROL CELL ADHESION AND GUIDE NEURAL GROWTH[204]

5.1 ABSTRACT

Developing materials that reduce or eliminate fibrosis encapsulation of neural prosthetic implants could significantly enhance implant fidelity by improving the tissue/electrode array interface. Here, we report on the photografting and patterning of two zwitterionic materials, sulfobetaine methacrylate (SBMA) and carboxybetaine methacrylate (CBMA) for controlling the adhesion and directionality of cells relevant to neural prosthetics. CBMA and SBMA polymers were photopolymerized and grafted on glass surfaces then characterized by X-ray photoelectron spectroscopy, water contact angle, and protein adsorption. Micropatterned surfaces were fabricated with alternating zwitterionic and uncoated bands. Fibroblasts, cells prevalent in fibrotic tissue, almost exclusively migrate and grow on uncoated bands with little to no cells present on zwitterionic bands, especially for CBMA-coated surfaces. Astrocytes and Schwann cells showed similarly low levels of cell adhesion and morphology changes when cultured on zwitterionic surfaces. Additionally, Schwann cells and inner ear spiral ganglion neuron neurites aligned well to zwitterionic patterns.

5.2 INTRODUCTION

The foreign body reaction is observed after virtually all medical device implantations.[55] In many cases, particularly for neural implants such as cochlear implants and deep brain or cortical electrodes, encapsulation by fibrotic tissue compromises the function of the implant. In some cases, fibrotic tissue formation also interferes with the normal function of the surrounding native tissue.[60] A number of different approaches to reducing foreign body response have been investigated in recent years with many focusing on using glucocorticoids to modulate the

immune and/or inflammatory response.[223,224] These drugs have been used systemically for many years and have more recently been used in a number of topical and local controlled-release formulations.[223,225] Other immunomodulatory drugs have also been studied in control-release formulations, such as IL-1 antagonist.[226] However, the drawback to all drug-eluting systems is that eventually the drug will deplete, which could potentially allow for a delayed foreign body response.

Nonspecific protein adsorption to implant surfaces often trigger the foreign body response, i.e. the inflammatory response evoked by the presence of a foreign object in host tissue.[54–56] Macrophages recognize these nonspecifically-protein labeled implants as foreign, attach to the surface, and attempt ingestion. Because the implant is large and not biodegradable, these macrophages fuse together and form foreign body giant cells, which secrete inflammatory cytokines and induce fibroblast adhesion.[16,67,68] After about three weeks of implantation, adhered fibroblasts fuse together to form an avascular collagenous capsule around the implant which permanently isolates the device and renders the implant less effective or even nonfunctional.[16]

Engineering materials that resist nonspecific protein adsorption, the theorized primary step in the foreign body response,[54–56] provide an alternative approach to drug treatment. The most commonly investigated materials to achieve this goal are hydrophilic polymers such as poly(ethylene glycol) (PEG) or poly(2-hydroxyethyl methacrylate) (PHEMA). However, both only partially reduce nonspecific protein adsorption and PEG is additionally subject to oxidative degradation *in vivo.*[16] More recently, zwitterionic polymers, or net neutral polymers containing positive and negative charges on the same repeat unit, have emerged as excellent alternatives.[80,170] It has been proposed that the proximity of intramolecular positive and negative charges strongly structures surrounding water molecules in a hydrogen-bonded network, making

adsorption of any other molecules energetically unfavorable.[65] Among these polymers, carboxybetaine methacrylate (CBMA), sulfobetaine methacrylate (SBMA), and phosphorylcholine chemistries have proven effective as ultra-low-fouling materials (Figure 5.1).[64] For example, Jiang et al. reported both CBMA and SBMA polymer brushes grown on gold surfaces demonstrated ultra-low nonspecific protein adsorption (0.4 and 9.1 ng/cm^2 respectively) from 100% human plasma.[64,110] Additionally, CBMA and SBMA brushes dramatically reduce cell adhesion and biofilm formation when compared to unmodified surfaces.[170,172,227] Therefore, great interest has developed in the use of zwitterionic materials in implantable and insertable devices, including urinary catheters and intravascular devices.[228,229] CBMA and SBMA materials have also been examined in a wide range of applications including glucose sensing in 100% blood serum,[58,113] antigen detection in complex media,[115] and prolonging the blood circulation time of coated drugs[6] among others.[89,116] Most important to biomedical implant research, promising results have been reported in animal models showing that a bulk CBMA hydrogel inhibits fibrotic capsule formation,[80] which demonstrates the ability of CBMA materials to not only prevent protein adsorption *in vitro,* but also fibrosis *in vivo* where many other materials with low nonspecific protein adsorption fail.

Methods to synthesize zwitterionic polymer brushes have focused largely on surface initiated atom transfer radical polymerization (ATRP), which utilizes a copper bromide catalyst.[79,109] This technique provides precise control over molecular chain length (molecular weight) and molecular weight distribution. Alternatively, photopolymerization offers a unique set of advantages over conventional polymerization methods in biomaterials fabrication. Among these advantages are precise spatial control over the rate of polymerization and mild reaction conditions (i.e. aqueous and ambient).[174] Photopolymerization initiates only in areas exposed to a

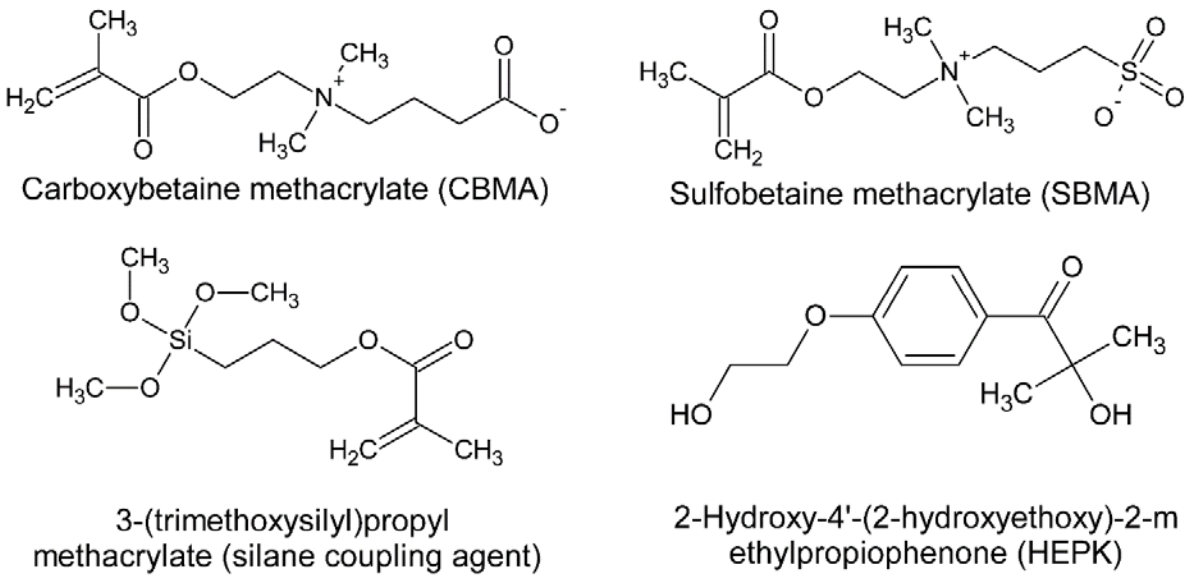

Figure 5.1. Molecular structures of zwitterionic monomers, methacrylate coupling agent, and photoinitiator.

light. Accordingly, patterns can be generated using a photomask with features on the same size scale as cell bodies.[147,184]

Neural prosthetic devices, such as the cochlear implant or developing retinal implant, rely on communication between stimulating elements and primary neural receptors.[128] The effectiveness of these devices is not only reduced by fibrous tissue on the surface, but also by the distance the electrode current must traverse in order to stimulate the neural cells.[230–232] Because of this separation, nonspecific excitation of adjacent neural cells, induced by current spread, significantly decreases stimulation specificity. Consequently, neural prosthetics fail to effectively relay the intricate information required for a high-fidelity device. Strategies to close this gap have focused largely on directing the regeneration of proximate neurites toward stimulating elements to narrow this distance or even contact electrode arrays.[233] Recent advances in microfabrication technology have allowed for a variety of approaches to direct neural processes including aligned microfibers,[234,235] parallel micro- and nano-channel topography,[145–149] chemo-

attractive gradients,[213,236,237] electrical fields,[238,239] oriented glial cells,[240] biomolecular patterning,[155] and chemo-repellents.[241–243] Many of these studies have focused on elucidating the fundamental mechanisms behind neurite pathfinding to improve the tissue/prosthetic interface. The chemo-repulsive properties of zwitterionic surfaces could potentially be used to guide neural cell in addition to reducing the foreign body response.[111]

In this work, we aim to develop materials that could improve the interface between biomaterials and neural prosthetics. Our approach is to develop patterned zwitterionic surfaces using photopolymerization to resist cell adhesion and fibrosis and control the outgrowth of neural cells among other cell types. To the best of our knowledge, this research represents the first use of a patterned zwitterionic substrate to control the adhesion and direct the growth of several cell types relevant to implant materials, including neuronal cells. We demonstrate that CBMA and SBMA polymers can be covalently grafted and patterned from glass surfaces via a one-step photopolymerization reaction. Surface coverage with the zwitterionic polymer is investigated by varying the solution concentration of the CBMA and SBMA monomers to generate surfaces with variable levels of atomic composition and protein adsorption. Due to the inherent spatial control afforded by the photopolymerization reaction, parallel patterned substrates with 100 μm periodicity were fabricated and used to study the ability of zwitterionic stripes to locally control cell adhesion. Fibroblasts, the cell type primarily comprising fibrotic tissue found on the surface of biomedical implants,[55,67] were grown on these substrates to understand their efficiency in preventing cell attachment and fibrotic tissue formation. Alignment behavior of spiral ganglion neuron (SGN) neurites, the cells responsible for transmission of hearing response to the brain, to CBMA and SBMA stripes was evaluated to understand the ability of these patterns in directing neural cells. The alignment of Schwann cells was also tested

due to the supportive role they play in neural regeneration.[244,245] Additionally, astrocytes were cultured to evaluate the effectiveness of these surfaces in repelling central glial cells that encapsulate brain and spinal cord prostheses.[246,247] These findings provide fundamental understanding of the biomaterial/cell interface and lay the framework for next generation neural prosthetic devices.

5.3 EXPERIMENTAL

5.3.1 Materials and Synthesis

2-(N,N'-dimethylamino)ethyl methacrylate (DMAEM), β-propiolactone, triethyl amine, hydroquinone, [2-(Methacryloyloxy)ethyl]dimethyl-(3-sulfopropyl)ammonium hydroxide (SBMA), mouse anti-CD20, rabbit anti-S100β, mouse anti-NF200, 3-(trimethoxysilyl)propyl methacrylate, paraformaldehyde, collagenase, dulbecco's modified eagle medium (DMEM), neurotrophin-3 (NT3), insulin, human fibrinogen, human anti-fibrinogen, and all organic solvents were purchased from Sigma Aldrich. Rabbit anti-vimentin and rabbit anti-glial fibrillary acidic protein (GFAP) antibodies were purchased from Abcam (Cambridge, MA). Hank's balanced salt solution (HBS), fetal bovine serum (FBS), poly-L-ornithine, trypsin-EDTA dissociation reagent, DAPI-containing mounting medium, were purchased from Gibco (Carlsbad, CA). Laminin was purchased from Labtek (Campbell, CA). Brain derived neurotrophic factor (BDNF) and neurotrophin-3 (NT-3) were purchased from R&D systems (Minneapolis, MN).

2-Carboxy-N,N-dimethyl-N-(2'-(methacryloyloxy)ethyl)ethanaminium inner salt (carboxybetaine methacrylate,CBMA) was synthesized as previously described.[111] Briefly, DMAEM was dissolved in acetone and cooled to 0^{o} C. β-propiolactone was dissolved in acetone and added to the DMAEM solution dropwise under inert atmosphere. The reaction was stirred overnight after which 10 mg of hydroquinone inhibitor was added and the solvent was removed.

The residual oil was dissolved in methanol and trimethylamine was added to quench any side reactions. The solution was then precipitated into chilled diethyl ether and filtered to yield a white solid. The product was dried under vacuum and used without further purification. The NMR spectrum was recorded on a Bucker spectrometer (Avance 300). 1H NMR (D_2O, 300 MHz), δ 6.06 (s, 1H, =CH), δ 5.68 (s, 1H, =CH), δ 4.55 (t, 2H, OCH3), δ 3.70 (t, 2H, NCH2), δ 3.59 (t, 2H, NCH2), δ 3.10 (s, 6H, NCH3), δ 2.64 (t, 2H CH2COO), δ 1.84 (s, 3H =CCH3).

5.3.2 Zwitterion-functionalized Glass Substrate Fabrication and Characterization

Standard 2.54 x 7.62 cm glass microscope slides were functionalized with a 3-(trimethoxysilyl)propyl methacrylate (silane coupling agent) as previously described[185] to allow covalent grafting of zwitterionic polymers from glass surfaces. Zwitterionic polymers were grafted from glass surfaces represented schematically in Figure 5.2. Aqueous monomer mixtures of zwitterion (CBMA or SBMA at 0.1, to 20 wt%) in phosphate buffered saline (PBS) containing 0.05 wt% 1-[4-(2-hydroxyethoxy)-phenyl]-2-hydroxy-2-methyl-1-propane-1-one (HEPK, photoinitiator) were pipetted onto activated glass surfaces. The liquid was then dispersed evenly across the sample using a 2.54 x 2.54 cm glass-chrome Ronchi rule photomask for patterned samples or a cut glass slide of the same dimensions for uniform samples. Substrates were subsequently illuminated for 10 min at 16 mW/cm^2 measured at 365 nm wavelength using a mercury vapor arc lamp (Omnicure S1500, Lumen Dynamics, Ontario, Canada). Samples were then copiously washed with distilled H_2O and dried using a nitrogen stream, then kept in a sealed container until use.

X-ray Photoelectron Spectroscopy (XPS) analysis was performed using Kratos Axis Ultra x-ray photoelectron spectrometer with concentric hemispherical electron energy analyzers combined with the established delay-line detector. The incident radiation monochromatic Al Ka

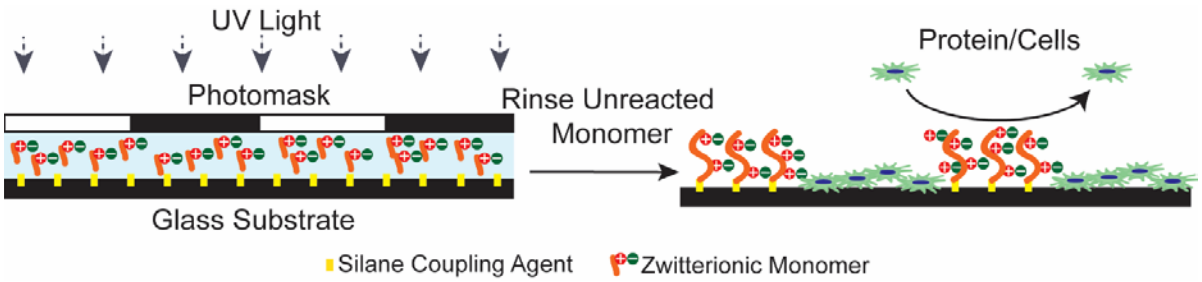

Figure 5.2. Schematic of the photografting/patterning process. UV-light is used to initiate polymerization and grafting of zwitterionic monomers forming polymer thin films in exposed regions. Functionalization is limited to illuminated regions, which in turn repel protein and cell adhesion.

X-ray (1486.6 eV) at 150 W (accelerating voltage 15 kV, emission current 15 mA) was projected 45° to the sample surface and the photoelectron data was collected at a takeoff angle of q = 90°. Survey scans were taken at a pass energy of 160 eV, and carried out over a 1200 eV ~-5 eV binding energy range with 1.0 eV steps and a dwell time of 200 ms. All spectral analyses were conducted using CasaXPS software. Shirley type calculations were used to account for the background spectrum when quantifying percent atom composition.[206] Relative sensitivity factors were used to normalize peak intensity for elemental quantification. The C 1s peak at 285.0 eV was used to calibrate all spectra before data analysis.

Water contact angles were measured using the sessile drop method on a Ramé-Hart Model 190 Goniometer. Five areas of each substrate were tested in triplicate at and the average contact angle was taken as the mean value of all fifteen measurements.

5.3.3 Protein Adsorption

Immunofluorescence was used to measure protein adsorption to substrates. The glass samples were first incubated in PBS (room temperature) for 30 min prior to protein exposure. Human fibrinogen (1mg/mL) was pipetted onto substrates and dispersed by placing a glass coverslip on the solution followed by a 1 hr incubation at room temperature. The samples were then soaked in PBS for at least 3 hrs with the PBS being changed every hour. After the rinsing

step, the substrates were incubated in paraformaldehyde (4%) for 15 min at 2°C. The samples were then rinsed three times with PBS followed by a blocking buffer solution being applied to block the areas unoccupied by fibrinogen for 30 min at room temperature. A horseradish peroxidase conjugated anti-fibrinogen antibody was applied to the samples overnight at 2° C. The substrates were then rinsed 3 times with PBS and the secondary antibody was applied for 1 hr at room temperature. The samples were washed three times with PBS and coverslips were applied before epifluorescent imaging. Digital epifluorescent images were captured on a Leica DMIRE2 microscope (Leica Microsystems, Bannockburn, IL) with Leica DFC350FX digital camera and Metamorph software (Molecular Devices, Silicon Valley, CA). Images were taken at each sample condition and gray-scale measurements were used to evaluate relative fluorescence intensity in Image J software (NIH, Bethesda, MD). All samples were made in triplicate and five representative images were taken for each condition.

5.3.4 Cell Culture and Immunofluorescence

All cell culture and quantification was conducted in Dr. Marlan R. Hansen's lab. Dissociated spiral ganglion (SG) culture from p4-7 perinatal rat cochleae were performed as previously described.[214,215] Dissociated fibroblast cultures were obtained from p4-7 perinatal rat skin. The tissue was scraped to remove subcutaneous fat and digested in 0.125% trypsin with EDTA and 0.2% collagenase for 1 hr at 37°C followed by gentle trituration. Astrocyte and Schwann cell cultures were prepared and maintained from p4-7 perinatal rat cerebral cortex and sciatic nerve, respectively, as previously described.[147,248,249] All cells were plated onto glass substrates without prior coating of protein.

SGN cultures were maintained in Dulbecco's Modified Eagle Medium (DMEM) supplemented with N2 additives, 10% fetal bovine serum (FBS), NT-3, (50 ng/ml) and BDNF,

(50 ng/ml). Fibroblast, Schwann cell, and astrocyte cultures were maintained in DMEM with 10% FBS. All cultures were fixed with 4% paraformaldehyde in PBS after 48 hrs of cell culture before immunostaining.

Spiral ganglia cultures were immunostained with anti-neurofilament 200 (NF200) antibodies to label neurons and their neurites. Astrocytes and Schwann cell cultures were immunostained with anti-GFAP or anti-S100 antibodies, respectively. Fibroblast cultures were immunostained with anti-vimentin antibodies. Coverslips with DAPI-containing mounting medium were placed onto the stained cultures to label nuclei.

5.3.5 Quantification of Cell Density and Alignment to Micropatterns

Cell density was determined by counting the total number of nuclei of each cell type (identified by immunostaining as described above) from digital images of randomly selected 20X microscopic fields using the cell counting feature of MetaMorph software package. At least 10 fields were taken for each culture and each culture was before on at least 3 substrates per experiment. The experiments were repeated at least three times.

SGN total neurite length was determined from digital images captured using the scan slide feature in MetaMorph by measuring the longest process of randomly selected neurites from each condition using the measurement tool in Image J (NIH, Bethesda, MD) as previously described.[250] Neurite alignment was calculated as previously published by our group.[185,201] Briefly, alignment to the pattern was defined as a ratio of total length per aligned length. The ratio is represented as $[T_L/A_L]$, where T_L is total neurite length and A_L represents aligned length in the pattern direction. Aligned length (A_L) was determined by measuring the distance from the neuronal cell body to the neurite terminus in a straight line in the direction of the micropattern. The pattern direction was always set horizontally prior to measurements. The total length to

aligned length ratio is referred to as the alignment ratio throughout the text. A ratio close to one represents a neurite that closely follows the pattern along its entire length. A wandering neurite, which does not strongly align to the pattern would be represented by a high alignment ratio. Schwann cell orientation to the pattern was determined as previously described by drawing the outline of the cell using Image J software and fitting an ellipse to the cell outline.[185,201] The angle made between the major axis of the ellipse and the pattern (θ) was measured in Image J as Schwann cell alignment.

5.3.6 Statistics

Statistical analysis was conducted using Graphpad Prism 7.01 software. To compare cell density between uncoated, CBMA-coated, and SBMA-coated and between striped groups on patterned substrates, a one-way ANOVA with *post hoc* Tukey test was used. A two-tailed t-test was used to compare cell density between coated and uncoated regions on striped substrates. Analysis of alignment of Schwann cells and SGN neurites was conducted using a one-way ANOVA by a *post hoc* Kuskal-Wallis analysis of variance on ranks and a Dunn's test.

5.4 RESULTS AND DISCUSSION

5.4.1 Zwitterion-functionalized Substrate Fabrication and Characterization

Surface properties are a key component when engineering low fouling materials because the surface comes into direct contact with host fluid, blood protein, and other immunogenic factors. These biomolecules and their nonspecific adsorption to implant surfaces play an integral role in fibrous tissue formation. A common approach to achieve nonfouling properties involves introducing functional groups onto the surface, which then act as anchors for polymer growth.[109] Glass was used as a proof of concept substrate because it can be easily modified with a variety of functional groups using silane coupling chemistry.[202] While glass has been used as a substrate for

other low-fouling surfaces,[111] our system uses photopolymerization as a simple method to covalently graft and pattern zwitterionic polymers on the surface. Our systems were used to investigate adhesion of cell types relevant to neural regeneration (astrocytes, Schwann cell, and spiral ganglion neurons), which have not been previously studied on these zwitterionic-coated substrates, in addition to fibroblasts, critical in fibrotic tissue formation. To fabricate these substrates, glass samples were first exposed to oxygen plasma to generate hydroxyl surface groups followed by reaction with a silane-containing coupling agent incorporating a reactive methacrylate group. Zwitterionic methacrylates were then covalently attached to glass surface methacrylates by illuminating a monomer- and photoinitiator-containing solution in contact with the substrate. UV-light was used to induce the polymerization reaction and covalently build a grafted zwitterionic polymer from the substrate (Figure 5.2). During UV-illumination, radicals in the solution are generated from photoinitiating molecules absorbing light that dissociate into initiating species. These initiating radicals then react with methacrylates on the surface and in the solution to generate a propagating species that builds the zwitterion zwitterionic polymer from the surface of the glass slide. For our experiments, SBMA and CBMA (Figure 5.1) were used as zwitterionic monomers to alter the surface properties of functionalized glass substrates. The concentration of zwitterionic monomer in solution was varied between 0.1 wt% and 20 wt% to change surface coverage and probe the physicochemical properties of the antifouling polymer-grafted surface.

Grafting of the methacrylate silane coupling agent and zwitterionic SBMA and CBMA polymers was characterized, as shown in Figure 5.3, through X-ray photoelectron spectroscopy (XPS) analysis, which provides elemental composition of the first 5-10 nm of a surface. The carbon 1s peak, located at 285 eV, was used to confirm the grafting of the methacrylate reactive

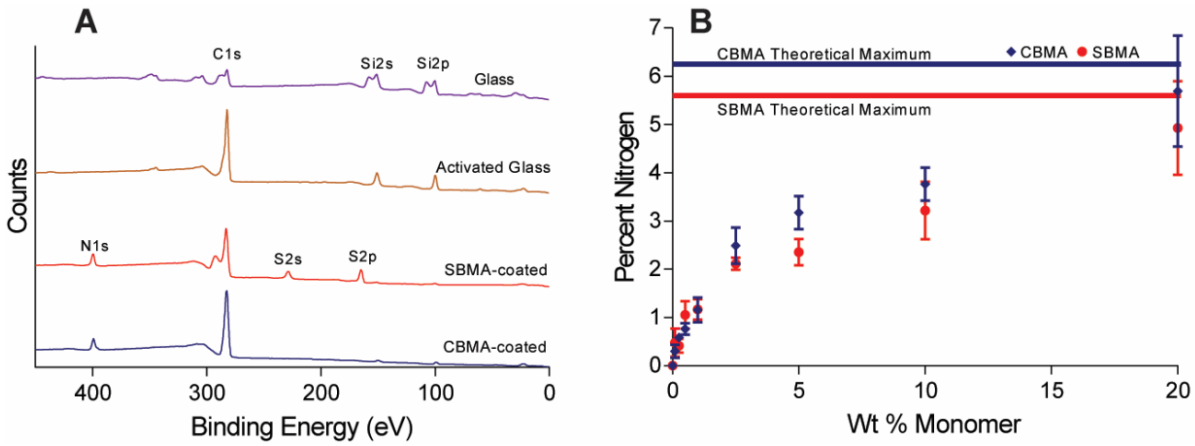

Figure 5.3. Characterization of zwitterion-coated glass surfaces using XPS. A) Representative XPS spectra for glass, activated glass, SBMA-coated glass (20 wt% monomer solution), and CBMA-coated glass (20 wt% monomer solution). The zwitterion-coated glass curves both show a characteristic N1s peak at 402 eV and the SBMA-coated sample exhibit S2s and S2p peaks at 231 and 168 eV respectively. B) Percent nitrogen as a function of wt% monomer for both SBMA- and CBMA-coated glass. Nitrogen percent increases for both zwitterions with monomer wt% and is shown to approach the theoretical maximum (pure polymer composition) at 20 wt%.

group. The silane-activated sample exhibited a much stronger band than the bare glass control at 285 eV, indicating higher carbon content at the surface as would be expected for a carbon-containing silane coupling agent (Figure 5.3A). The presence of the characteristic nitrogen 1s quaternary ammonium band found around 402 eV was used to confirm and quantify the successful photo-induced grafting of SBMA and CMBA polymers from the glass. Both the bare glass and silanized glass controls exhibited no peak at 402 eV, while the SBMA- and CBMA-coated samples (20 wt% uniformly coated sample depicted) showed distinct peaks in this region (Figure 5.3A). Additionally, the sulfur 2s and 2p peaks located at 231 and 168 eV, respectively, were used to confirm the grafting of the SBMA polymer, with its inherent anionic sulfate functional group. The silicon 2s and 2p peaks located at 153 and 102, respectively, were orders of magnitude lower in area for the 20 wt% samples confirming good surface coverage and thickness nearing the XPS depth penetration (5-10 nm).

To understand how the elemental composition of the surface changes as a function of SBMA and CBMA solution concentration, percent nitrogen was quantified using the 402 eV nitrogen peak of the XPS spectra (Figure 5.3B). At low SBMA solution concentrations (less than 1 wt%), the atomic nitrogen content is less than 1%, indicating low levels of grafting and surface coverage with the polymer. As the SBMA solution concentration increases, the atomic composition increases and approaches the theoretical maximum (5.6%) of a pure SBMA polymer, calculated using atomic percent. A similar trend was also observed in the CBMA-coated samples with slightly higher percent nitrogen due to the higher theoretical maximum (6.25% as calculated by atomic percent of the pure polymer). The nitrogen percent once again remains small at low concentrations then approaches the theoretical maximum at a solution concentration of 20 wt%. These observations imply that the surface coverage of the SBMA and CBMA polymers is strongly dependent on the concentration of monomer in the solution. Further, for both the SBMA- and CBMA-coated samples, the percent silicon decreased with increasing solution concentration of monomer and showed very low signal at higher concentrations.

These observations are consistent with increases in thickness with higher monomer solution concentrations. On the basis of the XPS data collected, it is estimated that the thickness of the polymer layers measured using all monomer solution concentrations is less than the penetration depth of XPS data collection. XPS only examines the atomic composition in the first 5-10 nm of the surface, and thus it is possible that changes (a few nanometers) in film thickness and/or changes in surface coverage of zwitterionic polymer occur on the surface giving rise to changes in nitrogen percent. Film thicknesses are likely less than the penetration depth of XPS causing atomic composition of the glass (Si and O) to be evident in the spectrum even at higher solution concentrations. As the solution concentration of zwitterion increases a corresponding

decrease in silicon and oxygen percent is observed. This decrease is caused by more zwitterionic polymer on the surface. With more zwitterionic monomers in solution, the probability of molecular collisions and reaction between methacrylate groups on the surface is increased before termination, thereby increasing the length of the polymer chains grafted from the surface. The longer polymer chain length induce greater coverage of zwitterion on the surface, increasing the percent nitrogen measured through XPS.

Surface grafting of a polymer or other molecule is accompanied by a corresponding change in surface properties including surface energy that can be evaluated using water contact angle measurements. Higher contact angles indicate a more hydrophobic surface as water avoids interaction with the surface. Conversely, low contact angles indicate hydrophilic surfaces as water spreads to maximize interactions with the substrate. The silanized glass was relatively hydrophobic with a contact angle of over 57 degrees as would be expected given the nonpolar nature of the coupling agent used to functionalize the glass substrates. Conversely, zwitterionic polymers are hydrophilic, due to the presence of charged atoms along the polymer side chains and are expected to decrease contact angles. As shown in Figure 5.4A, the contact angles of the SBMA-coated samples decreased sharply with increasing SBMA wt% in solution. At higher concentrations, the contact angles remained unchanged at approximately 15 degrees. A similar trend was also observed above 1 wt% for the CBMA-functionalized substrates with the contact angle leveling around 11 degrees with higher concentrations (Figure 5.4B). The marked decrease in contact angle for both SBMA- and CBMA-coated surfaces indicates increases in hydrophilicity and further corroborates that the surface was successfully functionalized with the zwitterionic polymer. These decreases in contact angle are consistent with the results of an SBMA polymer grafted from silicon wafers using thermally-initiated polymerization.[251] The

observation that the contact angle of the substrates remain constant at higher concentrations (Figure 5.4) implies that at a solution concentration of 1 wt% the surface has reached a maximal coverage: i.e., virtually all accessible methacrylate groups on the surface have reacted with the zwitterionic monomer. At lower concentrations, many of the reactive surface methacrylate groups are unreacted due to an insufficient number of zwitterions in the solutions available for functionalization. As solution concentrations increase above 1 wt%, the surface coverage of the glass does not change significantly evidenced by the relatively constant contact angle measurements. Water contact angles remain unchanged because the surface energy is directly related to the ability of the surface to bind water molecules which no longer changes once a sufficient grafting density has been reached. These findings further support the claim that changes in surface coverage could explain the variations in surface chemistry as measured by XPS for solution concentrations above 1 wt%.

With large changes in surface properties, it is reasonable to believe that the zwitterionic polymer will affect adsorption of molecules including proteins. As mentioned previously, the first step in foreign body response is nonspecific protein adsorption, such as would occur when a surface comes into contact with serum during implantation.[16,55] Hydrophilic, net neutral surfaces such as zwitterionic polymers have been shown to effectively prevent the nonspecific adsorption of protein.[64] Fibrinogen is of particular interest as adsorption would be expected to trigger an early foreign body response. We therefore quantified fibrinogen adsorption by first incubating substrates prepared from solutions of varying monomer concentration with a 1 mg/mL solution of fibrinogen in PBS. The surface was then fixed and stained with antibody to quantify the amount of protein (Figure 5.4). Five representative images were taken for each sample using epifluorescent microscopy followed by gray scale measurements to quantify levels of protein

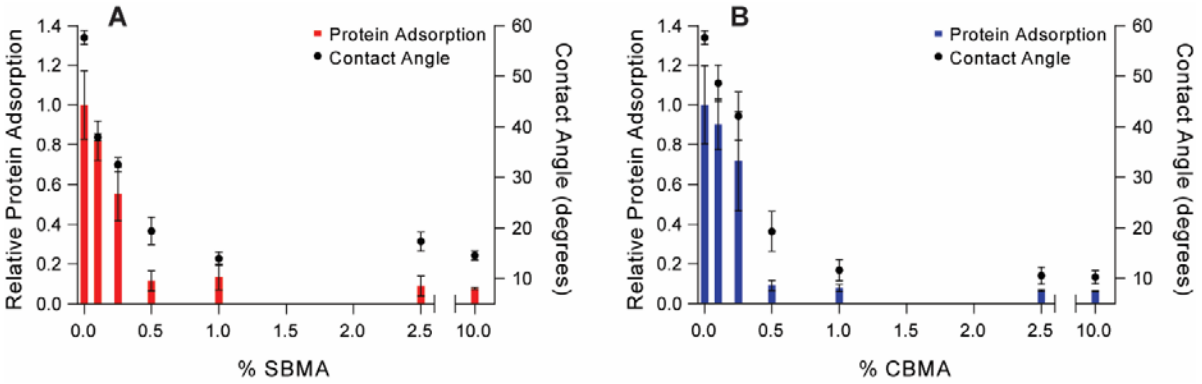

Figure 5.4. Tuning of physicochemical properties of (A) SBMA- and (B) CBMA-functionalized glass surfaces through varying the wt% monomer in solution. Relative protein adsorption (bars) refers to the left axis and is measured compared to an activated glass slide control. Contact angles (•) refer to the right axis. A strong correlation is observed between contact angle and relative protein adsorption.

adsorption. The relative fluorescence is normalized to that from the glass control. As shown in Figure 5.4A, SBMA protein adsorption correlates to water contact angles with sharp decreases up to solution concentrations of 0.5 wt% SBMA. At higher concentrations, protein adsorption drops to values less than 10% of the level observed with the uncoated control. CBMA-coated substrates performed similar to that of the SBMA samples with protein adsorption correlating to the water contact angles (Figure 5.4B). The CBMA samples exhibited lower, although not statistically significant, levels of protein adsorption reaching about 6% of that observed in the control. These observations suggest that, similar to the contact angle, a maximum in graft density is reached at low solution concentrations. The protein adsorption appeared to reach a minimum at slightly lower concentrations than observed with the contact angle (0.5 wt% compared to 1 wt%) implying that even less polymer is necessary to repel protein than to maximize surface energy. These results are consistent with those conducted by Jiang et al. who showed SBMA- and CBMA-coated gold surfaces resisted the nonspecific adsorption of fibrinogen equally well.[110] The protein adsorption data, in combination with the XPS data, suggest that only a very

thin film (a few nanometers) of the zwitterionic polymer film is necessary in order to achieve a significant decrease in protein adsorption and water contact angle.

To determine the ability of zwitterionic-functionalized glass to spatially control protein adsorption and direct cell growth, micropatterned substrates were fabricated with alternating zwitterion-coated and uncoated bands. Due to the inherent spatial control afforded by photopolymerization, areas of functionalization can be precisely defined through use of a photomask. In regions that are shielded from irradiation by the opaque bands of the photomask, the glass substrate remains chemically unchanged because no photoinitiating molecules are locally excited by photons. Conversely, in illuminated areas, absorption of photons by the photoinitiator induces polymerization causing covalent grafting of the polymer from the activated glass surface. Accordingly, alternating transparent and opaque parallel bands of with a periodicity of 100 μm (defined as the distance between repeating features in the pattern) were used in generating micropatterns of SBMA and CBMA polymers. Characterization of the micropatterns was determined by first adsorbing protein to the surface to the zwitterion-patterned surface followed by immunostaining to visualize areas with high protein adsorption. As described in the previous section, protein adsorption was greatly reduced by SBMA- and CBMA-coated surfaces. Representative images of both SBMA- and CBMA-striped substrates are shown in Figure 5.5. Green bands indicate areas where protein is adsorbed, as would occur on an unfunctionalized surface. Conversely, dark regions represent areas that have been successfully functionalized through photopolymerization, which result in significantly lower levels of protein adsorption. The width of the green bands precisely matches the width of the transparent and opaque bands of the photomask used to generate the zwitterionic pattern.

5.4.2 Fibroblast and Astrocyte Adhesion

Fibroblasts are the primary cell type that contribute to fibrosis on the surface of implanted devices.[55] Therefore, determining the effectiveness of these zwitterion-coated substrates in preventing adhesion of fibroblasts could serve as an effective *in vitro* measure of the ability of these materials to resist fibrosis. Accordingly, fibroblasts were seeded in equal densities onto uncoated (Figure 5.6A), uniformly-coated with SBMA (Figure 5.6B), coated with 100 µm periodicity SBMA stripes (image not shown), uniformly-coated CBMA (Figure 5.6C), and coated with 100 µm periodicity CBMA stripes (Figure 5.6D). Cell cultures were fixed after 48 hrs followed by immunostaining and epifluorescent microscopy. Vimentin immunostaining revealed that the morphology of fibroblasts was markedly altered on coated surfaces. On uncoated glass, fibroblasts showed a characteristic elongated multipolar shape, while they showed fewer cytoplasmic extensions and exhibited a round morphology on zwitterion-coated substrates (Figure 5.6A-C). Further, noticeably fewer cells adhered to CBMA-coated substrates compared to SBMA-coated substrates. Random images were analyzed and cell nuclei counts were performed to determine cell density. Analysis of fibroblast cell density on uniform substrates reveals a statistically significant reduction in adhered cells to SBMA-coated surfaces with less than half of the cell density when compared to uncoated glass. Very few fibroblasts adhered on CBMA-coated surfaces with less than one percent of the cell density as compared to the uncoated glass (Figure 5.6E). To test the stability of the SBMA- and CBMA-coated surfaces to extended culture, fibroblasts were seeded a second time after 48 hrs and cultured for 24 more hrs. These experiments showed consistency results from the 48 hr culture study (data not shown).

Analysis of cell density on striped substrates showed a distinct preference for cell adhesion to uncoated glass compared to adjacent SBMA- or CBMA-coated stripes. A

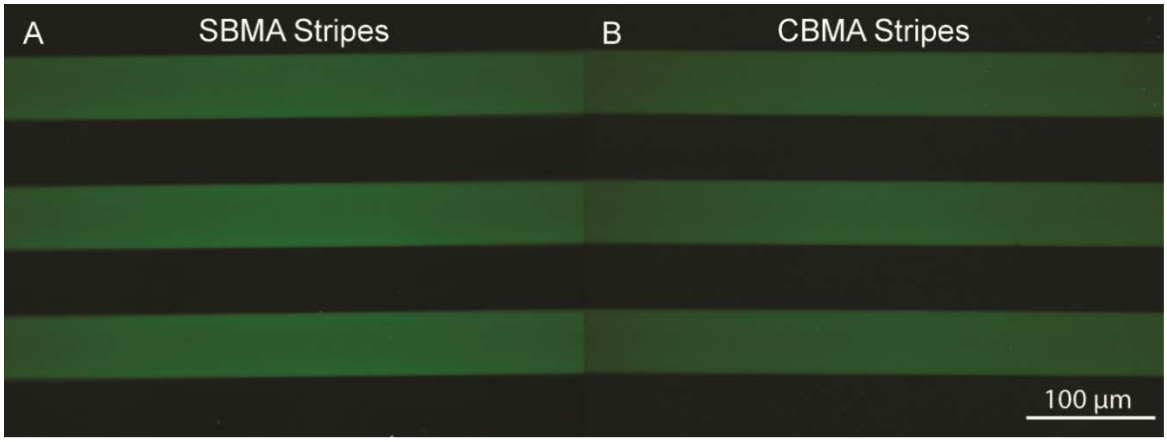

Figure 5.5. Epifluorescent images of protein (human fibrinogen) adsorption to zwitterionic stripes on glass substrates: A) SBMA stripes with a100 µm periodicity. B) CBMA stripes with 100 µm periodicity. Protein adsorbs to uncoated regions as observed by the green bands, while protein does not adsorb to zwitterion-coated bands as seen in black.

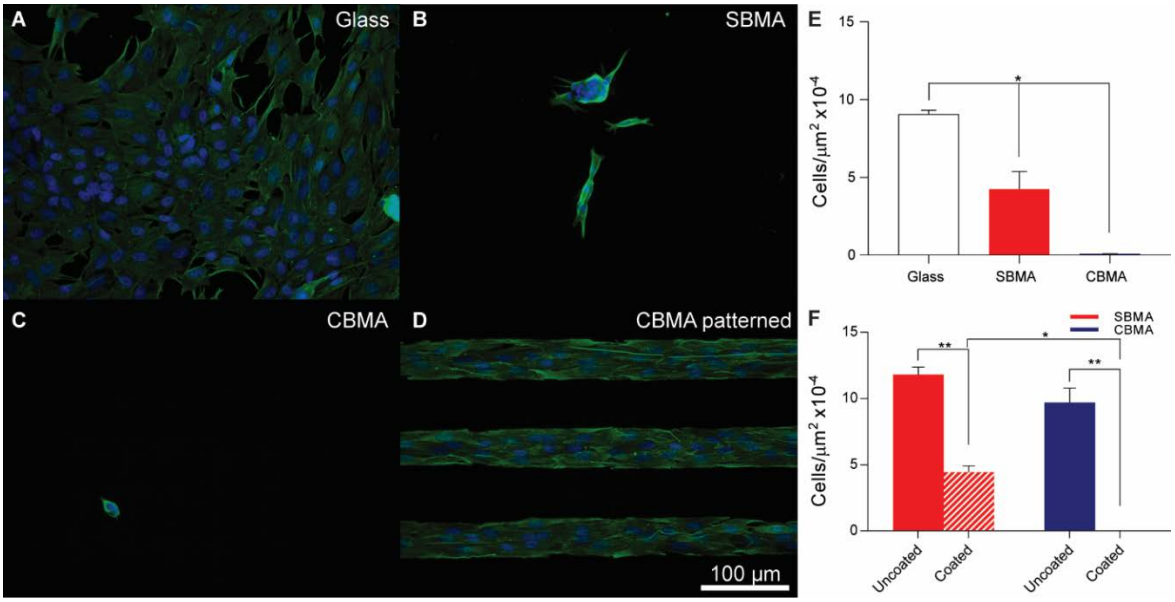

Figure 5.6. Representative epifluorescent images of fibroblasts grown on (A) glass, (B) uniformly SBMA-coated, (C) uniformly CBMA-coated, and (D) CBMA-striped surfaces and immnolabeled with anti-vimentin antibody (green). Nuclei are labeled with DAPI (blue). E) Fibroblast cell density on uniformly coated surfaces. A significant difference was observed between all groups (SBMA, CBMA, and uncoated glass) with CBMA exhibiting the lowest cell density (*$p < 0.001$ one way ANOVA). F) Fibroblast cell density on striped substrates, both on and off the zwitterionic pattern. A significant difference was determined between coated and uncoated regions for both SBMA- and CBMA-coated substrates (**$p < 0.001$ t-test). Cell density was shown to be statistically different between SBMA- (image not shown) and CBMA-coated stripes (*$p < 0.001$ one way ANOVA). Zwitterionic micropatterns used for cell culture have a periodicity of 100 µm. Error bars represent standard error of the mean.

statistically significant difference in cell density was found between stripes coated with SBMA and uncoated bands with a nearly 40% reduction in fibroblast adhesion (Figure 5.6F). While reductions in cell density were seen on SBMA stripes, in many regions cells were found bridging across SBMA-coated bands (images not shown). For CBMA-coated stripes, a distinct border is visible between coated and uncoated regions with fibroblasts growing up to the edge, but not extending into the coated regions. Remarkably, zero fibroblasts were observed adhered to CBMA stripes while uncoated regions had a similar cell density to the uncoated regions of the SBMA-striped substrates. A significant difference was found in cell density between SBMA and CBMA stripes, further corroborating the effectiveness of CBMA over SBMA films in preventing fibroblast cell adhesion.

To demonstrate the versatility of zwitterion-coated surfaces in controlling and directing a variety of cell types, glial cells of both the peripheral and central nervous system (CNS) were seeded onto the bare and both uniformly coated and patterned zwitterionic surfaces. Astrocytes, a glial cell of the CNS, provide trophic support to migrating neuronal cells in addition to guiding the formation and maintenance of neuronal pathways.[252,253] Furthermore, astrocytes function as immune effector cells in the CNS, and play critical roles in CNS inflammation and the formation of glial scar around implants.[246,247] Thus, zwitterion-coated surfaces were evaluated to determine if these substrates control astrocyte adhesion and growth. Cortical astrocytes were passaged from cell culture flasks that had been processed to remove oligodendrocyte precursor cells and microglia.[254] Anti-GFAP immunostaining confirmed >98% purity of the astrocyte cultures. Astrocytes seeded onto uncoated surfaces adapted a typical stellate astrocyte morphology as shown with anti-GFAP immunostain in green (Figure 5.7A). Few astrocytes were observed on SBMA- and CBMA-coated surfaces. Additionally, the cells that were present took on circular

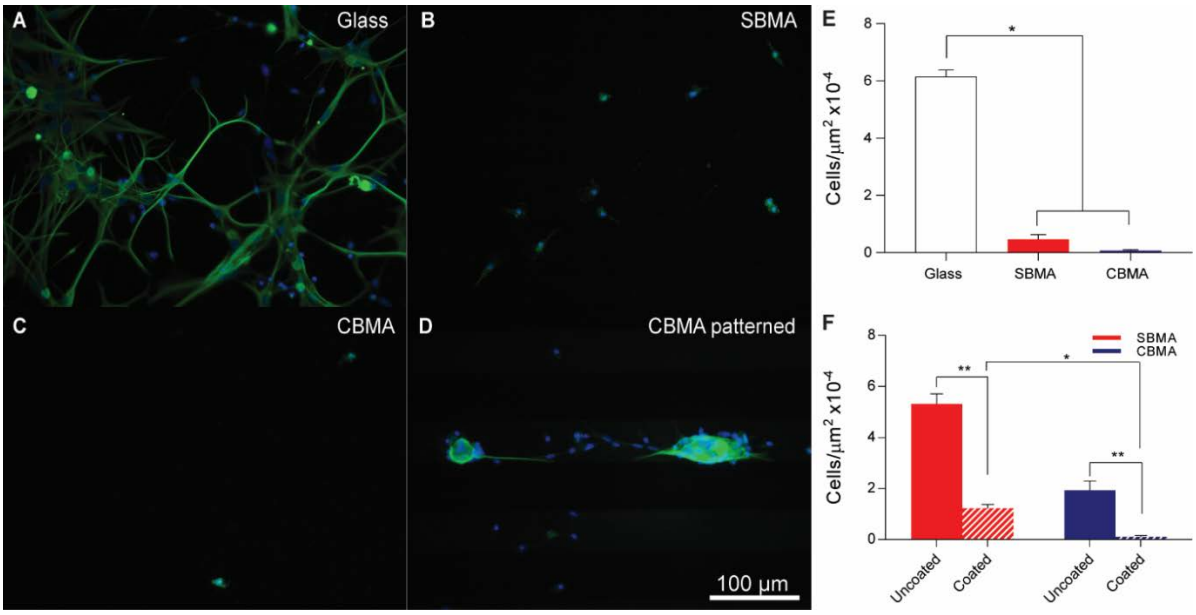

Figure 5.7. Representative epifluorescent images of astrocytes grown on (A) glass, (B) uniformly SBMA-coated, (C) uniformly CBMA-coated, and (D) CBMA-striped surfaces and immunostained with anti-GFAP antibody (green). Nuclei are labeled with DAPI (blue). E) Astrocyte cell density on uniformly coated surfaces. A significant difference was observed between the glass control and SBMA- and CBMA-coated surfaces (*$p < 0.001$ one way ANOVA). F) Astrocyte cell density on striped substrates, both on and off the zwitterionic pattern. A significant difference was determined between coated and uncoated regions for both SBMA- and CBMA-coated substrates (**$p < 0.001$ t-test). Cell density was shown to be statistically different between SBMA- (image not shown) and CBMA-coated stripes (*$p < 0.001$ one way ANOVA). Zwitterionic micropatterns used for striped substrates have a periodicity of 100 µm. Error bars represent standard error of the mean.

morphology with few cytoplasmic extensions (Figure 5.7B-C). Quantification of cell density on uniformly-coated surfaces revealed a 13 fold reduction in astrocyte density on SBMA-coated substrates verses plain glass substrates (Figure 5.7E). This effect was more pronounced than that seen with fibroblasts (Figure 5.6E) implying that astrocytes may be more sensitive than fibroblasts to SBMA. As observed for fibroblasts, the resistance to CBMA-coated substrates is even more pronounced with an astrocyte density decrease of over 90 times.

On SBMA-striped substrates a 75% reduction in astrocyte cell density was observed in coated stripes compared to uncoated regions (Figure 5.7F). The uncoated bands showed similar cell density to the uncoated controls implying that the presence of the stripes does not disrupt cell

adhesion to the bands. On the CBMA-striped sample, astrocyte cytoplasmic extensions were observed parallel to the pattern with few cytoplasmic extensions bridging across the striped pattern (Figure 5.7D). Cell density on CBMA-coated regions decreased about 20 fold in cell density as compared to the uncoated glass. Even though the magnitude of decrease was less for astrocytes when compared to fibroblasts, the cell density on CBMA-coated regions of the striped substrates was similar to that of uniformly-coated CBMA substrates. Astrocyte morphology was significantly altered on CBMA-striped substrates. On uncoated glass they exhibited a stellate shape, while on CBMA-striped substrates they became fusiform, failing to extend their cytoplasmic processes into coated regions.

5.4.3 Schwann Cell Adhesion and Alignment

Schwann cells are the principal myelinating cell type of the peripheral nervous system and function to support the growth and development of neurons.[255] It is therefore important to understand how these cells interact with zwitterion-coated substrates especially for potential neural prosthesis applications. Similar to the above-mentioned experiments, uncoated, SBMA- and CBMA-coated uniformly, and 100 μm periodicity (both SBMA and CBMA) substrates were examined for Schwann cell growth. Representative images of Schwann cells seeded onto these substrates are found in Figure 5.8A-D. Cell morphology on uncoated substrates was visibly different for SBMA- and CBMA-coated surfaces with cells spreading and interacting with adjacent cells (Figure 5.8A). Conversely, Schwann cells grown on SBMA-functionalized substrates appeared less dense and showed a rounded morphology (Figure 5.8B). Few cells were visible in CBMA-coated substrates with very little spreading (Figure 5.8C). Quantification of cell density on uniformly SBMA-coated substrates revealed more than a 40 fold decrease in Schwann cell density compared to uncoated substrates, a larger effect than seen for fibroblasts or

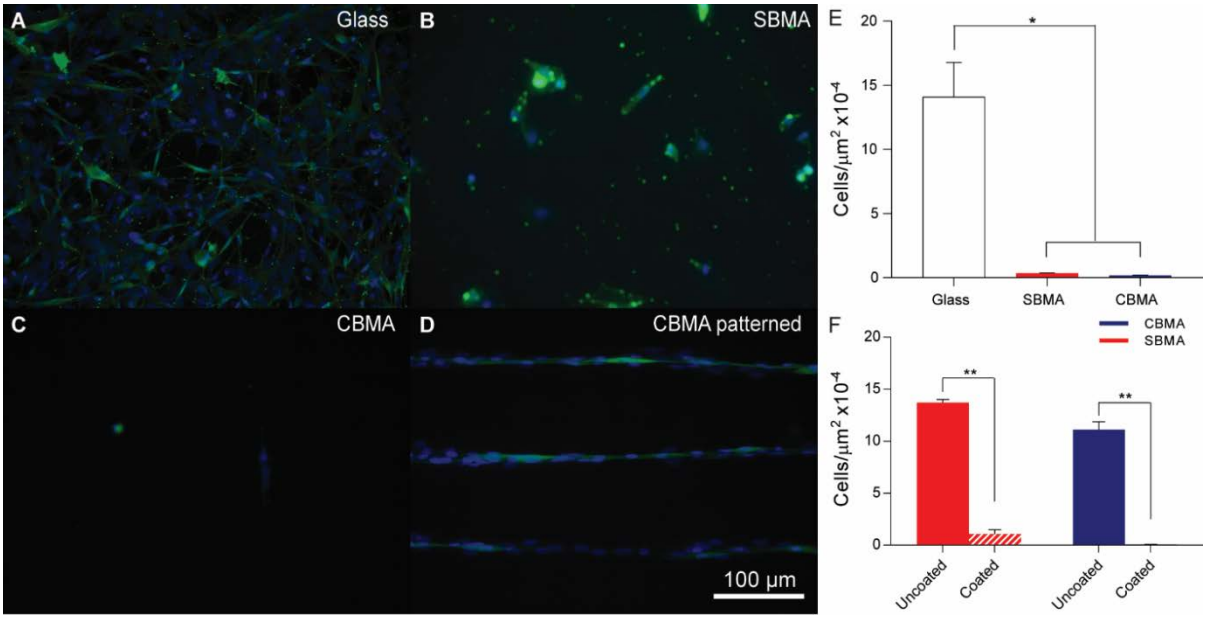

Figure 5.8. Representative epifluorescent images of Schwann cells cultured on (A) unmodified glass, (B) uniformly SBMA-coated, (C) uniformly CBMA-coated, and (D) CBMA-striped substrates and immunostained with anti-S100 antibody (green). Nuclei are labeled with DAPI (blue). E) Schwann cell density on uniformly coated substrates. A statistical difference was found between Schwann cells cultured on coated (both SBMA and CBMA) and uncoated (plain glass) surfaces (*$p < 0.001$ one way ANOVA). F) Schwann cell density on SBMA- and CBMA-striped substrates. Analysis of cell density showed significantly fewer cells adhered to both SBMA- and CBMA-coated stripes than the uncoated regions (**$p < 0.001$ t-test). Zwitterionic micropatterns used for striped substrates have a periodicity of 100 µm. Error bars represent standard error of the mean.

astrocytes. Similar to the findings with fibroblasts and astrocytes, CBMA-coated surfaces experienced more than double the reduction in cell density with over 80 times decrease in Schwann cell density on CBMA-coated substrates compared to uncoated controls.

Analysis of Schwann cell growth on patterned substrates showed similar results with a repulsion of cell adhesion on coated regions as opposed to uncoated areas. Schwann cells grown on substrates with both SBMA and CBMA stripes elongated parallel to the zwitterionic bands. Quantification of cell density on SBMA stripes showed a relatively modest 13 fold reduction in cell density on coated bands as opposed to uncoated bands, significantly less than for uniformly-coated substrates but still much greater than for most other cells. Conversely, on CBMA-striped

substrates, Schwan cell density decreased over 150 fold over coated regions compared to uncoated regions. This repulsion was even greater than that observed for uniformly-coated surfaces. While the CBMA-coated substrates yielded a larger decrease in cell density, both SBMA and CBMA polymer films showed a significant reduction when compared with the adjacent uncoated band ($p<0.001$, t-test).

Schwann cells provide trophic support to neurons, myelinate axons and guide axon regeneration when peripheral nerves are disrupted. Regenerating neural cells have been shown to closely align with Schwann cells in culture,[256,257] suggesting that the ability of our substrates to cause Schwann cell alignment might allow for control of axonal pathfinding. To determine the degree of Schwann cell alignment to striped substrates, Schwann cells were seeded onto 100 μm periodicity SBMA and CBMA stripes coated on glass. Alignment was evaluated by fitting an ellipse to the cell bodies using Image J software then measuring the angle of the long axis of the ellipse relative to the zwitterionic pattern (Figure 5.9A). An angle of 0° indicates the long axis of the cell was parallel to the pattern whereas an angle of 90°shows that the long axis of the cell was perpendicular to the pattern; a randomly oriented set of cells would be expected to yield an average angle of 45°. Representative images of Schwann cells grown on uncoated glass (Figure 5.8A), SBMA-striped (Figure 5.9A), and CBMA-striped (Figure 5.8C) substrates demonstrate the effectiveness of these patterns to induce alignment along the zwitterionic bands. Schwann cells grown on uncoated glass substrates were randomly oriented with a mean angle of about 42° (Figure 5.9B). By comparison, SBMA-patterned substrates were aligned parallel to the stripes with an average angle of less than 6 degrees. Cells on CBMA substrates were even more closely aligned to the stripes with an average angle of just under 2 degrees. The alignment of the Schwann cells appeared to occur because the cells were repelled by the zwitterionic stripes.

Schwann cells cultured on substrates with CBMA stripes almost never crossed into the zwitterionic regions forming distinct boarders between coated and uncoated areas (Figure 5.8D). Conversely, SBMA stripes were less effective at repelling cell adhesion and as such Schwann cells were observed forming bridges across zwitterionic bands. Thus, while SBMA appeared to strongly influence Schwann cell alignment, CBMA demonstrated a superior ability to direct growth.

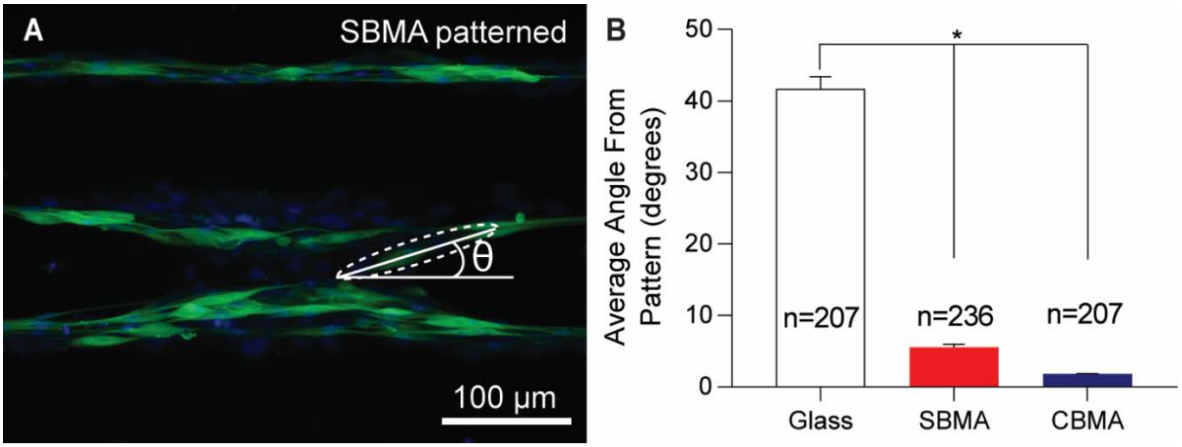

Figure 5.9. Representative image of Schwann cells cultured on 100 µm SBMA-striped substrates (A). Schwann cells elongate and extend between SBMA stripes occasionally forming bridges between SBMA bands. Cell alignment was determined by measuring the angle (θ) of an ellipse fitted to the major axis of the cell relative to the pattern. B) Average angle of Schwann cell alignment on uncoated and zwitterion-striped surfaces. A significant difference was found across all groups (* $p < 0.001$ one way ANOVA) with CBMA exhibiting the lowest average angle from the micropattern. The number inside or above each column represent the total number of cells evaluated. Cultures were immunostained with anti-S100 antibody (green). Nuclei are labeled with DAPI (blue). Error bars represent standard error of the mean.

5.4.4 SGN Neurite Alignment to Zwitterionic Micropatterns

Spiral ganglion neurons (SGNs) are the afferent neurons of the inner ear that innervate hair cells in the organ of Corti in the hearing ear. In deafened cochleae with a cochlear implant, SGNs are the target neural elements that are stimulated by cochlear implant electrodes. However, a number of factors (including scar tissue formation and distance between SGNs and cochlear implant electrodes) compromise the fidelity with which cochlear implants mimic native

hearing.[258,259] If patterned substrates affect the alignment of SGN neurites, these coatings may form the basis for an implant with an improved interface with its target neural elements. Accordingly, neonatal rat spiral ganglia were plated directly onto both plain glass and zwitterion-patterned substrates. Representative images of uncoated, SBMA-patterned, and CBMA-patterned samples are shown in Figure 5.10A-C. SGN neurite growth on uncoated substrates (Figure 5.10A) reveals random growth analogous to SGN neurites grown on glass and polymer substrates uniformly coated with laminin.[147,185,250] Alignment of SGN neurites along SBMA-coated substrates (Figure 5.10B) shows a preference to grow on the uncoated regions. However, neurites are occasionally observed crossing over SBMA-coated bands together with non-neuronal cells (nuclei depicted in blue) that have formed a bridge between SBMA-coated regions. Alignment of SGN neurites to CBMA-coated patterns revealed neurite segments that extend along the middle of the uncoated bands and almost never deviate from parallel patterns, in contrast to the occasional extension of a neurite across an SBMA-coated stripe.

To quantify alignment of SGN neurites to the zwitterionic patterns, alignment ratios were calculated by dividing the total length along the path of the neurite by the aligned length (T_L/A_L) as measured using the trace tool in Image J where the aligned length (A_L) is the distance the neurite travels in the direction of the pattern. Therefore, an alignment of 1 indicates perfect alignment while larger values indicate greater deviations from the parallel path. SGN neurites evaluated on glass showed an alignment ratio of over 2.2, whereas neurites on SBMA-striped substrates showed an alignment ratio of approximately 1.5. Neurites on CBMA-striped substrates exhibited an amazingly low alignment ratio of 1.09. A statistical difference was found between all samples groups ($p < 0.001$, one-way ANOVA). CBMA samples direct alignment almost perfectly to the pattern, while SBMA stripes also showed a noticeable effect on neurite

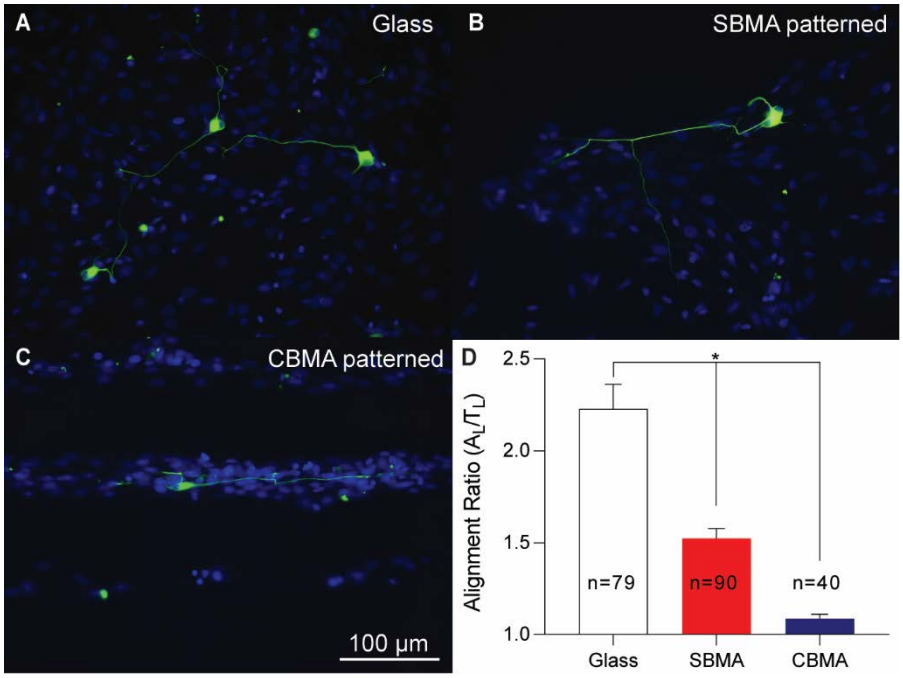

Figure 5.10. Alignment of SGN neurites on glass (A), SBMA-striped (B), and CBMA-striped (C) surfaces. Cultures were immunostained with anti-NF200 antibody (green) to label neurons. Nuclei are labeled with DAPI (blue). SGN neurites extend randomly on unpatterned glass substrates (A), but elongate and extend between SBMA (B) and CBMA (C) bands. D) Alignment ratios of SGN neurites grown on uncoated and zwitterion-striped surfaces. Quantification of alignment ratios confirms statistical difference between all groups (* $p < 0.001$ one way ANOVA). CBMA-coated surfaces exhibited the strongest alignment. The number inside or above each column represent the total number of neurites measured. A periodicity of 100 µm was used for patterned samples. Error bars represent standard error of the mean.

alignment. Previous experiments in our lab have shown similar alignment ratios of SGN neurites grown on polymer microchannels and demonstrate the efficacy of these zwitterionic patterns compared to previously studied substrates with physical microtopographical patterns.[147] These results suggest that zwitterionic coatings may be used to not only reduce undesirable cell adhesion, but also could be used to guide neurite extension toward a target such as a neural prosthetic device. Similarly, photopatterning could allow for directed fibroblast or glial adhesion and growth in circumstances where patterning of these cells is desirable.

5.5 CONCLUSIONS

Engineering surfaces that prevent the nonspecific adsorption of protein to biomedical implant surfaces may allow significant mitigation of fibrosis and directing of cell growth. Accordingly, we described a facile photopolymerization method to covalently graft two zwitterionic polymers from glass surfaces. These zwitterionic polymer thin films showed increases in surface composition with increasing solution concentration as measured by XPS. Nonspecific protein adsorption and contact angle also decreased sharply at solution concentrations much lower than the saturation observed using XPS indicating that a very thin coating of zwitterionic polymer is needed to induce significant changes in surface properties. We also directly compared the ability of SBMA- and CBMA-coated surfaces to reduce adsorption of fibrinogen and adhesion of various cell types. Fibroblasts, astrocytes, and Schwann cells all showed dramatic decreases in cell density on SBMA- and CBMA-coated surfaces as compared to uncoated substrates. Fibroblasts, the primary cell type in fibrotic tissue also exhibited a significant difference in cell density between SBMA- and CBMA-coated surfaces, with CBMA-coated systems showing orders of magnitude decreases in adhesion. Using the inherent spatial control of photopolymerization, zwitterionic parallel line patterns were generated to evaluate the cellular adhesion of coated compared to uncoated glass regions. All cell types grown on patterned substrates showed elongation along the both the SBMA and CBMA bands. However, CBMA stripes showed fewer cell crossings along the pattern and greater cellular repulsion along film edges. Alignment of Schwann cells and SGN neurites was evaluated on both SBMA and CBMA surfaces with CBMA directing alignment to a greater extent for both cell types. Therefore, CBMA-coated surfaces demonstrated a superior ability to resist cell adhesion and to direct cell growth. The described photopolymerizable surfaces enabled investigation of cell-material interactions that could enable engineering of surfaces that resist fibrotic tissue

formation. Additionally, generated micropatterns provide potential in directing regeneration of neurites for neural prosthetic development.

CHAPTER 6: ANTI-FOULING PHOTOGRAFTABLE ZWITTERIONIC COATINGS ON PDMS SUBSTRATES

6.1 ABSTRACT

The foreign body response (FBR) to implantable materials can negatively impact performance of medical devices such as the cochlear implant. Engineering surfaces that resist the FBR could lead to enhanced functionality including potentially improving outcomes for cochlear implant recipients through reduction in fibrosis. In this work, poly(dimethyl siloxane) (PDMS) surfaces were coated with two zwitterionic polymers, sulfobetaine methacrylate (SBMA) and carboxybetaine methacrylate (CBMA), using a photografting process to reduce nonspecific protein adsorption, the first step of the FBR. The coating process uses benzophenone, a photografting agent and type II photoinitiator, to covalently link the crosslinked zwitterionic thin film to the PDMS surface. As the concentration of benzophenone on the surface increases, the adhesive strength of the zwitterionic thin films to PDMS surfaces also increases as determined by shear adhesion. Interestingly, significantly lower levels of nonspecific protein adsorption on zwitterion-coated samples compared to uncoated controls was observed. Fibroblast adhesion was also dramatically reduced on coated substrates. These results suggest that fibrosis may be prevented using this novel coating method for implanted materials.

6.2 INTRODUCTION

Implantable medical devices including pacemakers, myringotomy tubes, joint replacements, and neural prosthetics have dramatically increased quality of life over the past several decades. The function of many of these implants is significantly limited by the formation of fibrotic tissue (fibrosis) around the devices[60,80,260] that occurs weeks to months after implantation.[16] Fibrosis is particularly problematic for neural prosthetic devices as it impedes the

transmission of electrical current between stimulating electrodes and the target neurons.[261] For example, fibrotic tissue formation in the scala tympani is an expected consequence of cochlear implantation but is detrimental to hearing outcomes.[262,263] A foreign body response (FBR) occurs with an initial inflammatory response that progresses to fibrosis that encapsulates the implant.[67] Fibrotic capsule formation around the electrode array increases electrical impedance, necessitating use of higher current thresholds resulting in increased current spread. More recently intracochlear fibrosis in response to the implanted electrode array has been linked to loss of residual acoustic hearing in the implanted ear.[60] Other neural prostheses and implanted medical devices face similar challenges to the FBR.

The initial step in the FBR is nonspecific adsorption of protein to device surfaces.[54] Mitigation of protein adsorption to reduce fibrosis has recently become an active area of research. Traditional anti-fouling materials are uncharged hydrophilic polymers, such as poly(ethylene glycol) (PEG) or hydroxyethyl methacrylate (HEMA). However both still allow some degree of protein adsorption and ultimately induce a fibrotic response.[16] Zwitterionic polymers, such as carboxybetaines and sulfobetaines, have emerged as a new class of anti-fouling materials. These polymers are generated from monomers that have a positively charged group and a negatively charged group on the same repeat unit. A unique aspect of these materials is that they are hydrophilic yet retain a net neutral charge. It has been proposed that charged groups on the zwitterionic repeat units tightly bind water molecules, forming a layer of hydration that makes displacement of the water energetically unfavorable, resulting in significantly reduced protein and other biomolecule adsorption.[66,99] Zwitterionic polymers have shown promise in a variety of applications including glucose sensing in blood serum,[58,113] antigen detection in complex media,[115] and prolonging the blood circulation time of coated drugs,[6] among others.[89]

Importantly, zwitterionic polymers have shown resistance to cell[111,227] and bacterial[170,172] adhesion *in vitro* in addition to mitigating the FBR *in vivo.*[80] Thus, zwitterionic polymers are ideally suited for coating implantable materials.

Many implantable devices utilize poly(dimethyl) siloxane (PDMS), a highly flexible, chemically inert, and easy to fabricate material used in urinary catheters and to house cochlear implant electrode arrays.[228,264] While this silicone-based polymer is not toxic to cells, the hydrophobic surface is especially prone to protein adsorption, resulting in a significant FBR and ultimate formation of a fibrotic capsule. Therefore, durable zwitterionic materials for coating PDMS surfaces have the potential to significantly reduce the FBR to implantable materials and improve implant quality and longevity. Silane coupling agents have previously been used to graft zwitterionic polymer brushes onto the surface of PDMS which involves plasma/O_3 treatment of the material followed by grafting a reactive group to the surface.[72,73] For example, Jiang et al. functionalized the surface of PDMS with an atom transfer radical polymerization (ATRP) initiator using O_3 treatment followed by application of a silane coupling agent to generate carboxybetaine methacrylate (CBMA) polymer brushes showing dramatic reduction in protein adsorption.[73] Further, Huang and coworkers immobilized a zwitterionic silane coupling agent with a sulfobetaine group onto a silicone substrate which showed resistance to protein, cellular, and bacterial adhesion.[72]

Another potential approach would be to use a photochemical process to graft zwitterionic polymers to the surface of PDMS. Research has shown that a type II photoinitiator, such as benzophenone (BP), can be adsorbed to a polymer surface followed by irradiation with UV light. The type II photoinitiator, is excited with the light to a highly reactive diradical state when a photon is absorbed which thenabstractis hydrogen from the grafting surface, producing a radical

that allows polymerization to occur from the surface.[199] Using this method, polymers can be covalently grafted from a variety of polymeric surfaces including PDMS. Furthermore, this approach also offers the inherent spatial and temporal control of photopolymerization. For example, Ishihara et al. grafted phosphoryl choline methacrylate polymerized from PDMS surfaces demonstrating decreased contact angles and reduced protein adsorption.[200]

In this work, we describe development of a process to form and graft a durable crosslinked coating for PDMS surfaces that resists protein, biomolecule, and cell adsorption to mitigate FBR. Our approach uses a one-step photoinitiated grafting process to covalently link sulfobetaine methacrylate (SBMA) and carboxybetaine methacrylate (CBMA) crosslinked polymers to PDMS. The relationship between the amount of BP adsorbed on the surface and the concentration of the BP in the feed was examined. The role of BP concentration on adhesion/delamination from the PDMS substrate was characterized by scanning electron microscopy (SEM). The durability of the grafted thin films is evaluated using a shear adhesion test for as prepared and swollen samples. The anti-fouling properties of the grafted surfaces are also tested using protein adsorption. To demonstrate the efficacy of these materials to resist the FBR, cell density of fibroblasts cultured on these substrates was measured. Finally, the resistance of the SBMA- and CBMA-coated PDMS to bacterial adhesion was evaluated using two strains of bacteria. These findings demonstrate that durable zwitterionic polymers can be rapidly grafted to implant materials to improve the anti-fouling properties of existing implant materials.

6.3 EXPERIMENTAL

6.3.1 Materials and Synthesis

2-(N,N'-dimethylamino)ethyl methacrylate (DMAEM), β-propiolactone, triethyl amine, hydroquinone, [2-(Methacryloyloxy)ethyl]dimethyl-(3-sulfopropyl)ammonium hydroxide

(SBMA), benzophenone (BP), poly(ethylene glycol) diacrylate (PEGDA, MW 575), paraformaldehyde, collagenase, Dulbecco's modified eagle medium (DMEM), human fibrinogen, human anti-fibrinogen, and all organic solvents were purchased from Sigma Aldrich. 1-[4-(2-hydroxyethoxy)-phenyl]-2-hydroxy-2-methyl-1-propane-1-one (HEPK, photoinitiator) was purchased from Ciba. Alexa 488 labeled phalloidin and Alexa 488 conjugated goat anti-rabbit secondary antibody were purchased from ThermoFisher Scientific (Waltham, MA). Hank's balanced salt solution (HBS), fetal bovine serum (FBS), poly-L-ornithine, trypsin-EDTA dissociation reagent, DAPI-containing mounting medium, were purchased from Gibco (Carlsbad, CA).

2-Carboxy-N,N-dimethyl-N-(2'-(methacryloyloxy)ethyl)ethanaminium inner salt (carboxybetaine methacrylate,CBMA) was synthesized as previously described.[111] Briefly, β-propiolactone was added to 10 mL of acetone. The solution was then added dropwise to DMAEM dissolved in acetone at 0^{o} C. The reaction was stirred overnight, after which a small amount of hydroquinone (radical inhibitor) was added. The solvent was removed under reduced pressure with the residual oil dissolved in methanol. Triethylamine was added to the solution to quench any side reactions and the CBMA product was precipitated into cold diethyl ether and vacuum filtered to yield a white solid. The product was then used without further purification. NMR spectra were collected on a Bruker Spectrometer (Avance 300) to confirm chemical structure. 1H NMR (D_2O, 300 MHz), δ 6.06 (s, 1H, =CH), δ 5.68 (s, 1H, =CH), δ 4.55 (t, 2H, OCH_3), δ 3.70 (t, 2H, NCH_2), δ 3.59 (t, 2H, NCH_2), δ 3.10 (s, 6H, NCH_3), δ 2.64 (t, 2H CH_2COO), δ 1.84 (s, 3H $=CCH_3$).

6.3.2 Zwitterion-functionalized PDMS Substrate Fabrication and Characterization

PDMS substrates were fabricated using Sylgard 184 (Dow Corning) by thoroughly mixing 10 parts base to 1 part curing agent. For shear adhesion tests the mixture was cured in an aluminum mold with 4 mm depth and 8 mm width. All other samples were cured in Petri dishes. The PDMS was cured by heating to 80^{o} C for 2 hrs. Once the samples cooled, slabs in the aluminum molds were cut to approximately 25 mm long strips. Samples cured in Petri dishes were cut into 15 mm x 15 mm squares. To allow photografting, PDMS was coated with BP by submersing in a solution of BP in acetone (0.01 to 50 mg/mL) for 1 hr. The BP-coated samples were removed and dried in a nitrogen stream to remove solvent then dried in a vacuum for 1 hr. The BP-coated PDMS slabs were kept in a sealed container until directly before film grafting and polymerization.

The concentration of BP adsorbed onto PDMS surfaces was determined using UV/Vis measurements. Coated samples were sonicated in an ethanol solution for 30 min to remove the adsorbed BP. The concentration of BP in the ethanol solution was then determined from UV/Vis absorbance at 253 nm as compared to a calibration curve of known concentrations. The calibration curve showed excellent linearity (R^2=0.9989) and all BP concentration measurements were evaluated within the calibrated concentrations.

The process for photografting the zwitterionic polymers to PDMS is shown in Figure 6.1. Zwitterionic polymers were generated from solutions containing 50 wt% SBMA or CBMA, 2.5 wt% poly(ethylene) glycol diacrylate (PEGDA, crosslinker), 1 wt% 1-[4-(2-hydroxyethoxy)-phenyl]-2-hydroxy-2-methyl-1-propane-1-one (HEPK, photoinitiator), and 46.5 wt% water. To

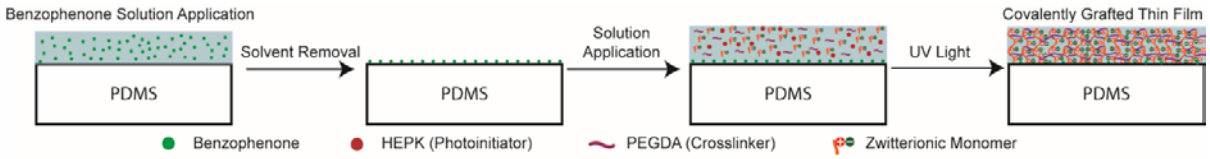

Figure 6.1. Schematic of the photografting process. UV-light is used to initiate polymerization and grafting of zwitterionic monomers from the PDMS surface forming a polymer thin film hydrogel covalently attached to the material substrate.

test the adhesion of the zwitterionic thin films to the PDMS substrate, 2.5 µL of monomer solution was pipetted onto a glass substrate, the PDMS was placed on top, and capillary action dispersed the solution evenly between the glass and PDMS to form a 8 mm x 8 mm contact area. The solution was then polymerized using a mercury vapor arc lamp (Omnicure S1500, Lumen Dynamics, Ontario, Canada) at 30 mW/cm^2 measured at 365 nm for 10 min Standard 2.54 x 7.62 cm glass microscope slides used for shear adhesion experiments were functionalized with a silane coupling agent, (3-(trimethoxysilyl)propyl methacrylate) as previously described.[147] The coupling agent contains a reactive methacrylate group which forms a covalent bond between the glass substrate and the crosslinked film upon polymerization. Shear adhesion of as prepared samples was measured directly after polymerization with a dynamic mechanical analyzer (DMA; Q800 DMA TA instruments). Swollen samples were immersed in deionized water for 48 hrs prior to testing. The adhered glass and PDMS samples were fractured in the DMA using a controlled force ramp rate of 0.5 N/min at room temperature. The force at break was recorded and normalized to the area of adhesion to the glass substrate.

Thickness of the zwitterion-coated thin films were measured using scanning electron microscopy (SEM, S-4800, Hitachi). Zwitterion-coated PDMS substrates were cut and mounted vertically on specimen stages. Prior to imaging, samples were sputter coated with gold. Electron accelerating voltage was set at 2.0 kV.

6.3.3 Protein Adsorption

Immunofluorescence was used to measure protein adsorption to substrates. The PDMS and zwitterion-coated samples were hydrated overnight in PBS (room temperature) prior to protein exposure. Human fibrinogen (1 mg/mL) was pipetted onto substrates and dispersed by placing a glass coverslip on the solution followed by a 1 hr incubation at room temperature. The samples were then soaked in PBS for 3 hrs, changing the PBS hourly. After rinsing, the samples were incubated in a blocking buffer solution to block the areas unoccupied by fibrinogen for 1 hr at room temperature. An anti-fibrinogen antibody (dilution 1:500) was applied to the samples overnight at 2^{o} C. The substrates were then immersed in PBS for 45 min with the solution PBS being exchanged every 15 min. The samples were incubated with Alexa 488 conjugated secondary antibody (dilution 1:1000) for 1 hr at room temperature. The samples were then again rinsed in PBS for 45 min with the PBS, changing the PBS every 15 min and coverslips were applied before epifluorescent imaging. Digital epifluorescent images were captured on a Leica DMIRE2 microscope (Leica Microsystems, Bannockburn, IL) with Leica DFC350FX digital camera and Metamorph software (Molecular Devices, Silicon Valley, CA). Gray-scale images were used to measure relative fluorescence intensity using Image J software (NIH, Bethesda, MD). All conditions were repeated in triplicate, and five representative images were used for analysis at each condition.

6.3.4 Cell Culture and Density Quantification

All cell/bacterial culture and quantification was conducted by Dr. Marlan Hansen's research group at the University of Iowa. Dissociated fibroblast cultures were obtained from p4-7 perinatal rat skin as previously described.[204] The tissue was scraped to remove subcutaneous fat, morcellized, then digested in 0.125% trypsin with EDTA and 0.2% collagenase for 1 hr at 37^{o}C.

Enzymatic dissociation was stopped with FBS and the cell suspension was spun, rinsed twice, then triturated. The resultant suspension was then seeded into poly-L-ornithine and laminin coated culture flasks. Fibroblasts were maintained in DMEM with 10% FBS, splitting the cells when cultures became confluent but not splitting more than twice prior to use.

Prior to seeding onto experimental substrates the fibroblasts were dissociated from the culture plastic. A cell suspension with a density of $1x10^7$ cells/mL was created. In all cases 0.5 mL of suspension was plated onto substrates. These cultures were maintained for 48 hrs prior to fixing with 4% paraformaldehyde in PBS. All samples were then labeled with Alexa 488 conjugated phalloidin (0.165 μM for 30 min) followed by three washes with PBS. Coverslips with DAPI-containing mounting medium were placed onto the stained cultures to label nuclei.

Cell density was determined by counting the total number of nuclei from digital images of randomly selected 20x microscopic fields using the cell counting feature of MetaMorph software package. At least 10 images were taken for each culture, with at least 3 substrates per experiment. All experimental conditions were repeated in triplicate.

6.3.5 Bacterial Ahesion

The silastic samples were divided into 4 groups: uncoated, SBMA, and CBMA with or without FBS. The samples were first sterilized by exposing UV light for 15 min. Groups with FBS were incubated with FBS for 1 hr at 37°C, and then washed with PBS 3 times. The bacterial suspension at 10^8 CFU per ml (*S. aureus* and *S. epidermidis*) was incubated with the samples for 48h at 37°C. The samples were rinsed 3 times with PBS after 24 hrs of incubation and were then re-inoculated and incubated an additional 24 hrs. At the conclusion of the incubation period, all samples were washed 3 times with PBS then the GFP signal was visualized using the

epifluorescent microscope. Ten random fields of view at 20X were chosen, and the bacterial colonies on the surface were counted by hand.

6.3.6 Statistics

Statistical analysis was conducted using Graphpad Prism 7.01 software. To compare cell density between uncoated, CBMA-coated, and SBMA-coated, a one-way ANOVA with *post hoc* Tukey test was used.

6.4 RESULTS AND DISCUSSION

6.4.1 Surface-initiated Zwitterionic Graft Polymerization

Engineering coatings for existing implantable material may represent a practical and quickly implemented approach to mitigating FBR without compromising the inherent mechanical properties. Because the surface is the only portion of a device that will come into direct contact with host fluids and tissues, functionalizing the substrate with a zwitterionic polymer thin film (<25 µm) may significantly reduce the FBR. Introducing hydrophilic polymers (poly(ethylene glycol) (PEG) or zwitterionic polymers) onto the surface of hydrophobic materials such as PDMS or other polymers may prevent the accumulation of proteins, other biomolecules, and cells on the surface.[74,200]

In this work, sulfobetaine methacrylate (SBMA) and carboxybetaine methacrylate (CBMA) were examined as photograftable monomers due to their excellent anti-fouling properties including ultra-low protein adsorption and cell adhesion.[76,265] SBMA and CBMA contain a methacrylate group which can be polymerized through a radical chain polymerization mechanism. To engineer a durable zwitterionic coating, poly(ethylene glycol) diacrylate (PEGDA), a crosslinking molecule, was incorporated into the formulation. The crosslinker allows the zwitterionic polymer to form a covalent network, which enables thicker film

fabrication and is more resistant to shear forces. These formulations were photografted to poly(dimethyl siloxane) (PDMS), which is used extensively in implantable devices such as orthopedics, shunts, and catheters.[28] To covalently graft the SBMA and CBMA thin films to PDMS substrates, a photografting process was used. Benzophenone (BP), a type II photoinitiator, can be applied to substrates to covalently photograft (meth)acrylates to a variety of polymers.[199] Adsorbing BP onto the surface of PDMS enables photografting/polymerization reaction resulting in covalent grafting to the substrate. Type II photoinitiators are excited to a short-lived singlet state by absorption of UV light which is quickly transformed to a triplet state.[266] This highly-reactive triplet state initiates the grafting process by abstracting aliphatic hydrogens from the substrate and transferring the radicals to the surface. After this step, polymerization is initiated from the surface and covalently bonds the polymer chain to the substrate (See Figure 6.2). A second water-soluble photoinitiator is added to the solution that also initiates polymerization in the bulk. Thus, initiation of polymerization simultaneously occurs in the bulk and at the surface to graft the film to the surface and form a strongly adhered thin film in a single step. One major advantage of this grafting mechanism is that it is effective for nearly all polymer surfaces because most polymers contain aliphatic hydrogens which can be abstracted to initiate polymerization.[267]

The ability of BP to abstract hydrogens from the surface plays a critical role in the process of grafting zwitterionic networks to PDMS surfaces. PDMS substrates were submersed in a BP/acetone solution with varying feed concentrations. Concentrations of 0.25 to 50 mg/mL were used to adsorb different amounts of BP on the surface required to effectively graft the zwitterionic polymer to the PDMS. After submersion in the BP solution and subsequent drying under vacuum, the coated samples were sonicated in an ethanol solution for 30 min to remove all

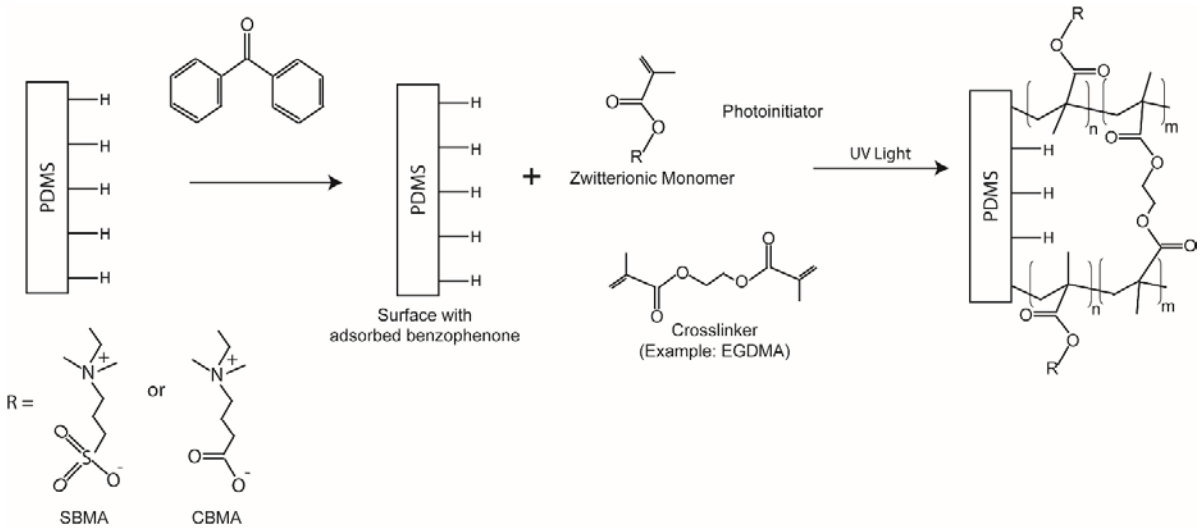

Figure 6.2. Schematic representing the basic chemistry of the photografting process. Benzophenone (BP) adsorbed on the substrates initiates covalent grafting and polymerization of the polymer to the PDMS.

adsorbed BP. The solution concentration was quantified by comparing absorbance of the BP at 253 nm to a calibration curve of known concentration via UV/Vis spectroscopy. The relationship between feed BP concentration and amount of BP physically adsorbed to the PDMS surface is shown in Figure 6.3. As the feed concentration increased, the amount of adsorbed BP increased by several orders of magnitude, ranging from just under 1 μg/cm^2 to over 500 μg/cm^2.

At concentrations above 50 mg/mL BP visible crystals started to form on the surface and as such were not used in thin film preparation. These findings demonstrate that the surface concentration of BP can be controlled by altering the feed concentration of BP. By changing the surface concentration of BP, the amount of initiation occurring at the surface is likely to change which will alter the degree of photografting to the surface.

6.4.2 Characterization of the Photografted Zwitterionic Polymer

To understand the dependence of the photografting process on the concentration of adsorbed BP, SBMA and CBMA thin films were photopolymerized onto PDMS substrates using feed concentrations as above. SBMA- and CBMA-grafted thin films were fabricated by

sandwiching 2.5 µL of zwitterionic monomer solution between a piece of methacrylate-functionalized glass and an 8 mm wide PDMS sheet. Capillary action allowed the monomer to disperse evenly between the two substrates. After polymerization, the glass slide was removed leaving a crosslinked thin film that may be covalently grafted to the PDMS substrate (Figure 6.1). SBMA- and CBMA-coated PDMS substrates were sliced and then imaged using scanning electron microscopy (SEM) to reveal cross-sectional images of the adhesion.

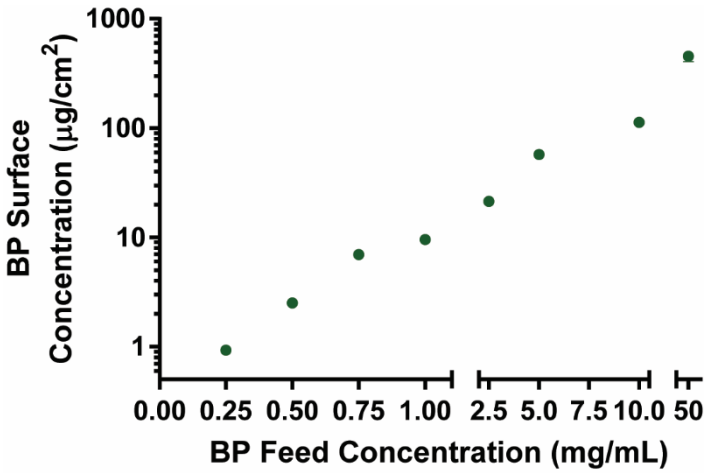

Figure 6.3. Quantification of BP surface concentration with respect to BP feed concentration. The surface concentration increases with increasing feed concentration.

At concentrations at or less than 2.5 mg/mL, the SBMA and CBMA polymers began to peel from the PDMS substrate as shown by SEM images in Figure 6.4A-B. While the polymer remained attached to the substrate after preparation, it only weakly adhered and could be easily removed. At these concentrations, insufficient covalent bonds were formed from the photografting reaction to create strong adhesion between the film and the surface, causing delamination after short-term use. As the amount of BP adsorbed onto the surface was increased, both the SBMA- and CBMA-coated surfaces demonstrated stronger adhesion to the PDMS, with no delamination observed as shown in Figure 6.4C-D. At higher BP solution concentrations, and thus greater available BP at the surface, the number of surface radicals generated upon illumination increases, allowing more covalent bonds to form between the substrate and the

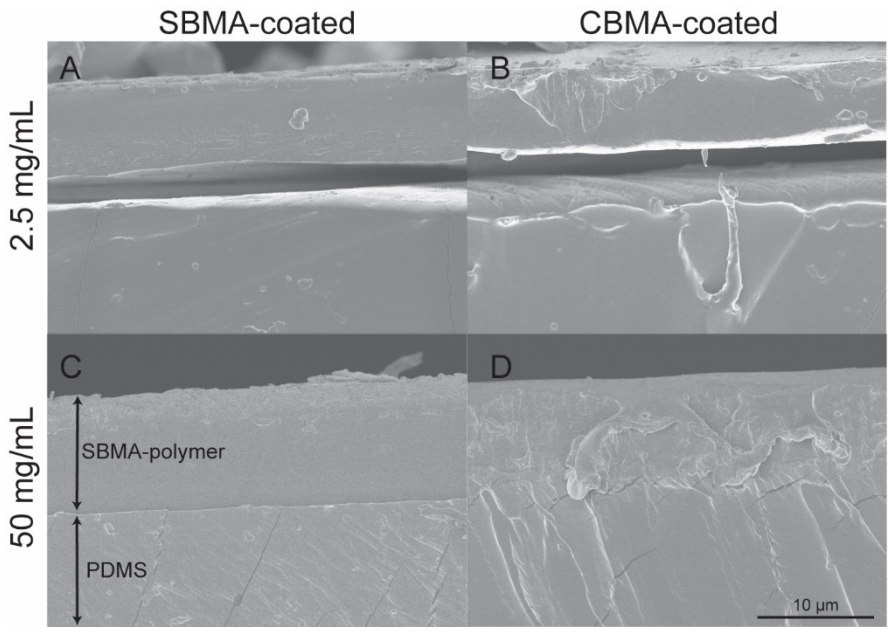

Figure 6.4. SEM images of photografted zwitterionic polymers. Shown are SBMA-coated PDMS using A) 2.5 and C) 50 mg/mL BP feed concentration and CBMA-coated PDMS using B) 2.5 and D) 50 mg/mL BP feed concentration.

polymer chains in the thin film. A greater number of covalent bonds between the zwitterionic thin film and the PDMS prevents film delamination. At higher concentrations of BP (10 or 50 mg/mL), delamination from the substrates was not observed during subsequent substrate testing, suggesting that these concentrations are more appropriate for further testing.

Additionally, the thicknesses of both the SBMA and CBMA films prepared as outlined were measured using SEM imaging. SBMA-coated samples were 7.3 (±2.8) µm thick while CBMA-coated samples were similarly 7.5 (±1.7) µm thick. Interestingly, the thickness of the thin films was independent of the surface concentration of BP. Because of the fabrication process, the thin film thickness is dictated by the amount of monomer in contact with the surface. A crosslinked network is formed upon polymerization, which will gel the monomer on the PDMS substrate. Thus, it is reasonable that no changes in thickness were observed with different concentrations of benzophenone as the concentration and amount of monomer solution did not

change. If desired, film thickness could easily be changed by increasing or decreasing the amount of monomer solution contacting the surface during polymerization.

To quantitatively assess the adhesion of the SBMA- and CBMA-grafted polymers to PDMS surfaces, shear adhesion to the PDMS was measured. This test evaluated how the materials responded to shear by measuring the force at which failure occurs along a plane parallel to the direction the force was applied. The strength of the bond between the thin film and the substrate is estimated by measuring the maximum force per unit area required to fracture the sample or delaminate the coating. Samples that require more force per unit area indicate stronger adhesion to the substrate. Figure 6.5 illustrates how this method was used to evaluate the adhesion of the zwitterionic polymers to the PDMS substrates. A solution of zwitterionic monomer (SBMA or CBMA), crosslinker (PEGDA, MW 575), and photoinitiator (HEPK) in aqueous solution was applied to a functionalized glass surface. A PDMS substrate was then placed on top of the liquid and capillary action was used to disperse the solution evenly between the substrates. The glass used was functionalized using a methacrylated silane coupling agent to ensure adhesion between the polymer and the glass.

As the bond between the glass and polymer is much stronger than what would be expected from the hydrogel coating or the adhesion between the coating and PDMS substrate, three potential modes of failure could occur using this method: 1) substrate/backing failure, 2) adhesive failure, and 3) cohesive failure. Substrate failure occurs when the substrate fractures, and indicates that the substrate is weaker than the forces from either adhesive or cohesive bonds from the coating. This type of failure would indicate a high degree of adhesion and high cohesive strength of the adhesive relative to the mechanical strength of the substrate. Adhesive failure occurrs when the bond between the substrate and the adhesive is broken. The forces exerted on

the connection are greater than the forces created between the substrate and the adhesive, which cause the adhesive to peel from the substrate (see left image in Figure 6.5). When failure of this type is observed, it often indicated relatively low levels of adhesion between the substrate and the adhesive. Finally, cohesive failure occurs when the bonds within the adhesive brake because the external force exceeded the cohesive bond (see right image in Figure 6.5). When this failure is observed, the adhesive is strongly adhered to the substrate, but the mechanical strength of the adhesive may have been relatively weak.

For the system in study, cohesive and adhesive failure were the only types observed due to the relatively high strength of the glass and PDMS compared to the zwitterionic crosslinked hydrogel. Further, adhesive failure would indicate that the grafted polymer was only weakly bonded to the PDMS. Adhesive failure between the glass and the zwitterionic polymer was never observed. The surface methacrylate groups provided a high degree of covalent grafting between the zwitterionic polymer and the glass which was stronger than the cohesive strength of the films. The strong bond between the zwitterionic thin film and the glass ensured that measurements would only measure failures between the PDMS and thin film or failures within the thin film.

Shear adhesion strength was examined for SBMA and CBMA grafted polymers that were either tested without further treatment after photografting (as prepared) or swollen to equilibrium in water. The zwitterionic hydrogels were fabricated with 50% water from the polymerization solution, but will absorb additional water. Upon swelling, the hydrogel thin films increased in volume inducing changes in mechanical properties. As fully swollen thin films more closely approximates *in vivo* conditions, it was important to identify changes in adhesion properties in the fully hydrated state. The same BP feed concentrations were evaluated to assess the role of BP

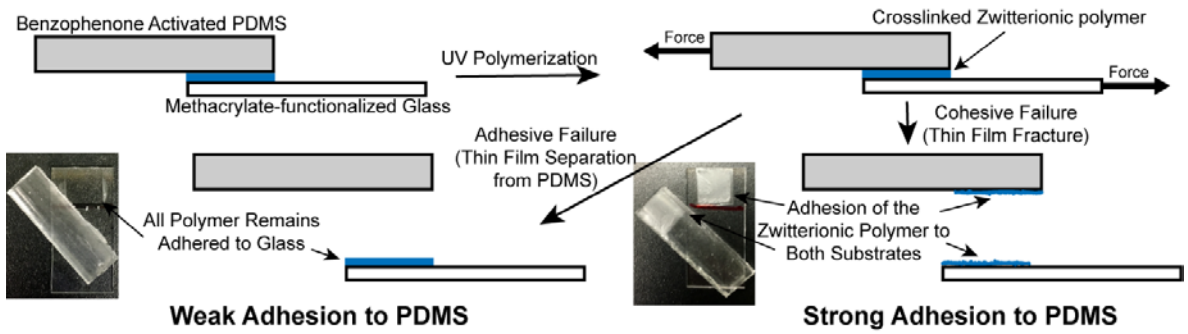

Figure 6.5. Schematic representing shear adhesion experiments. A benzophenone activated sample was covalently bound to methacrylate-functionalized glass by photografting/photopolymerizing the zwitterionic polymer between substrates. The samples were strained until fracture by applying a force to both ends of the substrates. The samples showed either adhesive failure (left image), where the polymer remains adhered to the glass, or cohesive failure (right image), where the film itself fractures yet remains adhered to both substrates.

in the photografting process. Examination of shear adhesion strength data as a function of BP concentration is shown in Figure 6.6. For as prepared SBMA-coated samples, an upward trend in maximum force per area is observed as BP feed concentrations were increased as would be expected with fewer covalent bonds formed during the photografting/polymerization process (Figure 6.6A). For BP feed concentrations below 2.5 mg/mL, adhesive failure between the PDMS and SBMA thin film was observed. At or above 2.5 mg/mL, cohesive failure occurred indicating a critical amount of BP is on the surface and therefore sufficient covalent bonds have formed to prevent delamination. Swollen SBMA samples follow a similar trend, but require less force per area to fracture. It is important to note that many of the samples below 2.5 mg/mL fractured adhesively before sample loading and were recorded as 0 N/m^2. Similar to the as prepared samples, at and above 2.5 mg/mL cohesive failure was observed. As the thin films absorbed water, the modulus and force required for fracture decreased even when cohesive failure was observed. When cohesive failure occurred, the force required to fracture the thin film was measured rather than force required to overcome adhesion between the PDMS and

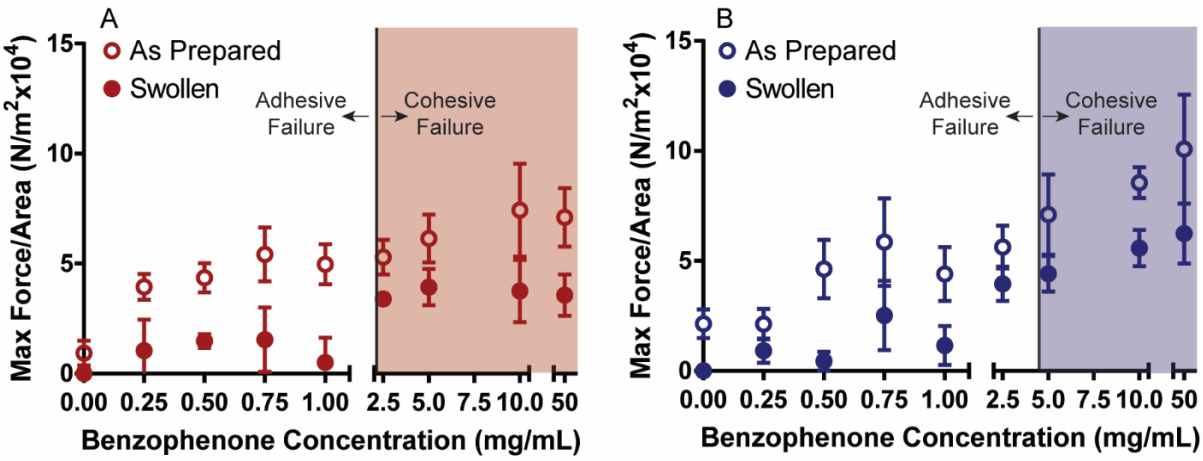

Figure 6.6. Maximum force per area results as measured using shear adhesion experiments as a function of BP feed concentration for zwitterion-grafted thin films to PDMS substrates. A) Shear adhesion test data for SBMA-grafted thin films. B) Shear adhesion results for CBMA-coated PDMS. Max force per area increases with increasing BP feed concentration. Shaded area represents samples that failed cohesively.

zwitterionic thin film. Therefore, no significant changes in maximum force per area were observed above concentrations where cohesive failure was recorded.

Adhesion of the CBMA thin films to PDMS followed a similar trend to the SBMA. For as prepared samples, the maximum force per area required to fracture the samples increased with increasing BP concentrations (Figure 6.6B). While the general trend was the same, cohesive failure was not observed until BP feed concentrations were greater than or equal to 5 mg/mL. CBMA swollen samples were very similar to the SBMA below 2.5 mg/mL, with many of the samples failing before testing. A decrease in maximum force per area was also evident compared to the as prepared samples across all concentrations, even when cohesive failure was observed. It is notable that the CBMA hydrogels in general exhibited higher maximum force per area values than SBMA at higher feed concentrations. This increase is likely due to the fact that CBMA forms a higher modulus hydrogel than SBMA.[112,114] At concentrations where cohesive failure was observed, the cohesive strength of the CBMA thin film was measured; as expected the maximum force required to cause failure was higher for CBMA than for SBMA. These findings

demonstrate that the adhesion of the crosslinked zwitterionic films increases with higher BP surface concentrations and that durable bonds can be formed between the PDMS and the hydrogel films.

6.4.3 Cell and Protein Adsorption to Zwitterion-coated PDMS

Resistance to protein adsorption is a key indicator of anti-fouling properties and such resistance could significantly change FBR.[16,54,55] Fibrinogen is abundant in serum, and was therefore used as a representative protein. For all experiments evaluating anti-fouling properties of the zwitterion-coated PDMS, 50 mg/mL BP feed was used to prevent delamination from the substrate. Epifluorescent images of immunostained adsorbed protein after incubation for 1 hr in a 1 mg/mL fibrinogen solution are shown in Figure 6.7A-C. The uncoated PDMS exhibited a bright green color where the SBMA- and CBMA-coated surfaces showed almost no fluorescence. Quantification of the adsorbed protein by measuring fluorescence intensity indicated a significant reduction in protein adsorption for both SBMA- and CBMA-coated surfaces compared to bare PDMS (Figure 6.7D). No statistically significant difference was observed between CBMA-coated compared to SBMA-coated samples (One way ANOVA, $p=0.9585$). These results demonstrate the efficacy of both SBMA and CBMA in preventing the adsorption of protein and potentially mitigating the FBR.

Fibroblasts are the predominant cell type found in the fibrotic capsules that form around implanted materials.[55] Thus, to further evaluate the ability of these crosslinked zwitterionic coatings to prevent fouling and the foreign body response, fibroblast adhesion was measured. Accordingly, SBMA-coated, CBMA-coated, and uncoated PDMS were evaluated for fibroblast adhesion with and without first incubating the samples in fetal bovine serum (FBS). Cells were allowed to remain in culture for 48 hrs and were then fixed, labeled with fluorescently tagged

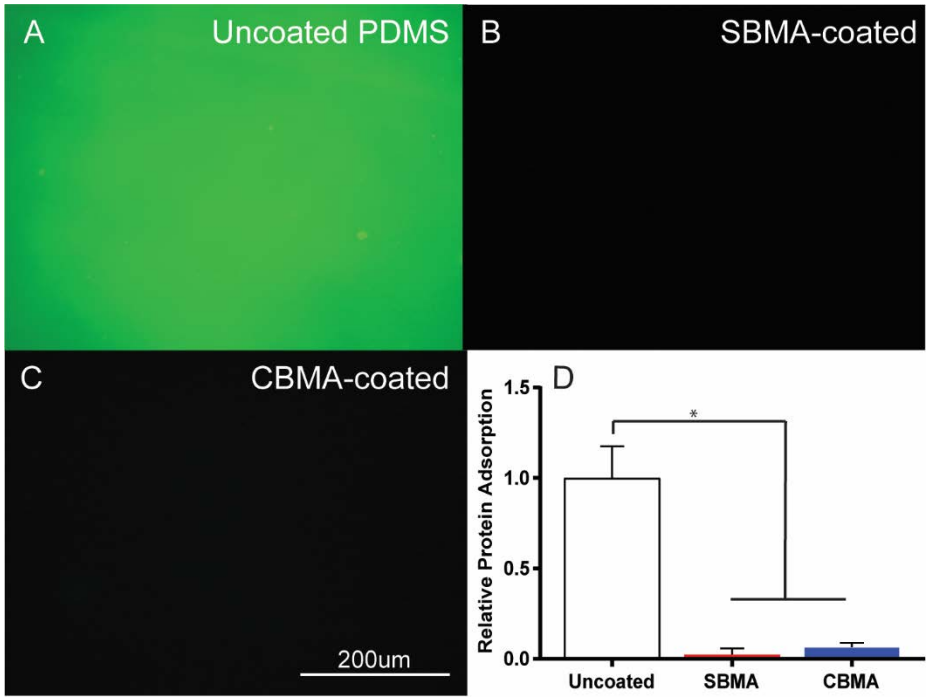

Figure 6.7. Characterization of protein adsorption. Representative epifluorescent images of immunostained fibrinogen (green) on A) uncoated, B) SBMA-coated, and C) CBMA-coated PDMS. D) Fibrinogen adsorption on uncoated, SBMA-coated and CBMA-coated PDMS as measured by epifluorescent microscopy. SBMA- and CBMA-coated substrates significantly reduce fibrinogen adsorption (*$p < 0.001$ one way ANOVA). Error bars represent standard deviation of the mean.

phalloidin which binds cytoskeletal actin, and epifluorescent microscopy was then performed. Images of fibroblast adhesion without FBS are shown in Figure 6.8A-C. Phalloidin staining revealed a markedly different cellular morphology on uncoated substrates compared to that seen on coated PDMS (Figure 6.8A). When cultured on uncoated PDMS, fibroblasts showed a characteristic elongated multipolar shape, indicating that the cells were healthy and adherent to the underlying substrate. In contrast, SBMA- and CBMA-coated substrates exhibited a rounded morphology with few if any cytoplasmic extensions (Figure 6.8B-C). Interestingly, fewer cells appeared to adhere to the CBMA-coated surfaces than the SBMA-coated substrates. Fibroblast cell density, a direct measure of the cell adhesion, without FBS was dramatically reduced over coated compared to uncoated substrates (Figure 6.8D). SBMA-coated surfaces showed less than

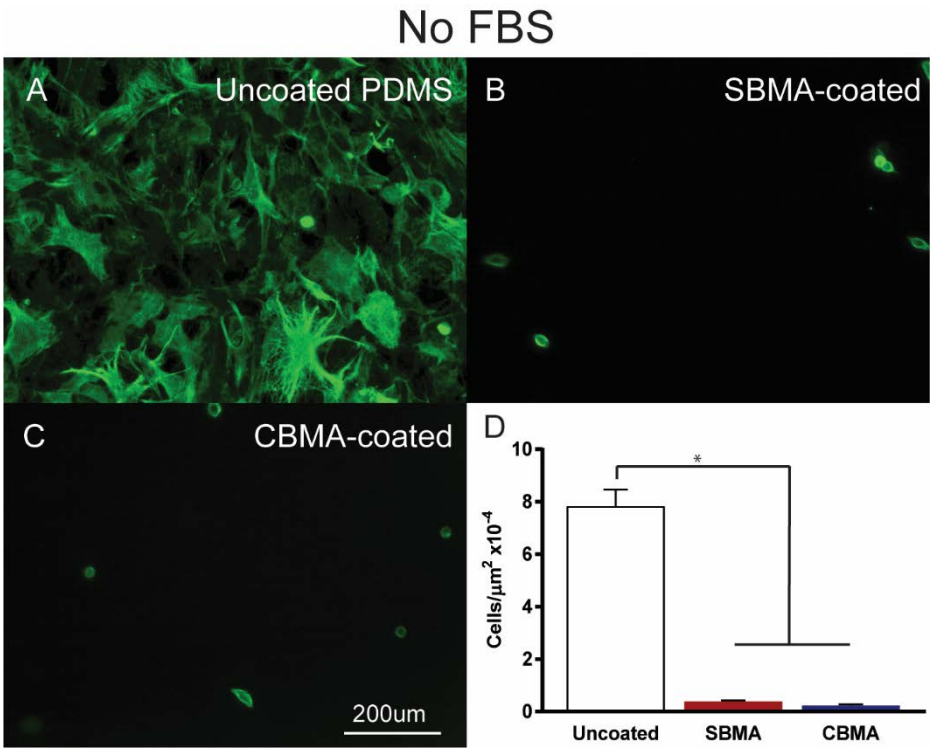

Figure 6.8. Representative epifluorescent images of fibroblasts grown on A) uncoated, B) SBMA-coated, and C) CBMA-coated PDMS without FBS in the culture medium. Fibroblast cytoskeletal actin is labeled with Alexa 488-phalloidin to demonstrate morphology (green). D) Fibroblast cell density on uncoated SBMA-coated, and CBMA-coated PDMS substrates. SBMA- and CBMA-coated PDMS significantly reduce fibroblast cell adhesion (*$p < 0.001$ one way ANOVA). Error bars represent standard error of the mean.

5% of the cells adhered when compared to the PDMS control. The CBMA-coated substrates had slightly lower cell adhesion with just above 3% of the cell density of the uncoated samples.

When devices are implanted into the body they are first exposed to serum proteins that can adhered to the implant surfaces. To mimic exposure to serum proteins, the samples were incubated with FBS prior to cell culture. This did not dramatically alter the cell density and adhesion. Fibroblasts adherent to the uncoated PDMS were dense and evenly distributed across the substrates (Figure 6.9A). In contrast, cell density was noticeably lower on SBMA- and CBMA-coated surfaces, with the remaining cells exhibiting a rounded morphology (Figure 6.9B-C). Quantification of cell density showed significant reductions in cell counts (Figure 6.9D).

Once again the SBMA-coated samples contained slightly more adherent cells than the CBMA-coated PDMS although not significantly (One-way ANOVA, p=0.8489). This result is consistent with prior work that has demonstrated improved efficacy of CBMA polymers when compared to SBMA.[110,268] Our lab also found that linear CBMA polymers photografted to glass were more effective than SBMA in preventing adhesion of multiple cell types including fibroblasts.[204] These results demonstrate the efficacy of crosslinked and photografted zwitterionic coatings in preventing fibroblast adhesion.

While SBMA- and CBMA-coatings on PDMS were effective in preventing protein and fibroblast adhesion over short time frames, it is also important to evaluate the long-term anti-fouling properties of the films. Thus, zwitterion-coated samples were incubated in culture media for 14 days before fibroblasts were seeded onto the substrates to test the efficacy after extended exposure to media. A parallel experiment was conducted where fibroblasts were seeded directly after substrate fabrication as a control (Day 0 samples). For the day 0 experiment, cell density on the uncoated PDMS was similar to the previous experiments with relatively high cell density (Figure 6.10D). The SBMA- and CBMA-coated surfaces were resistant as before to cell adhesion in the 0 day seeding with CBMA preventing all fibroblast adhesion. Epifluorescent images of fibroblasts seeded after 14 days are shown in Figure 6.10A-C. Cell density is slightly higher on the uncoated PDMS, and cells have spread and elongated. As seen before extensive exposure to culture media, cell density is noticeably reduced on the SBMA- and CBMA-coated PDMS. Quantification of the cell density revealed that the number of cells increased on all substrates after the 14 day exposure to media, but not to a statistically significant degree. The number of cells adhered in the uncoated PDMS increased from approximately 11 $x10^{-4}$ cells/μm^2 to 13 $x10^{-4}$ cells/μm^2. For the SBMA-coated samples, cell density doubled from about 0.6 $x10^{-4}$

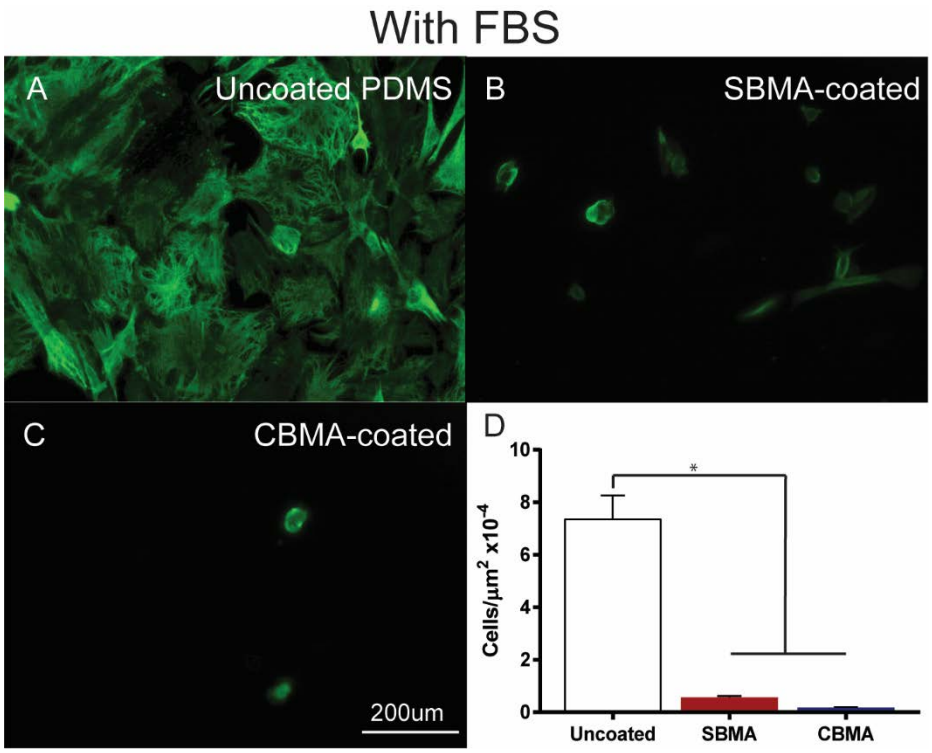

Figure 6.9. Representative epifluorescent images of fibroblasts grown on A) uncoated, B) SBMA-coated, and C) CBMA-coated PDMS with FBS in culture medium. Fibroblast cytoskeletal actin is labeled with Alexa 488-phalloidin to demonstrate morphology (green). D) Fibroblast cell density on uncoated SBMA-coated, and CBMA-coated PDMS substrates. SBMA- and CBMA-coated PDMS significantly reduce fibroblast cell adhesion (*$p < 0.001$ one way ANOVA). Error bars represent standard error of the mean.

cells/µm^{2}x to 1.3 x10^{-4} cells/µm^2 while CBMA-coated PDMS increased from no observable cells to 0.6 x10^{-4} cells/µm^2, almost 20 times less than the cell density on the PDMS control. For both experiments, cell density was dramatically lower for the zwitterion-coated surface and the incubation time did not result in a significant increase in cell density. Further, for the entirety of the experiment, the SBMA and CBMA thin films remained securely adhered to the PDMS. These results show that photografted/polymerized zwitterionic coatings show promise in maintaining anti-fouling properties while remaining durable for potential biological applications.

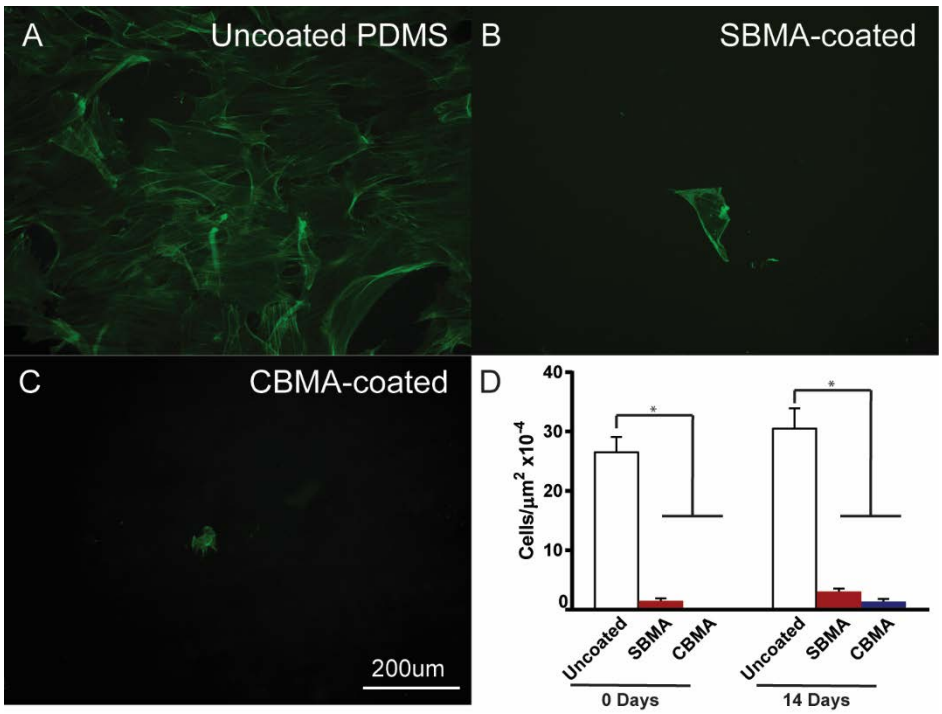

Figure 6.10. Representative epifluorescent images of fibrobasts grown on A) uncoated, B) SBMA-coated, and C) CBMA-coated PDMS after substrate immersion in culture medium for 14 days. Fibroblasts are labeled with Alexa 488-phalloidin (green). D) Fibroblast cell density at 0 and 14 days in culture medium for uncoated, SBMA-coated, and CBMA-coated PDMS. A significant difference was observed between uncoated and the zwitterion-coated PDMS at 0 and 14 days. No significant increase in cell density was observed after the 14 day incubation for all substrates. Error bars represent standard error of the mean.

6.4.4 Bacterial Adhesion to Zwitterion-coated PDMS

Another problem that can occur in implantable devices is bacterial infection associated with implantation and biofilm formation on the surface. Zwitterionic materials have also been shown to decrease bacterial adhesion and prevent the formation of biofilms.[170–172] Accordingly, the zwitterion-coated PDMS substrates were evaluated for their ability to resist bacterial adhesion. Two different bacterial strains were investigated: 1) *Staphylococcus Aureus* (*S. Aureus*) and 2) *Staphylococcus Epidermidis* (*S. Epidermidis*). *S. Aureus* is a Gram-positive bacteria that is a flora found in the nose, respiratory tract and on the skin. *S. Epidermidis* is also a Gram-positive bacteria and is typically a skin flora. Infections from *S. Epidermidis* area often

hospital acquired. These two strains of bacteria will serve as two likely bacteria that could form adhere to and potentially cause an implant infection.

In order to investigate the accumulation of bacteria on the sample surface, the uncoated, SBMA-coated, and CBMA-coated PDMS with or without FBS were incubated in a *S. Aureus* suspension for 48 hrs. At 48 hrs, the uncoated PDMS samples without FBS had a significant amount of adherent bacterial colonies (Figure 6.11A). The SBMA-coated surfaces reduced the bacterial adhesion by just under 70% of the uncoated PDMS. A more dramatic reduction in bacterial adhesion occurred on the CBMA-coated substrates with just under 7% of the uncoated control. A statistical difference was calculated between the uncoated and the SBMA- and CBMA-coated (one-way ANOVA, $p<0.0001$). The CBMA-coated PDMS reduced the bacterial adhesion significantly more than the SBMA-coated (one-way ANOVA, $p=0.0119$). These results demonstrate the ability for CBMA to repel bacteria more effectively than SBMA.

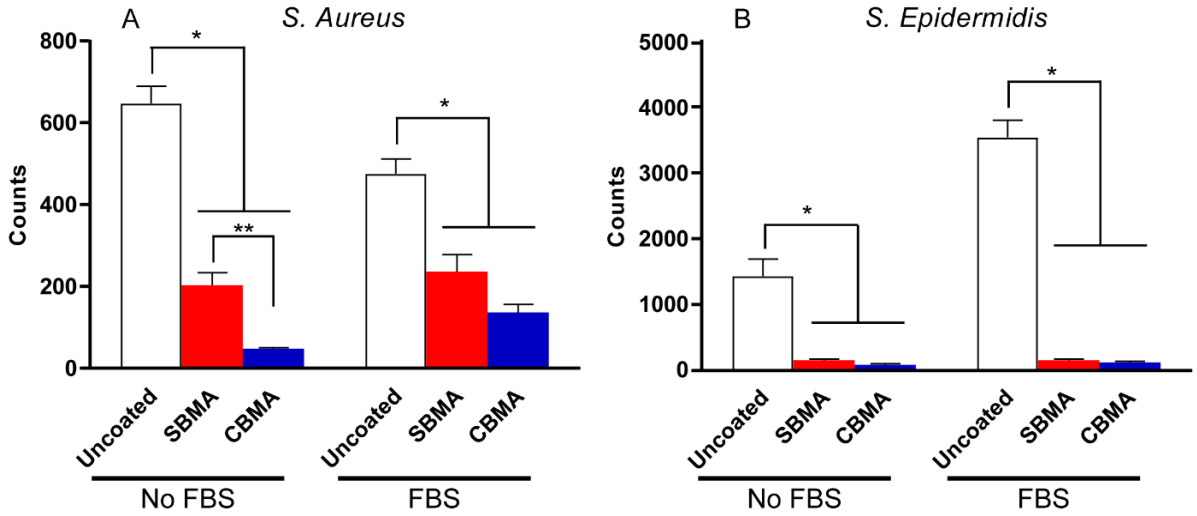

Figure 6.11. Bacterial adhesion onto coated and uncoated PDMS substrates in vitro. *S. aureus* (A) and *S. epidermidis* (B) growth at 48 h on implants treated with and without FBS. * indicates a statistical difference between groups (*$p<0.001$ one way ANOVA). ** indicates a statistical difference between groups ($p=0.0119$ one way ANOVA)

Examination of the bacterial adhesion for seedings containing FBS also demonstrated high levels of adhesion for the uncoated PDMS although not as high. Similar to samples containing no FBS, the bacterial adhesion was significantly reduced when the SBMA or CBMA coating was applied (one-way ANOVA, $p<0.0001$). The addition of FBS increased the bacterial adhesion to the SBMA- and CBMA-coated samples. While there were fewer bacteria adhered to the CBMA-coated PDMS, there was no statistical difference found (one-way ANOVA, $p=0.2422$). While the addition of FBS to the culture media increased the adhesion of *S. Aureus* for SBMA- and CBMA-coated samples, the coated substrates were still able to significantly reduce the adhesion.

To demonstrate the ability of the zwitterion-coated substrates in reducing multiple strains of bacteria, *S. Epidermidis* was then seeded onto the substrates. The results for these experiments are shown in Figure 6.11B. For experiments without FBS, the SBMA-coated samples reduced bacterial adhesion by just under 10% of the value for uncoated control while the CBMA-coated sample was just under 5%. This resistance to *S. Epidermidis* was better than that of *S. Aureus.* For samples containing FBS, the results for *S. Epidermidis* were very similar to those without FBS (Figure 6.11B). The adhesion to the uncoated substrate increased and there was a dramatic reduction in bacteria adhesion for both SBMA- and CBMA-coated substrates. These substrates both reduced the adhesion by more than 96%. The results from these bacterial adhesion studies demonstrate that zwitterion-coated materials not only can prevent adhesion of cell, but also are useful in potentially mitigating implant-associated infections.

6.5 CONCLUSIONS

Engineering surfaces that resist biofouling represents a critical first step in developing neural prosthetics that integrate effectively with biological systems. Coating existing implant

materials with a zwitterionic coating is one potential approach to mitigate the foreign body response. In this work, we describe a simple method to photograft SBMA and CBMA zwitterionic crosslinked hydrogels to PDMS, a common implant material. Photografting was achieved by adsorbing the type II photoinitiator benzophenone onto the PDMS surface, which initiated a polymerization reaction from the surface upon UV-light absorption. This process generated a durable covalently-grafted bond between the crosslinked zwitterionic hydrogels and the PDMS substrate. The amount of BP adsorbed on the surface was increased by with higher BP feed concentrations. At higher surface BP concentrations, the crosslinked zwitterionic thin films resisted delamination as examined by SEM imaging. Shear adhesion experiments quantitatively revealed that the strength of adhesion increased with higher BP surface concentrations until a critical concentration was reached between 1 and 2.5 g/L above which cohesive instead of adhesive failure was observed. Examination of anti-fouling properties of the crosslinked zwitterionic hydrogels revealed a greater than 90% reduction in fibrinogen adsorption for both SBMA- and CBMA-coated substrates. Fibroblast adhesion was also dramatically reduced 20 fold or greater for zwitterion-coated PDMS. Finally, the thin films maintained resistance to fibroblast adhesion after exposure to culture media for up to 14 days *in vitro*. This work demonstrates that zwitterionic hydrogel coatings are successfully grafted to PDMS substrates using a simple and controllable technique which could have significant potential function for anti-fouling in implantable materials.

CHAPTER 7: STRENGTHENING ZWITTERIONIC HYDROGELS FOR COATING PDMS MATERIALS

7.1 ABSTRACT

Zwitterionic materials have excellent anti-fouling properties leading to their potential as coatings on biomedical implants. However, these systems have limited long-term use due to their relatively weak mechanical properties. In this chapter, two approaches were employed to strengthen the hydrogel networks formed from sulfobetaine methacrylate (SBMA): 1) the crosslink density was varied by changing the concentration of a poly(ethylene glycol) diacrylate (PEGDA) crosslinker and 2) adding hydroxyethyl methacrylate (HEMA) to the formulation. Swelling, compressive modulus and toughness were examined with addition of PEGDA and HEMA to the SBMA system. Both higher crosslink density and higher HEMA concentrations decreased swelling. Increasing PEGDA content afforded over an order of magnitude increase in modulus. The addition of HEMA resulted in moderate increases in modulus, but over an order of magnitude increase in toughness. While the addition of PEGDA and HEMA to the hydrogels increased mechanical strength of the hydrogels, the anti-fouling properties of the material may be negatively impacted. Thus, nonspecific protein adsorption was evaluated and showed no significant changes with varying PEGDA and HEMA concentrations. Finally, increases in HEMA and PEGDA concentration increased cell adhesion indicating changes in fouling with the addition of non-zwitterionic monomers.

7.2 INTRODUCTION

In tissue engineering, hydrogels have long been of interest due to their high water content and tissue-like properties. The porous nature of hydrogels affords them excellent small molecule diffusivity and water permeability.[269,270] Further, their mechanical properties can be tuned to

mimic biological tissue.[271] Perhaps the most extensively studied synthetic hydrogels are poly(2-hydroxyethyl methacrylate) (pHEMA)-[272] and poly(ethylene glycol)-based materials.[51,273] These two types of synthetic hydrogels have found widespread use due to their low-fouling and non-cytotoxic properties allowing them to be easily integrated with host tissue. For example, pHEMA has been used in various applications including contact lenses, artificial cornea, drug delivery vehicles, cartilage substitutes, and tissue scaffolds.[274–277] PEG-based materials have also garnered significant interest in a variety of fields due to their excellent hydrophilicity and ability to be easily modified with various functional groups.[51,278] For example, PEG hydrogels are routinely used for applications that require a bioinert platform with specific bioactive functionalities for targeted *in vivo* and *in vitro* uses.[164]

While PEG and pHEMA-based materials have found use in biomedical applications, they do not resist biomolecule adhesion entirely especially in contact with host fluids.[64] As demonstrated in previous chapters, zwitterionic polymers have recently attracted significant interest in the field of low fouling materials, particularly for resisting biofouling and foreign body response (FBR).[99] For example, a hydrogel formed from carboxybetaine was used to coat the surface of a blood glucose sensor with accurate glucose readings for up to 45 days in whole blood while an uncoated device fouled within a few days.[58] Further, Jiang et al. generated a sulfobetaine hydrogel that resisted nonspecific protein adsorption and cell adhesion, demonstrating the ability of sulfobetaine materials to resist fouling.[114] Zwitterionic hydrogels have also been shown to resist the FBR *in vivo*. A carboxybetaine-based zwitterionic hydrogel was implanted into mice for 3 months with no fibrosis on the implant surface and even showed signs of angiogenesis around the hydrogel.[80] Therefore, zwitterionic hydrogels have the potential to be used in applications requiring low biofouling.

However, zwitterionic hydrogels have relatively weak mechanical stability and as such are susceptible to failure at low shear/compression forces.[114,279–282] Attempts to improve the mechanical properties of zwitterionic hydrogels have focused largely on changing the formulation using monomers or crosslinkers that strengthen the hydrogel matrix. For example, Jiang et al. altered the crosslinker concentration of carboxybetaine hydrogels to increase modulus by over an order of magnitude.[112] Another report from the same group used a vinylimidazole zwitterion to engineer the polymer backbone and also increase the modulus by an order of magnitude.[114] The addition of nanoclays has also been investigated to increase the elasticity and toughness of zwitterionic hydrogels. For example, Ning et al. increased the elongation at break from under 200% to over 2,000% using a nanoclay additive.[283] Thus, adding nanoparticles or second monomer to hydrogel formulations can significantly improve the mechanical properties of zwitterionic materials and their potential long-term use.

While changing zwitterionic formulations can improve the mechanical properties of the hydrogels formed, it also introduces chemical groups that could interfere with the anti-fouling properties of the material. These changes in chemistry may alter anti-fouling properties through changes in hydrophilicity and resistance to biomolecule/cell adhesion. Thus, altering zwitterionic hydrogel formulations may induce higher stiffness and overall toughness in the thin films while decreasing anti-fouling properties. While other work has focused on increasing mechanical properties, no reports have established a direct relationship between changing formulation to strengthen the hydrogel and the anti-fouling properties as described in this chapter. Two approaches are used to improve the strength of sulfobetaine methacrylate (SBMA) hydrogels: 1) the concentration of crosslinker, poly(ethylene glycol) diamethcrylate (PEGMDA, MW 750), is varied and 2) HEMA is added to the formulation. The changes in swelling with prepolymer

composition are established. Compressive modulus was determined for the PEGDA- and HEMA-containing formulations. Tensile mode toughness was established for the HEMA formulations. Nonspecific protein adsorption and cell adhesion were used to measure the changes in anti-fouling properties with monomer composition. These findings help establish the changes in anti-fouling properties with the addition of non-zwitterionic monomers to SBMA hydrogels.

7.3 MATERIALS/METHODS

7.3.1 Materials

[2-(Methacryloyloxy)ethyl]dimethyl-(3-sulfopropyl)ammonium hydroxide (SBMA), benzophenone (BP), poly(ethylene glycol) diacrylate (PEGDA, MW 575), poly(ethylene glycol) dimethacrylate (PEGDMA, MW 750), 2-hydroxyethyl methacrylate (HEMA), and all organic solvents were acquired from Sigma Aldrich. 1-[4-(2-hydroxyethoxy)-phenyl]-2-hydroxy-2-methyl-1-propane-1-one (HEPK, photoinitiator) was obtained from Ciba. Sylgard 184 was acquired from Dow-Corning. Hank's balanced salt solution (HBS), fetal bovine serum (FBS), poly-L-ornithine, trypsin-EDTA dissociation reagent, DAPI-containing mounting medium, were obtained from Gibco.

7.3.2 Hydrogel Fabrication

Zwitterionic hydrogels were fabricated with varying composition of SBMA, PEGDA, and HEMA. HEPK (photoinitiator) was dissolved in deionized water at 1.5 wt% and used for all hydrogel formulations. HEMA-based hydrogels were mixed with 2.5 wt% PEGDA (MW 575), 47.5 wt% photoinitiator/water solution, with the remaining 50 wt% varying between SBMA and HEMA depending on the formulation. Hydrogels prepared with the following SBMA:HEMA ratios were investigated: 1:0, 4:1, 1:1, 2:3, 1:4 and 0:1. These hydrogels will be referred to

throughout the text as SH Y:Z where SH represents SBMA:HEMA and Y:Z represents the ratio of the two components. Variable crosslinker hydrogels were similarly formulated using 50 wt% photoinitiator/water solution and the remaining percent being filled with PEGDA and SBMA in the following SBMA:PEGDMA ratios: 0:1, 1:3, 1:1, 3:1, and 19:1. These hydrogels will be referred to throughout the text as SX Y:Z where SX represents SBMA:PEGDA and Y:Z represents the ratio of the two components.

Hydrogel samples for dynamic mechanical analysis were fabricated using molds created by placing two standard 2.54 x 7.62 cm glass microscope slides together with a 1 mm thick piece of glass as a spacer. The liquid monomer was pipetted in the 1 mm space and illuminated for 10 min at ~25 mW/cm^2 measured at 365 nm wavelength using a mercury vapor arc lamp (Omnicure S1500, Lumen Dynamics, Ontario, Canada). After polymerization, the glass slides were removed and the samples were punched into either disks or rectangles using punches. The samples were soaked in water for at least 24 hrs before being transferred to a dynamic mechanical analyzer (DMA) for testing.

To examine the water uptake of the various formulations, 6 mm disks were cut from the free-standing hydrogel films described in the previous paragraph. The samples were immersed in water for at least 24 hrs and swollen mass measurements were taken. The samples were then dried at ambient temperature overnight and then placed in a vacuum for 12 hrs prior to recording the dry mass. The swelling ratio of the various formulations was calculated using the following equation:

$$Swelling\ Ratio = \frac{w - d}{d} \tag{7.1}$$

Where *w* is the swollen mass of the sample and *d* is the dry mass of the sample.

PDMS elastomer substrates were prepared from the commercially available two-component Sylgard 184 kit. The elastomer was prepared by thoroughly mixing 10 parts base to 1 part curing agent. The mixture was then poured into Petri dishes and placed in a vacuum to remove bubbles. The substrates were then cured at 80^{o} C for 3 hrs. After curing the slabs were cut into ~ 1 cm x 1 cm pieces to be used for fouling studies.

To test the ability of the SBMA hydrogels to resist protein/cell adhesion, PDMS substrates were coated with the SBMA formulations using methods outlined in Chapter 6. Briefly, benzophenone (BP) was applied to ~ 1 cm x 1 cm slabs of PDMS substrates by immersing the samples in a 50 g/L BP in acetone solution for 1 hr. The samples were removed and dried under a nitrogen stream and then placed in a vacuum for 30 min to remove residual solvent. After drying the samples, monomer formulations were pipetted on the PDMS and a glass slide was placed on top to evenly disperse the liquid across the surface. The samples were then cured for 10 min at ~25 mW/cm^2 measured at 365 nm wavelength using a mercury vapor arc lamp (Omnicure S1500, Lumen Dynamics, Ontario, Canada). The hydrogel-coated PDMS samples were transferred to a water bath for at least 24 hrs before use. All hydrogel samples were tested in triplicate.

7.3.3 Mechanical Properties

Mechanical testing of the hydrogels was completed using a dynamic mechanical analyzer (DMA; Q800 DMA TA instruments). For compression testing, circular disks were used and compressed using a submersion compression clamp and a controlled force ramp rate of 0.5 N/min at room temperature. The slope of the linear portion of the stress/strain graph was calculated as the Young's modulus. For tensile measurements, hydrogels were cut into

rectangular films and tested in tensile mode at a ramp rate of 0.1 N/min at room temperature. Toughness was calculated as the area under the stress/strain curve of the tensile graphs. All hydrogel samples were tested in triplicate.

7.3.4 Protein Adsorption and Cell Adhesion

Immunofluorescence was used to measure protein adsorption to substrates. Fluorescently-labeled bovine serum albumin (1 mg/mL) was pipetted onto substrates and dispersed by placing a glass coverslip on the solution followed by a 1 hr incubation at room temperature. The samples were then soaked in PBS for 1 hr with the PBS being changed every 15 min. After rinsing with PBS, coverslips were placed on the samples using mounting media. Digital epifluorescent images were captured on a Leica DMIRE2 microscope (Leica Microsystems, Bannockburn, IL) with Leica DFC350FX digital camera and Metamorph software (Molecular Devices, Silicon Valley, CA). Images were taken and gray-scale measurements were used to evaluate relative fluorescence intensity using Image J software (NIH, Bethesda, MD). All samples were prepared in triplicate, and five representative images were taken for each condition.

7.4 RESULTS AND DISCUSSION

7.4.1 Characterization of SBMA:PEGDA Hydrogels

Improving the mechanical properties of hydrogel thin films that coat biomedical implants has the potential to increase the lifetime of the coating and longevity of the implant. One primary indicator of mechanical properties is the elastic modulus, which is a measure of the resistance to deformation. Higher modulus materials indicate that a material is more resistant to dimensional changes from an applied force. One common method of changing the modulus in polymer networks is by altering the crosslink density which can be achieved by varying the concentration of crosslinker in the reaction mixture. While this method can strengthen a material, it often leads

to an increase in shrinkage stress and consequent brittleness. A second approach to improving the mechanical properties of a material is by adding a co-monomer to the formulation with desirable mechanical properties. By altering the concentration of these monomers, the mechanical properties of a material can be tuned for a given application. In this work, the mechanical properties of zwitterionic and anti-fouling SBMA hydrogels were varied by 1) changing the concentration of poly(ethylene glycol) diacrylate (PEGDA, MW 575) to alter crosslink density and 2) by adding the commonly used HEMA monomer.

To develop an understanding of how the mechanical properties of the SBMA hydrogels change with different crosslink density, the concentration of PEGDA in the hydrogel was increased. These formulations will be referred to as SX followed by the SBMA:PEGDA ratio. While the hydrogels were initially polymerized with 50 wt% water, immersion in aqueous solution after the polymerization process results in additional uptake of water. Additionally, a hydrogel swollen to equilibrium would better approximate end use conditions while also removing any residual monomer. To characterize the uptake of water for the hydrogels, swelling studies were conducted measuring the change in mass between the equilibrium swollen and dry samples. To quantify changes in water uptake, swelling ratios were calculated which describe the ratio of water to dry mass of the hydrogel. The swelling ratios for these variable PEGDA hydrogels are shown in Figure 7.1A. As expected, the swelling ratio decreased as the crosslink density increased (lower SBMA:PEGDA ratio). The increased water uptake at lower PEGDA concentrations was likely due in part to fewer crosslinks in the network that contributed to a larger mesh size leaving more free volume for water to be absorbed. Additionally, the flexibility of the network allowed the hydrogel to expand and absorb more water. When the PEGDA concentration and crosslink density is high, the swelling ratio is decreased. With more crosslinks

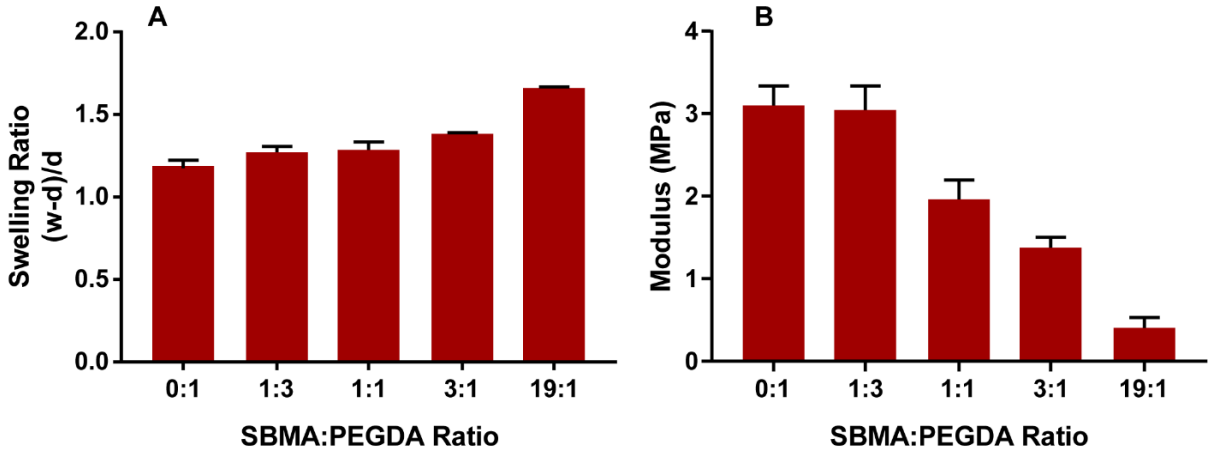

Figure 7.1. Characterization of the material properties of SX hydrogels. A) Swelling ratios of variable PEGDA hydrogels. The water uptake increases with lower crosslink density. B) Compressive modulus of variable PEGDA hydrogels. Lower crosslink density decreases the modulus. Error bars represent the standard deviation of the mean.

in the network, the hydrogel is not as flexible, and less volume is available for water to be absorbed. Similar findings have been reported elsewhere with changes in swelling with respect to crosslink density for zwitterionic hydrogels.[112,284]

Characterization of the mechanical properties of these hydrogels was conducted using dynamic mechanical analysis (DMA) in compression mode to determine the compressive Young's modulus. The Young's modulus of compression as a function of SBMA:PEGDA ratio is shown in Figure 7.1B. At higher SBMA:PEGDA ratios, where the crosslink density is low, the modulus was substantially lower than for samples with larger PEGDA content. As the SBMA:PEGDA ratio decreased, the modulus increased by almost an order of magnitude from just over 0.4 MPa at the SX 19:1 ratio to over 3 MPa at the SX 0:1 ratio (100% crosslinking monomer). This increase in modulus could be explained by the increase in crosslinks afforded by the diacrylate. The higher number of crosslinks in the network increases the hydrogel's resistance to deformation by increasing the number of covalent bonds that hold the material together. Intermediate SBMA:PEGDA ratios showed moduli between the two extremes,

demonstrating the control over the stiffness of the SBMA hydrogels using varying concentrations of PEGDA. Testing of the variable PEGDA hydrogels in tensile mode was attempted, but the materials were unable to be loaded due to limitations in flexibility of the films. It is important to note that as the crosslink density was increased, the susceptibility of the hydrogel to cracking increased as the material became stiffer and less ductile. Thus a material that remains flexible, yet also able to resist deformation is desirable.

7.4.2 Characterization of SBMA:HEMA Hydrogels

While PEGDA can provide increases in modulus, HEMA is an inherently tough hydrogel material that can potentially strengthen SBMA hydrogels.[279,280] Thus, formulations with variable concentrations of HEMA were tested to determine the effect of this monomer on mechanical properties of the anti-fouling hydrogels. Different ratios of SBMA to HEMA were tested ranging from 1:0 to 0:1. The crosslinker (PEGDA (MW 575)) was held at 2.5 wt% with the combined HEMA/SBMA monomer equaling 50 wt% for all samples tested. These formulations will be referred throughout the text as SH (SBMA:HEMA) followed by the monomer ratio. The swelling ratios of the hydrogels as a function of SBMA:HEMA ratio is shown in Figure 7.2A. At lower SBMA concentrations, the swelling ratio was lower. Adding SBMA monomer to the HEMA formulation increased the swelling ratio by more than 60 percent until the SH 1:1 ratio, where it reached a maximum. Higher concentrations of SBMA resulted in decreases in swelling. It is important to note that variations in crosslink density also occurred due to the difference in molecular weight between SBMA (279 g/mol) and HEMA (130 g/mol). Thus, at higher SBMA:HEMA ratios (higher SBMA concentrations), the crosslink density is higher due to the increase in molecular weight of SBMA and relatively lower concentration of noncrosslinking monomer. As the SBMA:HEMA ratio decreases (higher HEMA concentrations), the crosslink

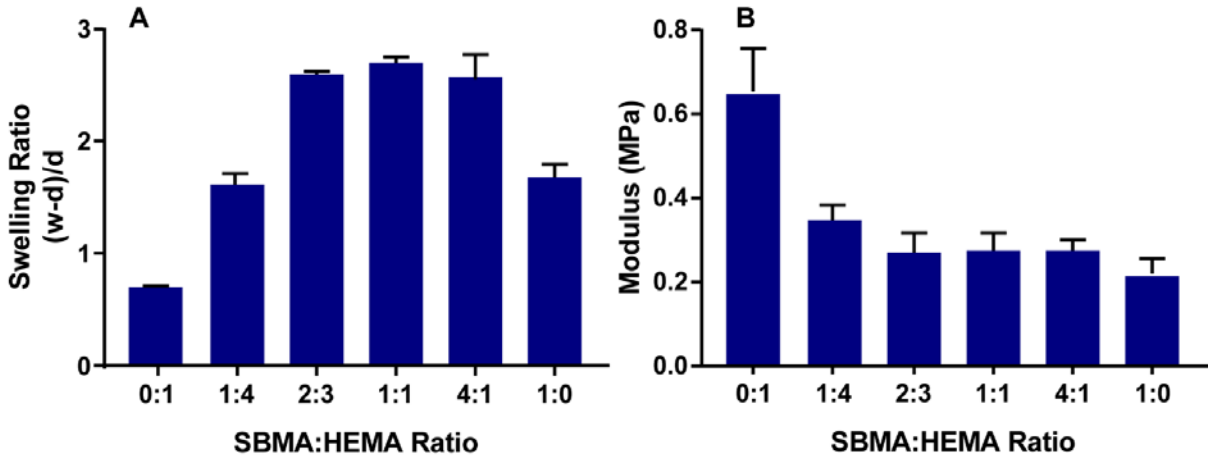

Figure 7.2. Characterization of the material properties of SH hydrogels. A) Swelling ratios of variable HEMA hydrogels. B) Compressive modulus of variable HEMA hydrogels. Lower HEMA concentrations decrease the modulus. Error bars represent the standard deviation of the mean.

density decreases due to the lower molecular weight of HEMA. Thus, the changes in swelling ratio are likely due to changes in chemistry rather than crosslink density as the highest concentration of HEMA (lowest crosslink density) contained the lowest swelling ratio. It should also be noted that the SH 0:1 hydrogels became cloudy upon polymerization indicating some degree of micro-phase separation.

The mechanical properties of the SH hydrogels were also examined using DMA. The compressive modulus of the SH hydrogels revealed a similar trend to the SX samples (Figure 7.2B). At the SH0:1 ratio (no SBMA), the Young's modulus was over 0.6 MPa, which decreased by over 50 percent for the SH 1:4 samples. Minor decreases in modulus were observed as HEMA concentrations were further decreased with no statistical differences in modulus. While a significant change in compressive modulus was observed for the SH hydrogels between extremes, the effect for the SX formulations was far greater (almost an order of magnitude between extremes). Thus, the addition of HEMA to the SBMA hydrogels only impacted the

Young's modulus moderately compared to changes in crosslinker concentration described in the previous section.

To further characterize the durability of the SBMA:HEMA hydrogels, tensile measurements were taken. The stress/strain curves for the six formulations are shown in Figure 7.3A. From these stress/strain curves, only small changes in Young's modulus (slope) occurred between different formulations, except for between the SH 0:1 and those containing SBMA. However, there were substantial changes in the elongation at break as the SBMA:HEMA ratio increased. One purpose of testing in tensile mode was to measure the toughness of the hydrogels, which may be difficult to determine using compression experiments. Toughness is defined as the area under the stress/strain curve and is a useful measure of the amount of energy absorbed by a material. Toughness accounts not only for changes in modulus, but also changes in elongation that may occur after the initial linear region in the stress/strain graph. The toughness measurements for the SH hydrogels are shown in Figure 7.3B. At the highest HEMA concentration (SH 0:1), the toughness approached 200 kPa. This value decreased with the addition of small amounts zwitterionic monomer to the formulation. The SH 1:4 hydrogel maintained a relatively high toughness of around 75 kPa, which decreased dramatically with the addition of more SBMA monomer. The tensile measurements of the SH 4:1 and SH 1:0 hydrogels revealed low modulus and low strain at break (Figure 7.3A), resulting in toughness values less than 1.5 kPa. Qualitatively, these formulations were difficult to handle and easily cracked. These toughness calculations provide a good basis for understanding how to increase the durability of the inherently weak SBMA hydrogels. With the addition of a HEMA monomer, the modulus and toughness of the material was increased. However, the overall impact on the

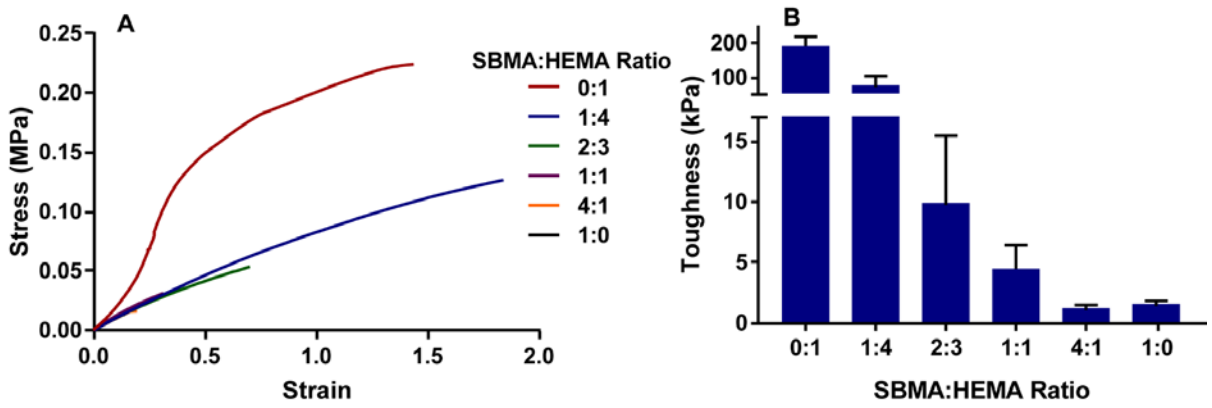

Figure 7.3. Tensile mechanical properties of SH hydrogels. A) Stress/strain curves of variable HEMA hydrogels. B) Toughness calculations of variable HEMA hydrogels. Higher HEMA concentrations increase the toughness. Error bars represent the standard error of the mean.

anti-fouling properties upon adding non-zwitterionic monomers may play an important role in the selection of these hydrogels as materials for biomedical implants.

7.4.3 Anti-fouling Properties of SBMA:PEGDA Hydrogels

It is well established from the previous work that SBMA hydrogels have excellent anti-fouling properties. However, the weak mechanical properties of zwitterionic hydrogels may limit their long-term performance. The addition of additives, such as PEGDA or HEMA, to an anti-fouling material has the potential to disrupt the properties that prevent the adsorption of protein and adhesion of cells. Therefore, a balance must be achieved where a material will have sufficient mechanical strength without significant sacrifices to anti-fouling properties. The direct relationship between changes in formulation and fouling have not been described. Accordingly, the anti-fouling properties of the SX and SH hydrogels were tested in order to establish this relationship.

Nonspecific protein adsorption is used as a technique to examine bio-fouling because it has been theorized as the initial step in the foreign body response.[55,67] Nonspecific adsorption of protein and adhesion of cells have been widely used to predict fouling and will be examined here

to evaluate the SBMA hydrogels.[66,77,84] To test the effect of changes in formulation on nonspecific protein adsorption, the hydrogel formulations were grafted to PDMS substrates as described in Chapter 6. A fluorescently-labeled bovine serum albumin (BSA) was applied to the hydrogel-coated surfaces for 1hr after which the sample was rinsed with PBS and imaged using fluorescence microscopy. Fluorescence images were taken and gray-scale measurements were made using Image J software to quantify nonspecific protein adsorption. An uncoated PDMS substrate was taken as a positive control and the fluorescent measurements were normalized to this value.

The nonspecific protein adsorption for the SX hydrogels is shown in Figure 7.4A. The SX-coated samples reduced nonspecific protein adsorption by at least 20-fold compared to the uncoated PDMS. Neat PDMS is known to foul and elicit a significant FBR due to the hydrophobic nature of the surface which causes protein to tightly bind to the substrate. All coated samples exhibited similar levels of nonspecific protein adsorption (around 4% of the uncoated) with no statistical difference observed. This result is not surprising since PEG-based materials have been shown to significantly reduce nonspecific protein adsorption.[64] While no apparent change in protein adsorption between the different formulations was observed, a cell adhesion test could potentially delineate the difference in fouling between the various coatings.

To better establish the relationship between fouling and changes in composition of the SX hydrogels, 3T3 mouse embryonic fibroblasts were cultured on the surface. Cell density measurements could provide a more rigorous test for fouling than nonspecific protein adsorption. The cells were cultured on the coated PDMS samples for 24 hrs, then stained and imaged using fluorescent microscopy. Cell density calculations were made using cell counts in Image J software and normalized to the area. The results for the cell density measurements are shown in

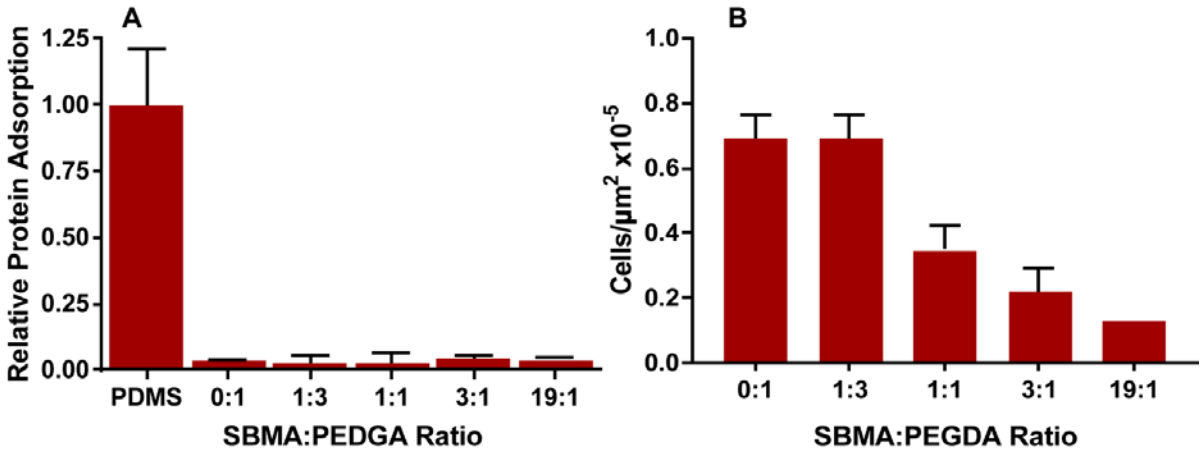

Figure 7.4. Fouling properties of SX hydrogels. A) Protein adsorption and B) cell adhesion onto variable PEGDA hydrogels. Error bars represent standard error of the mean.

Figure 7.4B. As the SBMA:PEGDA ratio increased (i.e. higher SBMA content) the cell density decreased, with over a factor of 5 decrease observed between the 0:1 and 19:1 ratios. While the decreases in cell density were significant, all coated substrates demonstrated low cell density. No more than a few cells were visible in the images and the cell morphology was rounded indicating unhealthy cells. PEGDA surfaces have been shown previously to be effective in reducing cell adhesion,[64] but the data presented indicates that SBMA is more effective than PEGDA and that changes in formulation impact the fouling of zwitterionic hydrogels. While protein adsorption between the various SX hydrogels was similar, changes in cell adhesion proved to be a more rigorous test and demonstrate that a higher standard for fouling is necessary for applications in contact with cells and tissue.

7.4.4 Anti-fouling Properties of SBMA:HEMA Hydrogels

The anti-fouling properties of the SH hydrogels were examined using the same protein and cell adhesion experiments. The results from nonspecific protein adsorption are shown in Figure 7.5A. Similar to the SX hydrogels, a dramatic reduction in protein was observed between the uncoated PDMS and all coated samples. While all the formulations reduced protein

adsorption, the SH 1:0 coating showed the lowest fouling. This change in protein adsorption was not statistically different from the other samples. However these small changes could potentially have an impact on cell adhesion and ultimately the FBR. Further, it is also not surprising that formulations containing HEMA have higher protein adsorption. Jiang et al. showed that poly(HEMA) hydrogels elicit a significantly larger FBR than zwitterionic hydrogels when implanted subcutaneously in a mouse model.[80]

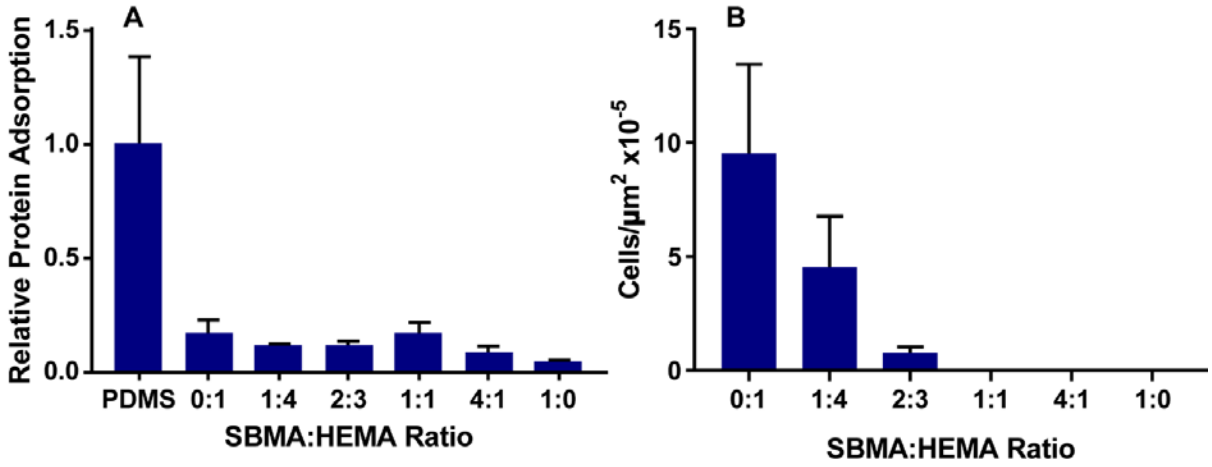

Figure 7.5. Fouling properties of SH hydrogels. A) Protein adsorption and B) cell adhesion onto variable HEMA hydrogels. Error bars represent standard error of the mean.

The anti-fouling properties of the SH hydrogels were also evaluated by measuring 3T3 cell adhesion using the same protocol as described for the SX hydrogels and are shown in Figure 7.5B. The cell density for the all HEMA sample (SH 0:1) was high at almost 10 cells/$\mu m^2 x10^{-5}$. As the concentration of SBMA in the formulation increased, the cell density decreased significantly and eventually reached zero at the SH 1:1 samples with further increases in SBMA concentration maintaining zero cell adhesion. At higher HEMA concentrations (SH 0:1, SH 1:4, and SH 2:3), the protein adsorption was similar to the other formulations, but the cell adhesion was higher. This observation suggests that taking protein adsorption as the only indicator to determine the fouling properties of a material is not adequate for predicting cell adhesion. We

found similar results in another study, where comparable levels of protein adsorption between SBMA- and carboxybetaine methacrylate (CBMA)-coated glass were observed, but significant differences in fibroblast adhesion were noted.[204]

7.5 CONCLUSIONS

Zwitterionic materials maintain excellent anti-fouling properties, but their use as coatings is limited due to their poor mechanical properties. Thus, engineering zwitterionic materials that are durable would be necessary to design anti-fouling coatings that will retain their advantageous properties long-term. In this work, we engineered SBMA hydrogels with improved mechanical properties by changing the concentration of the crosslinker PEGDA and HEMA in the formulation. Changing the crosslink density resulted in over an order of magnitude increase in modulus. The addition of HEMA to the SBMA hydrogels also resulted in moderate increases in modulus, but more dramatic improvements were observed in toughness of these materials. In addition, the anti-fouling properties of the various formulations were tested. All formulations demonstrated similar levels of nonspecific protein adsorption. In contrast, cell adhesion was increased at higher concentrations of both PEGDA and HEMA, with HEMA increasing cell adhesion to a greater extent. At moderate concentrations, cell density and protein adsorption were dramatically decreased and the mechanical properties were improved. These results demonstrate the balance between anti-fouling properties and strengthening zwitterionic hydrogel materials through PEGDA and HEMA additives. The advances reported herein stand to improve the longevity and integration of biomedical devices.

CHAPTER 8: CONCLUSIONS AND RECOMMENDATIONS

In the last century, the scientific understanding of how biomaterials interact with the body has changed dramatically. The use of synthetic organic polymers for medical applications has improved the efficacy of medical implants and prompted new avenues of research and understanding of tissue/material interactions. In particular, the treatment of sensorineural hearing loss has improved significantly since Dr. William House developed the first commercially available cochlear implants in the early 1970s. What began as a single-electrode device has evolved to incorporate as many as 22 independently stimulated electrodes. The research presented in this thesis explores the use of photopolymerizable materials that are specifically designed to drive favorable or prevent unfavorable biological interactions. To this end, the neural/material interactions that direct nerve growth by patterning bioactive molecules onto biomaterial surfaces have been examined. Further, engineering surfaces with zwitterionic polymers to prevent biofouling and the foreign body response has also been examined. The advances described herein stand to improve the materials used in CIs and the hearing outcomes of CI patients.

8.1 CONCLUSIONS

Spatial control of neurite regeneration from sensory neurons stimulated by neural prosthetics may serve as a viable method to improve resolution for many devices. A facile method to pattern laminin onto photopolymerizable acrylate polymers has been described. Illuminating adsorbed laminin through a photomask deactivated protein to form active protein patterns in unexposed areas and deactivated protein in exposed regions. Decreases in antibody binding to the exposed laminin demonstrated the photodeactivation process. While the protein was deactivated by UV-light, the protein remained adsorbed to the surface. SGN neurites

cultured on 50 μm active laminin stripes turned to align along the patterns. It was observed that the neurites preferentially grew on the active laminin regions. Previous research in our lab has shown that the strength of a physical cue can be modulated by changing either the amplitude or the periodicity of the microchannels. Greater alignment of SGN neurites was observed with higher amplitude and lower periodicity patterns. As neurites regrown *in vivo* are likely to encounter competing cues, SGN neurites were cultured on perpendicular biochemical and physical cues. At weak and intermediate physical cues, SGN neurites aligned more closely to the laminin pattern. When cultured on micro-patterns with stronger guidance cues, SGN neurite alignment to the laminin pattern was disrupted showing no distinct preference to either cue. These findings demonstrate that physical and/or biochemical cues can be used to align neurites and even overcome competing cues, which may be necessary for directing neurite *in vivo* when neurons encounter conflicting cues.

Engineering surfaces that prevent the nonspecific adsorption of protein to biomedical implant surfaces may allow significant mitigation of fibrosis and directing of cell growth. This work described a facile photopolymerization method to covalently graft two zwitterionic polymers from glass surfaces. The physicochemical properties of glass surfaces were tuned by altering zwitterionic monomer concentrations in the aqueous solution. X-ray photoelectron spectroscopy (XPS) measurements showed increases in surface composition with increasing monomer concentrations. The surface properties of the glass surfaces also responded to changes in concentration. Water contact angles and nonspecific protein adsorption decreased sharply at solution concentrations much lower than the saturation observed using XPS. These results indicate that only a very thin coating of zwitterionic polymer is necessary to elicit significant changes in surface properties. An important goal of this study was to directly compare the ability

of SBMA- and CBMA-coated surfaces to reduce adsorption of fibrinogen and adhesion of various cell types. Fibroblasts, astrocytes, and Schwann cells all showed dramatic decreases in cell density on SBMA- and CBMA-coated surfaces as compared to uncoated substrates. Fibroblasts also exhibited a significantly lower cell density between SBMA- and CBMA-coated surfaces, with CBMA-coated systems showing orders of magnitude decreases in adhesion. Using a photomask, 100 μm periodicity zwitterionic parallel line patterns were generated to evaluate the cellular adhesion of coated compared to uncoated glass regions. All cell types grown on patterned substrates showed cell growth in areas that were not coated with the zwitterionic polymer. The CBMA stripes proved to be more effective than SBMA stripes at preventing cell growth with fewer cell crossings along the CBMA patterns and greater cellular repulsion along film edges. Further, CBMA was better able to guide the alignment of Schwann cell and SGN neurites between the zwitterionic stripes. Therefore, CBMA-coated surfaces demonstrated a superior ability to resist cell adhesion and to direct cell growth. The described photopolymerizable surfaces enabled investigation of cell-material interactions that could enable engineering of surfaces that resist fibrotic tissue formation. Additionally, generated micropatterns provide potential in directing regeneration of neurites for cochlear implant materials development.

While the study described above demonstrated the efficacy of SBMA and CBMA polymers in preventing nonspecific protein adsorption and cell adhesion, glass is not a common implant material. Additionally, the linear polymers on glass could be easily sheared and would have limited long-term use. Thus, coating implant materials with a durable zwitterionic polymer will be necessary to improve existing implants. Accordingly, we described a simple method to photograft durable crosslinked SBMA and CBMA polymers to PDMS, the material that houses

cochlear implant electrode arrays. The type II photoinitiator benzophenone was used to covalently photograft the zwitterionic polymer to PDMS in a single step. The dependence of the photografting on the benzophenone was demonstrated by altering the amount adsorbed on the surface. Quantification of the adhesion was conducted using a shear adhesion test. The adhesion increased with benzophenone feed concentration until a critical concentration was reached between 1 and 2.5 g/L above which cohesive failure was observed.

Antifouling properties of the zwitterion-coated PDMS surfaces were then tested by evaluating protein adsorption and cell adhesion. SBMA- and CBMA-coated substrates both significantly reduced nonspecific adsorption of fibrinogen compared to uncoated controls. Fibroblast adhesion was also dramatically reduced when zwitterionic coatings were applied which showed resistance for up to 14 days *in vitro*. Finally, the adhesion of two strains of bacteria, *Staphylococcus Aureus* (*S. Aureus*) and *Staphylococcus Epidermidis* (*S. Epidermidis*) was evaluated. The CBMA-coated substrates demonstrated greater resistance to adhesion of both bacteria with both significantly decreasing the adhesion. These results demonstrate that zwitterionic coatings can be applied to PDMS substrates using a simple and controllable technique and lay the groundwork for use as coatings for existing implantable materials.

Zwitterionic materials maintain excellent anti-fouling properties, but their use as coatings is limited due to their relatively weak mechanical properties. Thus, engineering durable zwitterionic materials is necessary when designing antifouling coatings that will retain their advantageous properties long-term. SBMA hydrogels with improved mechanical properties were engineered by changing the concentration of crosslinking molecule and adding 2-hydroxyethyl methacrylate (HEMA) to the formulation. Changing the crosslink density resulted in almost an order of magnitude increase in modulus. The addition of HEMA to the SBMA hydrogels also

resulted in moderate increases in modulus with dramatic improvements in toughness. The addition of non-zwitterionic materials to the SBMA hydrogels changed the fouling properties of the material. While no significant differences in protein adsorption were observed, the addition of HEMA and PEGDA to the formulation increased cell adhesion. For HEMA samples, cell adhesion was entirely prevented up to a 1:1 ratio of SBMA to HEMA while the addition of PEGDA increased cell adhesion with each successive increase in PEGDA concentration. These results demonstrate that SBMA hydrogels can be strengthened by adding monomers but may alter fouling properties of the anti-fouling film.

8.2 RECOMMENDATIONS

While many significant advances in biomaterials science have recently been seen and our understanding of the bodily reaction to these materials has increased, considerable room for improvement still remains. Specifically, while cochlear implant patients are able to understand rudimentary sentences, the number of independent tonal channels is usually limited to around 8, due to the significant spatial separation between the stimulating electrode array and the primary neural receptors. Engineering guidance conduits to direct the regrowth of SGN neurites to approach or even contact stimulating electrodes has the potential to dramatically impact the number of independent tones a patient can perceive. Further, the long-term hearing outcomes of CI users can be preserved by improving the bodily response to CI electrodes. Next generation CIs are utilizing drug delivery mechanisms to mitigate the inflammatory response to implantation, but the long-term outcomes remain unknown. The future perspectives and recommendations for the work presented in this thesis can be categorized into two topics: 1) directing neurite growth and 2) mitigating the foreign body response. Perspectives on these two approaches will be described in the following sections.

The photodeactivation process used to pattern protein onto acrylate polymer surfaces could be more broadly applied to proteins of various types. While laminin provided a cell adhesive mechanism for directing neurites to preferentially grow along the stripes, cell repulsive proteins could also be examined. For example, EphA4-Fc is a chimeric peptide consisting of the chemorepulsive extracellular domain of EphA4 fused to the Fc portion of immunoglobulin that has been shown to repel SGN neurite growth. It is likely that this protein would also be photodeactivated by the UV-illumination process and could be applied to acrylate polymer. Further, other cell adhesion proteins such as collagen I and fibronectin could also be applied in a similar manner. The alignment of SGN neurites to these protein patterns would then be compared to that of laminin described in Chapter 4 to select a neurite-directing system that would be most suitable for nerve regeneration therapies.

Natural neurite growth is known to respond to a complex milieu of cellular signals *in vivo*. Competing guidance cues, as described in Chapter 4, provide a measure of the strength of each individual cue in directing neurite growth, however, combining these cues to synergistically guide neurite pathfinding could increase guidance beyond physical or chemical patterns alone. Therefore, it is likely that parallel biochemical (laminin) and physical (microgrooves) patterns will align SGN neurites more strongly than each independent cue alone. Microgroove fabrication and laminin patterning are separate and independent processes, thus it will be important to precisely align the physical pattern to the laminin pattern. To accomplish this fabrication, microgrooves must first be created. Laminin can then be adsorbed onto the polymer surface and a mask aligner will be used to precisely align the physical micropattern with the parallel bands of the photomask. Illumination of the sample through the photomask will enable the “active” laminin to be patterned parallel to the microgrooves of the polymer. Further, the position of the

laminin pattern (in the groove or on the ridge) is anticipated to play a significant role in directing neurite growth. Our lab has shown that SGN neurites exhibit preferential growth on depressed microfeatures, therefore it is hypothesized that laminin stripes found in the grooves will more precisely guide the growth of neurites when compared to stripes found on the ridges. The positioning of the laminin (on the grooves or the ridges) would also have an effect on the percent neurite length in the groove and the number of neurite crosses.

It has been reported previously in our lab that multidirectional 90^{o} patterns were ineffective in consistently guiding neurites along the right angle turns. It remains unclear why *de novo* neurite growth did not closely follow these multidirectional topographical cues. To elucidate the degree to which photopolymerized turning topographies control the pathfinding of SGN neurites, a series of micropatterns with varying degree of turning could be fabricated. For example, SGN neurites may respond more readily to gradually-turning features than the sharp 90^{o} patterns we previously investigated. The information gained from those experiments would help drive the design of directed nerve regeneration therapies.

In Chapter 5, photopolymerized zwitterionic patterns were fabricated to investigate the effect of these patterns on SGN neurite growth among other cell types. The CBMA-coated areas prevented almost all cell adhesion and precisely guided SGN neurites along 100 μm parallel micropatterns. To investigate this study further, a more diverse group of micropatterns could be examined. For example, the periodicity could be varied to determine at what width the neurites begin to deviate from alignment or the cell adhesion is prevented altogether. It is likely that wider features would result in alignment deviating significantly from the results reported in Chapter 5. Conversely, as the patterns become more frequent, the neurites may be guided to nearly perfect alignment. Another approach to using zwitterions to control neurite pathfinding is

engineering surfaces with complex patterns. Due to the repulsive nature of the zwitterionic patterns and lack of all cell growth on CBMA-coated regions, it is likely that angled microfeatures could guide the growth of SGN neurites more strongly than the topographical angled patterns. Accordingly, 90^{o} patterns could be fabricated and the outgrowth of SGN neurites could be determined to these patterns. Further, the ability of SGNs to turn to angles of varying curvature could be tested. Patterns with greater up to 180^{o} turns could be incorporated to see how neurite pathfinding is affected when approaching a curvature and how finely the patterns can control outgrowth.

While the focus of this thesis for directing SGN neurite growth has been largely on photopolymerized micropatterns, other topographies could be implemented to study their impact on neurite pathfinding. For example, a system that mimics the natural cellular environment could provide insight into how SGN neurites respond to topographical cues similar to those encountered *in vivo*. In particular, aligned nano/microfibers have been used as cell-directing topographies, but have yet to be investigated using SGN neurites. Fibers ranging in diameter from hundreds of nanometers to hundreds of micrometers can be fabricated using a process called electrospinning. The resulting aligned nano- or micro-scale fibers could give a topographical cue to adhered cells. Importantly, the fibers can be composed of a variety of polymeric materials and have similarities to the natural extracellular matrix. Some common features are thin and continuous strands, high surface-to-volume ratios, and a large number of variable sized pores. The fiber diameter could have an impact on the alignment of SGN neurites and varying parameters such as molecular weight, viscosity, needle gauge, and electric potential can control this diameter.

While much work has been conducted to direct neurite pathfinding in 2-dimensions, understanding which geometries can effectively guide neural processes in 3D has not been explored in any detail particularly using SGN neurites. Building upon the fundamental knowledge obtained from previous research in our lab, contact guidance cues could be fabricated in 3D using unique architectures to align neurites along user-defined pathways. The topography of a designed scaffold has an effect on cellular response to a given biomaterial. Specifically, the angle at which a neurite contacts a physical guidance cue strongly affects alignment along the pattern. Previous results from our lab have shown that the maximum slope of the microchannel correlates strongly to the alignment of SGN neurites grown on 2D substrates.[147] These results strongly imply that substrate geometry, specifically of a designed microchannel, will alter neurite behavior and can be user-defined to tune the pathfinding of SGN neurites. To investigate this effect, rigid 3D neurite guidance channels could be fabricated using two-photon lithography with various inner-channel shapes. The pathfinding and the deviation from the length along the channel would determine how well each geometry could guide neural processes. These experiments will help elucidate which geometries are most effective in controlling the pathfinding of SGN neurites. Further, the diameters of these channels could also be varied to investigate changes in dimension on pathfinding. While the design of these constructs would be challenging and achieving neurite penetration into the channels may also prove difficult, the information gained stands to greatly benefit the understanding of contact guidance in 3D.

While substrate geometry is crucial to the directed outgrowth of neurites, 3D chemical cues also play an important role. Recent research has shown that cells can be encapsulated in a 3D hydrogel matrix to study how cells migrate and proliferate in a 3D environment.[51] Importantly, the hydrogel matrix can be modified (i.e. modulus, chemistry etc.) to incorporate

cues that study cellular interactions with a material. Accordingly, bioactive molecules, such as the RGD (arginine-glycine-aspartic acid), could be patterned through a hydrogel matrix. By adding a cysteine peptide on the RGD sequence, thiol-ene chemistry could be utilized to covalently attach this bioactive peptide with light. Thiol moieties react readily with acrylates and could be patterned using similar photomasking techniques described throughout this thesis. A PEGDA hydrogel could be partially cured leaving unreacted acrylates available for post-functionalization. The hydrogel could then be swollen in a cysteine-containing RGD peptide and illuminated in regions where functionalization is desired. The system could then be washed to remove unreacted RGD, leaving the covalently-grafted bioactive pattern. These patterned systems can be seeded with cells to study the guidance of SGN neurites in 3D.

Zwitterionic materials have been shown to greatly reduce nonspecific protein adsorption, cell adhesion, and other biomolecule adsorption *in vitro*, but their durability is significantly limited due to the weak mechanical properties of CBMA and SBMA hydrogels. The strategies outlined in Chapter 8 represent two approaches to strengthen zwitterionic hydrogel materials, but significant work remains. For example, the system described in Chapter 8 focuses only on SBMA hydrogels, where the same parameters could also be applied to a CBMA hydrogel. Investigating how CBMA hydrogels could be strengthened by changing the concentration of PEGDA crosslinker and the additive HEMA could improve our understanding of their fouling properties. These experiments would likely provide greater insight into the effect of non-zwitterionic additives to these hydrogels due to the superior anti-fouling properties of CBMA compared to SBMA. Further, additional crosslinking molecules could be investigated to test their compatibility and effect on anti-fouling properties. For example, *N*,*N*′-methylenebis(acrylamide) is an alternative crosslinking molecule that could also be investigated to examine the changes on

mechanical at higher crosslink densities. It is possible that these non-zwitterionic molecules contribute significantly to fouling in particular the FBR. Thus, a hydrogel fabricated from one hundred percent zwitterionic monomers may be necessary. A CBMA derivative crosslinker could be synthesized which would allow a hydrogel to be formed with excellent control over the mechanical properties without sacrificing biological efficacy.

The mechanical properties of hydrogels can also be altered by incorporating nanoparticles into the formulation. Several reports have shown that the addition of nanoclays to prepolymer formulations increases elongation and overall toughness of the hydrogels.[283] These nanoclay additives could be added to SBMA and CBMA hydrogels to dramatically increase elongation and toughness of the materials. While the concentration of the nanoclay would be less than 10 wt%, the addition of a non-zwitterionic material has the potential to negatively impact the anti-fouling properties of the hydrogel. To prevent these deleterious effects, a zwitterionic silane coupling agent could be covalently grafted to the nanoclay surface. These zwitterionic nanoclays could then be added to hydrogels to increase elongation and toughness while still maintaining anti-fouling. The addition of these nanoclays has the potential to significantly impact durability and long-term use.

While the zwitterionic hydrogels could be engineered to increase durability, their impact on adhesion must also be investigated. Further, the benzophenone-grafted films, described in Chapter 6, demonstrated that lightly crosslinked, and therefore weak, hydrogels failed cohesively when testing adhesion. The cohesive failure indicates that the bond between the film and the substrate is stronger than the cohesive strength of the material. When the material is strengthened, it is unknown how strongly the zwitterionic hydrogels will remain adhered to the PDMS substrates. Thus, shear adhesion tests could be conducted on the grafted hydrogels to

characterize how the increase in hydrogel strength impacts the adhesion to the PDMS substrate. If the adhesion to the PDMS fails (demonstrated by adhesive failure), further strengthening of the adhesion is necessary. An alternative grafting approach could be implemented utilizing a silane coupling agent to covalently bind a reactive methacrylate group onto the PDMS surface. This strategy has the potential to improve the bond between the zwitterionic film and the PDMS substrate and could be evaluated using shear adhesion testing.

While the grafting process in this thesis has focused largely on PDMS materials, cochlear implant electrode arrays also contain platinum/iridium electrodes that come into direct contact with host fluid. These areas are of particular concern for fibrosis because the applied current is localized to these areas. Thus, fibrosis around the electrodes has the potential to significantly increase current attenuation and consequent current spread. Developing a process to coat platinum/iridium with a crosslinked durable zwitterionic hydrogel could mitigate the fibrosis and subsequent current attenuation. One approach to engineer a robust bond between platinum and crosslinked methacrylate polymers is by first generating an oxide layer on the surface. This thin layer can be achieved by plasma/O_3 treatment or through oven firing in the presence of oxygen. Once the oxide layer has formed, vinyl phosphonic acid can be reacted with the substrate to create a reactive group on the surface. The vinyl groups at the surface can then react with methacrylates, and a durable adhesive bond can be created. Evaluation of the strength of the bond between the crosslinked zwitterionic thin films and the platinum could be evaluated using shear adhesion experiments. The ability of the covalently grafted zwitterionic thin films to resist fouling on the platinum substrate could then be evaluated by nonspecific protein adsorption and cell adhesion.

While the addition of a crosslinked zwitterionic coating to a metal electrode is likely to dramatically decrease the amount of fibrosis and consequent current attenuation and spread, the thin film may also affect the electrical transport. To evaluate this effect, current could be applied to electrodes with the grafted zwitterionic polymer and the attenuation could be measured. The dependence of this attenuation on film thickness could also be altered by varying the amount of monomer that is in contact with the electrode during polymerization. To further examine the effect of these zwitterionic coatings on current attenuation, an electrode array could be fabricated and the broadening of the applied current could be mapped to demonstrate the effect of the zwitterionic coating on signal resolution. These experiments would establish how the zwitterionic thin films would affect current transport to the target neurons.

The substrates coated as described in this thesis have been of simple geometry (flat surfaces), but coating substrates with more complex geometry would be necessary to coat cochlear implant electrode arrays or other biomedical implants. To achieve a uniform coating across a cylindrical implant, similar to what a cochlear implant would be, a dip coating method could be applied. To effectively coat a material using this method, excellent wetting must be achieved to avoid aggregation of the liquid before polymerization occurs. PDMS is a hydrophobic material and the high water contact angles must be overcome before a dip coating method could be applied. Silicone surfactants could be added to the formulation to achieve dramatically lower water contact angles and increase wetting. To then apply the coating, the implant could be drawn out of a solution of zwitterionic monomer and UV-cured as the material leaves the vat of monomer. Parameters such as solution viscosity and draw rate impact the thickness of the films and would need to be tailored for the desired application. Developing these

techniques could expand the application of these materials and would allow them to be applied to a diverse group of implantable and geometrically complex implants.

Once strategies have been developed to effectively dip coat complex geometries, these zwitterion-coated devices could be evaluated for fibrosis *in vivo*. To achieve a material that maintains the strongest resistance to the FBR, it would be preferable to select the CBMA zwitterion and CBMA-based zwitterionic crosslinker mentioned previously due to their inherent superiority over other zwitterionic polymers. This system would be constructed from 100% zwitterion and thus the most likely to effectively mitigate the FBR. Cochlear implants are intended for long-term implantation, and a grafted zwitterionic polymer must remain adhered to the implant and resist the FBR for years to be an effective coating. To examine this effect, CBMA-coated PDMS could be implanted into the cochlea of a rat model, and the fibrosis/scarring could be evaluated. It is anticipated that CBMA-coated implants will prevent an inflammatory response that could impact hearing. This impact on hearing would be examined by measuring the difference in ABR thresholds for coated compared to uncoated implants. Further, to test the durability and adhesion of the zwitterionic polymer to the PDMS, the samples could be removed and immersed in an aqueous dye which would be absorbed by the CBMA hydrogel and expose the coated regions. The results from these experiments would help characterize the effectiveness of the implants in mitigating the FBR and the long term impacts on hearing.

A final approach to mitigating the FBR that has been investigated by other researchers is incorporating glucocorticoids as an immunomodulatory approach. These drugs have been incorporated as a systemic medication for many years and have more recently been used in a number of topical and immunomodulatory drugs. The initial inflammatory reaction in response to implantation of a cochlear implant and subsequent fibrosis could potentially be mitigated by

using the glucocorticoid dexamethasone. Several studies have shown promise that this drug can decrease inflammation and fibrosis around a cochlear implant. Accordingly, PDMS doped with dexamethasone could be coated with a CBMA hydrogel to examine the synergistic effect of an anti-fouling coating and a drug eluting cochlear implant. The differences in ABR thresholds and fibrosis around the implant could also be examined and compared for uncoated and CBMA-coated devices. These experiments will help establish how well these two mechanisms can be used to prevent fibrosis and inflammation.

The work presented in this thesis represents contributions and significant advances made to improving the tissue/material interaction for cochlear implant biomaterials. Specifically, this report demonstrates the effectiveness of photogenerated chemical and physical micropatterns used as a platform for directing cell adhesion and growth. Zwitterionic and protein micropatterns both show a strong effect on pathfinding of SGN neurites. This work also demonstrates the efficacy of two zwitterionic polymers, formed from SBMA and CBMA, to prevent protein adsorption and cell adhesion *in vitro*. Importantly, CBMA micropatterns generated on glass substrates revealed a remarkable ability to locally prevent fibroblast and other neural cells from adhering. Coating existing cochlear implant materials such as PDMS with crosslinked SBMA and CBMA polymers was accomplished by photografting using a type II photoinitiator. The dependence of the adhesion on the type II photoinitiator was elucidated. Finally, the strength and durability of zwitterionic hydrogels could be strengthened by altering monomer formulations. The fundamental understanding and design of cochlear implant materials described herein serves as a foundation for the development of next generation neural prosthetics. The advances made to grafting zwitterionic materials can be more broadly applied to any implantable device and could benefit the lives of millions of implant patients.

REFERENCES

(1) *2016 Top Markets Report Medical Devices*; 2016.

(2) Contreras-García, A.; Bucio, E. Biomedical Devices Based on Smart Polymers. *Responsive Mater. Methods* **2014**, 105–122.

(3) Toner, M.; Buettner, H. Microfabrication in Biology and Medicine. *Biotechnol. Prog.* **1998**, *14* (3), 355–355.

(4) Kubik, T.; Bogunia-Kubik, K.; M., S. Nanotechnology on Duty in Medical Applications. *Curr. Pharm. Biotechnol.* **2005**, *6* (1), 17–33.

(5) De Jong, W. H.; Borm, P. J. a. Drug Delivery and Nanoparticles:applications and Hazards. *Int. J. Nanomedicine* **2008**, *3* (2), 133–149.

(6) Cao, Z.; Zhang, L.; Jiang, S. Superhydrophilic Zwitterionic Polymers Stabilize Liposomes. *Langmuir* **2012**, *28* (31), 11625–11632.

(7) Cao, Z.; Yu, Q.; Xue, H.; Cheng, G.; Jiang, S. Nanoparticles for Drug Delivery Prepared from Amphiphilic PLGA Zwitterionic Block Copolymers with Sharp Contrast in Polarity between Two Blocks. *Angew. Chemie - Int. Ed.* **2010**, *49* (22), 3771–3776.

(8) Hoffman-Kim, D.; Mitchel, J. A.; Bellamkonda, R. V. Topography, Cell Response, and Nerve Regeneration. *Annu. Rev. Biomed. Eng.* **2010**, *12*, 203–231.

(9) Chou, L.; Firth, J. D.; Uitto, V. J.; Brunette, D. M. Substratum Surface Topography Alters Cell Shape and Regulates Fibronectin mRNA Level, mRNA Stability, Secretion and Assembly in Human Fibroblasts. *J. Cell Sci.* **1995**, *108* (4), 1563–1573.

(10) Spivey, E. C.; Khaing, Z. Z.; Shear, J. B.; Schmidt, C. E. The Fundamental Role of Subcellular Topography in Peripheral Nerve Repair Therapies. *Biomaterials* **2012**, *33* (17), 4264–4276.

(11) Ratner, B. D.; Bryant, S. J. Biomaterials: Where We Have Been and Where We Are Going. *Annu. Rev. Biomed. Eng.* **2004**, *6* (1), 41–75.

(12) Mackenzie, D. The History of Sutures. *Med. Hist.* **1973**, *17* (2), 158–168.

(13) Ratner, B. D.; Hoffman, A. S.; Schoen, F. J.; Lemons, J. E. *Biomaterials Science*; 2013.

(14) Bobbio, A. The First Endosseous Alloplastic Implant in the History of Man. *Bull. Hist. Dent.* **1972**, *20* (1), 1–6.

(15) Jay, B. Harold Ridley and the Invention of the Intraocular Lens. *Surv. Opthalmology* **1994**, *40* (4), 279–292.

(16) Ratner, B. D. Reducing Capsular Thickness and Enhancing Angiogenesis around Implant Drug Release Systems. *J. Control. Release* **2002**, *78*, 211–218.

(17) Branemark, P. I., Breine, U., Johansson, B., Roylance, P. J., R.; ¨ckert, H. & Yoffey, J. M. Regeneration of Bone Marrow. *J. Chem. Inf. Model.* **1964**, *53* (9), 1689–1699.

(18) Eftekhar, N. S. The Life and Work of John Charnley. *Clin. Orthop. Relat. Res.* **1986**, No. 211, 10–22.

(19) Jackson, J. Father of the Modern Hip Replacement: Professor Sir John Charnley (1911-82). *J. Med. Biogr.* **2011**, *19* (4), 151–156.

(20) Gunston, F. H. Polycentric Knee Arthroplasty: Prosthetic Simulation of Normal Knee Movement. *J. BONE Jt. Surg.* **1971**, *53* (2), 272–277.

(21) Twiss, E. E.; Kolff, W. J. Treatment of Uremia by Perfusion of an Isolated Intestinal Loop; Survival for Forty-six Days after Removal of the Only Functioning Kidney. *J. Am. Med. Assoc.* **1951**, *146* (11), 1019–1022.

(22) Anderson, A.; Kolff, W. J. Artificial Kidney in the Treatment of Uremia Associated with Acute Glomerulonephritis (with a Note on Regional Heparinization). *Ann. Intern. Med.* **1959**, *51*, 467–487.

(23) Blagg, C. Development of Ethical Concepts in Dialysis: Seattle in the 1960s. *Nephrology* **1998**, *4*, 235–238.

(24) Gruntzig, A. Transluminal Dilatation of Coronary-artery Stenosis. *Lancet* **1978**, *1* (8058), 263.

(25) Iqbal, J.; Gunn, J.; Serruys, P. W. Coronary Stents: Historical Development, Current Status and Future Directions. *Br. Med. Bull.* **2013**, *106* (1), 193–211.

(26) Aquilina, O. A Brief History of Cardiac Pacing. *Images Paediatr. Cardiol.* **2006**, *8* (2), 17–18.

(27) Ward, C.; Henderson, S.; Metcalfe, N. H. A Short History on Pacemakers. *Int. J. Cardiol.* **2013**, *169* (4), 244–248.

(28) Colas, A.; Curtis, J. *Silicone Biomaterials: History and Chemistry and Medical Applications of Silicones*; 2004.

(29) Rochow, E. *The Chemistry of Silicones*; 1946.

(30) Jaques, L. B.; Fidlar, E.; Feldsted, E. T.; Macdonals, M. D.; Macdonal, A. G. Silicones and Blood Coagulation. *Fed. Proc.* **1946**, *55* (1), 26–31.

(31) Lahey, F. H. Comments Made Following the speech “Results from Using Vitallium Tubes in Biliary Surgery,” read by Pearse HE before the American Surgical Association, Hot Springs, VA. *Annu. Surg.* **1946**, *124*, 1027.

(32) DeNicola, R. R. Permanent Artificial (Silicone)urethra. *J. Urol.* **1950**, *63* (1), 168–172.

(33) Burke, A.; Hasirci, N. Polyurethanes in Biomedical Applications. *Adv. Exp. Med. Biol.* **2004**, *553*, 83–101.

(34) Boretos, J. W.; Pierce, W. S. Segmented Polyurethane: A New Elastomer for Biomedical Applications. *Science.* **1967**, *158* (3807), 1481–1482.

(35) Boretos, J. W.; Detmer, D. E.; Donachy, J. H. Segmented Polyurethane: A Polyether Polymer, II. Two Years Experience. *J. Biomed. Mater. Res.* **1971**, *5* (4), 373–387.

(36) Boretos, J. W.; Pierce, W. S.; Baier, R. E.; Leroy, A. F.; Donachy, H. J. Surface and Bulk Characteristics of a Polyether Urethane for Artificial Hearts. *J. Biomed. Mater. Res.* **1975**, *9* (3), 327–340.

(37) Boretos, J. W. Past, Present and Future Role of Polyurethanes for Surgical Implants. *Pure Appl. Chem.* **1980**, *52* (7), 1851–1855.

(38) Ihlenfeld, J. V.; Mathis, T. R.; Riddle, L. M.; Cooper, S. L. Measurement of Transient Thrombus Deposition on Polymeric Materials. *Thromb. Res.* **1979**, *14* (6), 953–967.

(39) Pentz, W. J.; Krawiec, R. G. Hydrolytic Stability of Polyurethane Elastomers. *Rubber Age* **1975**, *107* (12), 39–43.

(40) Kolff, T.; Burkett, G.; Feyen, J. Copolyether-urethanes as Materials for Artificial Hearts. *Biomater. Med. Devices. Artif. Organs* **1973**, *1* (4), 669–679.

(41) Klinge, U.; Park, J. K.; Klosterhalfen, B. The Ideal Mesh? *Pathobiology* **2013**, *80* (4), 169–175.

(42) Longo, U. G.; Lamberti, A.; Maffulli, N.; Denaro, V. Tendon Augmentation Grafts: A Systematic Review. *Br. Med. Bull.* **2010**, *94* (1), 165–188.

(43) Klinge, U.; Klosterhalfen, B. Modified Classiffication of Surgical Meshes for Hernia Repair Based on the Analyses of 1,000 Explanted Meshes. *Hernia* **2012**, *16* (3), 251–258.

(44) Berardinelli, L. Grafts and Graft Materials as Vascular Substitutes for Haemodialysis Access Construction. *Eur. J. Vasc. Endovasc. Surg.* **2006**, *32* (2), 203–211.

(45) Kannan, R. Y.; Salacinski, H. J.; Butler, P. E.; Hamilton, G.; Seifalian, A. M. Current Status of Prosthetic Bypass Grafts: A Review. *J. Biomed. Mater. Res. - Part B Appl. Biomater.* **2005**, *74* (1), 570–581.

(46) Laustriat, S.; Geiss, S.; Becmeur, F.; Bientz, J.; Marcellin, L.; Sauvage, P. Medical History of Teflon. *Eur. Urol.* **1990**, *17* (4), 301–303.

(47) Maitz, M. F. Applications of Synthetic Polymers in Clinical Medicine. *Biosurface and Biotribology* **2015**, *1* (3), 161–176.

(48) Gautam, R.; Singh, R. D.; Sharma, V. P.; Siddhartha, R.; Chand, P.; Kumar, R. Biocompatibility of Polymethylmethacrylate Resins Used in Dentistry. *J. Biomed. Mater. Res. - Part B Appl. Biomater.* **2012**, *100 B* (5), 1444–1450.

(49) Vaishya, R.; Chauhan, M.; Vaish, A. Bone Cement. *J. Clin. Orthop. Trauma* **2013**, *4* (4), 157–163.

(50) Cramer, N. B.; Couch, C. L.; Schreck, K. M.; Boulden, J. E.; Wydra, R.; Stansbury, J. W.;

Bowman, C. N. Properties of Methacrylate-Thiol-Ene Formulations as Dental Restorative Materials. *Dent. Mater.* **2010**, *26* (8), 799–806.

(51) Lewis, K. J. R.; Anseth, K. S. Hydrogel Scaffolds to Study Cell Biology in Four Dimensions. *MRS Bull.* **2013**, *38* (3), 260–268.

(52) Burdick, J. a; Anseth, K. S. Photoencapsulation of Osteoblasts in Injectable RGD-Modified PEG Hydrogels for Bone Tissue Engineering. *Biomaterials* **2002**, *23* (22), 4315–4323.

(53) Anderson, J. M. Mechanisms of Inflammation and Infection with Implanted Devices. *Cardiovasc. Pathol.* **1993**, *2* (3 SUPPL.), 33–41.

(54) Rolfe, B.; Mooney, J.; Zhang, B.; Jahnke, S.; Le, S.-J.; Huang, Q.; Wang, H.; Campbell, G.; Campbell, J. The Fibrotic Response to Implanted Biomaterials: Implications for Tissue Engineering. *Regen. Med. Tissue Eng. - Cells Biomater.* **2011**, 552–568.

(55) Anderson, J. M. Biological Responses to Materials. *Annu. Rev. Mater. Res.* **2001**, *31*, 81–110.

(56) Wick, G.; Grundtman, C.; Mayerl, C.; Wimpissinger, T.-F.; Feichtinger, J.; Zelger, B.; Sgonc, R.; Wolfram, D. The Immunology of Fibrosis. *Annu. Rev. Immunol.* **2013**, *31*, 107–135.

(57) Wang, J. Electrochemical Glucose Biosensors. *Chem. Rev.* **2008**, *108*, 814–825.

(58) Yang, W.; Bai, T.; Carr, L. R.; Keefe, A. J.; Xu, J.; Xue, H.; Irvin, C. a.; Chen, S.; Wang, J.; Jiang, S. The Effect of Lightly Crosslinked Poly(carboxybetaine) Hydrogel Coating on the Performance of Sensors in Whole Blood. *Biomaterials* **2012**, *33* (32), 7945–7951.

(59) Heller, A.; Feldman, B. Electrochemical Glucose Sensors and Their Applications in Diabetes Management. *Chem. Rev.* **2008**, *108* (7), 2482–2505.

(60) Quesnel, A. M.; Nakajima, H. H.; Rosowski, J. J.; Hansen, M. R.; Gantz, B. J.; Nadol, J. B. Delayed Loss of Hearing after Hearing Preservation Cochlear Implantation: Human Temporal Bone Pathology and Implications for Etiology. *Hear. Res.* **2015**, *333*, 225–234.

(61) Wilk, M.; Hessler, R.; Mugridge, K.; Jolly, C.; Fehr, M.; Lenarz, T.; Scheper, V. Impedance Changes and Fibrous Tissue Growth after Cochlear Implantation Are Correlated and Can Be Reduced Using a Dexamethasone Eluting Electrode. *PLoS One* **2016**, *11* (2), 1–19.

(62) Anderson, J. M. Inflammatory Response to Implants. *ASAIO Trans.* **1988**, *34* (2), 101–107.

(63) Clark, R. A. F.; DellaPelle, P.; Manseau, E.; Lanigan, J. M.; Dvorak, H. F.; Colvin, R. B. Blood Vessel Fibronectin Increases in Conjunction with Endothelial Cell Proliferation and Capillary Ingrowth during Wound Healing. *J. Invest. Dermatol.* **1982**, *79* (5), 269–276.

(64) Blaszykowski, C.; Sheikh, S.; Thompson, M. Surface Chemistry to Minimize Fouling from Blood-Based Fluids. *Chem. Soc. Rev.* **2012**, *41* (17), 5599–5612.

(65) Schlenoff, J. B. Zwitteration: Coating Surfaces with Zwitterionic Functionality to Reduce Nonspecific Adsorption. *Langmuir* **2014**, *30* (32), 9625–9636.

(66) Estephan, Z. G.; Schlenoff, P. S.; Schlenoff, J. B. Zwitteration as an Alternative to PEGylation. *Langmuir* **2011**, *27*, 6794–6800.

(67) Anderson, J. M.; Rodriguez, A.; Chang, D. T. Foreign Body Reaction to Biomaterials.

Semin. Immunol. **2008**, *20* (2), 86–100.

(68) Hetrick, E. M.; Prichard, H. L.; Klitzman, B.; Schoenfisch, M. H. Reduced Foreign Body Response at Nitric Oxide-Releasing Subcutaneous Implants. *Biomaterials* **2007**, *28* (31), 4571–4580.

(69) Henson, P. M. Mechanisms of Exocytosis in Phagocytic Inflammatory Cells. *Am. J. Pathol.* **1980**, *101* (3), 494–514.

(70) Henson, P. M. The Immunologic Release of Constituents from Neutrophil Leukocytes. II. Mechanisms of Release during Phagocytosis, and Adherence to Nonphagocytosable Surfaces. *J. Immunol.* **1971**, *107*, 1547–1557.

(71) Potter, M.; Rose, N. *Immunology of Silicones*; 1996.

(72) Yeh, S.-B.; Chen, C.-S.; Chen, W.-Y.; Huang, C.-J. Modification of Silicone Elastomer with Zwitterionic Silane for Durable Antifouling Properties. *Langmuir* **2014**, *30* (38), 11386–11393.

(73) Keefe, A. J.; Brault, N. D.; Jiang, S. Suppressing Surface Reconstruction of Superhydrophobic PDMS Using a Superhydrophilic Zwitterionic Polymer. *Biomacromolecules* **2012**, *13* (5), 1683–1687.

(74) Goda, T.; Matsuno, R.; Konno, T.; Takai, M.; Ishihara, K. Photografting of 2-Methacryloyloxyethyl Phosphorylcholine from Polydimethylsiloxane: Tunable Protein Repellency and Lubrication Property. *Colloids Surfaces B Biointerfaces* **2008**, *63* (1), 64–72.

(75) Ratner, B. D. A Pore Way to Heal and Regenerate: 21st Century Thinking on

Biocompatibility. *Regen. Biomater.* **2016**, *3* (2), 107–110.

(76) Jiang, S.; Cao, Z. Ultralow-Fouling, Functionalizable, and Hydrolyzable Zwitterionic Materials and Their Derivatives for Biological Applications. *Adv. Mater.* **2010**, *22* (9), 920–932.

(77) Mi, L.; Jiang, S. Integrated Antimicrobial and Nonfouling Zwitterionic Polymers. *Angew. Chemie Int. Ed.* **2014**, *53* (7), 1746–1754.

(78) Sussman, E. M.; Halpin, M. C.; Muster, J.; Moon, R. T.; Ratner, B. D. Porous Implants Modulate Healing and Induce Shifts in Local Macrophage Polarization in the Foreign Body Reaction. *Ann. Biomed. Eng.* **2014**, *42* (7), 1508–1516.

(79) Fristrup, C. J.; Jankova, K.; Hvilsted, S. Surface-Initiated Atom Transfer Radical Polymerization—a Technique to Develop Biofunctional Coatings. *Soft Matter* **2009**, *5* (23), 4623–4623.

(80) Zhang, L.; Cao, Z.; Bai, T.; Carr, L.; Ella-Menye, J.-R.; Irvin, C.; Ratner, B. D.; Jiang, S. Zwitterionic Hydrogels Implanted in Mice Resist the Foreign-Body Reaction. *Nat. Biotechnol.* **2013**, *31* (6), 553–556.

(81) Karp, R. D.; Johnson, K. H.; Buoen, L. C.; Ghobrial, H. K. G.; Brand, I.; Brand, K. G. Tumorigenesis by Millipore Filters in Mice: Histology and Infrastructure of Tissue Reactions as Related to Pore Size. *J. Natl. Cancer Inst.* **1973**, *51* (4), 1275–1285.

(82) Marshall, A. J.; Irvin, C. A.; Barker, T.; Sage, E. H.; Hauch, K. D.; Ratner, B. D. Biomaterials with Tightly Controlled Pore Size That Promote Vascular in-growth. *ACS Polym. Prepr.* **2004**, *45* (2), 100–101.

(83) Madden, L. R.; Mortisen, D. J.; Sussman, E. M.; Dupras, S. K.; Fugate, J. A.; Cuy, J. L.; Hauch, K. D.; Laflamme, M. A.; Murry, C. E.; Ratner, B. D. Proangiogenic Scaffolds as Functional Templates for Cardiac Tissue Engineering. *Proc. Natl. Acad. Sci.* **2010**, *107* (34), 15211–15216.

(84) Chen, S.; Jiang, S. A New Avenue to Nonfouling Materials. *Adv. Mater.* **2008**, *20* (2), 335–338.

(85) Zheng, J.; Li, L.; Tsao, H.-K.; Sheng, Y.-J.; Chen, S.; Jiang, S. Strong Repulsive Forces between Protein and Oligo (Ethylene Glycol) Self-Assembled Monolayers: A Molecular Simulation Study. *Biophys. J.* **2005**, *89* (1), 158–166.

(86) Chen, S.; Li, L.; Zhao, C.; Zheng, J. Surface Hydration: Principles and Applications toward Low-Fouling/nonfouling Biomaterials. *Polymer.* **2010**, *51* (23), 5283–5293.

(87) Howard, M. D.; Jay, M.; Dziubla, T. D.; Lu, X. PEGylation of Nanocarrier Drug Delivery Systems: State of the Art. *J. Biomed. Nanotechnol.* **2008**, *4* (2), 133–148.

(88) Shen, M.; Martinson, L.; Wagner, M. S.; Castner, D. G.; Ratner, B. D.; Horbett, T. A. PEO-like Plasma Polymerized Tetraglyme Surface Interactions with Leukocytes and Proteins: In Vitro and in Vivo Studies. *J. Biomater. Sci. Polym. Ed.* **2002**, *13* (4), 367–390.

(89) Cao, B.; Tang, Q.; Cheng, G. Recent Advances of Zwitterionic Carboxybetaine Materials and Their Derivatives. *J. Biomater. Sci. Polym. Ed.* **2014**, *25* (14–15), 1502–1513.

(90) Mi, L.; Jiang, S. Integrated Antimicrobial and Nonfouling Zwitterionic Polymers. **2014**, 1746–1754.

(91) Merriam-Webster's Dictionary.

(92) Bretscher, M. S.; Raff, M. C. Mammalian Plasma Membranes. *Nature* **1975**, *258* (5530), 43–49.

(93) West, S. L.; Salvage, J. P.; Lobb, E. J.; Armes, S. P.; Billingham, N. C.; Lewis, A. L.; Hanlon, G. W.; Lloyd, A. W. The Biocompatibility of Crosslinkable Copolymer Coatings Containing Sulfobetaines and Phosphobetaines. *Biomaterials* **2004**, *25* (7–8), 1195–1204.

(94) Andrade, J. D.; Hlady, V. Protein Adsorption and Materials Biocompatibility: A Tutorial Review and Suggested Hypotheses. *Adv. Polym. Sci.* **1986**, *79*, 1–63.

(95) Hayward, J. A.; Chapman, D. Biomembrane Surfaces as Models for Polymer Design: The Potential for Haemocompatibility. *Biomaterials* **1984**, *5* (3), 135–142.

(96) Ikada, Y.; Iwata, H.; Horii, F.; Matsunaga, T.; Taniguchi, M.; Suzuki, M.; Taki, W.; Yamagata, S.; Yonekawa, Y.; Handa, H. Blood Compatibility of Hydrophilic Polymers. *J. Biomed. Mater. Res.* **1981**, *15* (5), 697–718.

(97) Ikada, Y. Blood-Compatible Polymers. *Adv. Polym. Sci.* **1984**, *57*, 103–140.

(98) He, Y.; Hower, J.; Chen, S.; Bernards, M. Molecular Simulation Studies of Protein Interactions with Zwitterionic Phosphorylcholine Self-Assembled Monolayers in the Presence of Water. *Langmuir* **2008**, *22* (17), 10358–10364.

(99) Shao, Q.; Jiang, S. Molecular Understanding and Design of Zwitterionic Materials. *Adv. Mater.* **2015**, *27* (1), 15–26.

(100) Southall, N. T.; Dill, K. A.; Haymet, A. D. J. A View of the Hydrophobic Effect. *J. Phys. Chem. B* **2002**, *106* (3), 521–533.

(101) Jeon, S. I.; Lee, J. H.; Andrade, J. D.; De Gennes, P. G. Protein-Surface Interactions in the Presence of Polyethylene Oxide. I. Simplified Theory. *J. Colloid Interface Sci.* **1991**, *142* (1), 149–158.

(102) Currie, E. P. K.; Norde, W.; Cohen Stuart, M. A. C. *Tethered Polymer Chains: Surface Chemistry and Their Impact on Colloidal and Surface Properties*; 2003; Vol. 100–102.

(103) Nakanishi, K.; Sakiyama, T.; Imamura, K. On the Adsorption of Proteins on Solid Surfaces, a Common but Very Complicated Phenomenon. *J. Biosci. Bioeng.* **2001**, *91* (3), 233–244.

(104) Li, B.; Yu, B.; Ye, Q.; Zhou, F. Tapping the Potential of Polymer Brushes through Synthesis. *Acc. Chem. Res.* **2015**, *48* (2), 229–237.

(105) Cringus-Fundeanu, I.; Luijten, J.; Van Der Mei, H. C.; Busscher, H. J.; Schouten, A. J. Synthesis and Characterization of Surface-Grafted Polyacrylamide Brushes and Their Inhibition of Microbial Adhesion. *Langmuir* **2007**, *23* (13), 5120–5126.

(106) Sundaram, H. S.; Han, X.; Nowinski, A. K.; Brault, N. D.; Li, Y.; Ella-Menye, J.-R.; Amoaka, K. A.; Cook, K. E.; Marek, P.; Senecal, K.; et al. Achieving One-Step Surface Coating of Highly Hydrophilic Poly(Carboxybetaine Methacrylate) Polymers on Hydrophobic and Hydrophilic Surfaces. *Adv. Mater. Interfaces* **2014**, *1* (6), 1400071.

(107) Sundaram, H. S.; Han, X.; Nowinski, A. K.; Ella-Menye, J. R.; Wimbish, C.; Marek, P.; Senecal, K.; Jiang, S. One-Step Dip Coating of Zwitterionic Sulfobetaine Polymers on Hydrophobic and Hydrophilic Surfaces. *ACS Appl. Mater. Interfaces* **2014**, *6*, 6664–6671.

(108) Hong, D.; Hung, H. C.; Wu, K.; Lin, X.; Sun, F.; Zhang, P.; Liu, S.; Cook, K. E.; Jiang, S.

Achieving Ultralow Fouling under Ambient Conditions via Surface-Initiated ARGET ATRP of Carboxybetaine. *ACS Appl. Mater. Interfaces* **2017**, *9* (11), 9255–9259.

(109) Neugebauer, D. Two Decades of Molecular Brushes by ATRP. *Polymer.* **2015**, *72*, 413–421.

(110) Zhang, Z.; Zhang, M.; Chen, S.; Horbett, T. A.; Ratner, B. D.; Jiang, S. Blood Compatibility of Surfaces with Superlow Protein Adsorption. *Biomaterials* **2008**, *29* (32), 4285–4291.

(111) Zhang, Z.; Chao, T.; Chen, S.; Jiang, S. Superlow Fouling Sulfobetaine and Carboxybetaine Polymers on Glass Slides. *Langmuir* **2006**, *22* (12), 10072–10077.

(112) Carr, L. R.; Xue, H.; Jiang, S. Functionalizable and Nonfouling Zwitterionic Carboxybetaine Hydrogels with a Carboxybetaine Dimethacrylate Crosslinker. *Biomaterials* **2011**, *32* (4), 961–968.

(113) Yang, W.; Xue, H.; Carr, L. R.; Wang, J.; Jiang, S. Zwitterionic Poly(carboxybetaine) Hydrogels for Glucose Biosensors in Complex Media. *Biosens. Bioelectron.* **2011**, *26* (5), 2454–2459.

(114) Carr, L.; Cheng, G.; Xue, H.; Jiang, S. Engineering the Polymer Backbone To Strengthen Nonfouling Sulfobetaine Hydrogels. *Langmuir* **2010**, *26* (18), 14793–14798.

(115) Zhu, Y.; Xu, X.; Brault, N. D.; Keefe, A. J.; Han, X.; Deng, Y.; Xu, J.; Yu, Q.; Jiang, S. Cellulose Paper Sensors Modified with Zwitterionic Poly(carboxybetaine) for Sensing and Detection in Complex Media. *Anal. Chem.* **2014**, *86* (6), 2871–2875.

(116) Chien, H.-W.; Cheng, P.-H.; Chen, S.-Y.; Yu, J.; Tsai, W.-B. Low-Fouling and Functional

Poly(carboxybetaine) Coating via a Photo-Crosslinking Process. *Biomater. Sci.* **2017**.

(117) Zeng, F. G.; Rebscher, S.; Harrison, W.; Sun, X.; Feng, H. Cochlear Implants: System Design, Integration, and Evaluation. *IEEE Rev. Biomed. Eng.* **2008**, *1*, 115–142.

(118) Dhanasingh, A.; Jolly, C. An Overview of Cochlear Implant Electrode Array Designs. *Hear. Res.* **2017**, *356*, 93–103.

(119) O'Leary, S. J.; Richardson, R. R.; McDermott, H. J. Principles of Design and Biological Approaches for Improving the Selectivity of Cochlear Implant Electrodes. *J. Neural Eng.* **2009**, *6* (5), 55002.

(120) Volta, A. On the Electricity Excited by the Mere Contact of Conducting Substances of Different Kinds. *Philos. Trans. R. Soc. London* **1800**, *90* (January), 403–431.

(121) Eshraghi, A. A.; Nazarian, R.; Telischi, F. F.; Rajguru, S. M.; Truy, E.; Gupta, C.; Hospitalier, C.; Lyon, U. De. The Cochlear Implant : Historical Aspects and Future Prospects. **2016**, *295* (11), 1967–1980.

(122) Ramsden, R. T. History of Cochlear Implantation. *Cochlear Implants Int.* **2013**, *14 Suppl 4*, S3-5.

(123) Wever, E. G.; Bray, C. W. The Nature of Acoustic Response: The Relation between Sound Frequency and Frequency of Impulses in the Auditory Nerve. *J. Exp. Psychol.* **1930**, *13* (5), 373–387.

(124) Djourno, A.; Eyries, C. Auditory Prosthesis by Means of a Distant Electrical Stimulation of the Sensory Nerve with the Use of an Indwelt Coiling. *Presse Med.* **1957**, *65* (63), 1417.

(125) House, W. F.; Urban, J. Long Term Results of Electrode Implantation and Electronic Stimulation of the Cochlea in Man. *Ann. Otol. Rhinol. Laryngol.* **1973**, *82* (4), 504–517.

(126) House, W. F. Cochlear Implants. *Ann. Otol. Rhinol. Laryngol.* **1976**, *85 suppl 2*, 1–93.

(127) Eshraghi, A. A.; Gupta, C.; Ozdamar, O.; Balkany, T. J.; Truy, E.; Nazarian, R. Biomedical Engineering Principles of Modern Cochlear Implants and Recent Surgical Innovations. *Anat. Rec.* **2012**, *295* (11), 1957–1966.

(128) Wilson, B. S.; Dorman, M. F. Cochlear Implants: A Remarkable Past and a Brilliant Future. *Hear. Res.* **2008**, *242* (1–2), 3–21.

(129) Bilger, C. R.; Black, F. O. Auditory Prostheses in Perspective. *Ann. Otol. Rhinol. Laryngol. Suppl.* **1977**, *86* (38), 3–10.

(130) Clark, G.; Tong, Y.; Martin, L. A Multiple-Channel Cochlear Implant: An Evaluation Using Open-Set CID Sentences. *The Laryngiscope*. 1981, pp 628–634.

(131) O'Leary, S. J.; Richardson, R. R.; McDermott, H. J. Principles of Design and Biological Approaches for Improving the Selectivity of Cochlear Implant Electrodes. *J. Neural Eng.* **2009**, *6* (5), 55002.

(132) Saunders, E.; Cohen, L.; Aschendorff, A.; Shapiro, W.; Knight, M.; Stecker, M.; Richter, B.; Waltzman, S.; Tykocinski, M.; Roland, T.; et al. Threshold, Comfortable Level and Impedance Changes as a Function of Electrode-Modiolar Distance. *Ear Hear.* **2002**, *23* (1 Suppl), 28S–40S.

(133) Wise, A. K.; Richardson, R.; Hardman, J.; Clark, G.; O'Leary, S. Resprouting and Survival of Guinea Pig Cochlear Neurons in Response to the Administration of the

Neurotrophins Brain-Derived Neurotrophic Factor and Neurotrophin-3. *J. Comp. Neurol.* **2005**, *487* (2), 147–165.

(134) Miller, J. M.; Chi, D. H.; O'Keeffe, L. J.; Kruszka, P.; Raphael, Y.; Altschuler, R. A. Neurotrophins Can Enhance Spiral Ganglion Cell Survival after Inner Hair Cell Loss. *Int. J. Dev. Neurosci.* **1997**, *15* (4–5), 631–643.

(135) Altschuler, R. A.; Cho, Y.; Ylikoski, J.; Pirvola, U.; Magal, E.; Miller, J. M. Rescue and Regrowth of Sensory Nerves Following Deafferentation by Neurotrophic Factors. *Ann. N. Y. Acad. Sci.* **1999**, *884*, 305–311.

(136) Harrison, R. G. The Cultivation of Tissues in Extraneous Medium as a Method of Morphogenetic. *Anat. Rec.* **1912**, *6*, 181–193.

(137) Weiss, P. The Problem of Specificity in Growth and Development. *Yale J. Biol. Med.* **1947**, *19* (3), 235–278.

(138) Curtis, A. S.; Varde, M. Control of Cell Behavior: Topological Factors. *J. Natl. Cancer Inst.* **1964**, *33*, 15–26.

(139) Lim, J. Y.; Donahue, H. J. Cell Sensing and Response to Micro- and Nanostructured Surfaces Produced by Chemical and Topographic Patterning. *Tissue Eng.* **2007**, *13* (8), 1879–1891.

(140) Miller, C.; Jeftinija, S.; Mallapragada, S. Synergistic Effects of Physical and Chemical Guidance Cues on Neurite Alignment and Outgrowth on Biodegradable Polymer Substrates. *Tissue Eng.* **2002**, *8* (3), 367–378.

(141) Hirono, T.; Torimitsu, K.; Kawana, A.; Fukuda, J. Recognition of Artificial

Microstructures by Sensory Nerve Fibers in Culture. *Brain Res.* **1988**, *446* (1), 189–194.

(142) Clark, P.; Connolly, P.; Curtis, A. S.; Dow, J. A.; Wilkinson, C. D. Topographical Control of Cell Behaviour: II. Multiple Grooved Substrata. *Development* **1990**, *108* (4), 635–644.

(143) Li, N.; Folch, A. Integration of Topographical and Biochemical Cues by Axons during Grown on Microfabrication. *Exp. Cell Res.* **2005**, *311* (2), 307–316.

(144) Cecchini, M.; Ferrari, A.; Beltram, F. PC12 Polarity on Biopolymer Nanogratings. *J. Phys. Conf. Ser.* **2008**, *100* (1), 12003.

(145) Johansson, F.; Carlberg, P.; Danielsen, N.; Montelius, L.; Kanje, M. Axonal Outgrowth on Nano-Imprinted Patterns. *Biomaterials* **2006**, *27* (8), 1251–1258.

(146) Teixeira, A. I.; Abrams, G. A.; Bertics, P. J.; Murphy, C. J.; Nealey, P. F. Epithelial Contact Guidance on Well-Defined Micro- and Nanostructured Substrates. *J. Cell Sci.* **2003**, *116* (10), 1881–1892.

(147) Tuft, B. W.; Li, S.; Xu, L.; Clarke, J. C.; White, S. P.; Guymon, B. A.; Perez, K. X.; Hansen, M. R.; Guymon, C. A. Photopolymerized Microfeatures for Directed Spiral Ganglion Neurite and Schwann Cell Growth. *Biomaterials* **2013**, *34* (1), 42–54.

(148) Tuft, B. W.; Xu, L.; White, S. P.; Seline, A. E.; Erwood, A. M.; Hansen, M. R.; Guymon, C. A. Neural Pathfinding on Uni- and Multidirectional Photopolymerized Micropatterns. *ACS Appl. Mater. Interfaces* **2014**, *6* (14), 11265–11276.

(149) Tuft, B. W.; Zhang, L.; Xu, L.; Hangartner, A.; Leigh, B.; Hansen, M. R.; Guymon, C. A. Material Stiffness Effects on Neurite Alignment to Photopolymerized Micropatterns. *Biomacromolecules* **2014**, *15* (10), 3717–3727.

(150) Tuft, B. W.; Xu, L.; Leigh, B.; Lee, D.; Guymon, C. A.; Hansen, M. R. Photopolymerized Micropatterns with High Feature Frequencies Overcome Chemorepulsive Borders to Direct Neurite Growth. *J. Tissue Eng. Regen. Med.* **2017**.

(151) Bernard, A.; Renault, J. P.; Michel, B.; Bosshard, H. R.; Delamarche, E. Microcontact Printing of Proteins. *Adv. Mater.* **2000**, *12* (14), 1067–1070.

(152) Hersel, U.; Dahmen, C.; Kessler, H. RGD Modified Polymers: Biomaterials for Stimulated Cell Adhesion and beyond. *Biomaterials* **2003**, *24* (24), 4385–4415.

(153) Bellis, S. L. Advantages of RGD Peptides for Directing Cell Association with Biomaterials. *Biomaterials* **2011**, *32* (18), 4205–4210.

(154) von Philipsborn, A. C.; Lang, S.; Bernard, A.; Loeschinger, J.; David, C.; Lehnert, D.; Bastmeyer, M.; Bonhoeffer, F. Microcontact Printing of Axon Guidance Molecules for Generation of Graded Patterns. *Nat. Protoc.* **2006**, *1* (3), 1322–1328.

(155) Offenhaeusser, A.; Boecker-Meffert, S.; Decker, T.; Helpenstein, R.; Gasteier, P.; Groll, J.; Moeller, M.; Reska, A.; Schaefer, S.; Schulte, P.; et al. Microcontact Printing of Proteins for Neuronal Cell Guidance. *Soft Matter* **2007**, *3* (3), 290–298.

(156) Ricoult, S. G.; Thompson-Steckel, G.; Correia, J. P.; Kennedy, T. E.; Juncker, D. Tuning Cell-Surface Affinity to Direct Cell Specific Responses to Patterned Proteins. *Biomaterials* **2014**, *35* (2), 727–736.

(157) Vogt, A. K.; Lauer, L.; Knoll, W.; Offenhäusser, A. Micropatterned Substrates for the Growth of Functional Neuronal Networks of Defined Geometry. *Biotechnol. Prog.* **2003**, *19* (5), 1562–1568.

(158) Lauer, L.; Vogt, A.; Yeung, C. K.; Knoll, W.; Offenhäusser, A. Electrophysiological Recordings of Patterned Rat Brain Stem Slice Neurons. *Biomaterials* **2002**, *23* (15), 3123–3130.

(159) Schwaab, D.; Zentis, P.; Winter, S.; Meffert, S.; Offenhäusser, A.; Mayer, D. Generation of Protein Nanogradients by Microcontact Printing Generation of Protein Nanogradients by Microcontact Printing. *Japenese J. Appl. Phys.* **2013**, *52* (5 pt. 2), 05DA19.

(160) Wasserberg, D.; Steentjes, T.; Stopel, M. H. W.; Huskens, J.; Blum, C.; Subramaniam, V.; Jonkheijm, P. Patterning Perylenes on Surfaces Using Thiol–ene Chemistry. *J. Mater. Chem.* **2012**, *22* (32), 16606.

(161) Hensarling, R. M.; Doughty, V. a; Chan, J. W.; Patton, D. L. "Clicking" polymer Brushes with Thiol-Yne Chemistry: Indoors and Out. *J. Am. Chem. Soc.* **2009**, *131* (41), 14673–14675.

(162) Alge, D. L.; Azagarsamy, M. a; Donohue, D. F.; Anseth, K. S. Synthetically Tractable Click Hydrogels for Three-Dimensional Cell Culture Formed Using Tetrazine-Norbornene Chemistry. *Biomacromolecules* **2013**, *14* (4), 949–953.

(163) Ingavle, G. C.; Gehrke, S. H.; Detamore, M. S. The Bioactivity of Agarose-PEGDA Interpenetrating Network Hydrogels with Covalently Immobilized RGD Peptides and Physically Entrapped Aggrecan. *Biomaterials* **2014**, *35* (11), 3558–3570.

(164) Hern, D. L.; Hubbell, J. A. Incorporation of Adhesion Peptides into Nonadhesive Hydrogels Useful for Tissue Resurfacing. *J. Biomed. Mater. Res.* **1998**, *39* (2), 266–276.

(165) Wu, J.; Huang, C.; Liang, W.; Wu, Y.; Yu, J.; Chen, H. Reactive Polymer Coatings: A

General Route to Thiol-Ene and Thiol-Yne Click Reactions. *Macromol. Rapid Commun.* **2012**, *33* (10), 922–927.

(166) van Wermeskerken, G. K. A.; van Olphen, A. F.; Smoorenburg, G. F. Intra- and Postoperative Electrode Impedance of the Straight and Contour Arrays of the Nucleus 24 Cochlear Implant: Relation to T and C Levels. *Int. J. Audiol.* **2006**, *45* (9), 537–544.

(167) Paasche, G.; Franziska, B.; Tasche, C.; Lesinski-Schiedat, A.; Lenarz, T. Changes of Postoperative Impedances in Cochlear Implant Patients: The Short-Term Effects of Modified Electrode Surfaces and Intracochlear Corticosteroids. *Otol. Neurotol.* **2006**, *27* (5), 639–647.

(168) Busby, P.; Plant, K.; Whitford, L. Electrode Impedance in Adults and Children Using the Nucleus 24 Cochlear Implant System. *Cochlear Implants Int.* **2002**, *3* (2), 87–103.

(169) Darouiche, R. O. Device-Associated Infections: A Macroproblem That Starts with Microadherence. *Clin. Infect. Dis.* **2001**, *33* (9), 1567–1572.

(170) Cheng, G.; Zhang, Z.; Chen, S.; Bryers, J. D.; Jiang, S. Inhibition of Bacterial Adhesion and Biofilm Formation on Zwitterionic Surfaces. *Biomaterials* **2007**, *28* (29), 4192–4199.

(171) Kyomoto, M.; Shobuike, T.; Moro, T.; Yamane, S.; Takatori, Y.; Tanaka, S.; Miyamoto, H.; Ishihara, K. Prevention of Bacterial Adhesion and Biofilm Formation on a Vitamin E-Blended, Cross-Linked Polyethylene Surface with a poly(2-Methacryloyloxyethyl Phosphorylcholine) Layer. *Acta Biomater.* **2015**, *24*, 24–34.

(172) Cheng, G.; Li, G.; Xue, H.; Chen, S.; Bryers, J. D.; Jiang, S. Zwitterionic Carboxybetaine Polymer Surfaces and Their Resistance to Long-Term Biofilm Formation. *Biomaterials*

2009, *30* (28), 5234–5240.

(173) Decker, C. Kinetic Study and New Applications of UV Radiation Curing. *Macromol. Rapid Commun.* **2002**, *23* (18), 1067–1093.

(174) Chatani, S.; Kloxin, C. J.; Bowman, C. N. The Power of Light in Polymer Science: Photochemical Processes to Manipulate Polymer Formation, Structure, and Properties. *Polym. Chem.* **2014**, *5* (7), 2187–2201.

(175) Bowman, C. N.; Kloxin, C. J. Toward an Enhanced Understanding and Implementation of Photopolymerization Reactions. *AIChE J.* **2008**, *54* (11), 2775–2795.

(176) Hoyle, C. E. Photocurable Coatings. *ACS Symp. Ser.* **1990**, *417*, 1–16.

(177) Lub, J.; Broer, D. J.; Van de Witte, P. Colourful Photo-Curable Coatings for Application in the Electro-Optical Industry. *Prog. Org. Coatings* **2002**, *45* (2–3), 211–217.

(178) Cheng, W. T.; Chih, Y. W.; Yeh, W. T. In Situ Fabrication of Photocurable Conductive Adhesives with Silver Nano-Particles in the Absence of Capping Agent. *Int. J. Adhes. Adhes.* **2007**, *27* (3), 236–243.

(179) Hirasawa, T.; Taniguchi, J.; Ohtaguchi, M.; Sakai, N. Photo-Curable Resins and Evaluation Methods for UV-Nanoimprint Lithography. *Electron. Commun. Japan* **2009**, *92* (11), 51–56.

(180) Spivey, E. C.; Ritschdorff, E. T.; Connell, J. L.; McLennon, C. a.; Schmidt, C. E.; Shear, J. B. Multiphoton Lithography of Unconstrained Three-Dimensional Protein Microstructures. *Adv. Funct. Mater.* **2013**, *23* (3), 333–339.

(181) Bates, C. M.; Maher, M. J.; Janes, D. W.; Ellison, C. J.; Willson, C. G. Block Copolymer

Lithography. *Macromolecules* **2014**, *47* (1), 2–12.

(182) Crivello, J. V.; Reichmanis, E. Photopolymer Materials and Processes for Advanced Technologies. *Chem. Mater.* **2014**, *26* (1), 533–548.

(183) Gao, W.; Zhang, Y.; Ramanujan, D.; Ramani, K.; Chen, Y.; Williams, C. B.; Wang, C. C. L.; Shin, Y. C.; Zhang, S.; Zavattieri, P. D. The Status, Challenges, and Future of Additive Manufacturing in Engineering. *Comput. Des.* **2015**, *69*, 65–89.

(184) DeForest, C. A.; Anseth, K. S. Photoreversible Patterning of Biomolecules within Click-Based Hydrogels. *Angew. Chemie* **2012**, *124* (8), 1852–1855.

(185) Clarke, J. C.; Tuft, B. W.; Clinger, J. D.; Levine, R.; Figueroa, L. S.; Guymon, C. A.; Hansen, M. R. Micropatterned Methacrylate Polymers Direct Spiral Ganglion Neurite and Schwann Cell Growth. *Hear. Res.* **2011**, *278* (1–2), 96–105.

(186) Shoichet, M. S. Polymer Scaffolds for Biomaterials Applications. *Macromolecules* **2010**, *43* (2), 581–591.

(187) Tsang, V. L.; Chen, a. a.; Cho, L. M.; Jadin, K. D.; Sah, R. L.; DeLong, S.; West, J. L.; Bhatia, S. N. Fabrication of 3D Hepatic Tissues by Additive Photopatterning of Cellular Hydrogels. *FASEB J.* **2007**, *21* (3), 790–801.

(188) Luo, Y.; Shoichet, M. S. Light-Activated Immobilization of Biomolecules to Agarose Hydrogels for Controlled Cellular Response. *Biomacromolecules* **2004**, *5* (6), 2315–2323.

(189) Li, S.; Tuft, B. W.; Xu, L.; Polacco, M. a.; Clarke, J. C.; Guymon, C. A.; Hansen, M. R. Microtopographical Features Generated by Photopolymerization Recruit RhoA/ROCK through TRPV1 to Direct Cell and Neurite Growth. *Biomaterials* **2015**, *53*, 95–106.

(190) Zhou, D.; Ito, Y. Visible Light-Curable Polymers for Biomedical Applications. *Sci. China Chem.* **2014**, *57* (4), 510–521.

(191) Torgersen, J.; Qin, X. H.; Li, Z.; Ovsianikov, A.; Liska, R.; Stampfl, J. Hydrogels for Two-Photon Polymerization: A Toolbox for Mimicking the Extracellular Matrix. *Adv. Funct. Mater.* **2013**, *23* (36), 4542–4554.

(192) Ovsianikov, A.; Mühleder, S.; Torgersen, J.; Li, Z.; Qin, X.-H.; Van Vlierberghe, S.; Dubruel, P.; Holnthoner, W.; Redl, H.; Liska, R.; et al. Laser Photofabrication of Cell-Containing Hydrogel Constructs. *Langmuir* **2014**, *30* (13), 3787–3794.

(193) Bent, D. V.; Hayon, E. Excited State Chemistry of Aromatic Amino Acids and Related Peptides. III. Tryptophan. *J. Am. Chem. Soc.* **1975**, *97* (10), 2612–2619.

(194) Bent, D. V.; Hayon, E. Excited State Chemistry of Aromatic Amino Acids and Related Peptides. II. Phenylalanine. *J. Am. Chem. Soc.* **1975**, *97* (10), 2606–2612.

(195) Bent, D. V.; Hayon, E. Excited State Chemistry of Aromatic Amino Acids and Related Peptides. I. Tyrosine. *J. Am. Chem. Soc.* **1975**, *97* (10), 2599–2606.

(196) Neves-Petersen, M. T.; Klitgaard, S.; Pascher, T.; Skovsen, E.; Polivka, T.; Yartsev, A.; Sundstrom, V.; Petersen, S. B. Flash Photolysis of Cutinase: Identification and Decay Kinetics of Transient Intermediates Formed upon UV Excitation of Aromatic Residues. *Biophys. J.* **2009**, *97* (1), 211–226.

(197) Bahney, C. S.; Lujan, T. J.; Hsu, C. W.; Bottlang, M.; West, J. L.; Johnstone, B. Visible Light Photoinitiation of Mesenchymal Stem Cell-Laden Bioresponsive Hydrogels. *Eur. Cells Mater.* **2011**, *22*, 43–55.

(198) Quick, D. J.; Anseth, K. S. Gene Delivery in Tissue Engineering: A Photopolymer Platform to Coencapsulate Cells and Plasmid DNA. *Pharm. Res.* **2003**, *20* (11), 1730–1737.

(199) Rånby, B. Surface Modification and Lamination of Polymers by Photografting. *Int. J. Adhes. Adhes.* **1999**, *19* (5), 337–343.

(200) Goda, T.; Konno, T.; Takai, M.; Moro, T.; Ishihara, K. Biomimetic Phosphorylcholine Polymer Grafting from Polydimethylsiloxane Surface Using Photo-Induced Polymerization. *Biomaterials* **2006**, *27* (30), 5151–5160.

(201) Cheng, E. L.; Leigh, B.; Guymon, C. A.; Hansen, M. R. Quantifying Spiral Ganglion Neurite and Schwann Behavior on Micropatterned Polymer Substrates. *Methods Mol. Biol.* **2016**, *1427*, 305–318.

(202) Sterman, S.; Marsden, J. G. Silane Coupling Agents. *Ind. Eng. Chem.* **1966**, *58* (3), 33–37.

(203) Leigh, B. L.; Truong, K.; Bartholomew, R.; Ramirez, M.; Hansen, M. R.; Guymon, C. A. Tuning Surface Properties on Acrylate Photopolymers to Investigate Competitive Guidance of Spiral Ganglion Neurons. *ACS Appl. Mater. Interfaces* **2017**, *9* (37), 31488–31496.

(204) Leigh, B. L.; Cheng, E. L.; Andresen, C.; Hansen, M. R.; Guymon, C. A. Photopolymerizable Zwitterionic Polymer Patterns Control Cell Adhesion and Guide Neural Growth. *Biomacromolecules* **2017**, *18* (8), 2389–2401.

(205) Wirthington, K. S. Ph.D. Thesis: Control of Polymer Biochemical, Mechanical, and Physical Properties for the Rational Design of Retinal Regenerative Tissue Scaffolds, The

University of Iowa, 2014.

(206) Végh, J. The Shirley-Equivalent Electron Inelastic Scattering Cross-Section Function. *Surf. Sci.* **2004**, *563* (1–3), 183–190.

(207) Kaewkhaw, R.; Scutt, A. M.; Haycock, J. W. Integrated Culture and Purification of Rat Schwann Cells from Freshly Isolated Adult Tissue. *Nat. Protoc.* **2012**, *7* (11), 1996–2004.

(208) Leach, J. B.; Achyuta, A. K. H.; Murthy, S. K. Bridging the Divide between Neuroprosthetic Design, Tissue Engineering and Neurobiology. *Front. Neuroeng.* **2010**, *2*, 18.

(209) Scholz, C. Perspectives on: Materials Aspects for Retinal Prostheses. *J. Bioact. Compat. Polym.* **2007**, *22* (5), 539–568.

(210) Tang, X.; Ali, M. Y.; Saif, M. T. A. A Novel Technique for Micro-Patterning Proteins and Cells on Polyacrylamide Gels. *Soft Matter* **2012**, *8* (27), 7197–7206.

(211) Truong, K.; Leigh, B.; Bartholomew, R.; Xu, L.; Guymon, C. A.; Hansen, M. R. Micropatterned Topographical and Biochemical Cues Direct Neurite Growth from Spiral Ganglion Neurons. *J. Tissue Eng. Regen. Med.* (Submitted).

(212) Deng, C.; Wu, J.; Cheng, R.; Meng, F.; Klok, H.-A.; Zhong, Z. Functional Polypeptide and Hybrid Materials: Precision Synthesis via α-Amino Acid N-Carboxyanhydride Polymerization and Emerging Biomedical Applications. *Prog. Polym. Sci.* **2014**, *39* (2), 330–364.

(213) Kundu, A.; Micholt, L.; Friedrich, S.; Rand, D. R.; Bartic, C.; Braeken, D.; Levchenko, A. Superimposed Topographic and Chemical Cues Synergistically Guide Neurite Outgrowth.

Lab Chip **2013**, *13* (15), 3070–3081.

(214) Hansen, M. R.; Vijapurkar, U.; Koland, J. G.; Green, S. H. Reciprocal Signaling between Spiral Ganglion Neurons and Schwann Cells Involves Neuregulin and Neurotrophins. *Hear. Res.* **2001**, *161* (1–2), 87–98.

(215) Hegarty, J. L.; Kay, A. R.; Green, S. H. Trophic Support of Cultured Spiral Ganglion Neurons by Depolarization Exceeds and Is Additive with That by Neurotrophins or cAMP and Requires Elevation of [Ca2+]i within a Set Range. *J. Neurosci.* **1997**, *17* (6), 1959–1970.

(216) Subramanian, A.; Krishnan, U. M.; Sethuraman, S. Development of Biomaterial Scaffold for Nerve Tissue Engineering: Biomaterial Mediated Neural Regeneration. *J. Biomed. Sci.* **2009**, *16*, 108.

(217) Kam, L.; Shain, W.; Turner, J. N.; Bizios, R. Axonal Outgrowth of Hippocampal Neurons on Micro-Scale Networks of Polylysine-Conjugated Laminin. *Biomaterials* **2001**, *22* (10), 1049–1054.

(218) Koh, H. S.; Yong, T.; Chan, C. K.; Ramakrishna, S. Enhancement of Neurite Outgrowth Using Nano-Structured Scaffolds Coupled with Laminin. *Biomaterials* **2008**, *29* (26), 3574–3582.

(219) Haile, Y.; Berski, S.; Dräger, G.; Nobre, A.; Stummeyer, K.; Gerardy-Schahn, R.; Grothe, C. The Effect of Modified Polysialic Acid Based Hydrogels on the Adhesion and Viability of Primary Neurons and Glial Cells. *Biomaterials* **2008**, *29* (12), 1880–1891.

(220) Luse, R. A.; McLaren, A. D. Mechamisn of Enzyme Inactivation by Uultraviolet Light

and the Photochemistry of Amino Acids. *Photochem. Photobiol.* **1963**, *2* (3), 343–360.

(221) Kerwin, B. A.; Remmele, L. J. Protect from Light: Photodegradation and Protein Biologics. *J. Pharm. Sci.* **2007**, *96* (6), 1468–1479.

(222) Xu, H.; Huskens, J. Versatile Stamps in Microcontact Printing: Transferring Inks by Molecular Recognition and from Ink Reservoirs. *Chemistry* **2010**, *16* (8), 2342–2348.

(223) Wrzeszcz, A.; Steffens, M.; Balster, S.; Warnecke, A.; Dittrich, B.; Lenarz, T.; Reuter, G. Hydrogel Coated and Dexamethasone Releasing Cochlear Implants: Quantification of Fibrosis in Guinea Pigs and Evaluation of Insertion Forces in a Human Cochlea Model. *J. Biomed. Mater. Res. Part B Appl. Biomater.* **2015**, *103* (1), 169–178.

(224) Honeder, C.; Zhu, C.; Schöpper, H.; Gausterer, J. C.; Walter, M.; Landegger, L. D.; Saidov, N.; Riss, D.; Plasenzotti, R.; Gabor, F.; et al. Effects of Sustained Release Dexamethasone Hydrogels in Hearing Preservation Cochlear Implantation. *Hear. Res.* **2016**, *341*, 43–49.

(225) Wang, X.; Dellamary, L.; Fernandez, R.; Ye, Q.; Lebel, C.; Piu, F. Principles of Inner Ear Sustained Release Following Intratympanic Administration. *Laryngoscope* **2011**, *121* (2), 385–391.

(226) Taub, A. H.; Hogri, R.; Magal, A.; Mintz, M.; Shacham-Diamand, Y. Bioactive Anti-Inflammatory Coating for Chronic Neural Electrodes. *J. Biomed. Mater. Res. Part A* **2012**, *100 A* (7), 1854–1858.

(227) Li, G.; Cheng, G.; Xue, H.; Chen, S.; Zhang, F.; Jiang, S. Ultra Low Fouling Zwitterionic Polymers with a Biomimetic Adhesive Group. *Biomaterials* **2008**, *29* (35), 4592–4597.

(228) Diaz Blanco, C.; Ortner, A.; Dimitrov, R.; Navarro, A.; Mendoza, E.; Tzanov, T. Building an Antifouling Zwitterionic Coating on Urinary Catheters Using an Enzymatically Triggered Bottom-up Approach. *ACS Appl. Mater. Interfaces* **2014**, *6* (14), 11385–11393.

(229) Wang, M.; Yuan, J.; Huang, X.; Cai, X.; Li, L.; Shen, J. Grafting of Carboxybetaine Brush onto Cellulose Membranes via Surface-Initiated ARGET-ATRP for Improving Blood Compatibility. *Colloids Surfaces B Biointerfaces* **2013**, *103*, 52–58.

(230) Dorman, M. F.; C, L. P.; Spahr, A. J.; Erin, M. A Comparison of the Speech Understanding Provided by and Channel-Picking Signal Processors for Cochlear Implants. *J. Speech, Lang. Hear. Res.* **2002**, *45* (4), 783–788.

(231) Ranck, J. B. Which Elements Are Excited in Electrical Stimulation of Mammalian Central Nervous System: A Review. *Brain Res.* **1975**, *98* (3), 417–440.

(232) Fu, Q. J.; Nogaki, G. Noise Susceptibility of Cochlear Implant Users: The Role of Spectral Resolution and Smearing. *J. Assoc. Res. Otolaryngol.* **2005**, *6* (1), 19–27.

(233) Daly, W.; Yao, L.; Zeugolis, D.; Windebank, A.; Pandit, A. A Biomaterials Approach to Peripheral Nerve Regeneration: Bridging the Peripheral Nerve Gap and Enhancing Functional Recovery. *J. R. Soc. Interface* **2012**, *9* (67), 202–221.

(234) Corey, J. M.; Lin, D. Y.; Mycek, K. B.; Chen, Q.; Samuel, S.; Feldman, E. L.; Martin, D. C. Aligned Electrospun Nanofibers Specify the Direction of Dorsal Root Ganglia Neurite Growth. *J. Biomed. Mater. Res. Part A* **2007**, *83A* (3), 636–645.

(235) Wang, H. B.; Mullins, M. E.; Cregg, J. M.; Hurtado, A.; Oudega, M.; Trombley, M. T.; Gilbert, R. J. Creation of Highly Aligned Electrospun Poly-L-Lactic Acid Fibers for

Nerve Regeneration Applications. *J. Neural Eng.* **2009**, *6* (1), 16001.

(236) Greiner, A. M.; Jäckel, M.; Scheiwe, A. C.; Stamow, D. R.; Autenrieth, T. J.; Lahann, J.; Franz, C. M.; Bastmeyer, M. Multifunctional Polymer Scaffolds with Adjustable Pore Size and Chemoattractant Gradients for Studying Cell Matrix Invasion. *Biomaterials* **2014**, *35* (2), 611–619.

(237) Adams, D. N.; Kao, E. Y.-C.; Hypolite, C. L.; Distefano, M. D.; Hu, W.-S.; Letourneau, P. C. Growth Cones Turn and Migrate up an Immobilized Gradient of the Laminin IKVAV Peptide. *J. Neurobiol.* **2005**, *62* (1), 134–147.

(238) Yao, L.; McCaig, C. D.; Zhao, M. Electrical Signals Polarize Neuronal Organelles, Direct Neuron Migration, and Orient Cell Division. *Hippocampus* **2009**, *19* (9), 855–868.

(239) Yao, L.; Shanley, L.; Mccaig, C.; Zhao, M. Small Applied Electric Fields Guide Migration of Hippocampal Neurons. *J. Cell. Physiol.* **2008**, *216* (2), 527–535.

(240) Richardson, J. a; Rementer, C. W.; Bruder, J. M.; Hoffman-Kim, D. Guidance of Dorsal Root Ganglion Neurites and Schwann Cells by Isolated Schwann Cell Topography on Poly(dimethyl Siloxane) Conduits and Films. *J. Neural Eng.* **2011**, *8* (4), 46015.

(241) Lah, G. J.; Key, B. Novel Roles of the Chemorepellent Axon Guidance Molecule RGMa in Cell Migration and Adhesion. *Mol. Cell. Biol.* **2012**, *32* (5), 968–980.

(242) Lah, G. J.; Key, B. Dual Roles of the Chemorepellent Axon Guidance Molecule RGMa in Establishing Pioneering Axon Tracts and Neural Fate Decisions in Embryonic Vertebrate Forebrain. *Dev. Neurobiol.* **2012**, *72* (11), 1458–1470.

(243) Heimrich, B.; Vogt, J.; Simbuerger, E.; Skutella, T.; Glumm, R. Axon Guidance and the

Formation of Specific Connections in the Hippocampus. *Neuroembryology* **2002**, *1* (4), 154–160.

(244) Thompson, D. M.; Buettner, H. M. Neurite Outgrowth Is Directed by Schwann Cell Alignment in the Absence of Other Guidance Cues. *Ann. Biomed. Eng.* **2006**, *34* (1), 161–168.

(245) Wen, X.; Tresco, P. A. Effect of Filament Diameter and Extracellular Matrix Molecule Precoating on Neurite Outgrowth and Schwann Cell Behavior on Multifilament Entubulation Bridging Device in Vitro. *J. Biomed. Mater. Res. Part A* **2006**, *76A* (3), 626–637.

(246) Turner, J. N.; Shain, W.; Szarowski, D. H.; Andersen, M.; Martins, S.; Isaacson, M.; Craighead, H. Cerebral Astrocyte Response to Micromachined Silicon Implants. *Exp. Neurol.* **1999**, *156* (1), 33–49.

(247) Xie, Y.; Martini, N.; Hassler, C.; Kirch, R. D.; Stieglitz, T.; Seifert, A.; Hofmann, U. G. In Vivo Monitoring of Glial Scar Proliferation on Chronically Implanted Neural Electrodes by Fiber Optical Coherence Tomography. *Front. Neuroeng.* **2014**, *7*, 34.

(248) Jeon, E. J.; Xu, N.; Xu, L.; Hansen, M. R. Influence of Central Glia on Spiral Ganglion Neuron Neurite Growth. *Neuroscience* **2011**, *177*, 321–334.

(249) Mccarthy, K.; De Vellis, J. Preparation of Separate Astroglial and Oligodendroglial Cell Cultures from Rat Cerebral Tissue. *J. Cell Biol.* **1980**, *85* (3), 890–902.

(250) Roehm, P. C.; Xu, N.; Woodson, E. A.; Green, S. H.; Hansen, M. R. Membrane Depolarization Inhibits Spiral Ganglion Neurite Growth via Activation of Multiple Types

of Voltage Sensitive Calcium Channels and Calpain. *Mol. Cell. Neurosci.* **2008**, *37* (2), 376–387.

(251) Sin, M.-C.; Lou, P.-T.; Cho, C.-H.; Chinnathambi, A.; Alharbi, S. A.; Chang, Y. An Intuitive Thermal-Induced Surface Zwitterionization for Versatile, Well-Controlled Haemocompatible Organic and Inorganic Materials. *Colloids Surfaces B Biointerfaces* **2015**, *127*, 54–64.

(252) Powell, E. M.; Geller, H. M. Dissection of Astrocyte-Mediated Cues in Neuronal Guidance and Process Extension. *Glia* **1999**, *26* (1), 73–83.

(253) Barres, B. A. The Mystery and Magic of Glia: A Perspective on Their Roles in Health and Disease. *Neuron* **2008**, *60* (3), 430–440.

(254) Schildge, S.; Bohrer, C.; Beck, K.; Schachtrup, C. Isolation and Culture of Mouse Cortical Astrocytes. *J. Vis. Exp.* **2013**, No. 71, e50079.

(255) Monk, K. R.; Feltri, M. L.; Taveggia, C. New Insights on Schwann Cell Development. *Glia* **2015**, *63* (8), 1376–1393.

(256) Whitlon, D. S.; Tieu, D.; Grover, M.; Reilly, B.; Coulson, M. T. Spontaneous Association of Glial Cells with Regrowing Neurites in Mixed Cultures of Dissociated Spiral Ganglia. *Neuroscience* **2009**, *161* (1), 227–235.

(257) Boström, M.; Khalifa, S.; Boström, H.; Liu, W.; Friberg, U.; Rask-Andersen, H. Effects of Neurotrophic Factors on Growth and Glial Cell Alignment of Cultured Adult Spiral Ganglion Cells. *Audiol. Neurotol.* **2010**, *15* (3), 175–186.

(258) Roche, J. P.; R., H. M. On the Horizon: Cochlear Implant Technology. *Otolaryngol. Clin.*

North Am. **2015**, *48* (6), 1097–1116.

(259) Pfingst, B. E.; Bowling, S. A.; Colesa, D. J.; Garadat, S. N.; Raphael, Y.; Shibata, S. B.; Strahl, S. B.; Su, G. L.; Zhou, N. Cochlear Infrastructure for Electrical Hearing. *Hear. Res.* **2011**, *281* (1–2), 65–73.

(260) Ishai, R.; Herrmann, B. S.; Nadol, J. B.; Quesnel, A. M. The Pattern and Degree of Capsular Fibrous Sheaths Surrounding Cochlear Electrode Arrays. *Hear. Res.* **2017**, *348*, 44–53.

(261) Nadol J.B., J.; Burgess, B. J.; Gantz, B. J.; Coker, N. J.; Ketten, D. R.; Kos, I.; Roland J.T., J.; Jiun Yih Shiao, D. K.; Eddington, D. K.; Montandon, P.; et al. Histopathology of Cochlear Implants in Humans. *Ann. Otol. Rhinol. Laryngol.* **2001**, *110* (9), 883–891.

(262) Seyyedi, M.; Nadol, J. B. Intracochlear Inflammatory Response to Cochlear Implant Electrodes in Humans. *Otol. Neurotol.* **2014**, *35* (9), 1545–1551.

(263) Ishiyama, A.; Doherty, J.; Ishiyama, G.; Quesnel, A. M.; Lopez, I.; Linthicum, F. H. Post Hybrid Cochlear Implant Hearing Loss and Endolymphatic Hydrops. *Otol. Neurotol.* **2016**, 1516–1521.

(264) Yoda, R. Elastomers for Biomedical Applications. *J. Biomater. Sci. Polym. Ed.* **1998**, *9* (6), 561–626.

(265) Yang, W.; Xue, H.; Li, W.; Zhang, J.; Jiang, S. Pursuing “Zero” Protein Adsorption of Poly(carboxybetaine) from Undiluted Blood Serum and Plasma. *Langmuir* **2009**, *25* (19), 11911–11916.

(266) Yang, W. T.; Rhnby, B. The Role of Far UV Radiation in the Photografting Process.

Polym. Bull. **1996**, *37* (1), 89–96.

(267) Bengt, R. Surface Modification of Polymers by Photointiated Graft Polymerization. *Makromol. Chemie, Macromol. Symp.* **1992**, *63*, 55–67.

(268) Lin, W.; Ma, G.; Wu, J.; Chen, S. Different in Vitro and in Vivo Behaviors between Poly(carboxybetaine Methacrylate) and Poly(sulfobetaine Methacrylate). *Colloids Surfaces B Biointerfaces* **2016**, *146*, 888–894.

(269) Ratner, B. D.; Miller, I. F. Transport through Crosslinked poly(2-hydroxyethyl Methacrylate) Hydrogel Membranes. *J. Biomed. Mater. Res.* **1973**, *7* (4), 353–367.

(270) Hoffman, A. S. Hydrogels for Biomedical Applications. *Adv. Drug Deliv. Rev.* **2002**, *54*, 3–12.

(271) Lee, K. Y.; Mooney, D. J. Hydrogels for Tissue Engineering. *Chem. Rev.* **2001**, *101* (7), 1869–1879.

(272) Wichterle, O.; Bartl, P.; Rosenberg, M. Water-Soluble Methacrylates as Embedding Media for Preparation of Ultra-Thin Sections. *Nature* **1960**, *186* (4723), 494–495.

(273) Tibbitt, M. W.; Anseth, K. S. Hydrogels as Extracellular Matrix Mimics for 3D Cell Culture. *Biotechnol. Bioeng.* **2009**, *103* (4), 655–663.

(274) Castillo, E. J.; Koenig, J. L.; Anderson, J. M.; Lo, J. Protein Adsorption on Hydrogels. *Biomaterials* **1985**, *6* (5), 338–345.

(275) Refojo, M. F.; Yasuda, H. Hydrogels from 2-Hydroxyethyl Methacrylate and Propylene Glycol Monoacrylate. *J. Appl. Polym. Sci.* **1965**, *9* (7), 2425–2435.

(276) Refojo, M. F. *Application of Materials in Medice and Dentistry: Ophthalmologic*

Applications; 1996.

(277) Peppas, N. A.; Hilt, J. Z.; Khademhosseini, A.; Langer, R. Hydrogels in Biology and Medicine: From Molecular Principles to Bionanotechnology. *Adv. Mater.* **2006**, *18* (11), 1345–1360.

(278) Lin, C. C.; Anseth, K. S. PEG Hydrogels for the Controlled Release of Biomolecules in Regenerative Medicine. *Pharm. Res.* **2009**, *26* (3), 631–643.

(279) Abraham, S.; Brahim, S.; Ishihara, K.; Guiseppi-Elie, A. Molecularly Engineered p(HEMA)-Based Hydrogels for Implant Biochip Biocompatibility. *Biomaterials* **2005**, *26*, 4767–4778.

(280) Kostina, N. Y.; Rodriguez-Emmenegger, C.; Houska, M.; Brynda, E.; Michálek, J. Non-Fouling Hydrogels of 2-Hydroxyethyl Methacrylate and Zwitterionic Carboxybetaine (Meth)acrylamides. *Biomacromolecules* **2012**, *13* (12), 4164–4170.

(281) Zhang, Z.; Chao, T.; Jiang, S. Physical, Chemical, and Chemical-Physical Double Network of Zwitterionic Hydrogels. *J. Phys. Chem. B* **2008**, *112* (17), 5327–5332.

(282) Huglin, M. B.; Rego, J. M. Influence of Temperature on Swelling and Mechanical Properties of a Sulphobetaine Hydrogel. *Polymer.* **1991**, *32* (18), 3354–3358.

(283) Ning, J.; Li, G.; Haraguchi, K. Synthesis of Highly Stretchable, Mechanically Tough, Zwitterionic Sulfobetaine Nanocomposite Gels with Controlled Thermosensitivities. *Macromolecules* **2013**, *46* (13), 5317–5328.

(284) Carr, L. R.; Zhou, Y.; Krause, J. E.; Xue, H.; Jiang, S. Uniform Zwitterionic Polymer Hydrogels with a Nonfouling and Functionalizable Crosslinker Using

Photopolymerization. *Biomaterials* **2011**, *32* (29), 6893–6899.